ASME
SETTING THE STANDARD

Transactions of the ASME, Journal of Fluids Engineering (ISSN 0098-2202) is published monthly by The American Society of Mechanical Engineers, Three Park Avenue, New York, NY 10016. Periodicals postage paid at New York, NY and additional mailing offices.
POSTMASTER: Send address changes to Transactions of the ASME, Journal of Fluids Engineering, c/o THE AMERICAN SOCIETY OF MECHANICAL ENGINEERS, 22 Law Drive, Box 2300, Fairfield, NJ 07007-2300.
CHANGES OF ADDRESS must be received at Society headquarters seven weeks before they are to be effective. Please send old label and new address.
STATEMENT from By-Laws. The Society shall not be responsible for statements or opinions advanced in papers or ... printed in its publications (B7.1, Par. 3).

Journal of Fluids Engineering

Published Monthly by ASME

VOLUME 130 • NUMBER 1 • JANUARY 2008

RESEARCH PAPERS

Flows in Complex Systems

Fundamental Issues and Canonical Flows

Multiphase Flows

(Contents continued on inside back cover)

This journal is printed on acid-free paper, which exceeds the ANSI Z39.48-1992 specification for permanence of paper and library materials. ♾™
♻ 85% recycled content, including 10% post-consumer fibers.

Journal of Fluids Engineering **Volume 130, Number 1** **JANUARY 2008**

Techniques and Procedures

The ASME Journal of Fluids Engineering is abstracted and indexed in the following:

Applied Science & Technology Index, Chemical Abstracts, Chemical Engineering and Biotechnology Abstracts (Electronic equivalent of Process and Chemical Engineering), Civil Engineering Abstracts, Computer & Information Systems Abstracts, Corrosion Abstracts, Current Contents, Ei EncompassLit, Electronics & Communications Abstracts, Engineered Materials Abstracts, Engineering Index, Environmental Engineering Abstracts, Environmental Science and Pollution Management, Excerpta Medica, Fluidex, Index to Scientific Reviews, INSPEC, International Building Services Abstracts, Mechanical & Transportation Engineering Abstracts, Mechanical Engineering Abstracts, METADEX (The electronic equivalent of Metals Abstracts and Alloys Index), Petroleum Abstracts, Process and Chemical Engineering, Referativnyi Zhurnal, Science Citation Index, SciSearch (The electronic equivalent of Science Citation Index), Shock and Vibration Digest, Solid State and Superconductivity Abstracts, Theoretical Chemical Engineering

Discrete Particle Study of Turbulence Coupling in a Confined Jet Gas-Liquid Separator

Wayne Strasser
Eastman Chemical Company,
P.O. Box 511, Building 54-D,
Kingsport, TN 37662

A 3D computational fluid dynamics investigation of particle-induced flow effects and liquid entrainment from an industrial-scale separator has been carried out using the Eulerian–Lagrangian two-way coupled multiphase approach. A differential Reynolds stress model was used to predict the gas phase turbulence field. The dispersed (liquid) phase was present at an intermediate mass loading (0.25) but low volume fraction (0.05). A discrete random walk method was used to track the paths of the liquid droplet releases. It was found that gas phase deformation and turbulence fields were significantly impacted by the presence of the liquid phase; these effects have been parametrically quantified. Substantial enhancement of both the turbulence and the anisotropy of the continuous phase by the liquid phase was demonstrated. It was also found that a large number ($\geqslant$1000) *of independent liquid droplet release events were needed to make conclusions about liquid entrainment. Known plant run conditions and entrainment rates validated the numerical method.* [DOI: 10.1115/1.2816008]

Introduction and Method

Background. Gas-liquid, gas-solid, and liquid-solid separators are integral operations in many industrial processes. The goal of the gas-liquid separator, for example, is to separate a mixture of gas and liquid into two distinct, essentially pure, streams. A gas stream exiting with no liquid is said to contain no carryover or entrainment. The presence of dispersed particulate material in a continuous stream can influence the dynamics of the continuous stream (two-way coupling). An experimental cyclone study by Obermair et al. [1] discussed the effects of particles on vortex flow at a loading of 6.5×10^{-4}. They found that the presence of the particles greatly increased turbulence and reduced the strength of the vortex in the cyclone downcomer. Similarly, the reduction of the tangential velocity in the bottom of a cyclone by the presence of solids was discussed by Gil et al. [2]. The authors showed that for solids loading in the range of 0.1, the solids-induced swirl reduction lowered the overall pressure drop of the unit. Vandu and Krishna [3] found that the mass transfer coefficient in a bubble column is reduced by the presence of solids at a loading of 0.25. They proposed that this is a result of increased gas bubble coalescence caused by a solids-induced decrease of turbulence dissipation. Faeth [4] found that anisotropy was increased in gas jets involving liquid sprays. Ahmadi and Abu-Zaid [5] performed a numerical analysis of anisotropic dense two-phase flows with a similar density ratio as in the present work. They showed significant mixture normal stress differences for shear rates two orders of magnitude greater than those of the present study. The turbulence production and dissipation were governed by the continuous phase, generally, but there was significant fluctuation energy transfer from the particulate phase to the continuous phase for a particulate volume fraction $>$0.5. Graham [6] discussed an analytical study of particles in a homogeneous shear flow. He found the carrier phase production:dissipation ratio and anisotropy increased by the inclusion of particles. He proposes, however, for a given strain rate that the turbulence kinetic energy is attenuated if the particle diameter is low compared to turbulence scales (wakeless). He showed that continuous phase turbulence enhancement is only possible for very high mass loadings ($>$1) and Stokes numbers above $\sim$5. Mostafa et al. [7] showed a reduction in turbulence and increase in anisotropy by particulates in an unconfined jet using experimental and k-ε calculations. They expanded on previous work, showing that the attenuation is greater, the smaller the ratio of particle to gas phase velocity fluctuations is. It should be noted that their figures do not show much of an effect by the particles. Early in the jet development, it appears that there is even a slight kinetic energy enhancement by the particles. The interpretation of these plots is made more difficult by the fact that they are not the same physical size on the page. Also, perhaps area-averaged results might be more valuable since the velocity profile is altered by the particles. Lastly, a thorough study of interparticle collisions in particle-laden tube flow was provided by Boree and Caraman [8]. They found a departure from the Tchen theory even at mass loadings as low as 0.11. They also found gas phase turbulence attenuation and a flatter mean velocity profile, but the local damping was dependent on mass loading. At higher loadings (1.1), the damping was only near the walls, while at 0.6 loading, damping occurred at the axis. They proposed that near-wall anisotropy caused by particle collisional effects is influential on the radial tube flow profile down to volume fractions lower than 0.01. To the author's knowledge, no study exists in the open literature that quantifies particle-induced anisotropy in parametric terms for a complex flow field.

Objective. The objective of the present work is twofold. Primarily, the work was begun in order to develop a model that would be useful in predicting responses in costly liquid carryover to changes in geometric configuration for a large-scale industrial gas-liquid separator. Before separator geometry changes could be evaluated, a basis had to be established using sound numerical methods within the most advanced commercially available Eulerian–Lagrangian (EL) options from Fluent, Inc. It was desired to match the experimental carryover value to within 10% with an experimentally determined droplet size as the dispersed phase ba-

Contributed by the Fluids Engineering Division of ASME for publication in the JOURNAL OF FLUIDS ENGINEERING. Manuscript received November 15, 2006; final manuscript received August 7, 2007; published online December 19, 2007. Review conducted by Malcolm J. Andrews. Paper presented at the Turbulence, Heat and Mass Transfer 5, 2006.

sis. Secondly, due to the apparent deficit of parametric particle-induced anisotropy information in the open literature, it is valuable to quantify said effects within the context of the aforementioned commercially available numerics.

Physics. Thorough comparisons of typical methods for numerically treating fluid-particle flows were given in Crowe et al. [9]. It has been argued (Heinl and Bohnet [10] and Fluent, Inc. [11]) that it is more advantageous to treat the dispersed phase via Lagrangian tracking (as opposed to Eulerian) methods for particle volume fractions below ~0.1. Of course, this is a controversial topic. It is explained in Crowe et al. [9] that for particle volume fractions above 0.1, particle volume should not be ignored. The question, therefore, is: Can we find a useful solution for a system with a solids volume fraction of half of this value using a discrete method? For the purposes of modifying the design of an industrial separator and evaluating any improvements in carryover, it is probable that we can. The methods set forth here are not perfect, as is no numerical method, but the quantification of anisotropy and modulation discussed herein gives the reader a reasonable starting point.

In the EL method, paths of individual particles, or statistical groups of particles (sometimes referred to as "parcels"), are tracked through the continuous phase via Newton's second law force balance,

$$\frac{du_{pj}}{dt} = F_{Dj} + F_{gj} + F_{Lj} \quad \text{(forces due to drag, gravity, and lift, respectively)} \tag{1}$$

$$F_{Dj} = \frac{C_D \mathrm{Re}_p}{24\tau_p}(u_{pj} - u_{cj}) \quad \tau_p = \frac{\rho_p d_p^2}{18\mu_c}$$

$$\mathrm{Re}_p = \frac{\rho_c u_s d_p}{\mu_c} \quad u_s = \sqrt{(u_{pj} - u_{cj})^2} \tag{2}$$

$$F_{gj} = \frac{g_j(\rho_p - \rho_c)}{\rho_p} \quad \text{and}$$

$$F_{Lj} = \frac{5.19\upsilon^{1/2}\rho_c(\partial u_{ci}/\partial x_j)}{\rho_p d_p((\partial u_{cl}/\partial x_k)(\partial u_{ck}/\partial x_l))^{1/4}}(u_{ci} - u_{pi}) \tag{3}$$

$$C_D = a_1 + \frac{a_2}{\mathrm{Re}_p} - \frac{a_3}{\mathrm{Re}_p^2} \tag{4}$$

A series of fixed monodisperse particle diameters is tested in the present study. Considering the Morton, Eotvos, and particle Reynolds numbers for these droplets, it is estimated that they are spherical in shape (Clift et al. [12]). Although droplet internal circulations and surface tension/contamination effects are known to influence drag coefficient (Clift et al. [12], others), the rigid particle assumption is valid for the extremely high viscosity ratio (>55) in this study. The drag coefficient can, therefore, be approximated by the correlation of Morsi and Alexander [13] for rigid spherical particles, as shown in Eq. (4). The coefficients $a_1 - a_3$ depend on the particle Reynolds number, as outlined in Fluent, Inc. [11]. The lift force correlation is valid only for relatively low shear Reynolds numbers (<1.0, Clift et al. [12]), which is the case in the present work.

Discrete random walk (DRW) falls into a general class of discrete element methods, which Crowe et al. [9] proposed are useful for studying dilute or dense flows. Both phases are fully coupled through mean and fluctuating velocities. It is assumed that particle groups (or parcels that might contain 10^4 particles, for example) and fluid elements follow different trajectories and only interact for finite periods of time. The particle groups interact with eddies whose scales are resolved by the continuous phase turbulence model. When using DRW in Eqs. (1)–(4), the continuous phase velocity is expressed as the mean plus the fluctuating value. The fluctuating velocity values are discrete piecewise functions of time. They are assumed to remain constant as long as the parcel is under the influence of a given eddy structure. This length of interaction time is the minimum of two values, either the randomized characteristic eddy lifetime or the eddy crossing time scale shown below,

$$\tau_{\mathrm{el}} = -0.3\frac{k}{\varepsilon}\ln(r) \quad \text{or} \quad \tau_{\mathrm{ec}} = -\tau_p \ln\left[1 - \frac{l}{\tau_p|u_c - u_p|}\right] \quad \text{with} \quad l = 0.24\frac{k^{3/2}}{\varepsilon} \tag{5}$$

The constant 0.3 can be a function of mass loading (Graham [6]), but that aspect has been ignored here in that this study involves much lower loadings than that of Graham [6]. Fluent, Inc. [11] suggested using the Lagrangian constant 0.3 and the Eulerian constant 0.24 when the Reynolds stress model (RSM) approach is employed. Typical Reynolds-averaged Navier–Stokes (RANS)-resolved length scales are two orders larger than the particle diameters of the present work, so the particles would be classified as wakeless according to Graham. When the smaller of these two time scales is exceeded, a new random fluctuating continuous phase velocity component is generated via

$$u'_{cj,\mathrm{new}} = \zeta\sqrt{\overline{u'^2_{cj,\mathrm{old}}}} \tag{6}$$

If the product of the slip velocity and the particle relaxation time is less than the resolved length scale, the eddy crossing time is not even computed; the eddy lifetime value is utilized. A known shortcoming (Crowe et al. [9]) of methods that superimpose chaotic fluctuations on the mean is the inability to predict antidispersion of particles in the peripheries of vortical structures for intermediate (near unity) Stokes numbers (Zheng et al. [14]). The continuous phase time scale in the Stokes number calculation is that of the turbulence and not the mean velocity field, as discussed in Sommerfeld [15]. For the range of particle diameters studied, the particle Stokes numbers are in this intermediate regime; however, the DRW method includes enough physics to be a useful approximation to the real particle spreading in the separator for this design study. The maximum diameter for which interparticle collisions can be ignored can be deduced from discussions in Crowe et al. [9] and Soo [16],

$$d_p < \frac{1.33\mu_c}{Z\rho_c\sigma_p} \quad \frac{\sigma_p}{\sigma_c} \approx 0.02 \quad \sigma_c = \sqrt{\frac{2}{3}k} \tag{7}$$

Monodisperse particle sizes for this computational fluid dynamics (CFD) study are near or below this critical value. As a result, ignoring interparticle collisions is reasonable.

Turbulence modulation by Lagrangian particles can involve additional terms included in the turbulence closure equations, as discussed in Faeth [4], Amsden et al. [17], Xiong et al. [18], Mostafa et al. [7], and Graham [6]. All, except Graham [6], framed the additional terms as sources/sinks in the typical eddy-viscosity k and ε transport equations; Graham [6] developed sources for an algebraic RSM based on the Stokesian drag assumption. Fluent followed the methods of Amsden et al. [18], in which the particles act to extract turbulence kinetic energy from the continuous phase as long as the particle diameter is smaller than 10% of the largest turbulent length scale (l in Eq. (5)); above this, the reverse occurs. A preliminary test using a two-equation turbulence model was carried out to estimate the influence of these terms for the current separator flow scenario. The results with and without the source terms were indistinguishable; therefore, additional source terms were not considered in the present work.

The steady incompressible RANS Eulerian linear momentum balance in Cartesian coordinates for the continuous phase is shown in

$$\frac{\partial u_{cj}u_{ci}}{\partial x_j} = \nu_c \frac{\partial^2 u_{ci}}{\partial x_j \partial x_j} - \frac{\partial \langle u'_{ci}u'_{cj}\rangle}{\partial x_j} - \frac{1}{\rho_c}\frac{\partial p}{\partial x_i} + S_i \tag{8}$$

$$S_i = \frac{m_h}{\nu_{\text{cell}} t_{\text{res}}}(u_{pi,\text{cell–exit}} - u_{pi,\text{cell–inlet}})_h \tag{9}$$

Notice that the volume fraction occupied by the dispersed phase is not explicitly included in Eq. (8), which is the reason for the ~0.1 upper limit on the dispersed phase volume fraction.

The advantages of using the RSM approach in modeling continuous phase turbulence include natural realizability and the ability to capture the effects of streamline curvature, turbulence anisotropy, and rapid changes in strain rate. Streamline curvature is a dominant feature of the present work as the flowing material must turn 180 deg onto itself between entering and exiting the separator. Since the goal was to investigate anisotropy, it has to be computed. The Reynolds stress tensor components are obtained by the solution of the steady, incompressible differential equation

$$\frac{\partial(u_{ck}\langle u'_{ci}u'_{cj}\rangle)}{\partial x_k} = \frac{\partial}{\partial x_k}\left[\nu_c \frac{\partial\langle u'_{ci}u'_{cj}\rangle}{\partial x_k} - \langle u'_{ci}u'_{cj}u'_{ck}\rangle - \frac{1}{\rho_c}\langle p(\delta_{kj}u'_{ci} + \delta_{ik}u'_{cj})\rangle\right] - \left(\langle u'_{ci}u'_{ck}\rangle\frac{\partial u_{cj}}{\partial x_k} + \langle u'_{cj}u'_{ck}\rangle\frac{\partial u_{ci}}{\partial x_k}\right) + \frac{1}{\rho_c}\left\langle p\left(\frac{\partial u'_{ci}}{\partial x_j} + \frac{\partial u'_{cj}}{\partial x_i}\right)\right\rangle - 2\nu_c\left\langle \frac{\partial u'_{ci}}{\partial x_k}\frac{\partial u'_{cj}}{\partial x_k}\right\rangle \tag{10}$$

The terms on the right-hand side are as follows: Diffusion (molecular, followed by turbulent), production, pressure strain, and dissipation. Production and molecular diffusion need no modeling, but the others do. The Launder, Reece and Rodi-Isotropization of Production (LLR-IP) (Launder et al. [19] and Fluent, Inc. [11]) approach for modeling Reynolds stresses is used for the present work. The turbulent diffusive stress transport is treated with the gradient-diffusion hypothesis, and the dissipation is modeled assuming isotropy. Pressure strain is well known to be one of the most important terms; it has zero trace and serves to redistribute the stresses and move toward the isotropic state. In the present work, the pressure-strain model incorporates a linear return-to-isotropy term (or "slow"), a rapid pressure-strain term, and a wall-reflection term. The Speziale–Sarkar–Gatski (SSG) [20] approach offers a quadratic return-to-isotropy approach with no wall reflection. Employment of the SSG model was attempted on multiple occasions using various "coaxing" techniques (including temporarily adjusting the nonlinear slow term's model coefficient), but the commercial solver continually diverged. Hanjalic [21] proposed that RSM convergence difficulty is a fundamental problem with the typical Navier–Stokes solver and outlined improvements to alleviate these problems. A nonequilibrium wall function approach was used for the near-wall cells as discussed in Fluent, Inc. [11]. This method involves typical wall functions that have been modified to relax the production=dissipation assumption. Given that this geometry has no severe adverse pressure gradients, this option seems reasonable for the intent of the present work.

The author is aware that the RANS approach cannot resolve turbulence scale information below that of the largest scale, and results in the smearing out of some transients/unsteadiness (Speziale [22], many others). Pope [23] presented that the normalized Reynolds stress tensor is not enough to completely describe the evolution of turbulence. He showed direct numerical simulation (DNS) simulations resulting in two differing trajectories on the ξ-η plane (definitions forthcoming) with the same starting RANS conditions. In the present work, the shedding of vortices where the entry jet meets the counterflow in the vessel should produce a rich, time-dependent 3D solution. However, because the overall effort aims at eventual optimization of the real industrial-scale process, it was desired to focus the investigation on steady, Reynolds-averaged methods more suitable for design applications.

Numerics and Boundary Conditions. Second-order upwinding with linear reconstruction (Fluent, Inc. [11]) was used for all spatial variables except turbulence dissipation rate, as second-order upwinding dissipation inhibited convergence. A third-order monotone upstream-centered schemes for conservation laws (MUSCL) scheme is available in this commercial release but does not contain flux limiters and could cause local overshoots where the flow is not aligned with the grid. Derivatives were discretized using the nodal method (weighted by nodal values on surrounding faces instead of simple arithmetical grid cell center averages). The solver was run in double precision mode due to expectations of low values of carryover. The SIMPLE algorithm was used for pressure-velocity coupling via the segregated implicit solver. An advanced multidimensional slope limiting scheme (total variation diminishing) was utilized to prevent a variable overshoot. Pressure checkerboarding was prevented using a second-order Rhie–Chow method. An algebraic multigrid was used to reduce large wave error propagation. The author is aware of the proliferation of CFD "abuse" (quotation from Hanjalic [21] regarding LES), so more details on the importance and ramifications of sound numerics are discussed in Strasser [24].

The mesh, involving prisms, tetrahedra, hexahedra, and pyramids, was built with the intent to balance computational load and accuracy. The smallest grid length scales were near the inlet and outlet. The expansion of cells away from the inlet and outlet to areas with lesser gradients was carried out in such a way as to minimize cell aspect ratios, centroid shifts, and skewness. More on these concepts can be found in the transonic gas turbine blade passage research of Strasser et al. [25]. Wall resolution was set such that the first cell was within the log-law region. More will be discussed on grid dependence in upcoming sections. Particle trajectory ordinary differential equations are solved using a high-order Runge–Kutta with embedded error control, as discussed in Fluent [11]. As previously discussed, the present computations ignore the volume of the particles. The smallest computational cell length scale is, therefore, kept much larger than the particle diameter.

The diverging gas jet inlet is given a fixed uniform velocity, while the parcels injected (or released) at this inlet are given the same uniform velocity. The parcels are equally distributed over the inlet by area since that is the case for the commercial production-scale unit. It is expected that carryover will be sensitive to the placement of the particles at the inlet, so the commercial unit had to be mimicked as much as possible. The results below will represent data from sequential parcel release events with a prescribed number of continuous phase numerical iterations between each release. During these in-between continuous phase iterations, no particles are released; they are only tracked from the inlet to the outlet in a Lagrangian sense. The outlet is a fixed pressure outlet. It is known from internal testing that the liquid droplets will adhere to any wall whenever they come into contact inside the separator. All of the wall boundaries were, therefore, set to "escape." In other words, the particles were no longer accounted for after they contacted a wall. Only those particles that were found in the outlet at the top of the vessel were considered to be carried over (entrainment). Wall effects, such as adhesion, electrostatics, particle-particle effects, wall roughness (Heinl and Bohnet [10]), and particle-collision-induced anisotropy (Boree and Caraman [8]) have been ignored in the present work since they do not apply.

Measures. Turbulence anisotropy is important for a number of reasons, one of which being that normal turbulent stresses only contribute to the production of turbulence kinetic energy and momentum transport when they are unequal (Pope [23]). Also, anisotropy dictates that the turbulence modeling approach, i.e. two-equation linear eddy-viscosity models, are, by definition, not able

to predict anisotropy. Quantification of anisotropy will be carried out using the Lumley triangle (from Pope [23] and Lumley [26]) two-parameter approach,

$$6\eta^2 = b_{cij}b_{cji} = -2\mathrm{II}_{\mathrm{NRAT}} \quad \text{and} \quad 6\xi^3 = b_{cij}b_{cjk}b_{cki} = 3\mathrm{III}_{\mathrm{NRAT}} \tag{11}$$

Each normalized Reynolds stress anisotropy tensor (NRAT) component is found by

$$b_{cij} = \frac{\langle u'_{ci}u'_{cj}\rangle - (2/3)k\delta_{ij}}{2k} \quad \text{with determinant } F = 1 - 27\eta^2 + 54\xi^3 \tag{12}$$

The Lumley triangle is a nearly triangular map bounded by stress realizability and centered about $\xi=0$. The boundary curves represent special states of turbulence, with the point farthest away from the origin being a one-component turbulence (one fluctuating velocity component dominates) at $\eta=\xi=1/3$. All values of η are positive. Positive values of ξ have been shown to exist in near-wall flow, while negative values of ξ have been found in a turbulent mixing layer. A determinant of zero indicates anything on the uppermost bounding curve of the triangle (two component and one component), while a value of unity indicates isotropic turbulence. Also, from a mixing study of Galletti et al. [27], a single parameter is proposed for measuring the deviation from the origin on the Lumley triangle,

$$L = \sqrt{\mathrm{III}_{\mathrm{NRAT}}^2 + (-\mathrm{II}_{\mathrm{NRAT}})^2} \quad \text{normalized by } L_{\max} = 0.34 \tag{13}$$

Deformation classification is addressed by Pirozzoli and Grasso [28] for both the incompressible flow of the present study and compressible flow. They characterize flow based on the three principal mean deformation tensor invariants (Aris [29]),

$$P = -\mathrm{I}_{\mathrm{DT}} = -(\lambda_1+\lambda_2+\lambda_3) \quad Q = \mathrm{II}_{\mathrm{DT}} = \lambda_1\lambda_2+\lambda_1\lambda_3+\lambda_2\lambda_3$$

$$R = -\mathrm{III}_{\mathrm{DT}} = -\lambda_1\lambda_2\lambda_3$$

$$\Delta = \frac{27}{4}R^2 + R\left(P^3 - \frac{9}{2}PQ\right) + \left(Q^3 - \frac{1}{4}P^2Q^2\right) \tag{14}$$

which is the "discriminant." The authors also discussed the relative size of the eigenvalues to one another, with typical values being related by the ratio 1:-4:3.

Results

Overall Flow Field and Carryover. The separator geometry is a vertical cylindrical vessel, half of which is shown in Fig. 1. The gas-particle mixture enters from the top of the vessel through a divergent entry that extends into the vessel about a third of its total height. The feed mixture disperses into a turbulent jet that interacts with a reverse mixture flow returning upward from the vessel bottom. Jet spreading is coupled with stagnation. Gravity, dispersion, and residence time allow most of the droplets to segregate toward the bottom of the vessel, while the gas escapes through an exit near the top. Figure 1 depicts radial velocity contours from a preliminary gas-only analysis. Red on this plot indicates any velocity that is greater than the theoretical particle slip velocity. The vessel average velocity magnitude is larger than the theoretical particle slip velocity, so there is a propensity for liquid material to be carried over. Only the bottom section of the vessel is "safe" (blue) for droplets.

A typical scatter sample series of carryover (liquid exiting through gas outlet) for the "base" particle diameter is shown in Fig. 2. These represent 1000 sequential independent particle injections (particle release events), as discussed in the section on boundary conditions. The DRW approach allows for randomization within the turbulence field computations, so truly random releases of particles are considered. The average is ~900 ppm by weight based on the inlet liquid-particle feed rate. The standard

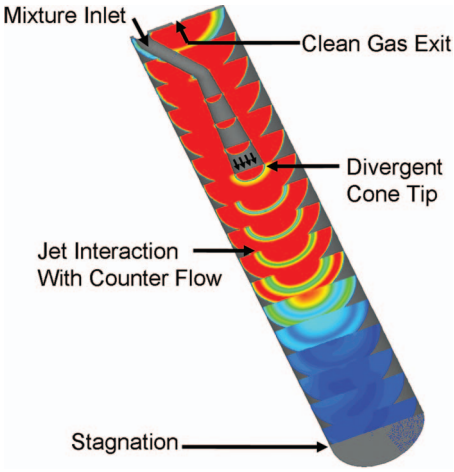

Fig. 1 Contours of velocity along radial slices for a preliminary 3D gas-only study. Red indicates the gas that has a velocity magnitude greater than the base particle slip velocity. The gray color marks the vessel walls.

deviation is ~1000 pmm by weight. With a standard deviation larger than the mean, it is expected that many samples have to be run before confidence can be gained in the mean. For example, two pairs of tests were run with identical CFD setups. When 70 particle release events were used, the two resulting means were 660 ppm by weight and 820 ppm by weight. For 1000 release events, the mean carryover rates were 920 ppm by weight and 940 ppm by weight. Because the last pair's means were close enough for purposes of this study, a minimum data set size of 1000 injections will be used from here forward.

Carryover rates were sensitive to fluid-particle coupling. For example, if the particles are just released into the fluid with no feedback onto the continuous phase, the carryover rates are more than three times the coupled carryover value. Coupling allows more droplets to accumulate in the vessel bottom. Figure 3 shows typical instantaneous droplet concentration contours without (left) and with (right) coupling on a vessel center cut. The radial particle spreading is much greater without coupling, so more of the particles get caught in the gas upwash. The flow issues that contribute to this will be discussed later.

The carryover results (average and standard deviation) were extremely sensitive to assumed particle size, as one might expect. When the mean particle diameter was increased 50% above the base particle size, the mean carryover rate fell to 0. Not one of the 1000 injections resulted in any liquid carryover. On the other hand, when the particle size was reduced to ~50% of the base value, the mean carryover rose from 900 ppm by weight to nearly 5000 ppm by weight. The standard deviation fell from a value

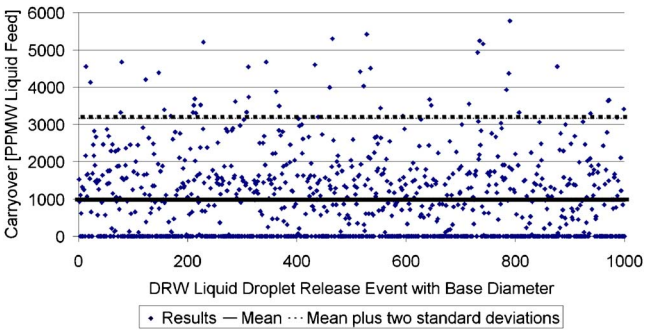

Fig. 2 Typical carryover samples for coupled base particle size. The mean is ~900 ppm by weight.

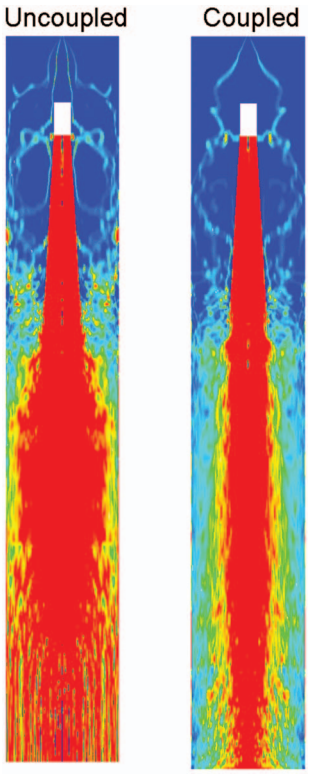

Fig. 3 Typical instantaneous contours of particle concentration with and without feedback from particles of base diameter on a vessel center cut

larger than the mean to a value that was about half of the mean. Experimental data were provided for a real production unit of the same dimensions, feed rates, and properties of those modeled here. The experimental carryover rate was 5200 ppm by weight. It is known through internal plant testing (and results from external consultant experimentation with Plexiglass units) that the three CFD particle size values considered in this work are within a reasonable range for the real industrial mean particle size. The base diameter is at the upper end of the diameter range found from the experimental work, and the smaller size (50% of the base diameter) is at the lower end of the range. The standard deviation is not able to be obtained from the experimental data due to the fact that each experimental data point represents an average of 120 vessel residence times worth of continuous particle feed data. There are no independent samples to measure in a production unit. In addition, no turbulence field information is available from the separator units. Just as particle size plays an important role, the drag coefficient calculations would play an equally important role. The correlation used in Eq. (4) is valid over the range of parameters studied, so no further investigation was executed.

Numerical Tests and Grid Independence. There remains some questions in the open literature as to the importance of various features of the EL approach. In the present study, EL features were evaluated for their effects on the results, both in terms of the mean and standard deviation liquid carryover. It is has been proposed in Faeth [4] that approximately 5000 particle groups are needed per injection for a stochastic two-way coupled approach. Li and Wang [30] proposed that 1250 particle groups are required for independent results in their gas turbine film cooling effectiveness study. They also proposed that the number of particle groups per grid point plays little importance in the outcome and that higher turbulence intensity augments droplet dispersion, as one would expect.

Table 1 summarizes the findings in the present set of studies. "Not significant" is defined as a change of $\leqslant 3\%$. The number of groups tracked per injection, number of groups per inlet grid cell, momentum under-relaxation, and particle steps per cell length proved to be unimportant considerations in the EL setup, in terms of the mean. More groups tracked per injection resulted in reduced variability. For reference, each particle group of 1000 contains O (10^5) particles. Substantially increasing the number of continuous phase iterations per particle injection only changed the mean of 10%. Increasing intensity reduced carryover by spreading particles out more radially and azimuthally. The eddy lifetime constant had an inverse effect on carryover. Increasing this constant increases the length of time a continuous phase flow structure interacts with relatively small particles, holding them back. It makes sense that this would reduce the number of particles carried out of the vessel. Lastly, grid resolution was increased in all three dimensions until a grid-independent solution was reached. Increased resolution gives the particles less resistance to radial and azimuthal dispersion. Less liquid is carried over as a result. Since the flow resistance is lessened, injection-to-injection uniqueness is cultivated, and the standard deviation is increased. The carryover mean only changed 1% from 3× to 4× grid resolution, so 3× was considered sufficient. Grid independence, along with the other numerical findings from Table 1 tests, was incorporated in the run that produced the 5000 ppm by weight results mentioned in the previous experimental validation discussion.

2.3 Particle Feedback Onto the Continuous Field. The turbulence field is sensitive to the presence of the particles. Figure 4 shows a typical instantaneous continuous phase turbulent viscosity ratio without (left) and with (right) fluid-particle coupling for the base particle size. The turbulent viscosity ratio is defined as the ratio of turbulent viscosity to the molecular viscosity. The range on this figure is 0 (blue) to the peak ratio seen in the uncoupled case (red). The peak turbulent viscosity region is much larger and is pulled axially downward in the vessel due to particle drag and fluid-particle shear. The sensitivity of the turbulence field to particle inclusion is consistently shown in Fig. 5, offering con-

Table 1 Numerical test effects on liquid droplet carryover

Item tested	Range tested	Effect on	
		Mean	Standard deviation
N continuous phase iterations between particle injection	10→500	+10%	Not significant
N particle groups injected per inlet cell	10→20	Not significant	−30%
N particle groups tracked	1000→2000	Not significant	−30%
Characteristic eddy lifetime Constant	0.15→0.3	−25%	Not significant
Momentum coupling under-relaxation	0.1→0.3	Not significant	Not significant
Feed turbulence intensity	5%→10%	−10%	Not significant
Particle Lagrangian steps per cell length scale	5→10	Not significant	Not significant
Grid resolution	1×→3×	−40%	+20%

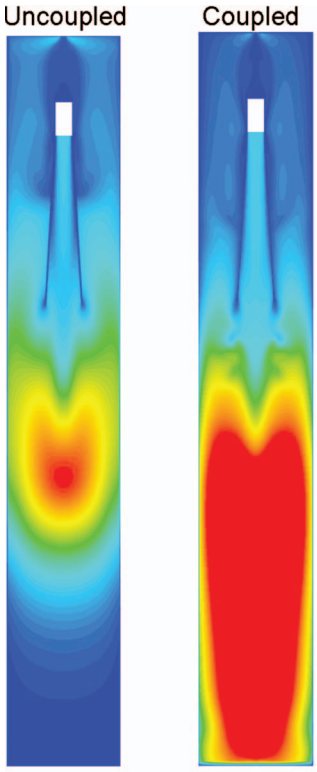

Fig. 4 Typical instantaneous contours of turbulence viscosity ratio with and without feedback from particles of base diameter on a vessel center cut

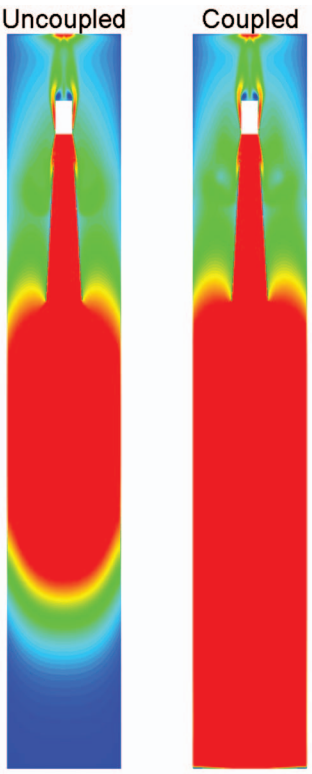

Fig. 6 Typical instantaneous contours of turbulence intensity (normalized by superficial velocity) with and without feedback from particles of base diameter

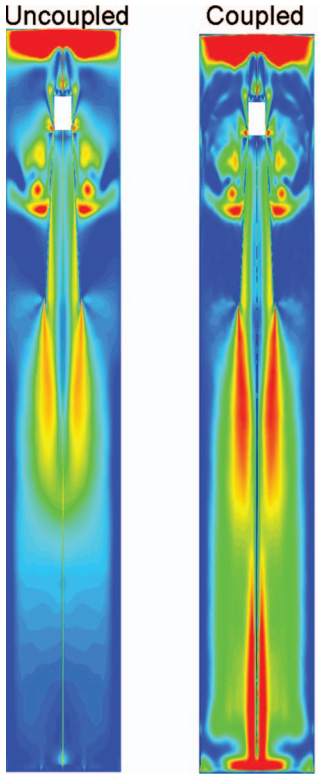

Fig. 5 Typical instantaneous contours of production:dissipation ratio with and without feedback from particles of base diameter

tours of the ratio of production:dissipation of turbulence kinetic energy. The range on these plots is ≤ 0 (blue) to ≥ 2 (red), so anything blue represents a negative production. Production is increased both at the inlet jet interface and the near-bottom centerline area by the inclusion of the particle-fluid feedback. Turbulence intensity (normalized by superficial velocity) is shown in Fig. 6 over the range of 0–100%. Intensity appears to only be increased by particle feedback, the opposite of the attenuation spoken of in the Background section. More will be discussed on this later.

Figures 7–9 depict these same effects graphically for a few CFD cases. Each quantity is mass weighted area averaged (MFWAA) on axial cutting planes beginning at the tip of the inlet

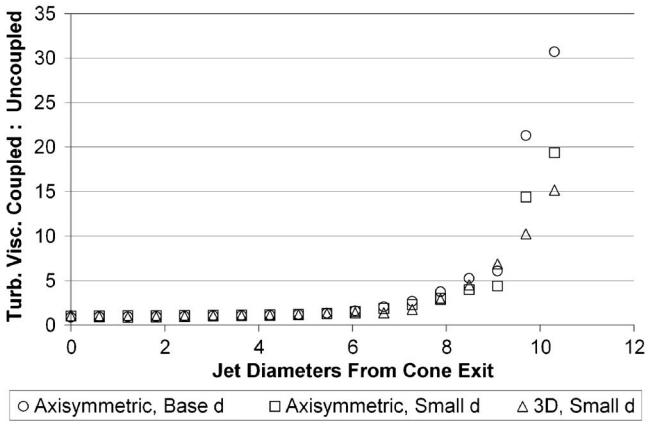

Fig. 7 Planar average coupled:uncoupled ratios on axial slices showing turbulence viscosity ratio for three pairs of cases

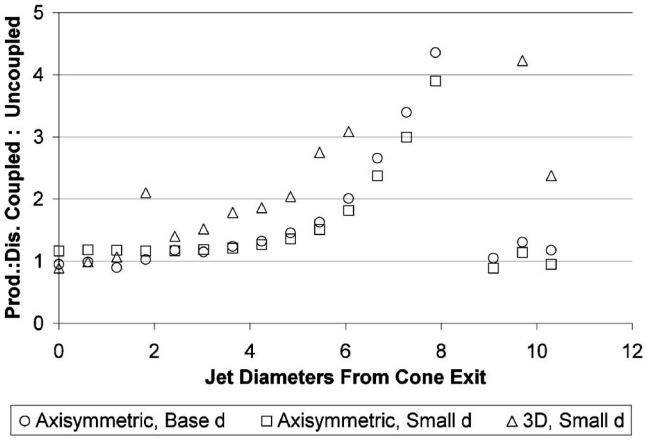

Fig. 8 Planar average coupled:uncoupled ratios on axial slices showing turbulence production:dissipation for three pairs of cases

divergent cone. These cutting planes extend more than 10 jet diameters down from the cone, with the bottom of the vessel at 13 diameters. The graphed value is a ratio of the value calculated in the coupled (EL) model to the value calculated in the uncoupled (gas-only) model. Starting in Fig. 7, it is seen that the turbulent viscosity ratio increases dramatically along the axis as a result of particle inclusion. The base particle diameter axisymmetric model, the smaller diameter axisymmetric model, and the smaller diameter 3D model all respond in about the same manner. The "smaller" diameter here is ~50% of the base diameter, as discussed in the section on carryover. Coupling suppresses turbulence at the beginning of the jet (less than 1.0), but increases turbulent viscosity ratio by a factor of ~15 near the cutting plane at ten jet diameters. Production:dissipation (Fig. 8) is increased substantially at most axial planes. The peak increase depends on whether the model is 2D or 3D and, to a much lesser extent, on the size of the droplets. The 3D model shows a much more rapid increase in production:dissipation with increasing distance from the cone. Lastly, axial turbulence intensity (normalized by superficial velocity) dependence is shown in Fig. 9. Intensity is increased substantially as the flow proceeds along the jet, interacts with the reverse flow, and stagnates at the vessel bottom. As with turbulent viscosity ratio, particle size and 2D/3D effects play almost no role in the intensity results. All of these show a trend opposite of what was expected based on the attenuation discussions in the open literature. It is proposed that the primary cause of said enhancement is the increase in strain rate by the particles. The volume-averaged strain rate is 60% larger for the coupled case for the base particle diameter. In terms of area-averaged values at various axial locations (like Figs. 7–9, but not shown), the couple:uncoupled strain rate values are all above 1.0 and reach as high as 10 along the vessel. The most recent applicable open literature study, that of Graham [6], showed that production:dissipation is increased by particles. It was only when the strain field was held constant that the turbulence was attenuated by the particles. Another reason for the turbulence enhancement in the present work is the unique geometry of the present study. This is not a homogeneous shear flow like that discussed in Graham [6] or an unconfined jet like that of Mostafa et al. [7]. As the mixture approaches the bottom, the particles begin disengaging while the gas is redirected. This raises the slip velocity, reduces eddy crossing time, and pumps fluctuations of the continuous phase velocity into equations shown previously. Presumably, this would involve a situation similar to that of cyclone separators, like that of Obermair et al. [1], in which turbulence enhancement has been found.

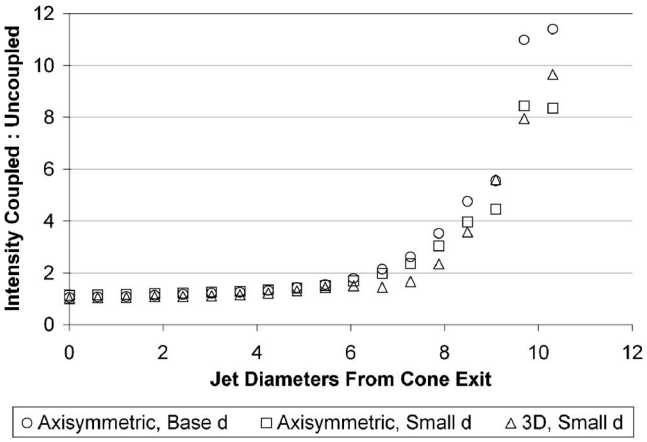

Fig. 9 Planar average coupled:uncoupled ratios on axial slices showing turbulence intensity (normalized by superficial velocity) for three pairs of cases

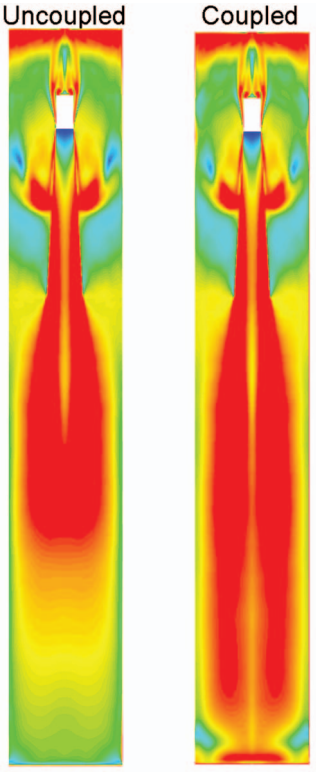

Fig. 10 Typical instantaneous contours of the first Reynolds stress anisotropy tensor parameter on a vessel center cut

The next four figures help explain the turbulence anisotropy fields, with and without coupling for the base particle size. In all cases, blue is $\leqslant$ the lowest value and red is $\geqslant$ the highest value mentioned in the corresponding text discussion. Figure 10 shows contours of the first stress anisotropy tensor parameter, η, with a range of 0–0.125. It can be seen that there is an increase in overall anisotropy by coupling, especially along the vessel center near the bottom. The second stress anisotropy tensor parameter, ξ, effects can be seen in Fig. 11 for the range of −0.1 to 0.1. There is a range of states present, but the coupling increases the tendency toward one component in the bottom half. Figure 12 depicts contours of the determinant (Eq. (12)) of the NRAT over the range of 0 to 1. Just as in the other cases, there is more anisotropy (lower values of determinant) in the lower vicinity of the vessel caused by particles. Contours of the normalized distance (Eq. (13)) from the

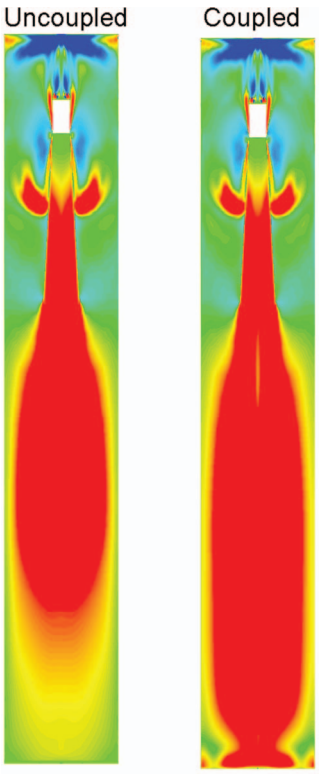

Fig. 11 Typical instantaneous contours of the second Reynolds stress anisotropy tensor parameter on a vessel center cut

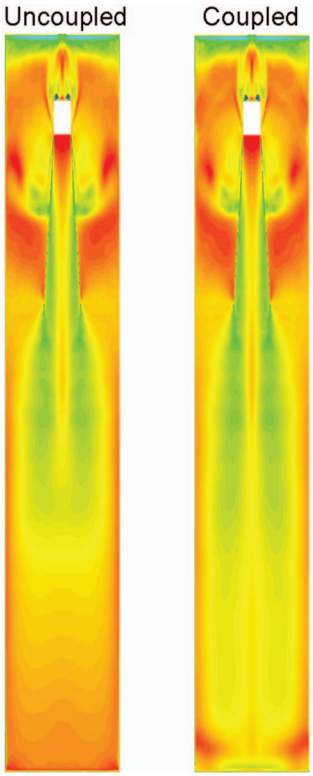

Fig. 12 Typical instantaneous contours of the Lumley triangle determinant on a vessel center cut

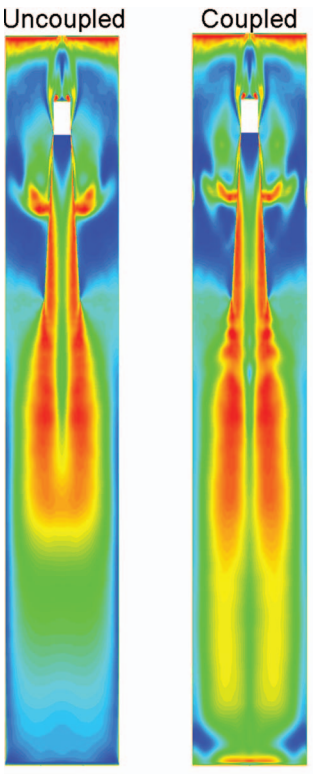

Fig. 13 Typical instantaneous contours of the normalized length on a vessel center cut

Lumley origin (0–0.2) are shown in Fig. 13. These plots look similar to those in Fig. 10, where coupling causes an increase in departure at the jet interface and jet impingement zone.

Figures 14 and 15 show MFWAA coupled:uncoupled ratios for both the normalized length (Eq. (13)) and determinant (Eq. (12)), respectively, for the same three pairs of cases discussed in previous figures along the vessel axial direction. Both show increasing departure from isotropy with distance. The axisymmetric results did not depend heavily on particle diameter. One would expect these two figures to be nearly mirror images of one another since they measure anisotropy in opposite directions. The normalized distance appears to be a more sensitive measure (than F) of the departure from isotropy, as it shows more relative deviation from

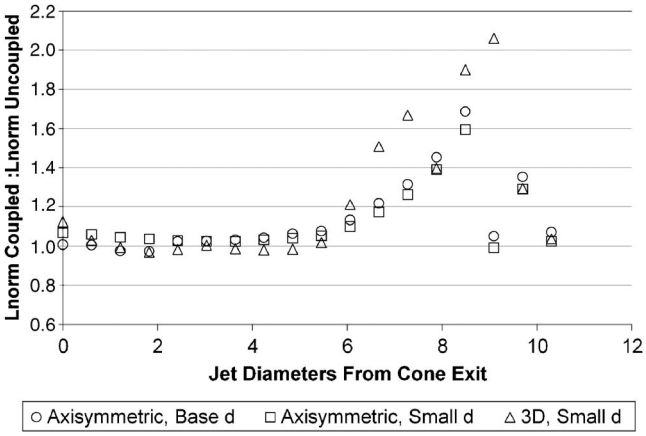

Fig. 14 Planar average coupled:uncoupled ratios on axial slices showing the normalized length of departure from isotropy (Eq. (13)) for three pairs of cases

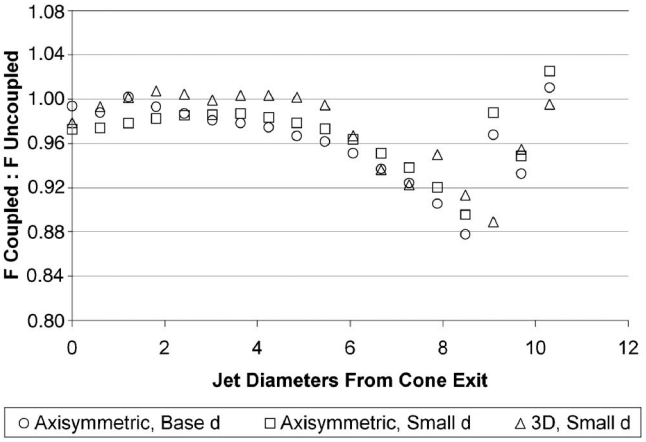

Fig. 15 Planar average coupled:uncoupled ratios on axial slices showing the NRAT determinant (Eq. (12)) for three pairs of cases

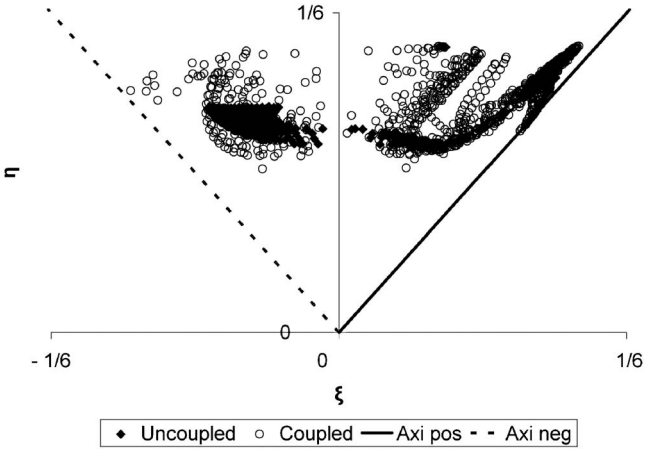

Fig. 17 A Lumley-style plot at the same location as in Fig. 16.

1.0. As in previous and upcoming figures, 3D effects appear to play a role in the results. Neither of the 3D model plots follows the exact trend of the axisymmetric results.

Figure 16 shows azimuthally averaged radial values of anisotropy (again, summed up in a single parameter from Eq. (13)) and intensity for a case involving the base particle diameter. They are plotted as the ratio of coupled:uncoupled values at a plane that was one jet diameter away from the cone exit. From previous figures, it is expected that the overall planar average of both anisotropy and intensity is near 1.0, but it is desired to look for the radial variability within the plane. The jet interface at this axial location is about 0.3 vessel radii. It can be seen that, in general, the turbulence enhancement increases with distance out from the centerline, while the anisotropy also increases. Both the intensity ratio and anisotropy ratio are typically above 1.0 outside the jet and below 1.0 inside the jet.

A Lumley plot of η versus ξ is given in Fig. 17 for the 3D case across the cutting plane one jet diameter from the cone exit. The flow through this cutting plane area would include near-wall flows (at the separator walls), as well as a turbulent shear layer from the inlet jet. The goal of this part of the investigation is to ensure realizability of both the coupled and uncoupled turbulence states. All of the values found on the plane are bound correctly by the positive and negative ξ axisymmetric lines. No values in either the coupled or uncoupled approach are very close to the upper triangle boundary two-component curve at $\eta=1/6$ or close to the one-component turbulence state of $\eta=\xi=1/3$. Some of both cases approach the axisymmetric curves. The average η values between the two cases plotted are nearly identical, but the ξ average is slightly shifted to the right by coupling. In other words, the departure from isotropy for the coupled and uncoupled cases on this cutting plane is nearly unchanged, as was shown in Fig. 16. The average, however, did shift toward a state closer to that of near-wall turbulence by the inclusion of the particles.

Contours of the second deformation tensor invariant for the coupled and uncoupled base diameter cases are shown in Fig. 18. The range is $\leqslant -1$ (blue, regions of high strain) to $\geqslant 1$ (red, regions of high vorticity). With the inclusion of particles, the flow field has changed from a localized region of high vorticity near the jet interface to axially alternating regions of high vorticity and

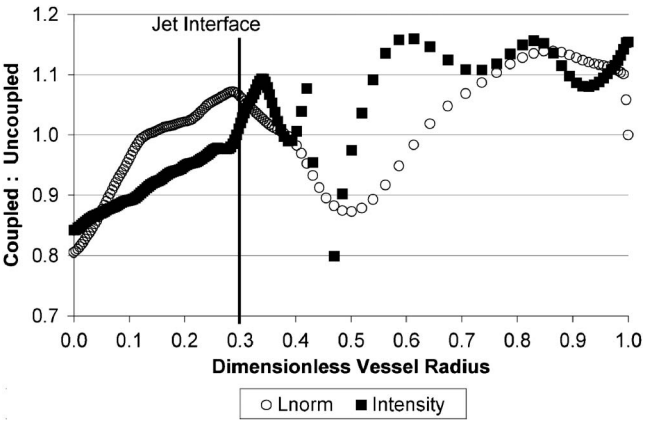

Fig. 16 Azimuthally averaged coupled:uncoupled ratios on an axial slice at a distance of one jet diameter from the cone exit showing the normalized length of departure from isotropy and local turbulence intensity for the base diameter

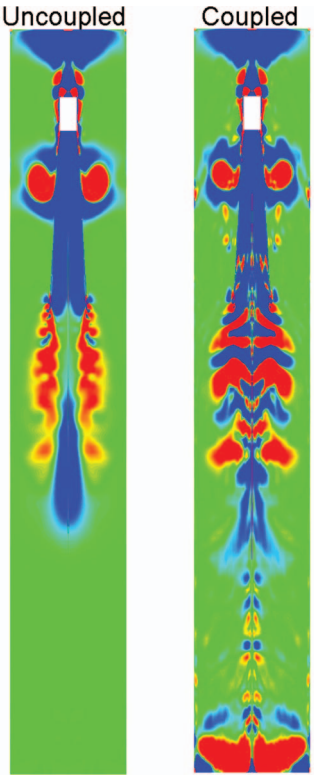

Fig. 18 Typical instantaneous contours of *Q* on a vessel center cut

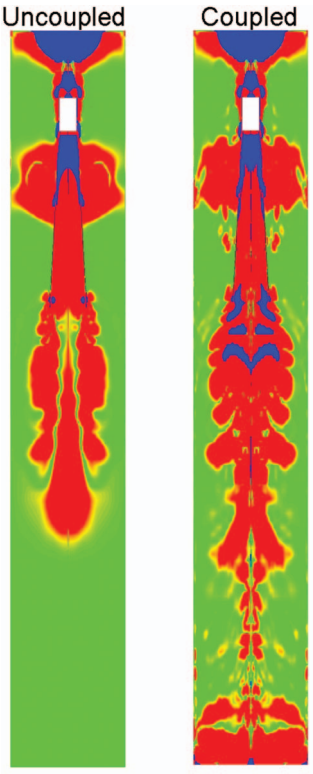

Fig. 19 Typical instantaneous contours of Δ on a vessel center cut

high strain along the jet centerline. The changes in the mean deformation discriminant, Δ, are given in Fig. 19. The range is $\leqslant -1$ (blue, nonfocal turbulent structures with three real deformation eigenvalues) to $\geqslant 1$ (red, focal turbulent structures with only one real eigenvalue). The inclusion of particle effects has caused the flow to exhibit much more of a focal character. To further illustrate this effect, Fig. 20 shows contours (same range as in Fig. 19) of the discriminant on a cross section of the vessel one jet diameter from the cone exit. Overall, there is more of a focal nature to the coupled flow with some traces of nonfocal both within the jet and around the vessel periphery.

There are two items not shown graphically here, but are worth mentioning. The third invariant measure, R, did not change much as a result of particle coupling with the continuous phase. The overall vessel averages were negative numbers (similar in magnitude) for the base particle size comparison, indicating that both coupled and uncoupled flows were typically stable, focus stretching. Also of interest are some typical mean deformation eigenvalue combinations found in the flow fields. Time did not permit gathering enough data to make global conclusions, but a few nonfocal (three real tensor eigenvalues) points were found on the vessel cross-sectional plane one jet diameter from the cone. In the uncoupled case, a typical eigenvalue ratio was 1:−3:2 (compared to 1:−4:3 previously mentioned in the section on measures). In a coupled case on the same plane, a typical ratio was 1:−11:11. The author does not propose to build a theory on a few CFD point values from a steady RANS model, but the possibility of a coupling effect here could be worthy of further pursuit with large eddy simulation (LES)/DNS.

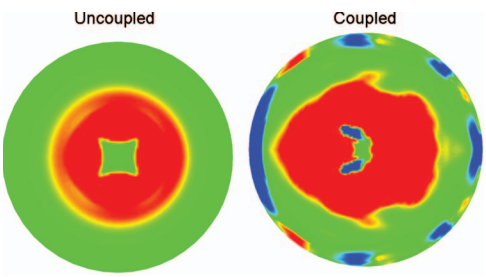

Fig. 20 Typical instantaneous contours of Δ on a plane at a distance of one jet diameter from the cone exit

Conclusions

A series of RSM DRW models has been used to attempt to quantify the effects of particle coupling at 0.25 mass loading on the continuous phase mean deformation and turbulence fields. Numerical sensitivity tests, grid-independent solutions, and data from an experimental counterpart helped establish the method. The basis and caveats for various aspects of modeling were also presented. Certain aspects of the EL approach were shown to be very important in ensuring an accurate, statistically sound outcome. The following continuous phase features were, in general, increased as a result of particle coupling (feedback) effects: Turbulence viscosity, turbulence production:dissipation, turbulence intensity (normalized by superficial velocity), turbulence anisotropy, vorticity-dominant regions, and the focal aspect of the turbulent structures. Parametric quantification was given for these various measures. Turbulence attenuation (for wakeless particles) that is discussed in the open literature was not found for the Stokes number and other conditions of the present work. It is proposed that the turbulence enhancement presented in the current work is facilitated by (1) increased strain rate induced by the particles and (2) increased slip due to stagnation/particle ejection approaching the closed vessel bottom. Preliminary results indicate that there may be an important effect of coupling on the mean deformation tensor eigenvalues. For some measures discussed in this work, particle size and 3D effects appear to play an important role.

Future Work

The ultimate goal is to make mechanical modifications to the separator geometry and to reduce the carryover rate. Now that a reasonable method has been established, mechanical change numerical evaluations will be possible. A number of items could be considered to improve the method. Liquid droplet coalescence and breakup effects could be incorporated only with an experimental counterpart. The use of particle-induced Reynolds stress source terms could offer improvements in the results of related studies. More time could be spent further investigating 3D, particle size, and mean deformation eigenvalue effects. Also, the potential for false migration of particles due to kinetic energy gradients could be explored as discussed in Strutt and Lightstone [31]. In addition, other measures of anisotropy such as Taylor's anisotropy coefficient utilized in Keirsbulck et al. [32] could be pursued. Lastly, the use of a transient, non-RANS approach could provide a deeper understanding of the phenomena discussed in this work.

Nomenclature

a = coefficients
b = normalized anisotropy tensor
d = particle diameter
F = determinant of NRAT
g = gravity
I = turbulence intensity (superficial velocity)
k = turbulence kinetic energy
l = Eulerian turbulent length scale
L = distance from Lumley origin
m = mass
$P \rightarrow R$ = invariants used in discriminant
r = uniform random number $(0 \rightarrow 1)$
S = source term
T = time

u' = fluctuating velocity component
v_{cell} = cell volume
Z = particle mass loading, $\text{mass}_p/\text{mass}_c$
$\text{I} \rightarrow \text{III}$ = tensor invariants
$\langle\ \rangle$ = time-averaged quantity

Greek

τ = response time
δ = Kronecker delta
ε = turbulence dissipation rate
ξ, η = Lumley triangle parameters
ν = kinematic viscosity
ζ = normally distributed random number
μ = molecular viscosity
σ = rms fluctuation velocity
λ = eigenvalues
Δ = deformation discriminant

Subscripts

c = continuous phase
D = drag
DT = deformation tensor
el = eddy lifetime
ec = eddy crossing
h = parcel summation index
i,j,k,l = tensor indices
L = lift
p = dispersed phase
s = slip

References

[1] Obermair, S., Gutschi, C., Woisetschlager, J., and Staudinger, G., 2005, "Flow Pattern and Agglomeration in the Dust Outlet of a Gas Cyclone Investigated by Phase Doppler Anemometry," Powder Technol., **156**, pp. 34–42.

[2] Gil, A., Cortes, C., Romeo, L., and Velilla, J., 2002, "Gas-Particle Flow Inside Cyclone Diplets With Pneumatic Extraction," Powder Technol., **128**, pp. 78–91.

[3] Vandu, C., and Krishna, R., 2004, "Volumetric Mass Transfer Coefficients in Slurry Bubble Columns Operating in the Churn-Turbulent Flow Regime," Chem. Eng. Process., **43**, pp. 987–995.

[4] Faeth, G., 1986, "Spray Atomization and Combustion," AIAA Paper No. 86-0136.

[5] Ahmadi, G., and Abu-Zaid, S., 1997, "Anisotropic Model for Dense Two-Phase Flows," *ASME-ASCE-SES Joint Summer Meeting, Mechanics of Deformation and Flow of Particulate Materials*, pp. 308–320.

[6] Graham, D., 2004, "The Influence of Small Particles on the Structure of a Turbulent Shear Flow," ASME J. Fluids Eng., **126**, pp. 613–619.

[7] Mostafa, A., Mongia, H., McDonell, V., and Samuelsen, G., 1990, "Experimental and Numerical Study of Particle-laden Coaxial Jet Flows," Int. J. Heat Fluid Flow, **11**, pp. 90–98.

[8] Boree, J., and Caraman, N., 2005, "Dilute Bidispersed Tube Flow: Role of Interclass Collisions at Increased Loadings," Phys. Fluids, **17**, p. 055108.

[9] Crowe, C., Sommerfeld, M., and Tsuji, Y., 1998, *Multiphase Flows With Droplets and Particles*, CRC, Boca Raton, FL.

[10] Heinl, E., and Bohnet, M., 2005, "Calculation of Particle-Wall Adhesion in Horizontal Gas-Solids Flow Using CFD," Powder Technol., **159**, pp. 95–104.

[11] Fluent, Inc., 2005, FLUENT 6.2 User's Guide, Lebanon, NH.

[12] Clift, R., Grace, J., and Weber, M., 1978, *Bubbles, Drops, and Particles*, Academic, New York.

[13] Morsi, S., and Alexander, A., 1972, "An Investigation of Particle Trajectories in Two-Phase Flow Systems," J. Fluid Mech., **55**, pp. 193–208.

[14] Zheng, Y., Fan, J., Lou, K., and Cen, K., 2004, "Direct Numerical Simulation on the Particle Dispersion by the Vortex Structures in a Three-Dimensional Mixing Layer: The Roll-Up," Powder Technol., **146**, pp. 102–110.

[15] Sommerfeld, M., 2001, "Validation of a Stochastic Lagrangian Modelling Approach for Inter-Particle Collisions in Homogeneous Isotropic Turbulence," Int. J. Multiphase Flow, **27**, pp. 1829–1858.

[16] Soo, S., 1967, *Fluid Dynamics of Multiphase Systems*, Blaisdell, Waltham.

[17] Amsden, A., O'Rourke, P., and Butler, T., 1989, "KIVA-II: A Computer Program of Chemically Reactive Flows With Sprays," Los Alamos Report No. LA-11560-MS.

[18] Xiong, Y., Zhang, M., and Yuan, Z., 2005, "Three-Dimensional Numerical Simulation Method for Gas-Solid Injector," Powder Technol., **160**, pp. 180–189.

[19] Launder, B., Reece, G., and Rodi, W., 1975, "Progress in the Developments of a Reynolds-Stress Turbulence Closure," J. Fluid Mech., **68**, pp. 537–566.

[20] Speziale, C., Sarkar, S., and Gatski, T., 1991, "Modelling the Pressure-Strain Correlation of Turbulence: An Invariant Dynamical Systems Approach," J. Fluid Mech., **277**, pp. 245–272.

[21] Hanjalic, K., 2005, "Will RANS Survive LES? A View of Perspectives," ASME J. Fluids Eng., **127**, pp. 831–839.

[22] Speziale, C., 1998, "Turbulence Modeling for Time-Dependent RANS and VLES: A Review," AIAA J., **36**, pp. 173–184.

[23] Pope, S., 2000, *Turbulent Flows*, Cambridge University Press, Cambridge, UK.

[24] Strasser, W., 2007, "CFD Investigation of Gear Pump Mixing Using Deforming/Agglomerating Mesh," ASME J. Fluids Eng., **129**, pp. 476–484.

[25] Strasser, W., Feldman, G., Wilkins, C., and Leylek, J., 2004, "Transonic Passage Turbine Blade Tip Clearance With Scalloped Shroud: Part II—Losses With and Without Scrubbing Effects in Engine Configuration," ASME Paper No. IMECE2004-59116.

[26] Lumley, J., 1978, "Computational Modeling of Turbulent Flows," Adv. Appl. Mech., **18**, pp. 123–176.

[27] Galletti, C., Brunazzi, E., Pintus, S., Paglianti, A., and Yianneskis, M., 2004, "A Study of Reynolds Stresses, Triple Products, and Turbulence States in a Radially Stirred Tank With 3-D Laser Anemometry," Chem. Eng. Res. Des., **82**, pp. 1214–1228.

[28] Pirozzoli, S., and Grasso, F., 2004, "Direct Numerical Simulations of Isotropic Compressible Turbulence: Influence of Compressibility on Dynamics and Structures," Phys. Fluids, **16**, pp. 4386–4407.

[29] Aris, R., 1962, *Vectors, Tensors, and the Basic Equations of Fluid Mechanics*, Dover, New York.

[30] Li, X., and Wang, T., 2005, "Effects of Various Modeling Schemes on Mist Film Cooling Simulation," ASME Paper No. IMECE2005-81780.

[31] Strutt, H., and Lightstone, M., 2006, "Analysis of Tracer Particle Migration in Inhomogeneous Turbulence," Int. J. Heat Mass Transfer, **49**, pp. 2557–2566.

[32] Keirsbulck, L., Labraga, L., and Haddad, M., 2006, "Influence of Blowing on the Anisotropy of the Reynolds Stress Tensor in a Turbulent Channel Flow," Exp. Fluids, **40**, pp. 654–662.

Three-Dimensional Modeling and Geometrical Influence on the Hydraulic Performance of a Control Valve

Guillermo Palau-Salvador
e-mail: guipasal@agf.upv.es

Pablo González-Altozano

Jaime Arviza-Valverde

Department of Rural Engineering,
Polytechnic Hydraulic Division,
University of Valencia,
Camino de Vera s/n,
46022 Valencia, Spain

The ability to understand and manage the performance of hydraulic control valves is important in many automatic and manual industrial processes. The use of computational fluid dynamics (CFD) aids in the design of such valves by inexpensively providing insight into flow patterns, potential noise sources, and cavitation. Applications of CFD to study the performance of complex three-dimensional (3D) valves, such as poppet, spool, and butterfly valves, are becoming more common. Still, validation and accuracy remain an issue. The Reynolds-averaged Navier–Stokes equations were solved numerically using the commercial CFD package FLUENT V6.2 *to assess the effect of geometry on the performance of a 3D control valve. The influence of the turbulence model and of a cavitation model was also investigated. Comparisons were made to experimental data when available. The 3D model of the valve was constructed by decomposing the valve into several subdomains. Agreement between the numerical predictions and measurements of flow pressure was less than 6% for all cases studied. Passive flow control, designed to minimize vortical structures at the piston exit and reduce potential cavitation, noise, and vibrations, was achieved by geometric smoothing. In addition, these changes helped to increase C_v and reduce the area affected by cavitation as it is related to the jet shape originated at the valve throat. The importance of accounting for full 3D geometry effects in modeling and optimizing control valve performance was demonstrated via CFD. This is particularly important in the vicinity of the piston. It is worth noting that the original geometry resulted in a lower C_v with higher velocity magnitude within the valve, whereas after smoothing C_v increased and served to delay cavitation inception.*
[DOI: 10.1115/1.2813131]

Keywords: CFD, modeling, control valve, cavitation

Introduction and Objectives

The comprehension and better management of hydraulic control valves along with computational fluid dynamics (CFD) techniques have acquired a growing significance due to their common usage in many automatic and manual industrial processes. Over the past few years, there has been an intense effort for knowing, classifying, and analyzing these valves, as seen in Skousen [1] or similar review books about the characterization and classification of hydraulic valves.

Deep insights of the flow behavior inside hydraulic devices such as turbulence, cavitation, particle paths, and velocity or pressure distributions have become more and more relevant in the attempts to improve their hydraulic characteristics. Together with this, the development of the computational calculations using numerical methods has made its way to solving complex flows. Thus, the CFD techniques enable the resolution of all the fluid dynamics equations (Versteeg and Malalasekera [2] or Chung [3]). Interesting applications of CFD have been carried out with pipe junctions (Sierra-Espinosa et al. [4,5]), pipeline design (Famiyesin et al. [6]), hydraulic structures (Lavedrine and Woolf [7]), aerial spreaders (Bansal et al. [8]), and jets (Xing and Frankel [9]). More specifically, several research works using CFD techniques have been applied to model valves to analyze their hydraulic characteristics, for instance, studies on poppet (Ito et al. [10] and Nadarajah et al. [11,12]), spool (Min et al. [13]), spring-waded poppet (Kehr et al. [14]), and butterfly valves (Huang and Kim [15]). Furthermore, Davis and Stewart [16,17] led a study where an axisymmetric subdomain was used around the piston path. They suggested that better results could be achieved in extreme regulations by using a three-dimensional model around the piston path. CFD has been used not only to describe the internal flow behavior, but also to improve the internal geometry of the valve. The works accomplished by Roorda [18] or Ueno et al. [19] deal with these CFD applications and their results.

On the other hand, the phenomenon of cavitation has also been proven to be of high relevance in several industrial processes and engineering applications. According to Knapp et al. [20], cavitation can be classified into several different regimes: traveling, fixed, and vortex. In each, the onset of cavitation occurs due to the flow acceleration and the consequent pressure drop at a point in the liquid flow that causes vapor bubble formation. Bubbles travel downstream until the recovery of pressure causes the bubble to implode. This two-step process (the formation of the bubble and its subsequent implosion downstream) is called cavitation.

Yet, cavitating flows often have a negative impact on many engineering devices, resulting in performance degradation and structural damage. Pumps, valves, propellers, nozzles, and numerous other devices can be affected by cavitation. For several years, numerous researchers have obtained detailed experimental data of cavitation from flow elements such as nozzles, orifices, venturis, and Schiebe headforms (Abuaf et al. [21]; Stutz and Reboud [22]). With reference to cavitation in valves, it gives rise to excessive seat leakage and, thus, distorts the flow characteristics, or causes

Contributed by the Fluids Engineering Division of ASME for publication in the JOURNAL OF FLUIDS ENGINEERING. Manuscript received December 4, 2006; final manuscript received July 16, 2007; published online December 19, 2007. Review conducted by Paul Durbin.

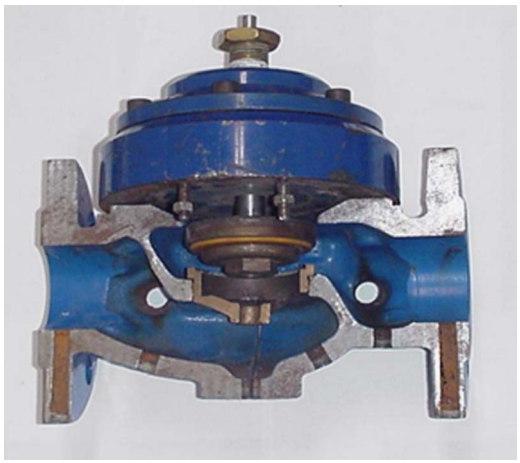

Fig. 1 Section of the original control valve studied by CFD

the eventual failure of the pressure vessels (valve body, piping, etc.). In some applications where a severe reduction of pressure takes place, valve ports may be destroyed quickly by cavitation, limiting the life expectancy of the valve (Skousen [1]). These constitute some weighty reasons to prevent cavitation from developing in valves. Although there are numerous factors affecting cavitation inception (nucleation sites, dissolved gases, etc.), the present work is focused on the geometrical influence in the cavitation phenomenon.

Therefore, the main objective of this work is to provide a three-dimensional CFD model inside a piston control valve without any geometrical simplification in order to study velocity fields, pressure distributions, and flow separations and reattachments in any piston position. To start off, a comparison was carried out between the numerical results and experimental data using different piston positions. After the validation of the model, several modifications were introduced in the original geometry to study their influence on the flow patterns and the cavitation inception.

Materials and Methods

Physical System. The valve used in this study was a double chamber control valve with an internal diameter of 2 in. In this case, the valve was connected as a pressure reducing valve, as it regularly happens. Its geometry was complex, with a symmetry plane in the middle of the valve (Fig. 1). Several modifications were made in the original geometry to compare the flow patterns and cavitation inception. These changes consisted of remodeling the piston path and smoothing the geometrical configuration of both the upstream and downstream chambers.

Experimental Loop. The valve was installed and tested in the laboratory loop shown in Fig. 2. It consisted of a tank, two pumps whose connections supplied a wide range of flow and pressure values, an electromagnetic flow meter, a test section where the valve was installed, and two manual valves located upstream and downstream of the test section. Ten pressure taps (eight within the valve body and two just before and after it) were installed in the strategic locations showed in Fig. 2. Piezoresistive transducers ranging from 0 MPa to 1.6 MPa with an accuracy of 0.25% of the full scale value, previously calibrated, were used to measure the pressure in each of the ten locations. The flow meter had an error of 1% of the reading. A linear voltage displacement transducer (LVDT) ranging from −25 mm to 25 mm, with an uncertainty of calibration of 13 μm, was aligned with the piston of the valve to determine the piston position in each test. Water was the working fluid at a temperature fixed to $20°C \pm 0.1°C$. As a result, the flow, the pressure in the ten locations, and the position of the piston were obtained in several positions and circumstances. These data were used to validate the numerical model.

Experimental Procedure. First, a test was performed on the valve completely opened to measure the static pressure field with a flow rate ranging from 0 l/s to 20 l/s. Second, the flow, the pressure at ten pressure taps, and the piston position were recorded for the flow ranging from 0 l/s to 14 l/s, the upstream pressure varying from 4×10^5 Pa to 16×10^5 Pa and the downstream pressure fixed to 2×10^5 Pa, 2.5×10^5 Pa, 3×10^5 Pa, 3.5×10^5 Pa, and 4×10^5 Pa in five different studies. The results of these experimental tests are shown in Fig. 3.

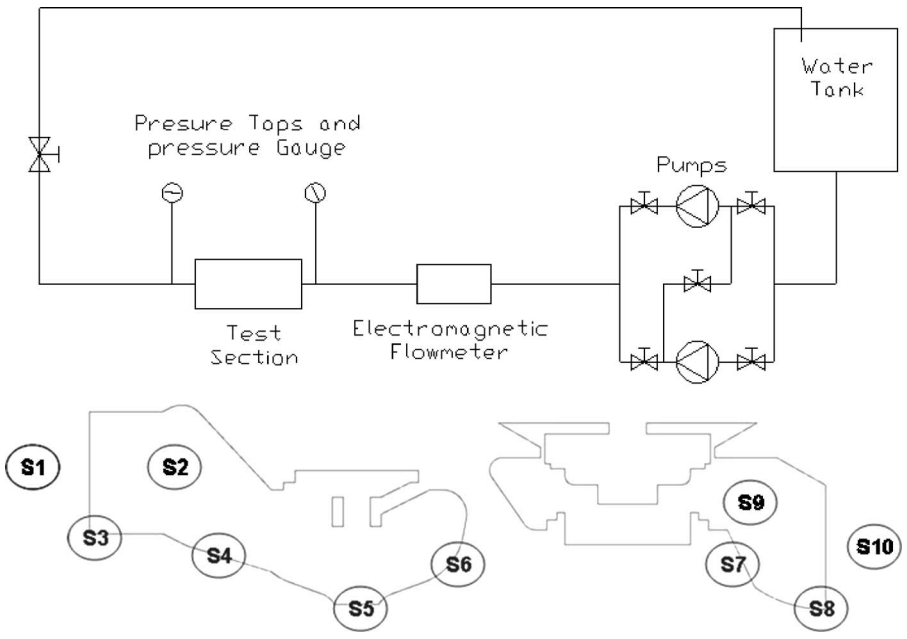

Fig. 2 Experimental loop and schematic position of the pressure sensors used in the experimental test

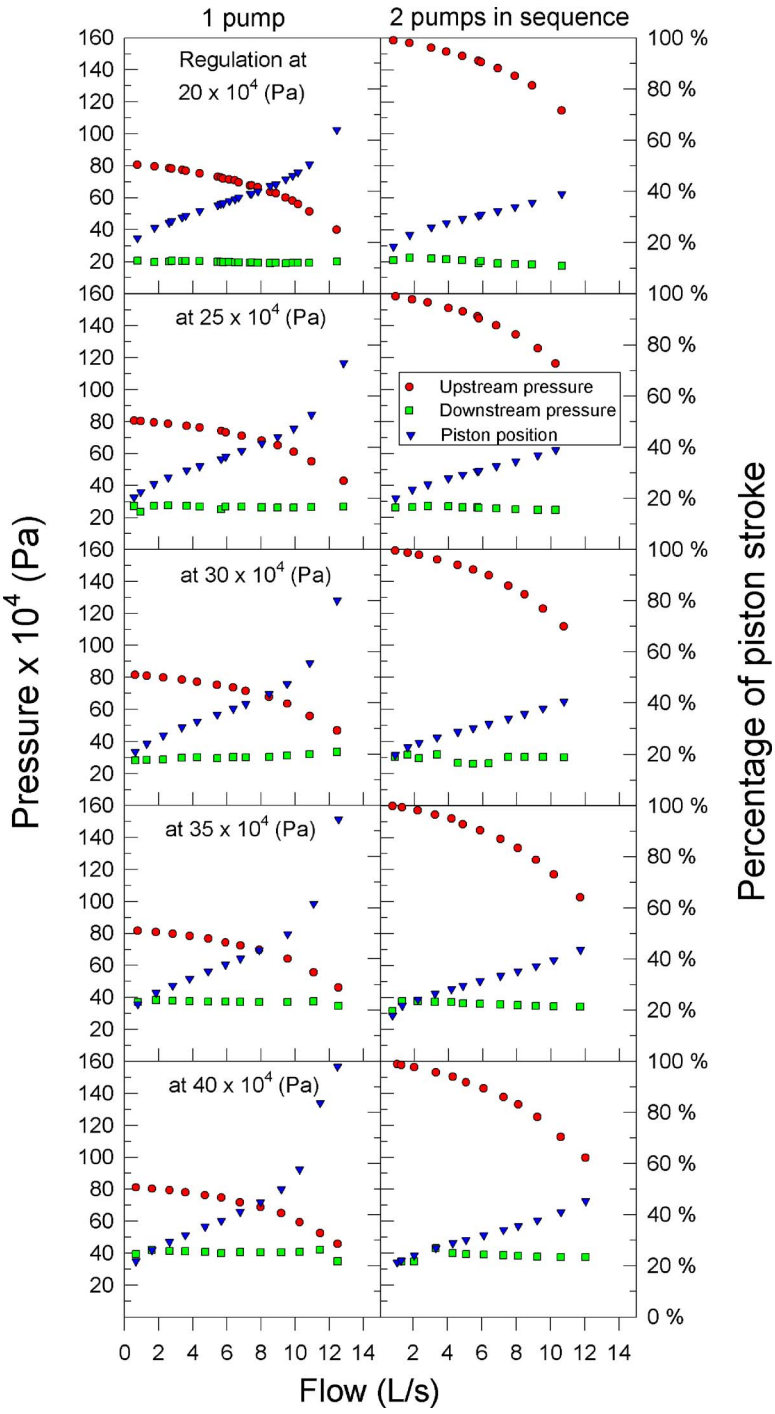

Fig. 3 Valve upstream and downstream pressure. Percentage of piston stroke in the five regulation rehearsals with one pump and with two pumps in sequence.

The valve coefficient (C_v) was determined to characterize the valve. C_v is a parameter inherent to the valve, and it is a measurement of the valve capacity. C_v is defined as the flow that produces a pressure drop of 10^5 Pa. In the SI system, the units of C_v are $(m^3/h)/(kPa^{0.5})$, and it is formulated as follows:

$$C_v = Q\sqrt{\frac{\gamma}{\Delta P}}$$

where Q is the flow, γ the liquid specific gravity, and ΔP the drop of pressure.

Numerical Study. In the numerical model, the valve was modeled in three dimensions without any geometrical simplification, with the same piston positions that corresponded to those of the experimental test (the input values used for the numerical runs are shown in Table 1). The CFD model applied is based on the volume finite method via finite difference (see Chung [3] or Ferziger and Peric [23] for further information). The computational code used was FLUENT 6.2, whereas the grid was meshed with GAMBIT 2. The valve geometry was drawn using PRO-ENGINEER. The selected turbulence model was the standard κ-ε (Launder and Spalding

Table 1 Case modeled in the CFD study, with the inflow rate and the piston position

Opening rate	Run	Flow rate ($\times 10^{-3}$ m^3/s)	Drop pressure ($\times 10^4$ Pa)
5	1	3.86	129.62
10	2	5.21	114.70
15	3	7.26	97.58
20	4	2.82	44.05
25	5	9.22	102.04
30	6	3.24	41.67
35	7	4.72	33.26
40	8	9.91	34.82
100	9	12.3	10

[24]) after a previous work (Palau-Salvador et al. [25]) where a comparison between a Reynolds stress model and the standard κ-ε revealed that no significant changes occurred in the predictions. This model has been widely validated in hydraulic simulations with high Reynolds' numbers. An incompressible steady flow was then assumed. The governing equations were the mass conservation and the momentum balance, neglecting the temperature effects and, therefore, the energy equation. These equations were solved using the SIMPLE algorithm developed by Patankar [26].

A computational three-dimensional grid was built for each geometry domain studied, using an unstructured mesh of more than 10^6 cells of 1 mm in size. Mesh sensibility was tested using a smaller cell size, but no influence was found on the final results. As there is a mirror plane at the center line of the valve, a symmetry boundary was defined. Uniform velocity and pressure profiles were adopted, respectively, as the inlet and outlet boundaries. Turbulence intensity was set to 5% at the inlet and outlet boundaries. Normalized residuals were used for the convergence criteria set at six orders of magnitude. The origin of a coordinate system was placed at the middle of the valve, and x, y, and z represent the streamwise, spanwise, and vertical directions, respectively.

Model Proceeding. Analyzing the whole domain of the valve at once was rather difficult due to the large number of cells needed to mesh the complex internal geometry of the valve. Then, a new model (a schematic diagram of the designed protocol outlined in Fig. 4) was successfully tried out. It was based on simulating a preliminary central domain of the valve, which included the main upstream and downstream geometric characteristics, with a uniform inlet velocity condition. A velocity and pressure profile of a plane (π in Fig. 4) located at the beginning of the throat was obtained from this preliminary domain with information of velocity and pressure of each cell of the plane. This profile was then used as a boundary condition of the two domains in which the valve was finally divided by the π plane: "entrance" and "exit" domains. As far as we know, this is the first investigation using this procedure to analyze a control valve.

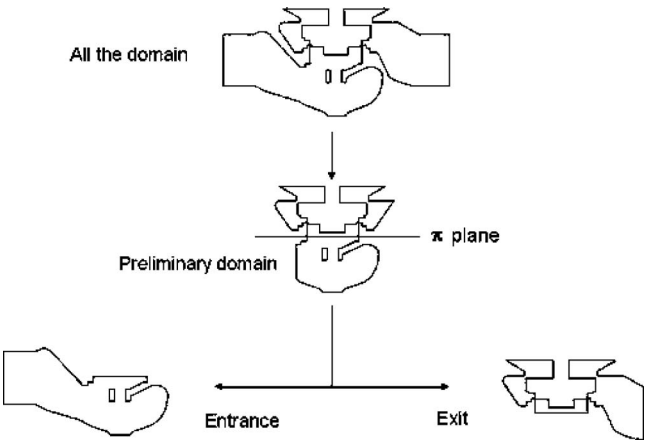

Fig. 4 Schematic protocol used to model the valve

Cavitation Model. It is very useful to estimate the cavitation inception and its development as well as to know qualitatively where the cavitation occurs. The cavitation model of FLUENT V6.2 used is based on the full cavitation model developed by Singhal et al. [27]. This model involves two phases and a specific fraction of noncondensable gases, whose mass fraction is known in advance. It considers the formation and collapse of the bubbles. The new code improves the old cavitation model in FLUENT V5, where, for instance, the bubbles were neither created nor destroyed. The numerical model is based on the Reynolds-averaged Navier–Stokes equations as well as a conventional turbulence model (for example, standard κ-ε model or renormalization group (RNG) κ-ε model). The working fluid is assumed to be a mixture of three species (liquid, vapour, and noncondensable gas). In a previous work, Palau-Salvador and Frankel [28] validated FLUENT's new cavitation model for different geometries studying the impact of different parameters such as temperature, domain size, or dissolve gases. The κ-ω shear stress transport (SST) model offers the best convergence situation allowed by the program.

Thus, this will be the model chosen for the present work.

However, based on the Eulerian/Eulerian approach, there are several limitations in this model. For example, it points out that bubbles cannot be represented as separated particles. Also, this model cannot be used together with the large eddy simulation (LES) approach. All this reflects the basic nature of the research efforts related to applying LES to simple cavitating flows such as jets (Gopalan et al. [29]; Cerutti et al. [30]; Xing and Frankel [9]).

This research paper also attempts to convey information about the cavitation inception around the piston. The first trial was performed with the flow rate fixed to 7.26 l/s, the drop of pressure to 0.9758 MPa, and the position of the piston to 15% open. No cavitation was observed in these conditions during the experimental test, though the flow rate in the numerical simulation was gradually increased in successive runs to determine the cavitation inception in both the original and the modified geometry. The results must be considered valid because of the previous validation of this model (Palau-Salvador and Frankel [28]), although no data for the cavitation inception were obtained during these experiments.

Results and Discussion

Computation Fluid Dynamics Validation. The experimental tests of the control valve were used for the validation of the CFD model. Several cases with different piston positions were simulated and compared to the experimental results. At this point, all simulations were single phased because all of them were below the threshold of the cavitation inception. In Fig. 5, it is represented as the comparison between the pressure in each pressure tap for the numerical and experimental tests for three piston positions: 100%, 35%, and 15% opening, and flow rates of 0.0123 m^3/h, 0.00472 m^3/h, and 0.00726 m^3/h, respectively. As shown in Fig. 5, the difference between the numerical and experimental values is less than 6% in all pressure locations for these three particular cases, although similar values were obtained for all the cases analyzed. The maximum difference was observed at the piston throat, as reported by Davis and Stewart [17]. However, the assumption of a three-dimensional domain reduces the differences and leads to better results than those obtained by Davis and Stewart [16]. It confirms their prediction of a three-dimensional flow around the piston. Hence, it is possible to conclude that the three-dimensional CFD model inside the control valve has been successfully validated.

Geometrical Modifications. The original valve had a complex piston geometry. Figure 6(a) shows a detail of the piston and the

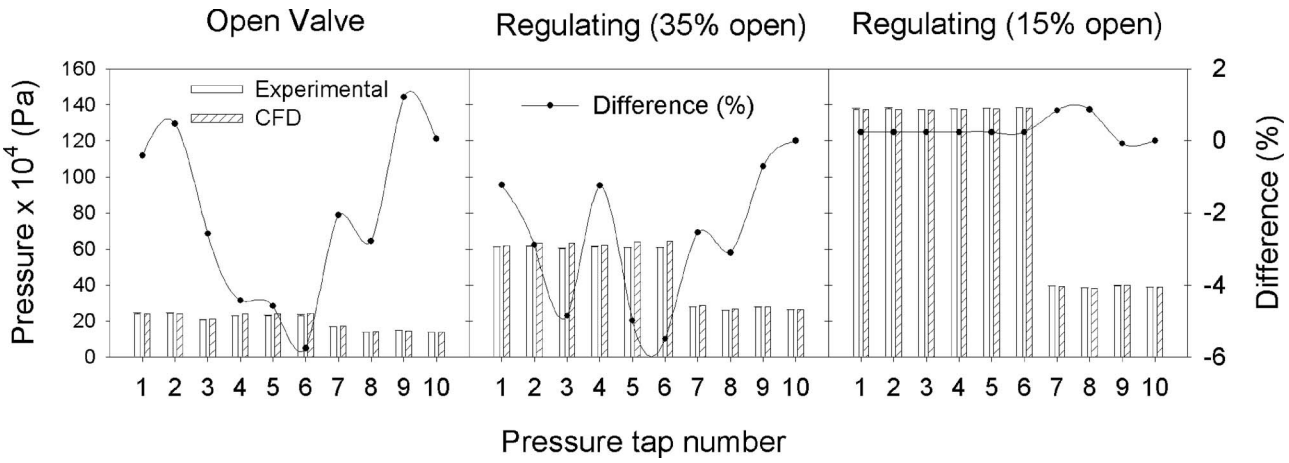

Fig. 5 Comparison of the pressure values between the experimental test and the CFD results for openings of 100%, 35%, and 15% and flow rates of 0.0123 m^3/h, 0.00472 m^3/h, and 0.00726 m^3/h, respectively

throat of the valve. The fluid behavior through the piston path presented several vortexes and a wall jet that hit the piston with high velocities (Fig. 6(*c*)). Vibrations and strong forces on the piston are then produced. The original geometry was thus modified by simplifying the piston geometry and broadening the piston path (Fig. 6(*b*)). These changes produced the displacement of the piston jet into the middle of the downstream chamber and reduced the recirculation vortexes around the piston (Fig. 6(*d*)). Furthermore, as the valve opening percentage decreases, the jet through the piston path also varied depending on the piston shape and the connection to the downstream chamber. Figure 7 shows the geometry and velocity vectors and contours of an opening of 15% and a flow rate of 0.00726 m^3/s. The original geometry presented a small downstream chamber, with a pronounced step to fit in the internal diameter of the downstream pipe, as shown in Fig. 7(*a*). In this case, the jet described a horizontal course into the downstream chamber (Figs. 7(*c*) and 7(*e*)), which developed into a downstream recirculation region, as observed by Davis and Stewart [16,17]. However, this recirculation was not fully developed at the end of the valve affecting the downstream pipe. Figure 8 depicts the *x*-velocity profiles in *y* and *z* axes contrasted in three sections in a tram of pipe just downstream of both geometries: just in the exit, 12.5 cm and 25 cm downstream. This effect is not desirable, as reported in Palau et al. [31], because of the impact on the behavior of sensors or flow meters usually installed after a control valve.

In order to get rid of this problem, several changes in the downstream chamber of the original geometry were introduced and analyzed. As a first modification, the step to connect the valve's downstream chamber with the external pipe was changed into a slight and progressive reduction of the internal diameter (Figs. 7(*a*) and 7(*b*)). This change produced several modifications in the flow behavior. First of all, a recirculation closed to the piston appeared and produced an oblique jet orientated to the bottom of the downstream chamber (Fig. 7(*d*)). This jet led to a different

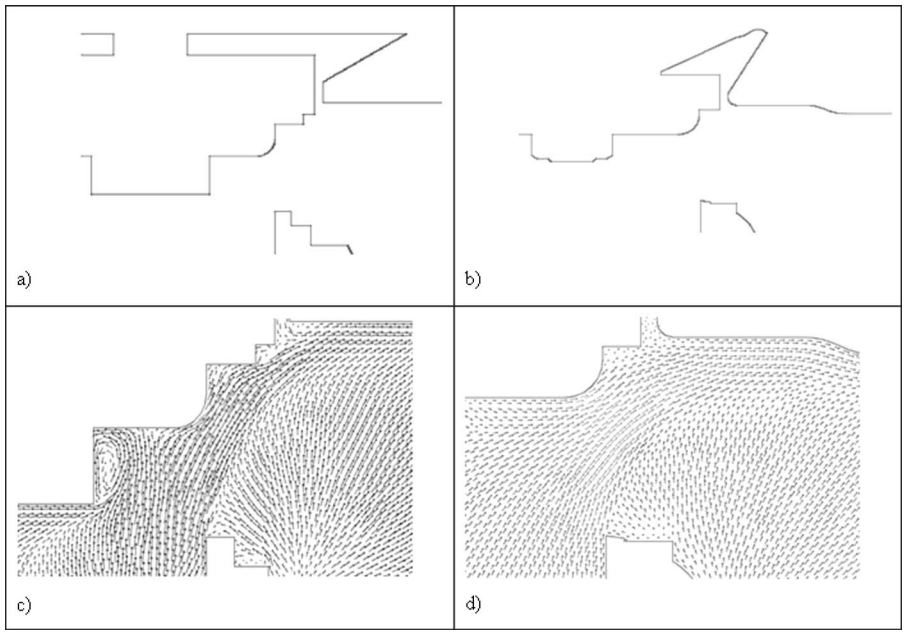

Fig. 6 Effect of the piston shape on the hydraulic behavior of the valve when it was completely open and the flow rate equal to 0.0123 m^3/h. (*a*) Original geometry, (*b*) modified geometry, (*c*) velocity vectors around the piston of the original shape, and (*d*) velocity vectors around the modified piston shape.

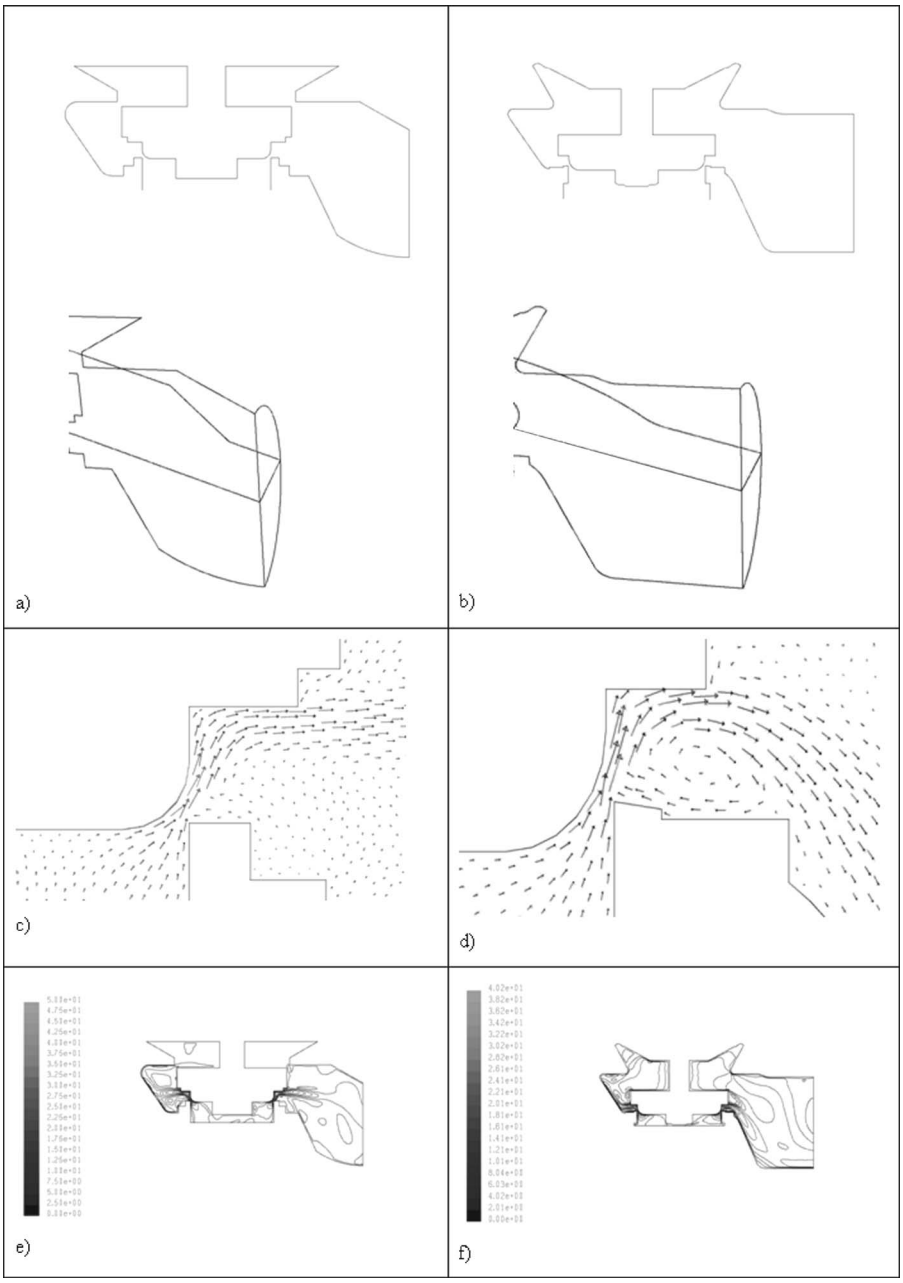

Fig. 7 Effect of the downstream chamber geometry on the hydraulic behavior of the valve when it was 15% open and a flow rate of 0.00726 m^3/h. (*a*) Original geometry, (*b*) modified geometry, (*c*) velocity vectors around the piston of the original shape, (*d*) velocity vectors around the modified piston shape, (*e*) velocity contours in the original chamber geometry, and (*f*) velocity contours in the modified chamber geometry.

recirculation pattern in the downstream chamber and reduced the area distorted by the turbulences (Figs. 7(*f*) and 8). This was confirmed by simulating the flow in a tram of pipe of 25 cm downstream of both geometries using as velocity inlet the valve outflow velocity profile. Thus, the x-velocity profiles in y and z axes are compared in three sections in a tram of pipe just downstream of both geometries in Fig. 8. In the original geometry, the velocity profiles in both directions were still highly distorted at the end of the 25 cm tram of simulated pipe. As far as the modified geometry is concerned, a steady turbulent velocity distribution was recovered at the end of the tram. Similar patterns were observed with the other opening percentages.

Regarding the inherent valve characteristics, Fig. 9 displays the experimental and numerical values for the original and the modified geometries with different opening percentages. As this figure shows, the numerical results of the original valve geometry matched accurately the experimental determined values. In all cases, the behavior is quite similar to a predominantly linear characteristic. In general terms, two observations can be drawn from these results. First of all, as it was observed by Davis and Stewart [16] with an axisymmetric model, the agreement between the experimental and modeled values was better at the lower percentage openings. However, when the valve was completely open, the agreement was also favorable with the new three-dimensional procedure (error of less than 4%). This confirmed that a three-dimensional model better predicts the turbulence flow behavior inside a control valve, as suggested by Davis and Stewart [16]. Second, the CFD simulations report that the C_v for the original

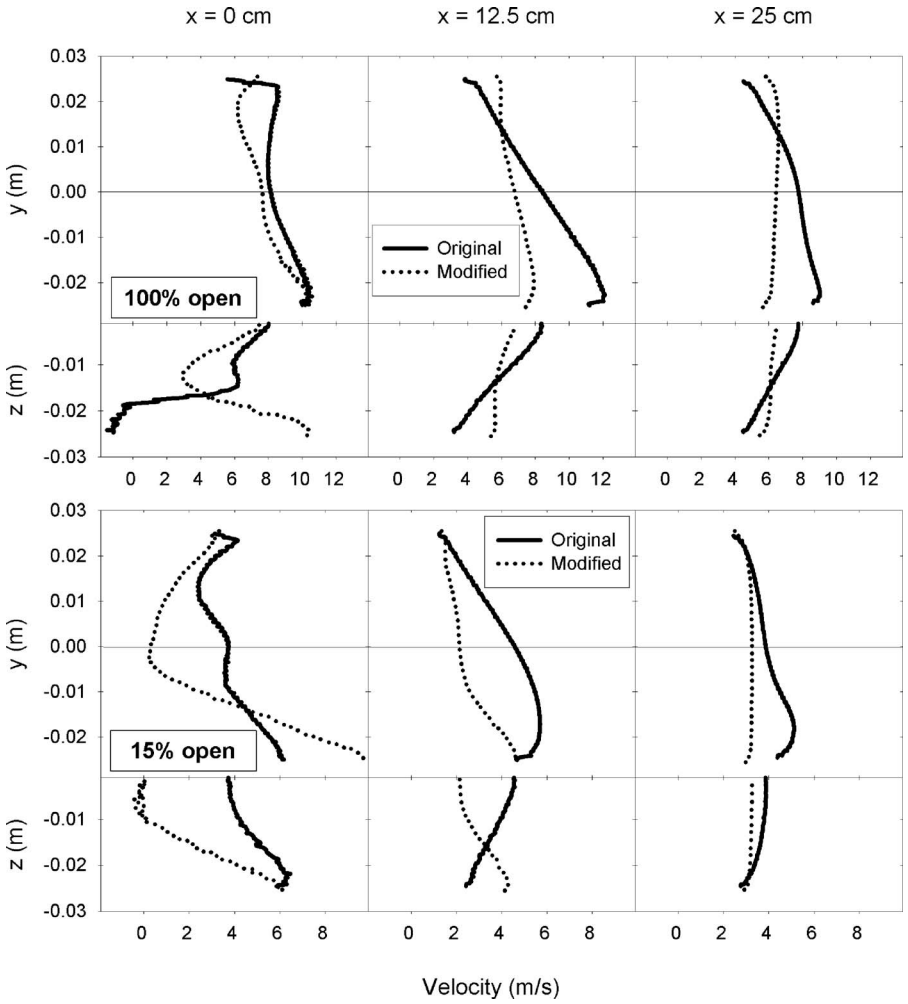

Fig. 8 Comparison of the *x* velocity in three sections located 0 cm, 12.5 cm, and 25 cm from the exit of the valve, on the original and modified geometries, with an opening of 100% and 15% and a flow rate of 0.0123 m^3/h and 0.00726 m^3/h, respectively. The origin of the coordinate system was placed at the exit of the valve in the center of the pipe, and *x*, *y*, and *z* represent the streamwise, spanwise, and vertical directions, respectively.

geometry was lower than the C_v for the modified geometry for all opening percentages (Fig. 9). This reaffirms that the original geometry produced a larger distorted area and, thus, a bigger drop of pressure.

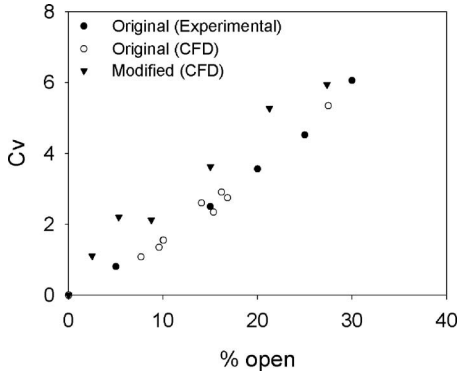

Fig. 9 C_v values from the experimental CFD model with the original geometry and the CFD model with the modified geometry for different opening values

Cavitation Study. Figure 10 displays an area around the throat pass between the piston and the valve body with different flow rates for both geometries, original and modified, with an opening of 15%. Regarding the experimental flow rate (7.26 l/s), where no cavitation was observed, both models did not show any vapor formation inside the valve. However, when the flow rate increased to 9.01 l/s, cavitation began in the original geometry in the piston wall. A flow rate of 9.41 l/s was then necessary to obtain the cavitation inception for the modified geometry. When the flow increased, a full cavitation process could be observed in both valve geometries with considerable differences. In the original one, the vapor formation was concentrated on the piston surface and in the throat pass, coinciding with the jet observed in Figs. 7(*c*) and 7(*e*). However, in the modified geometry, the vapor generates a cloud downstream the throat in agreement with the recirculation around the piston path of Figs. 7(*d*) and 7(*f*). Hence, these results demonstrate that the cavitation affected different zones of each valve, depending on the flow pattern that originated at the valve throat. Moreover, the original geometry, which presented a lower C_v and higher velocity magnitude values inside the valve, had a sooner cavitation inception as expected.

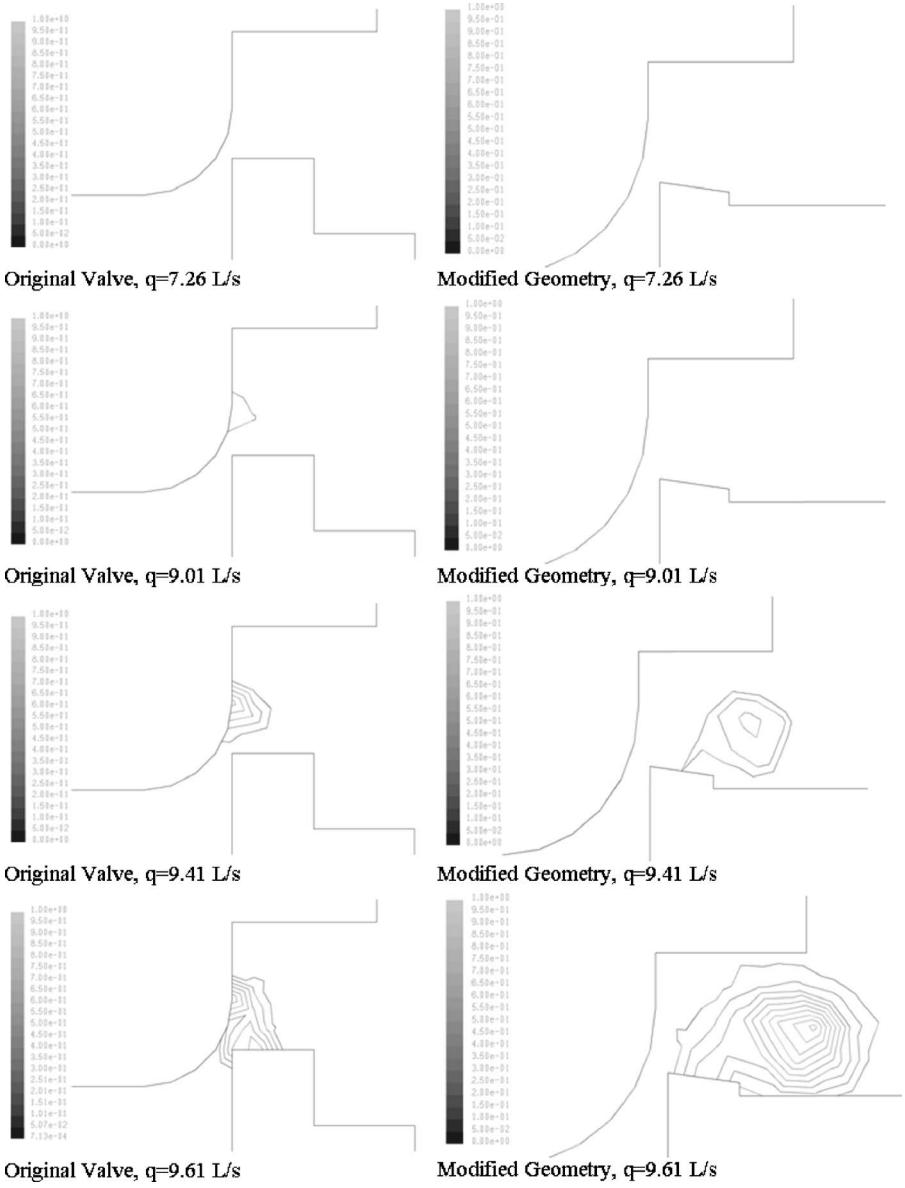

Fig. 10 Vapor fraction around the piston path for both piston shape and downstream chamber (original and modified geometries) with an opening of 15% for four different flow rates, from 7.26 l/s (experimental flow rate without any observed cavitation process) to 9.61 l/s

Conclusions

A three-dimensional CFD model using the commercial code FLUENT V6.2 has been validated as a successful tool for analyzing the flow behavior inside a control valve. A new protocol has been favorably used to modeling the complex three-dimensional geometry of a control valve. This contributes significantly to get accurate simulation performances compared to the experimental results. Also, the more realistic assumption of a three-dimensional flow around the piston improves the numerical simulation.

Moreover, the relevance of the geometric characteristics has also been under the scope of analysis. A modification of the geometry in the piston exit leads to different vortex structures and helps reduce vibrations and forces on the piston. On the other hand, a less complex geometry, which simplifies steps in the downstream chamber, decreases the area affected by the distorted flow that originated inside the valve and also increases the C_v.

Finally, cavitation has been studied inside both valves for different flow rates. The results show that the cavitation affects different zones of the valve related to each type of jet that was originated at the valve throat. Furthermore, the original geometry, which presents a lower C_v and higher velocity magnitude values inside the valve, has an earlier cavitation inception. These results encourage authors to go on with their research studies so as to achieve useful insights on the cavitation effects in control valves.

Acknowledgment

The authors acknowledge Steven Frankel for his help, suggestions, and advice.

References

[1] Skousen, P. L., 1998, *Valve Handbook*, McGraw-Hill, New York.
[2] Versteeg, H. K., and Malalasekera, W., 1995, *An Introduction to Computational Fluid Dynamics. The Finite Volume Method*, Longman, England.
[3] Chung, T. J., 2002, *Computational Fluid Dynamics*, Cambridge University Press, Cambridge.
[4] Sierra-Espinosa, F. Z., Bates, C. J., and O'Doherty, T., 2000, "Turbulent Flow in a 90° Pipe Junction Part 1: Decay of Fluctuations Upstream the Flow Bi-

furcation," Chimia, **29**, pp. 197–213.
[5] Sierra-Espinosa, F. Z., Bates, C. J., and O'Doherty, T., 2000, "Turbulent Flow in a 90° Pipe Junction Part 2: Reverse Flow at the Branch Exit," Chimia, **29**, pp. 215–233.
[6] Famiyesin, O. O. R., Oliver, K. D., and Rodger, A. A., 2002, "Semi-Empirical Equations for Pipeline Design by the Finite Element Method," Comput. Struct., **80**, pp. 1369–1382.
[7] Lavedrine, I., and Woolf, D., 1995, *Application of CFD Modelling to Hydraulic Structures*, Water Software Systems, Theory and Application, Research Studies, Baldock, Hertfordshire, England.
[8] Bansal, R. K., Walker, J. T., Gardisser, D. R., and Grift, T. E., 1998, "Validating Fluent for the Flow of Granular Materials in Aerial Spreaders," Trans. ASAE, **41**, pp. 29–35.
[9] Xing, T., and Frankel, S. H., 2002, "Effect of Cavitation on Vortex Dynamics in a Submerged Laminar Jet," AIAA J., **40**, pp. 2266–2276.
[10] Ito, K., Takahashi, K., and Inoue, K., 1993, "Flow in a Poppet Valve (Computation of Pressure Distribution Using a Streamline Coordinate System)," Trans. Jpn. Soc. Mech. Eng., Ser. A, **36**, pp. 42–50.
[11] Nadarajah, S., Balabani, S., Tindal, M. J., and Yianneskis, M., 1998, "The Turbulence Structure of the Annular Non-Swirling Flow Past an Axisymmetric Poppet Valve," Proc. Inst. Mech. Eng., Part C: J. Mech. Eng. Sci., **212**, pp. 455–472.
[12] Nadarajah, S., Balabani, S., Tindal, M. J., and Yianneskis, M., 1998, "The Effect of Swirl on the Annular Flow Past an Axisymmetric Poppet Valve," Proc. Inst. Mech. Eng., Part C: J. Mech. Eng. Sci., **212**, pp. 473–484.
[13] Min, B., Xin, F., and Ying, C., 2001, "Computational Fluid Dynamics Approach to Pressure Loss Analysis of Hydraulic Spool Valve," *Fifth International Conference on Fluid Power Transmission and Control, ICFP 2001*, Hangzhou, China.
[14] Kerh, T., Lee, J. J., and Wellford, L. C., 1997, "Transient Fluid-Structure Interaction in a Control Valve," ASME J. Fluids Eng., **119**, pp. 354–359.
[15] Huang, C., and Kim, R. H., 1996, "Three-Dimensional Analysis of Partially Open Butterfly Valve Flows," ASME J. Fluids Eng., **118**, pp. 562–568.
[16] Davis, J. A., and Stewart, M., 2002, "Predicting Globe Control Valve Performance-Part I: CFD Modeling," ASME J. Fluids Eng., **124**, pp. 772–777.
[17] Davis, J. A., and Stewart, M., 2002, "Predicting Globe Control Valve Performance-Part II: Experimental Verification," ASME J. Fluids Eng., **124**, pp. 778–783.
[18] Roorda, O., 1998, "Computer Simulation Helps Reduce Pressure Loss," Water Eng. Manage., **145**, pp. 22–24.
[19] Ueno, H., Okajima, A., Tanaka, H., and Hasegawa, T., 1994, "Noise Measurement and Numerical Simulation of Oil Flow in Pressure Control Valves," Trans. Jpn. Soc. Mech. Eng., Ser. A, **37**, pp. 336–341.
[20] Knapp, R. T., Daily, J. W., and Hammit, F. G., 1970, *Cavitation*, McGraw-Hill, New York.
[21] Abuaf, N., Wu, B. J. C., Zimmer, G. A., and Saha, P., 1981, "A Study of Nonequilibrium Flashing of Water in a Converging-Diverging Nozzle," Office of Nuclear Regulatory Research, Report No. NUREG/CR 1864.
[22] Stutz, B., and Reboud, J. L., 2000, "Measurements Within Unsteady Cavitation," Exp. Tech., **29**, pp. 545–552.
[23] Ferziger, J. H., and Peric, M., 1997, *Computational Methods for Fluid Dynamics*, Springer, Berlin.
[24] Launder, B. E., and Spalding, D. B., 1972, *Lectures in Mathematical Models of Turbulence*, Academic, London.
[25] Palau-Salvador, G., Arviza, J., and Frankel, S. H., 2004, "Three-Dimensional Control Valve With Complex Geometry: CFD Modeling and Experimental Validation," *34th AIAA Fluid Dynamics Conference and Exhibit*, Portland, OR.
[26] Patankar, S. V., 1980, *Numerical Heat Transport and Fluid Flow*, Taylor & Francis, New York.
[27] Singhal, A. K., Athavale, M. M., Huiying, L., and Jiang, L., 2002, "Mathematical Bases and Validation of the Full Cavitation Model," ASME J. Fluids Eng., **124**, pp. 617–624.
[28] Palau-Salvador, G., and Frankel, S. H., 2004, "Numerical Modeling of Cavitation Using Fluent: Validation and Parametric Studies," *34th AIAA Fluid Dynamics Conference and Exhibit*, Portland, OR.
[29] Gopalan, S., Katz, J., and Knio, O., 1999, "The Flow Structure in the Near Field of Jets and Its Effect on Cavitation Inception," J. Fluid Mech., **398**, pp. 1–43.
[30] Cerutti, S., Omar, M. K., and Katz, J., 2000, "Numerical Study of Cavitation Inception in the Near Field of an Axisymmetric Jet at High Reynolds Number," Phys. Fluids, **12**, pp. 2444–2460.
[31] Palau, C. V., Arregui, F. J., Palau-Salvador, G., and Espert, V., 2004, "Velocity Profile Effect on Woltman Water Meters Performance," *12th International Conference on Flow Measurement*, Beijing, China.

Experimental Investigation of the Submarine Crashback Maneuver

David H. Bridges
Associate Professor
Department of Aerospace Engineering,
Mississippi State University,
Mississippi State, MI 39762

Martin J. Donnelly
Mechanical Engineer

Joel T. Park
Mechanical Engineer

Naval Surface Warfare Center,
Carderock Division,
E. Bethesda, MA 20817

In order to decelerate a forward-moving submarine rapidly, often the propeller of the submarine is placed abruptly into reverse rotation, causing the propeller to generate a thrust force in the direction opposite to the submarine's motion. This maneuver is known as the "crashback" maneuver. During crashback, the relative flow velocities in the vicinity of the propeller lead to the creation of a ring vortex around the propeller. This vortex has an unsteady asymmetry, which produces off-axis forces and moments on the propeller that are transmitted to the submarine. Tests were conducted in the William B. Morgan Large Cavitation Channel using an existing submarine model and propeller. A range of steady crashback conditions with fixed tunnel and propeller speeds was investigated. The dimensionless force and moment data were found to collapse well when plotted against the parameter η, which is defined as the ratio of the actual propeller speed to the propeller speed required for self-propulsion in forward motion. Unsteady crashback maneuvers were also investigated with two different types of simulations in which propeller and tunnel speeds were allowed to vary. It was noted during these simulations that the peak out-of-plane force and moment coefficient magnitudes in some cases exceeded those observed during the steady crashback measurements. Flow visualization and LDV studies showed that the ring vortex structure varied from an elongated vortex structure centered downstream of the propeller to a more compact structure that was located nearer the propeller as η became more negative, up to $\eta=-0.8$. For more negative values of η, the vortex core appeared to move out toward the propeller tip.
[DOI: 10.1115/1.2813123]

1 Introduction

When a submarine is traveling in the forward direction and a rapid deceleration is required, the propeller of the submarine is put into reverse rotation. For some time the submarine continues to move forward while the propeller, operating in the reverse direction, is acting to decelerate the submarine. This condition of forward body velocity and reverse propeller rotation is referred to as *crashback*, and the maneuver is referred to as a *crashback maneuver*. All that is desired during the maneuver is a decrease in the submarine's forward velocity. No trajectory changes are commanded. However, because of the relative flow velocities in the vicinity of the propeller, a ring vortex develops around the propeller. This condition is illustrated schematically in Fig. 1. The velocities shown in this figure are relative to an observer fixed to the submarine. Because of the forward motion of the submarine, the flow velocities outside the propeller are directed rearward. However, because of the flow induced by the propeller operating in reverse, the velocities on the axis are directed upstream, toward the submarine. This shear between the velocities on the axis and the velocities outside the propeller causes the ring vortex to form. The ring vortex is not axisymmetric, however, and the asymmetry moves around the vortex. This asymmetry in the location and strength of the vortex results in unsteady asymmetric loads on the propeller, which are then transmitted to the submarine itself. These asymmetric forces and moments lead to uncommanded trajectory changes, so that in addition to continued forward motion, the submarine may pitch or yaw in an uncommanded fashion. In the shallow waters of littoral regions, where submarines have begun to operate, pinpoint control is a much larger issue than it was when most submarine actions took place in deep water.

The existence of a ring vortex around a propeller operating in a direction counter to forward motion has been known for some time, and according to Jiang et al. [1] was first reported by Lock [2], based upon observations of the flow past a propeller in a wind tunnel. Glauert [3] presented an estimate of propeller performance in the vortex ring state using a blade element analysis. Glauert [3] pointed out that the standard momentum analysis for propeller performance could not be performed, because a true slipstream did not form.

The determination of propeller performance in crashback is a standard component of so-called "four-quadrant" propeller performance tests. The term four quadrant is a reference to the fact that propeller performance in all four quadrants of the velocity-rotational speed (V-n) plane is measured: forward motion ($V>0$, $n>0$), backing motion ($V<0$, $n<0$), crashback ($V>0$, $n<0$), and crashahead ($V<0$, $n>0$). The reports by Hecker and Remmers [4] and Boswell [5] contain examples of such performance measures. In terms of actual flow physics, however, the work of Jiang et al. [1] appears to be one of the first studies of the fluid dynamic phenomena associated with the crashback maneuver on a submerged marine propeller. Jiang et al. [1] studied the flow past David Taylor Model Basin (DTMB) propeller 4381through the use of flow visualization and force measurements. These were propeller only or open-water studies conducted with the propeller mounted on a drive shaft in the DTMB 24 in. water tunnel. Jiang et al. [1] noted the unsteadiness of the ring vortex and also its frequent "bursting" and reformation. The force measurements indicated strong out-of-plane forces and moments generated on the propeller by the unsteady asymmetry of the ring vortex.

Propeller 4381 has been the subject of a number of experimental and numerical studies. Chen and Stern [6] performed a four-quadrant computational study of P4381. This study used the un-

Contributed by the Fluids Engineering Division of ASME for publication in the JOURNAL OF FLUIDS ENGINEERING. Manuscript received October 4, 2006; final manuscript received August 17, 2007; published online January 16, 2008. Review conducted by James A. Liburdy. Paper presented at the AIAA 43rd Aerospace Sciences Meeting and Exhibit, Reno, NV, Jan. 10–13, 2005, AIAA Paper No. 2005-0236.

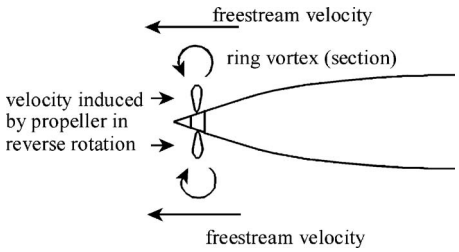

Fig. 1 Schematic of flow (velocities in reference frame of submarine in forward motion)

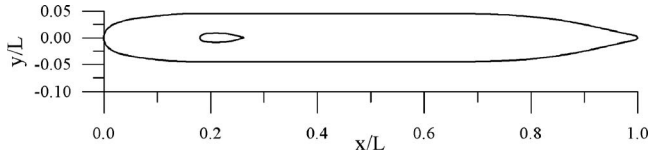

Fig. 2 Submarine hull contour; sail not used in experiments but indicates location of strut

steady, three-dimensional, incompressible, Reynolds-averaged Navier–Stokes equations in generalized coordinates and the Baldwin–Lomax turbulence model. Their computed results for thrust and torque were in generally good agreement with measured open-water values for P4381 as reported by Hecker and Remmers [4] and cited by Chen and Stern [6]. The results of Chen and Stern related to the crashback maneuver were confined to a comparison of their computed streamline patterns with the flow visualization photographs of Jiang et al. [1] and a comment that both the experiments and the computations indicate that the ring vortex grows in size and moves outboard as the advance ratio J becomes less negative, where J is defined as $J=V/nD$, with V equal to the velocity of flow, n equal to the rotational velocity of the propeller, and D equal to the propeller diameter.

The results of a considerably more in-depth computational study of the crashback maneuver are included in the report edited by Zierke [7]. These results are part of a larger study involving various aspects of submarine maneuvering problems. In these studies, the propellers were modeled as being mounted on the SUBOFF submarine body (see Groves et al. [8] for details of the SUBOFF geometry). The crashback studies in Ref. [7] made use of P4381. The unsteady Reynolds-averaged Navier–Stokes equations for incompressible flow were used, along with an algebraic turbulence model. These studies examined not only the fluid mechanics of the ring vortex around the propeller but also the trajectory of the submarine during the crashback maneuver. The studies showed the existence of a ring vortex around the propeller with an unsteady asymmetry that essentially rotated around the submarine axis. The frequency of this rotation was matched to the frequencies of out-of-plane forces and moments obtained from the computations. The studies also demonstrated some of the behavior of the ring vortex relative to the propeller, such as instances where the ring vortex "touched" a propeller blade and the corresponding pressure signatures on the blade. The submarine trajectories predicted by the computations demonstrated the "wandering" motion caused by the out-of-place forces and moments generated by the asymmetry of the ring vortex. It is precisely these "wanderings" that are the major concern for shallow-water maneuvers. The results of the computational studies did not demonstrate vortex bursting or reformation, however, and the behavior of the ring vortex was generally much more benign than that usually observed in experiments.

The study of crashback to be described in this paper was performed in the U. S. Navy's William B. Morgan Large Cavitation Channel. Propeller 4381 was attached to a standard axisymmetric submarine hull model (DTMB model 5495-3), which was then suspended in the large cavitation channel (LCC). Forces and moments were measured on both the body and the propeller for steady and unsteady crashback conditions. The unsteady conditions were simulated by allowing the propeller to "windmill" in the forward direction and then engaging the propeller in the reverse direction, with the tunnel velocity held constant. Forces and moments were measured during the change in propeller speed. A further simulation was undertaken whereby the tunnel motor was shut off once the windmilling propeller engaged in reverse rotation, and the tunnel speed was allowed to coast down to zero. Forces and moments were measured during this simulation also. In addition to the force and moment measurements, laser Doppler velocimeter (LDV) measurements of the flow field around the propeller during steady crashback were obtained, in addition to extensive flow visualization studies.

2 Experimental Apparatus and Procedure

The LCC is part of the Carderock Division of the Naval Surface Warfare Center (NSWCCD) and was first made operational in 1991. The LCC has a test section that is 3.05 m (10 ft) high, 3.05 m (10 ft) wide, and 12.2 m (40 ft) long. The maximum test section speed is approximately 18 m/s (35 kts), and the pressurization range for the test section extends from 3.5 kPa (0.05 psi (absolute)) to 415 kPa (60 psi (absolute)). The freestream turbulence level is less than 0.5%. Details of the design, construction, and operation of this facility may be found in Etter and Wilson [9,10]. More recently, Park et al. [11] have done an extensive study of the performance characteristics of the LCC and have documented in detail the flow temporal and spatial uniformity and the turbulence levels in the facility, as well as the data acquisition equipment and procedures for velocity measurements in the LCC test section. According to Ref. [11], the temporal stability of the LCC test section flow speed is ±0.15% for test section velocities between 0.5 m/s and 18 m/s. The test section velocity is spatially uniform to within ±0.60% for velocities between 3 m/s and 16 m/s. The turbulence level in the facility is between 0.2% and 0.5% for test section velocities from 0.5 m/s to 15 m/s, with no harmonics appearing in the power spectra of the velocity signals. For all of the tests conducted during the current study, the tunnel pressure was set at 50 psi (gauge) at the test section top.

The model used in these experiments was a standard axisymmetric hull with a sail and four standard cruciform stern appendages (DTMB model 5495-3). The hull length L was 6.92 m (272.36 in.) and the diameter D_h was 0.623 m (24.54 in.). The hull outline is shown in Fig. 2. The model was suspended using the standard LCC strut. A fairing that essentially duplicated the sail was initially wrapped around the strut, but during preliminary tests it was decided that the fairing was not necessary and so it was removed before the actual testing began. The placement of the stern appendages is illustrated in Fig. 3. The fin cross sections were NACA 0012 airfoil sections. When it had been determined that the propeller dynamometer results were consistent with the body dynamometer results, a stabilization strut was added to the rear of the model, connecting one of the stern fins to the LCC test section wall. This strut was added to secure the model against possible damage caused by large-amplitude oscillations at higher tunnel and propeller speeds. When this strut was in place, only propeller dynamometer readings could be obtained.

The propeller used in this test was DTMB Propeller No. 4381 (hereinafter referred to as P4381). This propeller was originally designed and built as part of a study of the effects of skew on marine propellers [5]. P4381 was the unskewed propeller in this series. Interestingly, this study was funded by several commercial shipping companies, and so the propeller design itself and the results of the study were unclassified. The fact that P4381 has an unclassified geometry and that the actual model propeller still exists has resulted in a number of both experimental and computa-

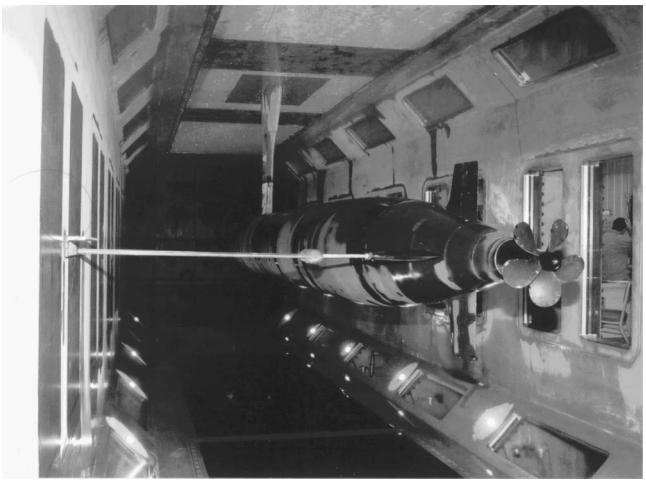

Fig. 3 Illustration of propeller, stern appendage placement, and stabilization strut

tional studies being performed on it, including the current study. P4381 may be seen in Fig. 3. P4381 is a five-bladed propeller with a diameter of 1 ft, an expanded area ratio of 0.725, a NACA $a=0.8$ section meanline, and an NACA 66 section thickness distribution with NSRDC modifications to the nose and tail thicknesses. The design advance coefficient J was 0.889, and the design thrust loading coefficient C_{th} was 0.534 (Ref. [5]).

The forces on the model were measured using a AMTI six-component dynamometer. This device is an internal force balance that was attached between the strut and the model. It was set up to measure forces in all three directions and moments about all three axes. The MicroCraft six-component propeller dynamometer was a multicomponent cylindrical assembly that attached to the propeller on its upstream face. It was used to measure three orthogonal forces and three moments. An absolute position digital encoder, Model 25HN from Sequential Information Systems Inc., was used to monitor the angular location of the propeller and dynamometer. The encoder had a resolution of 2^{11} resulting in an angular position accuracy of 0.18 deg. The output of the encoder was passed through a frequency-to-voltage converter so that the speed of the propeller could be recorded along with the force and moment and other data acquired by the computer.

Measurements of the velocity field were obtained using the LCC's Dantec LDV system. This system is described in great detail in the report by Park et al. [11]. The system consists of four Dantec BSA 57N11 signal processors, three fiber optic probes, two Spectra Physics 6 W argon-ion lasers, a Dantec 3D traverse, and Dantec flow software. The LDV system was calibrated using a rotating disk. The resulting uncertainty in the calibration is reported in Ref. [11] to be less than 0.018 m/s at a disk speed corresponding to a tunnel speed of 15 m/s.

Data were collected from 16 channels: 3 propeller force components, 3 propeller moment components, 3 body force components, 3 body moment components, the tunnel pressure, the venturi velocity, the propeller speed, and the tunnel temperature. These were usually sampled at a rate of 200 Hz and the number of samples taken per channel was usually 48,000, yielding a total of 768,000 measurements for each test. The coordinate system used was the standard body-fixed coordinate system. Positive x was taken to be forward, in the direction of forward motion. The coordinate y was taken to be positive to starboard, and z was positive down through the keel, completing the right-handed coordinate system. Body forces in the x, y, and z directions are denoted as F_x, F_y, and F_z forces, respectively, and body moments about the x, y, and z axes are denoted as M_x, M_y, and M_z. Propeller forces in the x, y, and z directions are denoted as f_x, f_y, and f_z, respectively, and propeller moments about the x, y, and z axes are denoted as m_x, m_y, and m_z. Note that an upper case F or M is used to indicate a body force or moment, and a lower case f or m is used to indicate a propeller force or moment.

Traditionally, the dimensionless parameter associated with propeller performance data has been the advance ratio J, defined by $J=V/nD$, where V is the forward velocity of the vehicle, n is the propeller rotational speed (usually in rev/s), and D is the diameter of the propeller. However, recent studies have shown that the data may also be collapsed well by using the similarity parameter η, defined as $\eta=n/n_{sp}$, where n is the actual propeller speed and n_{sp} is the propeller speed required for self-propulsion; that is, the propeller speed at a given forward velocity V at which the thrust produced by the propeller is equal to the drag of the vehicle. As will be seen later in this report, the data do collapse well when plotted versus η. However, the use of η requires the determination of n_{sp}, which must be determined experimentally and usually during the test itself, since the thrust of the propeller and the drag of the vehicle will depend on such things as the propeller mount, the interaction between the propeller and the vehicle body, the manner in which the vehicle is mounted in the water tunnel, and so forth. The values of n_{sp} were determined in the following manner. The propeller motor in the model was set for forward rotation. The tunnel speed V was set at a particular speed. Then the propeller speed was varied until the net thrust force as measured by the body force balance was nominally zero. Since it was usually not possible to get a reading of exactly zero, points were obtained on either side of zero and then a linear interpolation was performed to obtain the actual value of n_{sp}. These points were obtained at tunnel set speeds of 2.5 kts, 5 kts, 7.5 kts, and 10 kts (1.29 m/s, 2.57 m/s, 3.86 m/s, and 5.14 m/s, respectively). The variation of n_{sp} with tunnel speed V turned out to be very close to a straight line, and so a linear regression was performed to obtain a relation between n_{sp} and V. The resulting regression was

$$\frac{n_{sp}}{\text{rpm}} = 102.04\frac{V_{\text{venturi}}}{\text{kts}} + 19.831 \tag{1}$$

Ideally the intercept would be zero, since the propeller speed required for self-propulsion at zero forward velocity is zero. However, adding the intercept increased the accuracy of the linear regression so that the standard R^2 value for the regression was greater than 0.99995. The speed V_{venturi} was the test section speed obtained by a calibration of the pressure drop across the tunnel contraction.

In addition to using two different dimensionless representations of the propeller speed, it is also possible to normalize the resulting force and moment data in two different ways, depending on the quantities of interest. One is to use the dynamic pressure and model length scale as the normalizing values, so force and moment coefficients are calculated as follows:

$$C_F = \frac{F}{q_\infty L^2} \quad C_M = \frac{M}{q_\infty L^3} \quad q_\infty = \frac{1}{2}\rho_\infty V_\infty^2 \tag{2}$$

In these formulas, F and M are arbitrary forces and moments, C_F and C_M are the corresponding force and moment coefficients, q_∞ is the freestream dynamic pressure based on the freestream density and velocity, and L is a body length scale. The other way in which the forces and moments may be normalized is through the use of propulsive quantities, as follows:

$$C_F = \frac{F}{\rho_\infty n^2 D^4} \quad C_M = \frac{M}{\rho_\infty n^2 D^5} \tag{3}$$

Here, n is the propeller speed in rev/s, and D is the propeller diameter. Both of these definitions were used in reducing the data as necessary, and, in particular, they were used to normalize the rms values of the forces and moments. Both definitions were found to collapse the data well.

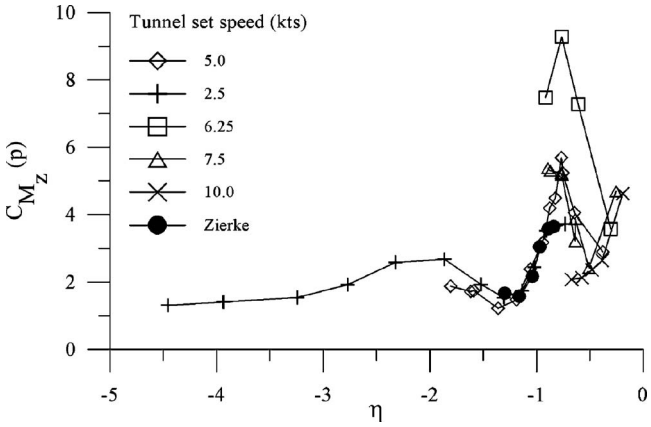

Fig. 4 Body rms yawing moment coefficient (based on propulsive scaling)

Estimating the uncertainties in the force and moment coefficients presented something of a challenge, because twice the standard deviation (2σ) is usually used as the measure of the random uncertainty of the measurement, for a sufficiently large number of samples. However, in these tests, the quantities of interest *were* the standard deviations or rms values of the forces and moments, represented as dimensionless coefficients. It was the variations of these quantities, used as a measurement of the unsteadiness of the flow, that were being tracked as a function of the parameter η. A procedure was developed for determining the uncertainty in the rms values using essentially a rms value of the rms value. For details of this procedure, see the report by Bridges [12]. The total uncertainties were estimated using standard techniques, as outlined in Coleman and Steele [13]. The results indicated an uncertainty of approximately 6% in the value of the yawing moment coefficient obtained using the rms values at a value of η where the magnitude of the yawing moment coefficient tended to reach its peak. Since the yawing moment coefficient demonstrated the greatest variations, this value should be representative of the uncertainties in the other force and moment coefficients. The uncertainty in η itself ranged from approximately 18% at low propeller speeds to 2.4% at the highest propeller speeds (see Ref. [12] for the details of this analysis). The data themselves demonstrated a strong repeatability with η, so it is believed that the relatively large uncertainty at low values of the propeller speed was overestimated for reasons that are not clear.

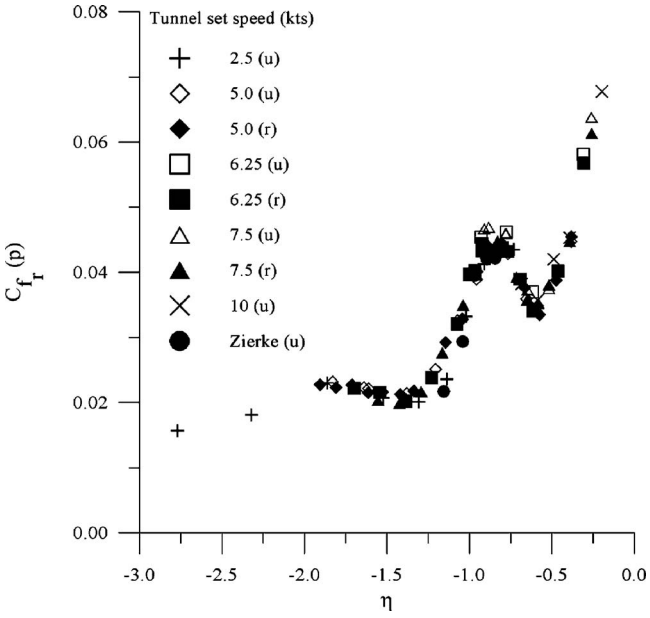

Fig. 6 Propeller rms resultant force coefficient (based on propulsive scaling)

The first set of tests conducted studied cases of steady crashback, which means that both propeller speed and tunnel speed were held constant and data were collected over a period of time. Data were collected from the body and propeller force balances for a set of crashback conditions and when it was ascertained that the propeller force balance was producing results in line with the body force balance, the restraint strut was added and further measurements were made. Two different types of unsteady crashback

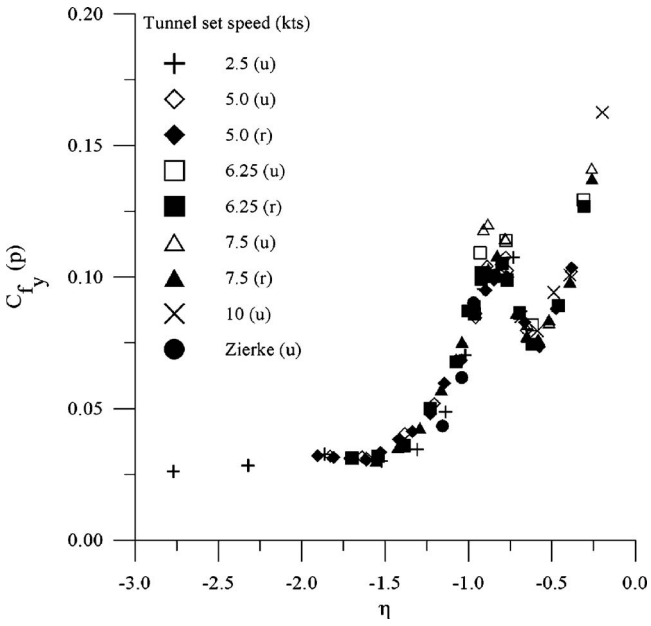

Fig. 5 Propeller rms side force coefficient (based on propulsive scaling)

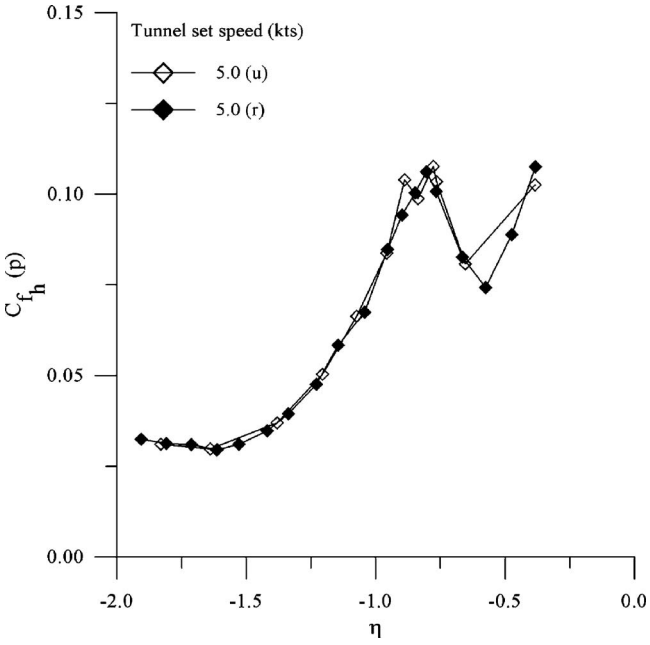

Fig. 7 Comparison of propeller rms horizontal force coefficient values with and without restraint strut

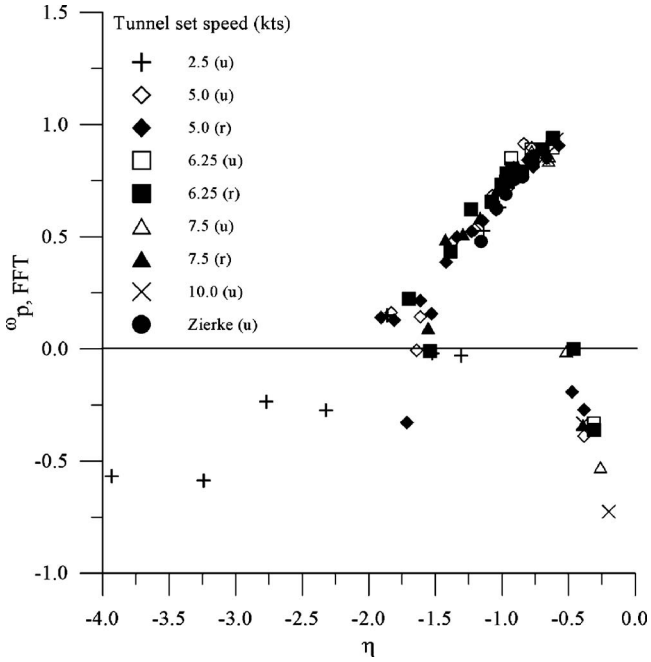

Fig. 8 Dimensionless frequency of peak propeller *y* force amplitude (*u*/*r*—restraint strut off /on)

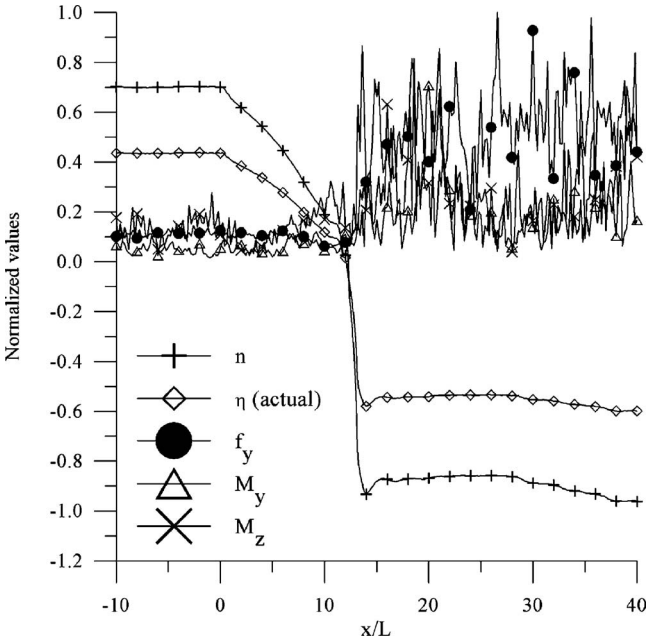

Fig. 10 Development of rms propeller *y* force and rms body pitching and yawing moments during constant tunnel velocity, ramped propeller speed simulation of unsteady crashback maneuver (values normalized by maximum data value in each set)

studies were conducted. Because of the way the power was connected to the propeller motor, the motor was "hard wired" for either forward or reverse rotation in a given test. The only way to reverse propeller direction was to manually reverse the motor leads. This meant that the propeller could not be started in the forward direction, stopped, and then placed in reverse rotation. However, it was noted that with the propeller motor off and the tunnel speed set at some value, the propeller would "windmill" in forward rotation at some speed. The propeller motor could then be engaged in reverse rotation. Once engaged, it would slow its forward rotation to zero and then begin rotating in reverse, reaching its commanded reverse speed in a fairly short time. This behavior was used to simulate the initiation of the crashback maneuver. The fact that the fluctuating force and moment component amplitudes were now functions of time required a modification to the data reduction procedure. The rms values of the forces and moments were obtained for 200-sample subsets of the complete record. The time associated with each rms value thus obtained was taken as the time midpoint of the 200-sample subset. The second unsteady crashback study simulated the actual deceleration of the submarine. In these studies, the tunnel speed was set at a particular value (usually 7.5 kts) and the propeller was allowed to windmill in forward rotation. The propeller motor was then engaged. As soon as the personnel observing the test noted the propeller speed beginning to change, the tunnel operator sets the tunnel speed to zero. This would cause the tunnel speed to gradually coast down to zero. The same procedure for using 200-sample subsets to compute rms values was implemented.

When the force and moment measurements were completed for the steady crashback studies, detailed LDV surveys of the propel-

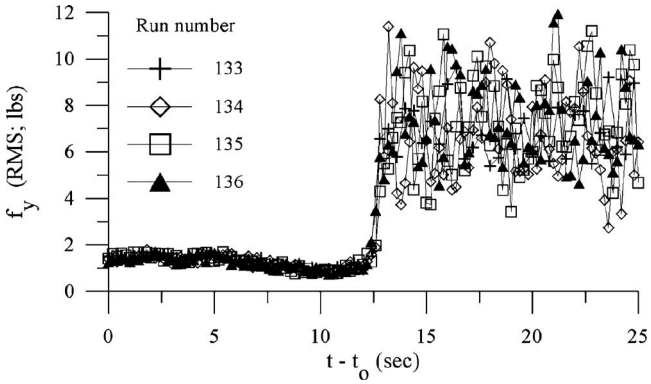

Fig. 9 rms propeller side force development for ramped propeller speed simulation of unsteady crashback

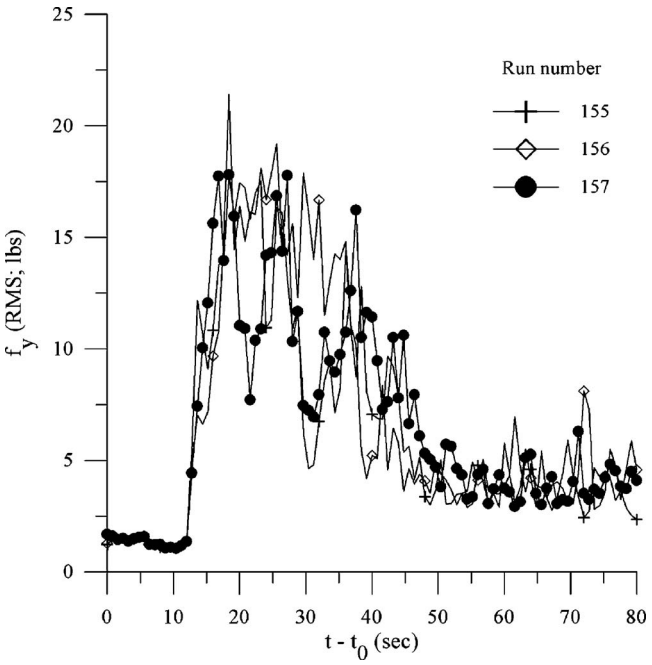

Fig. 11 Development of rms propeller *y* force during ramped tunnel velocity, ramped propeller speed simulation of unsteady crashback maneuver

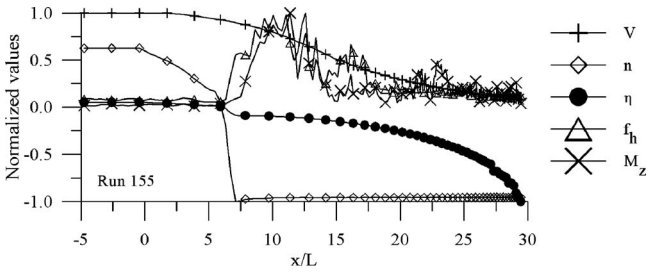

Fig. 12 Development of rms propeller horizontal force and rms body yawing moment during unsteady crashback maneuver simulation

ler flowfield were conducted at flow conditions of interest noted in the steady crashback results. Flow visualization studies using a laser sheet, fluorescent dye, and bubbles were also conducted at these flow conditions of interest.

3 Results

Figure 4 shows the variation of the coefficient of body rms yawing moment with η for the different tunnel speeds tested. It was observed throughout the results that the data at 6.25 kts tended to be somewhat noisier than the rest of the data and hence had higher rms values. These are the data points that are separated from the others in Fig. 4. The data show good repeatability and all of the curves demonstrate a local maximum around $\eta=-0.8$. Figure 5 shows the results for the coefficient of propeller rms side force with η. These data exhibit a high degree of repeatability and produce what appears to be a very characteristic response curve. The local maxima again occur around $\eta=-0.8$. The propeller side force is the y component of the force on the propeller measured in a reference frame attached to the propeller. Figure 6 shows the variation of the coefficient of propeller rms resultant force with η. The rms resultant force is simply the resultant of the propeller rms y and z (i.e., off axis) forces that act perpendicular to the axis of the propeller. Again the high degree of repeatability, the local maximum around $\eta=-0.8$, and the characteristic response are all exhibited. Figures 4–6 are representative of the results for all of the out-of-plane body and propeller rms forces and moments.

There had been some concern that the addition of the restraint strut would interfere with the flow to the point of invalidating the forces and moments measured with the propeller dynamometer. Figure 7 compares the results obtained for the propeller horizontal force (propeller y and z forces resolved into a component perpendicular to the wall of the tunnel) for restrained and unrestrained model conditions. As can be seen in this figure, the results track each other very well, indicating that the restraint strut did not unduly interfere with the flow or the force and moment measurements.

As was noted in the Introduction, the ring vortex asymmetry rotates around the propeller, creating the unsteady out-of-plane forces and moments for which the rms values have just been presented. The frequencies of these rotations were also determined by performing a Fourier spectral analysis of the propeller side force data records. The frequency at which each record had a maximum amplitude, denoted here by f, was recorded. A reduced frequency ω was computed from $\omega=2\pi(f-n)D/V$, where n is the propeller rotation speed, D is the propeller diameter, and V is the free stream velocity. The variation of σ with η is shown in Fig. 8. These data demonstrate the repeatability exhibited by the force data. For low magnitudes of η, ω begins with a negative value, indicating that the peak amplitude frequency is less than the propeller rotational speed. This actually means that seen in the reference frame of the rotating propeller, the asymmetry is rotating in the same direction as the propeller rotation. As η becomes more negative, ω changes sign rapidly around $\eta=-0.5$ and becomes

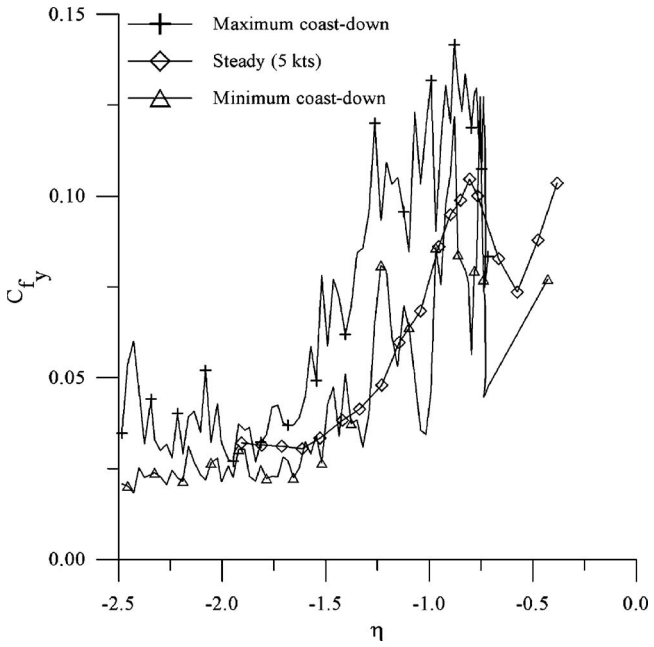

Fig. 13 Comparison of coefficients of rms propeller *y* force between unsteady crashback conditions and the minimum and maximum values of the three ramped tunnel velocity, ramped propeller speed simulations of the unsteady crashback maneuver

positive, indicating that the peak amplitude frequency is now higher than the rotational speed. Now the asymmetry is rotating in the opposite direction as the propeller, as seen in the propeller reference frame. The value of σ then reduces gradually as η becomes more negative, changing sign again around $\eta=-1.7$. The data become rather noisy around these values of η, since it be-

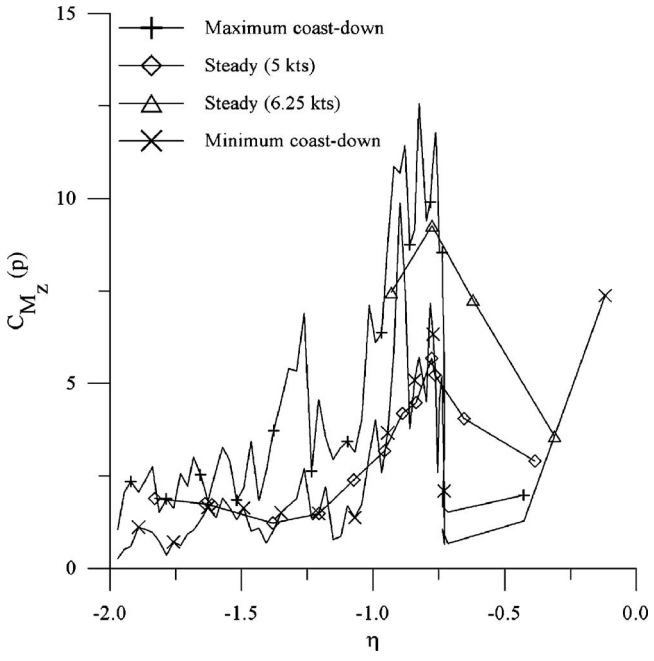

Fig. 14 Comparison of coefficients of rms body yawing moment between steady crashback conditions and the minimum and maximum values of the three ramped tunnel velocity, ramped propeller speed simulations of the unsteady crashback maneuver

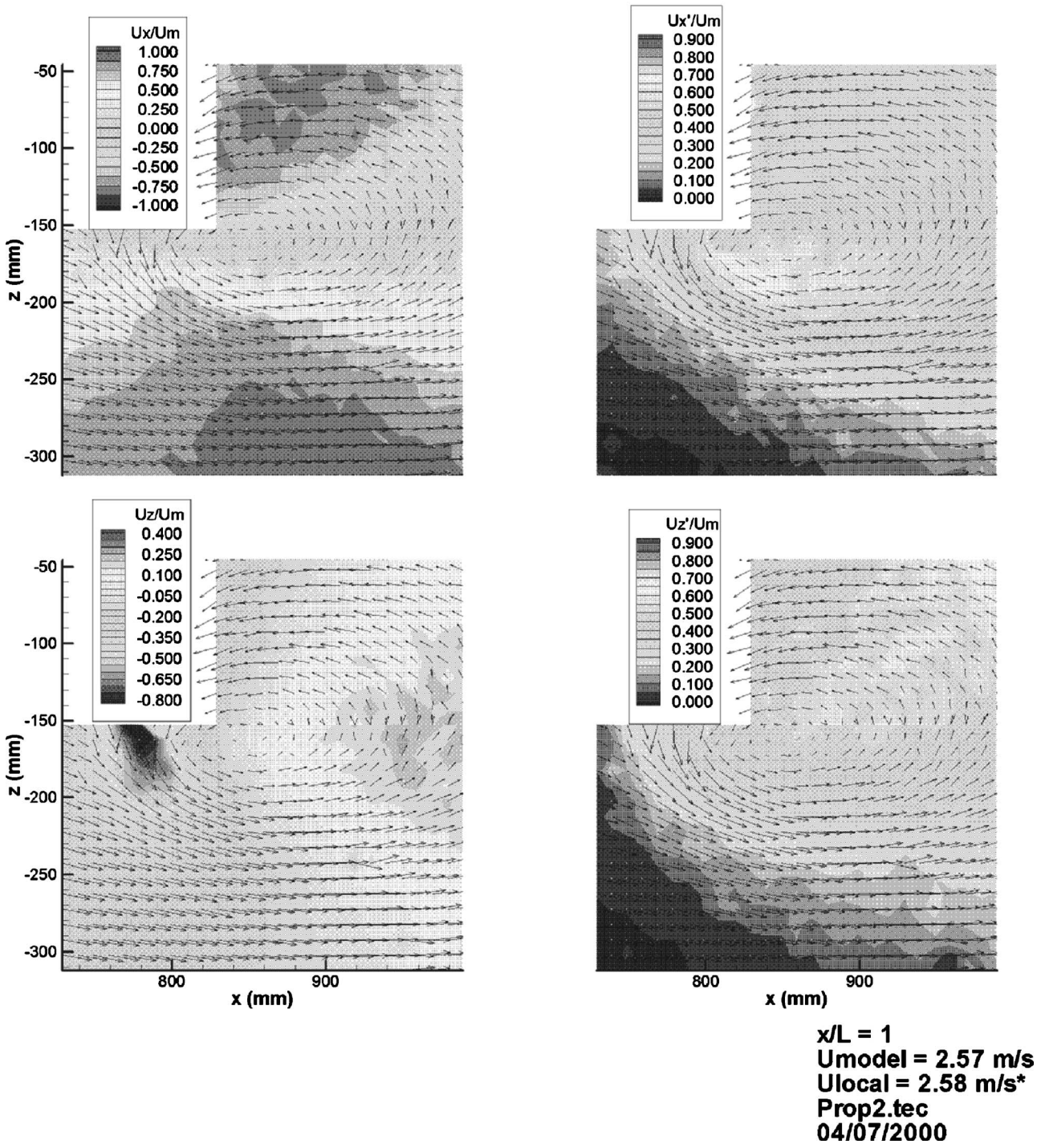

Fig. 15 Summary of LDV velocity field surveys for $\eta=-0.801$ (in coordinates shown, propeller tip would be located at $x=809.2$ mm, $z=152.4$ mm)

comes difficult to distinguish the peak in the force signal arising from the rotation of the vortex asymmetry and the peak arising from the propeller rotation itself in this range of η.

Figure 9 shows the results of one of the unsteady crashback simulations in which the tunnel speed was held constant and the propeller was engaged in reverse rotation, having been allowed to windmill in forward rotation at a speed of +330 rpm. This figure shows the development of the dimensional propeller side force fluctuations with time. The variable t_0 is the time at which the propeller first began to decelerate, as indicated by the values for

propeller speed in the data record. This figure shows that the propeller side force develops extremely rapidly then oscillates about some mean, nonzero value. It is the rms of this value that was examined in previous figures. Figure 10 illustrates the development of the propeller side force and body pitching and yawing moments for the same type of unsteady crashback simulation. This figure includes the time history of the propeller speed and the instantaneous value of η, obtained from instantaneous values of the propeller and tunnel speeds. In this figure, all of the values have been normalized by the maximum value for each variable (with the exception of η) so that they could all be displayed on the same figure. The time axis has been renormalized as a dimensionless variable x/L, where L is the total length of the model. The position variable x was obtained by integrating numerically in time the tunnel free stream velocity. This figure essentially shows that the propeller completes its transition from positive to negative rotation in approximately 13 model lengths and that the propeller side force and the body moments develop in less than 2 model lengths.

Figure 11 shows the results of some of the unsteady crashback simulations in which the propeller speed was allowed to vary as described in the previous paragraph, but the tunnel speed was set to zero when the propeller was observed to engage in reverse rotation and the tunnel was allowed to coast down to zero speed. This figure again shows the rapid buildup of the propeller side force but then its gradual decay as the tunnel velocity decreased, presumably due to the decreased shear between the free stream flow and the reversed flow induced by the propeller and the corresponding weakening of the ring vortex. This explanation is reinforced by Fig. 12, which shows the development of the propeller horizontal force and the body yawing moment, along with the propeller speed, tunnel speed, and η (all normalized by their maximum values). The abscissa is again a dimensionless length that represents the number of model lengths over which the phenomena occur, and again is obtained by integrating numerically in time the tunnel free stream velocity. These curves show the rapid development of the out-of-plane force and moment but then their gradual reduction as the tunnel speed decreases. The propeller horizontal force tracks the tunnel speed fairly closely, but the body yawing moment tends to damp out a little more quickly. The value of η in this figure would in theory approach minus infinity since the propeller speed is fixed but the tunnel speed and hence the self-propulsion propeller speed are approaching zero. Figures 13 and 14 compare some of the steady and unsteady crashback simulation results. The instantaneous values of the free stream speed V and propeller speed n recorded during the unsteady crashback simulations just discussed were used to calculate instantaneous values of η at each instant in the data record. For each value of 0 so obtained, the minimum and maximum values of the coefficients of propeller side force and body yawing moment were determined. These were plotted in Figs. 13 and 14 along with the corresponding values from the steady crashback studies. The propeller side force data are shown in Fig. 13 and the body yawing moment data are shown in Fig. 14. These figures show that the magnitudes of the coefficients in the unsteady crashback studies exceeded those obtained in the steady crashback studies in some instances.

Figure 15 shows the LDV data obtained at $\eta=-0.801$. In each figure, the variable being plotted (mean and fluctuating streamwise velocities and mean and fluctuating transverse velocities) are overlaid with the mean velocity vectors. Similar data sets were obtained at values of η of -0.380, -0.570, and -1.1. The surveys at $\eta=-0.380$ indicated that the ring vortex was somewhat elongated in the streamwise direction. As η became more negative, the apparent position of the vortex core moved upstream and radially outward, in agreement with flow visualization results obtained by Jiang et al. [1] for a propeller in an "open-water" test. This vortex core "migration" is shown in Fig. 16. These core positions were obtained by examining the LDV surveys and determining the survey point at which the magnitude of the mean velocity was a minimum. Figure 17 shows some further results of the LDV measurements. This figure shows the mean and fluctuating streamwise and transverse velocity components measured at the LDV grid location closest to the propeller for which a full transverse survey was obtained (i.e., the x location at the right edge of the "notches" in Fig. 15). The velocities at this streamwise location are repre-

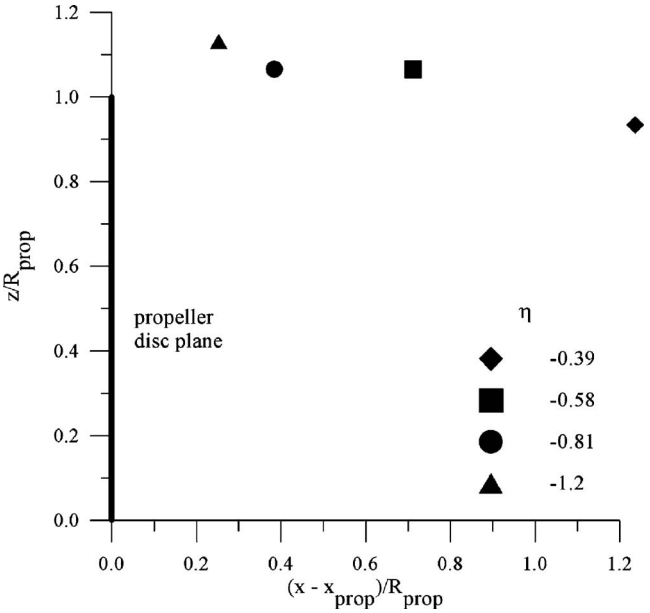

Fig. 16 Vortex center positions estimated from LDV measurements (downstream direction is to the right in this figure)

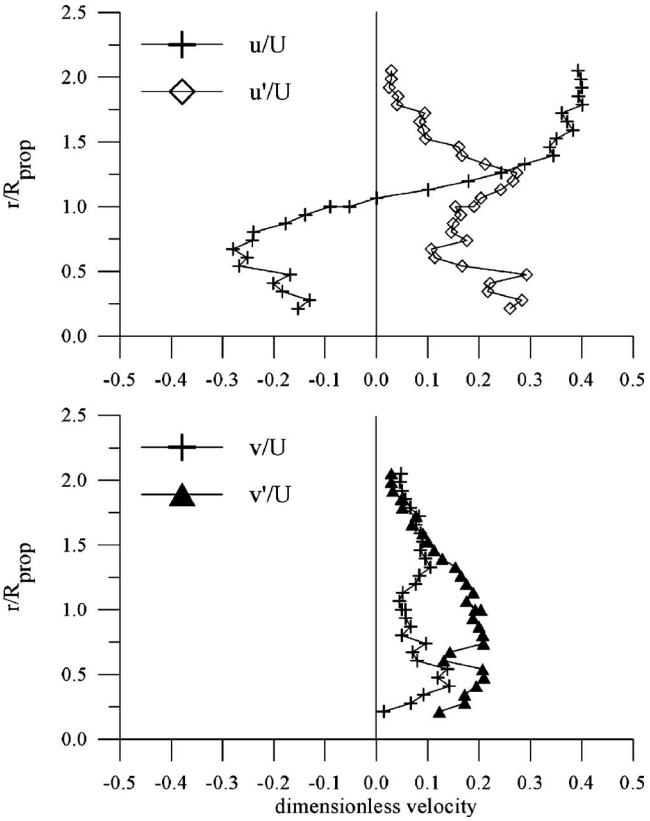

Fig. 17 Velocity components at complete survey position nearest propeller for $\eta=-0.80$

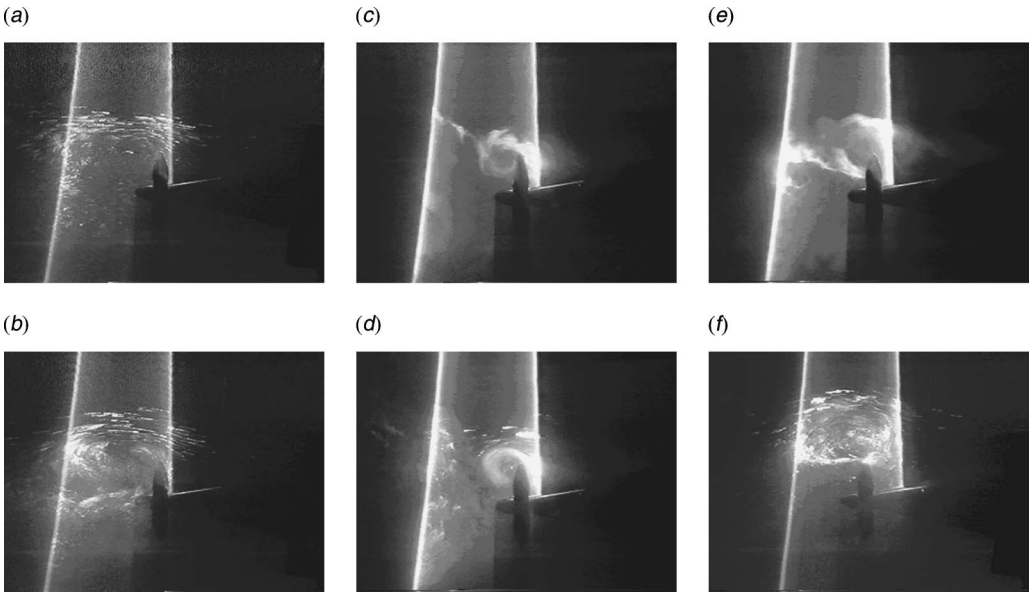

Fig. 18 Comparison of "formed vortex" positions at different values of η: (*a*) $\eta=-0.387$, (*b*) $\eta=-0.580$, (*c*) $\eta=-0.725$, (*d*) $\eta=-0.825$, (*e*) $\eta=-1.09$, and (*f*) $\eta=-1.52$

sentative of the inflow velocities for the propeller. These profiles were examined at each of the values of η listed above. One feature, in particular, exhibited by these profiles was the movement of the peak in the fluctuating velocity components radially outward as η became more negative. This movement would tend to increase the magnitude of the out-of-plane forces and moments acting on the propeller, since the changes in the forces on the blades caused by the fluctuating velocities would act through larger moment arms thus magnifying the forces and moments exerted on the propeller shaft and thereby transmitted to the submarine body.

The migration of the apparent vortex core position is shown by the flow visualization photographs contained in Fig. 18. The vortex in these figures demonstrates the behaviors inferred from the LDV measurements as discussed in the previous paragraph. These figures are similar to those obtained by Jiang et al. [1]. However, it should be noted that the flows observed by Jiang et al. apparently were more steady than the flows in the current experiments, based on the comments by Jiang et al. They noted occasional disturbances in which the vortex would apparently disappear altogether in a random burst of bubbles and then reform, but on the whole would tend to oscillate about a more or less fixed position. In the current experiments, two different types of large-scale disturbances were noted in the flow visualization images. The first was a large-scale disruption similar to that reported by Jiang et al. [1]. The second was a vortex shedding event in which the vortex would apparently detach from the propeller and move off downstream, and a new vortex would form on the propeller. Figure 19(*a*) illustrates a vortex shedding event, in which the shed vortex is just about to move out of the laser sheet, and a new vortex is forming near the propeller tip. Figure 19(*b*) is an example of a large-scale disruption.

The vortex shedding events and the large-scale disruptions of the flow did not appear to be quite periodic but did occur on a fairly frequent basis for the appropriate values of η. The "frequency" of these events seemed to be dictated more by the free stream flow speed than by the propeller speed. The sheddings and disruptions occurred more frequently at higher tunnel set speeds. Generally speaking, the large-scale disturbances were separated by intervals during which the formed vortex structure was present. These intervals tended to decrease as the magnitude of η increased. Recall from the earlier discussion that the peak values of the dimensionless out-of-plane force and moment coefficients occurred in the vicinity of $\eta=-0.8$. The flow visualization studies showed that the ring vortex seemed to have its most organized structure at this value of η. There were some large disturbances. At $\eta=-0.8$, these large disturbances, mostly vortex shedding events, exhibited their most periodic behavior. The ring vortex would form and shed in almost equal intervals of time. The resulting wake behind the propeller appeared to swirl about the propel-

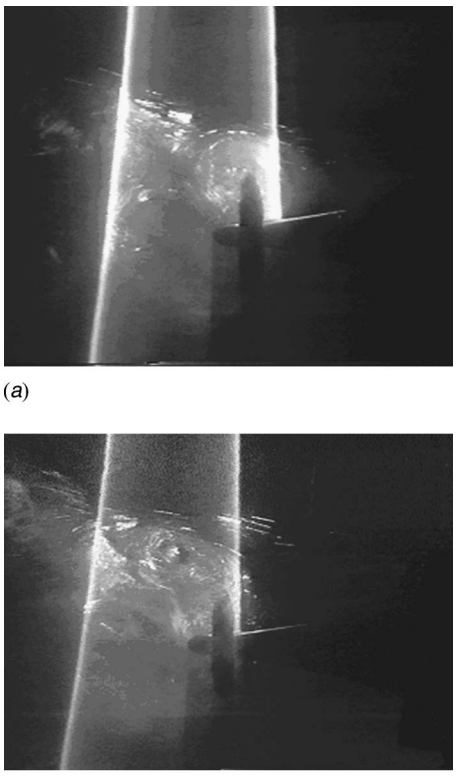

Fig. 19 Examples of large-scale disturbances to vortex flow for $\eta=-0.780$: (*a*) vortex shedding event and (*b*) large-scale disruption

ler and acquired a corkscrewlike appearance downstream. In the two-dimensional view provided by the laser sheet, the flow most closely resembled that of vortex shedding behind a circular cylinder. Recall the earlier discussion, which said that the large disturbance aspect of the flow seemed to be influenced more by the free stream speed than the propeller speed. In the author's opinion, the best way to describe what is happening in the flow in the vicinity of $\eta=-0.8$, as illustrated by these flow visualization images, is that the apparently free stream dominated phenomenon that is causing the large disturbances is coupling with the vortex ring flow, creating a periodic large disturbance that in turn is producing the peak in the dimensionless out-of-plane force and moment coefficients.

4 Conclusions

The LDV measurements revealed a variation in the vortex structure and core location as η varied, with the propulsion parameter η defined as the ratio of the propeller rotational speed to the propeller speed required for self-propulsion. At the smaller magnitudes of η, the vortex structure appeared to be elongated somewhat in the streamwise direction. As the magnitude of η increased, the vortex structure became tighter and the vortex core appeared to move upstream and radially outward toward the propeller tip. Profiles of the fluctuating velocity components at the LDV streamwise measurement position closest to the propeller showed that the spatial peaks in the fluctuations moved radially outward as η became more negative.

The flow visualization results confirmed the movements of the vortex core indicated by the LDV measurements and also showed that at very large negative values of η, the ring vortex could actually be located upstream of the propeller. The flow visualization experiments also revealed that the ring vortex could experience large-scale disturbances, either through apparent "vortex-shedding" events or through large-scale disruptions where the ring vortex essentially disappeared for brief periods of time. These large-scale disturbances did not appear to be periodic, except in the vicinity of $\eta=-0.8$, where the large-scale disturbances and the inherent unsteadiness in the ring vortex appeared to couple and produce a very large periodic disturbance to the wake, resulting in large periodic forces on the propeller and the submarine. Both the LDV measurements and the flow visualizations seemed to suggest that the vortex structure was the most organized in the vicinity of $\eta=-0.8$.

The out-of-plane force and moment coefficient values obtained from both the propeller and body dynamometers for the steady crashback simulations were correlated well with η. The coefficients demonstrated a relative maximum for values of η near -0.8 for both the propeller and body data. It was near this value of η that the LDV and flow visualization measurements indicated the most-organized vortex structure. Spectral analyses of the propeller data indicated a reversal in the direction of the ring vortex asymmetry rotation relative to the propeller as the magnitude of η was increased past its lowest value. The magnitude of this relative rotation frequency then decreased in magnitude as the magnitude of η was increased further (i.e., as 0 became more negative).

The unsteady crashback simulations revealed that the magnitudes of the out-of-plane force and moment coefficients could exceed those obtained during the steady crashback measurements. The data from the ramped propeller and tunnel speed tests also indicated that the magnitudes of the coefficients tracked the tunnel speed fairly closely, suggesting that the strength of the ring vortex decreased as the relative shear between the free stream flow and the propeller-induced flow decreased.

Acknowledgment

This work was performed under an Office of Naval Research Defense Experimental Program to Stimulate Competitive Research (DEPSCoR) Grant No. N00014-97-1-1069. The program monitor was L. Patrick Purtell of the ONR. Part of the funding for this project was in the form of matching funds provided by the principal investigator's department, the Department of Aerospace Engineering at Mississippi State University.

Nomenclature

C_F = generic force coefficient
C_{fh} = coefficient of rms propeller horizontal force
C_{fr} = coefficient of rms propeller resultant force
C_{fy} = coefficient of rms propeller side force
C_M = generic moment coefficient
C_{Mz} = coefficient of rms body yawing moment
C_{th} = thrust loading coefficient
D = propeller diameter
D_h = model hull diameter
F = generic force component
F_x = force component on body in x direction
F_y = force component on body in y direction
F_z = force component on body in z direction
f = hydrodynamic frequency
f_x = force component on propeller in x direction
f_y = force component on propeller in y direction
f_z = force component on propeller in z direction
J = advance ratio, $J=V/nD$
L = model hull length
M = generic moment component
M_x = moment component on body in x direction
M_y = moment component on body in y direction
M_z = moment component on body in z direction
m_x = moment component on propeller in x direction
m_y = moment component on propeller in y direction
m_z = moment component on propeller in z direction
n = propeller rotational speed
n_{sp} = propeller rotational speed at self-propulsion point
q = dynamic pressure
R_{prop} = propeller radius
r = radial distance from hull centerline
t = time
t_0 = time of propeller direction reversal
U, V, V_4 = free stream velocity
u = mean streamwise velocity component
u' = fluctuating streamwise velocity component
v = mean radial velocity component
v' = fluctuating radial velocity component
x = coordinate direction parallel to body axis, positive forward
y = coordinate direction perpendicular to body axis, positive starboard
z = coordinate direction perpendicular to body axis, positive down through keel
η = ratio of actual propeller rotational speed to speed required for self-propulsion, $\eta=n/n_{\mathrm{sp}}$
ρ_∞ = fluid density
σ = standard deviation
ω = reduced hydrodynamic frequency
$\omega_{p,\mathrm{FFT}}$ = reduced hydrodynamic frequency at peak fast Fourier transform (FFT) amplitude of propeller side force

References

[1] Jiang, C.-W., Dong, R., Liu, H.-L., and Chang, M.-S., 1996, "24-Inch Water Tunnel Flow Field Measurements During Propeller Crashback," *Proceedings of the 21st Symposium on Naval Hydrodynamics*, Jun. 24–26, Trondheim, Norway, National Academy, Washington, DC, pp. 86–96.
[2] Lock, C. H. H., 1928, "Photographs of Streamers Illustrating the Flow around an Airscrew in the Vortex Ring State," British ARC R&M 1167.
[3] Glauert, H., 1943, "Airplane Propellers," *Aerodynamic Theory*, W. F. Durand ed., California Institute of Technology (reprint), Pasadena, CA, Vol. IV, pp. 348–351.

[4] Hecker, R., and Remmers, K., 1971, "Four Quadrant Open-Water Performance of Propellers 3710, 4024, 4086, 4381, 4382, 4383, 4384 and 4426," Naval Ship Research and Development Center Report No. 417-H01.
[5] Boswell, R. J., 1971, "Design, Cavitation Performance, and Open-Water Performance of a Series of Research Skewed Propellers," Naval Ship Research and Development Center Report No. 3339.
[6] Chen, B., and Stern, F., 1998, "Computational Fluid Dynamics of Four-Quadrant Marine-Propulsor Flow," *Proceedings of the 1998 ASME Fluids Engineering Division Summer Meeting*, ASME Paper no. FEDSM98-4872.
[7] Zierke, W. C., 1997, "A Physics-Based Means of Computing the Flow Around a Maneuvering Underwater Vehicle," Applied Research Laboratory, Pennsylvania State University, Technical Report TR 97-002.
[8] Groves, N., Huang, T., and Chang, M., 1989, "Geometric Characteristics of DARPA SUBOFF Models," David Taylor Research Center Report No. SHD-1298-01.
[9] Etter, R., and Wilson, M., 1992, "The Large Cavitation Channel," *Proceedings of the 23rd American Towing Tank Conference*, University of New Orleans, New Orleans, LA, pp. 243–252.
[10] Etter, R., and Wilson, M., 1992, "Testing Ship Designs in a Water Tunnel," Mech. Eng. (Am. Soc. Mech. Eng.), **13**(10), pp. 74–80.
[11] Park, J. T., Cutbirth, J. M., and Brewer, W. H., 2002, "Hydrodynamic Performance of the Large Cavitation Channel," Naval Surface Warfare Center Carderock Division, Report No. NSWCCD-50-TR-20002/068.
[12] Bridges, D. H., 2004, "A Detailed Study of the Flowfield of a Submarine Propeller During a Crashback Maneuver," Office of Naval Research Grant No. N00014-97-1-1069 Final Report, Department of Aerospace Engineering, Mississippi State University, Report No. MSSU-ASE-04-1.
[13] Coleman, H. W., and Steele, W. G., Jr., 1999, *Experimentation and Uncertainty Analysis for Engineers*, 2nd ed., Wiley, New York, Chap. 4.

Analysis of Turbulent Mixing Jets in a Large Scale Tank

Si Y. Lee
e-mail: si.lee@srnl.doe.gov

Richard A. Dimenna
e-mail: richard.dimenna@srnl.doe.gov

Robert A. Leishear
e-mail: robert.leishear@srnl.doe.gov

David B. Stefanko
e-mail: david.stefanko@srnl.doe.gov

Savannah River National Laboratory,
Washington Savannah River Company,
Aiken, SC 29808

Flow evolution models were developed to evaluate the performance of the new advanced design mixer pump for sludge mixing and removal operations with high-velocity liquid jets in one of the large-scale Savannah River Site waste tanks, Tank 18. This paper describes the computational model, the flow measurements used to provide validation data in the region far from the jet nozzle, and the extension of the computational results to real tank conditions through the use of existing sludge suspension data. A computational fluid dynamics approach was used to simulate the sludge removal operations. The models employed a three-dimensional representation of the tank with a two-equation turbulence model. Both the computational approach and the models were validated with onsite test data reported here and literature data. The model was then extended to actual conditions in Tank 18 through a velocity criterion to predict the ability of the new pump design to suspend settled sludge. A qualitative comparison with sludge removal operations in Tank 18 showed a reasonably good comparison with final results subject to significant uncertainties in actual sludge properties. [DOI: 10.1115/1.2820989]

1 Introduction

Tank 18 is a 1.3×10^6 gal capacity, single-wall waste tank located in the F-Tank Farm at Savannah River Site (SRS). It was placed into service as a receiver of low radioactive decay heat waste. The tank is a 26 m diameter flat-bottomed, domed roof, cylindrical carbon steel tank with a height of about 10.4 m with no cooling coils or internal supports. The waste in the tank was originally salt and sludge, but the salt has been dissolved and transferred to other tanks. The remaining sludge was hydraulically resuspended and transferred to other tanks.

SRS has successfully used numerous slurry pump designs from different manufacturers over the past 25 years to mix the contents of radioactive waste storage tanks [1–4]. One of these slurry pump designs is the advanced design mixer pump (ADMP) built by Lawrence Pumps, Inc. [2] and is schematically shown in Fig. 1. ADMP is a 16.76 m long shaft, vertical pump, which includes a top mounted motor, a rotating turntable, a segmented drive shaft, a centrifugal impeller, and a pipe column that surrounds the shaft and suspends the pump inside the tank. Power is provided to the motor through slip rings to permit the pump to rotate continuously at 1/5–1/4 rpm. A smaller separate motor drives the turntable. Shaft sections are coupled together between the motor and the impeller at the bottom of the pump. Enclosing the shaft, the column contains pressurized water to prevent diffusion of waste into the column through the lower seal and out onto the upper tank surface through the upper seal. These mechanical seals are mounted to the drive shaft at the top and bottom of the pump to contain the pressure in the column. Typically, several pumps are inserted into the waste tanks through 0.57 m diameter cylindrical openings, referred to as risers, and mounted to the rotating turntables. Once installed in a waste tank, the pumps act as mixers by drawing nuclear waste into the pump suction and discharging a high-velocity stream of liquid back into the tank. The discharge stream, or jet, entrains waste as it expands into the tank and lifts sedimented waste, called sludge, from the tank bottom.

To suspend the settled sludge, water was added to Tank 18 as a slurry medium and the ADMP was used to suspend the sludge. The pump has a bottom suction and two opposing discharge nozzles, as shown in Fig. 1. Each nozzle is 0.1524 m in diameter. Performance is 19.7 m^3/min (per nozzle) at 1185 rpm and 15.85 m of head. The nozzle discharge velocity is 17.98 m/s. The pump suction and nozzle diameters are 0.44 m and 0.15 m, respectively. The pump is immersed in the sludge layer, allowing a recirculating mixture of sludge and water to serve as the feed flow. The pump is located in the center of Tank 18. The cleaning pattern generated on the tank bottom when the pump rotates defines the effective cleaning radius (ECR). A maximum cleaning distance can be defined when the pump is stationary, and this distance is also used as the ECR. After the ADMP suspends the sludge, the waste is transferred to another tank. Detailed operating conditions are summarized in Table 1. Waste removal operating conditions were discussed in the previous work [4], with the tank liquid level maintained at about 1.78 m, as shown in Fig. 1.

This paper has two main objectives. The first is to document the extension of empirically observed sludge suspension performance in the form of an ECR to other pumps or tank conditions by computational methods. The second objective is to document the benchmark data used to validate the computational method and models used to accomplish this goal, since the data gathered for that purpose extend the literature to include high-velocity jet data at distances far from the jet nozzle.

To accomplish these objectives, local velocity measurements were made for the discharge jet of a submerged ADMP in a 26 m diameter full scale tank, known as the full tank facility (FTF) to establish the flow patterns induced by the jet. At the same time, a computational model containing the ADMP mixer used in FTF was developed. The model was validated by benchmarking it against the full scale test data [1]. It was then used to evaluate flow patterns in the Tank 18 and estimate the cleaning capabilities of the ADMP. Sensitivity analyses were performed to investigate the influence of key operating parameters. In addition, a smaller mixer pump design with a 0.0762 m nozzle diameter was evaluated, as shown in Table 1. A schematic diagram for the Tank 18 system used in the analysis is illustrated in Fig. 1. The analysis results were used to evaluate hydraulic cleaning operations and provide information that assisted in developing the operating plan for Tank 18 waste removal. The results also helped identify special requirements for sampling and monitoring the sludge suspension.

Although turbulent jets have been studied extensively, the specific configuration needed for this evaluation has not received much attention: horizontally oriented nozzle exits with one bottom

Contributed by the Fluids Engineering Division of ASME for publication in the JOURNAL OF FLUIDS ENGINEERING. Manuscript received January 26, 2006; final manuscript received August 15, 2007; published online January 16, 2008. Review conducted by Joseph Katz. Paper presented at the 2004 ASME Heat Transfer/Fluids Engineering Summer Conference.

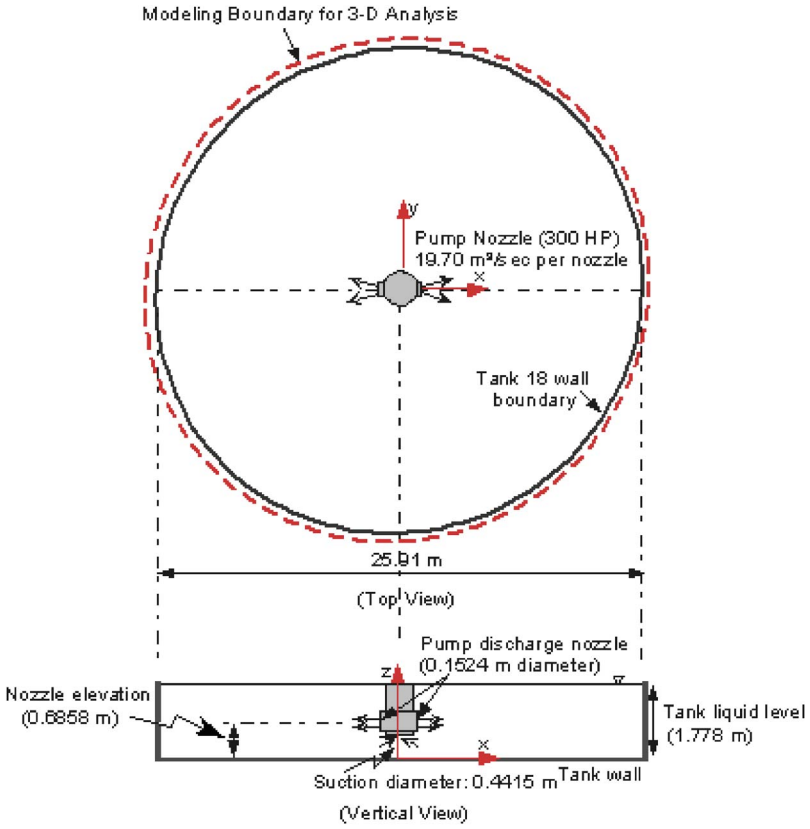

Fig. 1 Schematic of tank operation system showing the present modeling boundary and slurry mixing pump

suction located near the bottom of a large-scale tank. A multidimensional model employing the k-ε model for turbulence was used to compute near-/far-field entrainments in turbulent liquid jets in the tank. Flow measurements were made to provide validation data for prototypic tank size and conditions for the benchmarking analysis. The computed results are compared with test results measured in the far-downstream field more than 60 nozzle diameters from the jet pump, since test data and analysis for regions farther than about 40 nozzle diameters from the pump are not available in the literature. It is noted that local velocities along the centerline are about 40% lower than the existing literature correlation in the far field, in agreement with the measured results. The near-field predicted values of centerline velocity are reproduced within about 15%.

This paper will first discuss the detailed computational approach, since this lays the foundation for evaluating the applicability of the far-field jet velocity measurements for benchmark applications. The discussion will include experimental setups, data acquisitions for FTF tests, descriptions of the computational approaches, and benchmarking results. Applications of the benchmarked model to the simulations of the Tank 18 mixing operations to evaluate the hydraulic cleaning capabilities of the ADMP mixer submerged inside the tank follow.

2 Computational Approach

The fundamental model presented here is that of a turbulent jet submerged near the bottom of a large tank. The distant tank wall

Table 1 Reference design and operating conditions used for the analysis of Tank 18 model

Parameters		Conditions
Tank dimensions ($D_{tank} \times H_{tank}$)		25.91 m diameter × 1.78 m liquid level (or 1.02 m high[a])
Mixing pump		ADMP
Number of nozzles per pump		2
Pump nozzle diameter		0.1524 m (or 0.0762 m[a])
Pump position	Vertical	0.6858 m (0.5842 m[a]) above tank bottom
	Horizontal	Center
Tank fluid temperature		20°C
Tank fluid		Water
		Slurry[a] (SG: 1.2, viscosity: 2 cp)
Flowrate for each nozzle		19.70 m^3/min min for ADMP (9.84 m^3/min[a])
Nozzle velocity (U_o)		17.98 m/s
Pump orientation		Indexed operation

[a]This is for the sensitivity run.

serves as an important flow boundary, even though it is far distant from the pump discharge nozzle. The focus of the present work is to evaluate the ability of the ADMP to suspend sludge in Tank 18. Prior to discussing the experimental setup and modeling approaches, the literature results for a free turbulent jet flow are reviewed briefly, since the free jet flow is similar in many respects to the bounded wall jet.

2.1 Model Development

2.1.1 Steady-State Model. Previous work [3] and literature data [5] show that when a turbulent jet is discharged from a nozzle with a diameter d_o, it both entrains fluids and expands. Most mixing action and entrainment take place in the region of fully developed flow, which begins at a distance of approximately eight nozzle diameters from the exit plane. The nondimensional velocity distribution φ_v along the jet axis of this region for a homogeneous fluid jet is given by [5]

$$\varphi_v = \left(\frac{u}{U_o}\right) = C_o\left[\frac{x}{d_o}\right]^{-1} = C_o\eta^{-1} \tag{1}$$

In Eq. (1), C_o is a constant determined by the turbulence characteristics of the jet, U_o the nozzle exit velocity, and x the distance from nozzle. Abramovich [5] correlated experimental data for a free turbulent jet submerged in fluid using the nondimensional form provided by Eq. (1). From his work, the proportionality constant C_o was determined to be 6.32. It shows that the velocity at any point in the region of established flow is directly proportional to the product, $d_o \cdot U_o$. Thus, the axial entraining distance corresponding to minimum entrainment velocity can be estimated with nozzle diameter and flow rate. Kiser [6] measured a centerline velocity and studied axial velocity behavior and the spreading of the turbulent jet up to the distance range of 10–40 diameters from the nozzle jet submerged in water. All other previous works [6–9] were related to the near-field flow characteristics and entrainments of the turbulent jets.

The present work is primarily focused on the decay of the axial jet velocity and the evolution of flow patterns for the far-field region from the pump nozzle, since local flow patterns in the remote regions near the wall boundary are important for sludge suspension and mixing operations in a large tank. The fluid domain for the tank has both a solid boundary and a free surface boundary as the jet expands into the downstream region and ultimately recirculates via the suction on the bottom of the pump, as shown in Fig. 1. The spreading fluid is retarded by the interaction with the wall, and the inner part of the flow may be expected to show a certain structural similarity to a boundary layer. Entrainment of quiescent fluid occurs near the outer edges of the flow and accordingly resembles a free jet.

A measure of the ability to shear the sludge layer, the scouring wall shear, is directly related to the local fluid velocity. The initial movement of solids deposited at the bottom of the tank identifies the critical condition or initial scour. It is usually described by two criteria, the minimum flow velocity and the frictional shear to scour and initiate movement of the solid particles deposited on the bottom of waste tank. From these two criteria and the fact that the sludge in Tank 18 contains a range of 5–10 μm of fine particles [3,4], a local fluid velocity can be determined as a performance indicator for adequate mixing or suspension of sludge materials.

When liquid flow passes over a stationary cohesive sludge mound containing solid particles, the flow results in hydrodynamic forces being exerted on individual particles in the mound. For the initial movement of the top layer of the mound, the degree of erosion resistance for a given particle to the hydrodynamic forces of the flowing fluid depends on the cohesion and adhesion forces. An increase in the fluid momentum causes an increase in the magnitude of the hydrodynamic forces. Hence, for a particular stationary sludge mound, a condition is eventually reached at which particles in the movable bed are not able to resist the hydrodynamic forces and solids in the top layer start to erode.

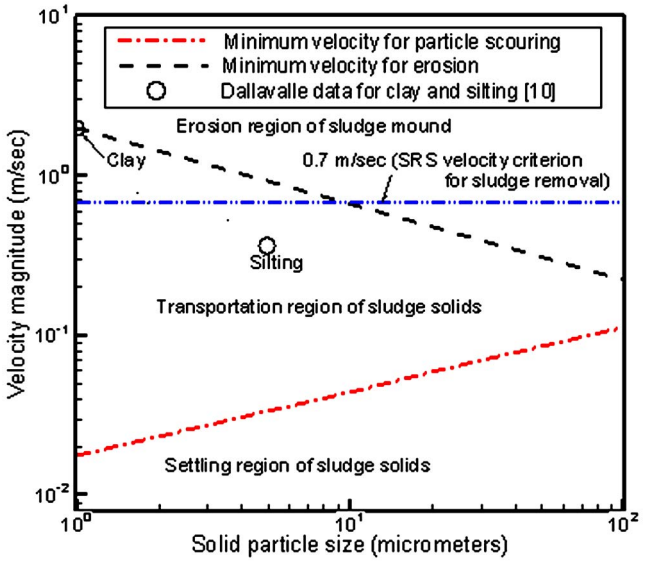

Fig. 2 Velocity criteria for deposition, scouring, and erosion of sludge solids based on Graf's correlation [11] and literature data

The literature data [10] show that large particles are more easily eroded by streams than smaller ones. This phenomenon is more pronounced with small particles since the cohesive forces increase with decreasing size. Figure 2 shows for each particle size a certain velocity, below which it will experience sedimentation, and a critical scour velocity, above which it will be eroded. Fluid velocity between these two velocities will transport solids of that size. The literature data [11] show that fluid velocity, particle size, specific gravity of particle, and tank liquid level are key parameters associated with particle suspension. It should be emphasized that the incipient velocity of erosion is actually dependent on the critical shear stress at which settled sediment begins to move. The critical shear stress of the cohesive materials in Tank 18 depends on the composition of the sludge material, the particle-size distribution, particle shape, and packing. A minimum fluid velocity for suspending cohesive sludge at SRS has been confirmed and established as 0.7 m/s (2.27 ft/s) [12]. Figure 2 shows that this velocity, 0.7 m/s, will erode the sludge layer for the particle sizes larger than clay material (about 5 μm). Establishing this characteristic velocity for SRS sludge allows the local fluid velocity at any distance from the nozzle to be employed as a measure of the slurrying capability of the ADMP.

Two types of materials are identified in Tank 18, both of which are discussed in detail in the previous work [12]. One is particulate zeolite. The sizes of the zeolite particles in the tank are between 300 μm and 700 μm [13,14]. Because it is fast settling, it can be suspended by the slurry pumps, but it cannot be effectively removed from the tank using a discharge pump. The other material is sludge, which can be removed because it remains in suspension longer. Unfortunately, there are scant data available for particle dimensions in the sludge. However, studies of the ECR based on measured yield stress and density provide reasonable estimates for both the ECR and the velocity at the ECR required to suspend sludge. A complete discussion of material properties and their relationship to the minimum required velocity of 0.7 m/s is provided in the previous work [12]. In this work the velocity criterion required for the flow stream to shear the waste into suspension was discussed in detail by the theoretical and experimental basis. The work also provided SRS data for sludge settling velocities.

2.1.2 Transient Model. The transient model used to estimate

the time needed for steady-state flow development was an extension of the steady-state model. The difficulty of modeling pump rotation accurately and the anticipated computational time penalty to be incurred pointed to using a quasisteady approach.

To represent transient behavior in the large tank, the model was run in transient mode for 20 s in a fixed pump orientation. For an actual rotation speed of 1/4 rpm, this was the time required for a 30 deg rotation. The orientation of the pump was then rotated 30 deg and the calculation was restarted from the final conditions of the previous run. The transient was then run for another 20 s and the pump was rotated another 30 deg. This resulted in a 180 deg rotation being modeled in six steps to represent 2 min of operation. The flow patterns generated were compared with each other to determine when they started repeating, an indication that a steady flow pattern had been achieved for the rotating pump condition. The patterns were also compared with qualitative observations from the flow measurements used as benchmark data for the model.

2.2 Computational Model Validation. The analysis consists of two major parts. One part is to develop a model for the test facility used to simulate Tank 18 to benchmark the calculations with no sludge mounds. The second part is to calculate the flow patterns for the turbulent jet induced by the mixer and to estimate the extent of the slurry mixing zone in Tank 18. Flow obstructions such as a cohesive sludge mound are also considered based on the fluid velocity that would be developed at the sludge mound if the tank bottom were clean. Erosion of the sludge surface is not addressed.

The modeling work considers four basic cases with different boundary conditions to investigate how sensitive the flow patterns are to different tank liquid levels and pump elevations. Flow patterns were calculated to evaluate the effects on jet dissipation and suspension efficiency. A three-dimensional computational fluid dynamics (CFD) approach was used to calculate velocity distributions for the fluid domain in tank. A commercial finite volume code, FLUENT [15], was used to create a prototypic geometry file in a nonorthogonal mesh environment. The model geometry was created using a body-fitted coordinate system and structured multiblock grids. Reference design conditions including the mixing pump and fluid properties are given in Table 1. The ADMP (0.1524 m nozzle) was compared to a theoretical pump having a smaller nozzle diameter of 0.0762 m as a sensitivity study.

Detailed wave motion of the free surface at the top of the tank was neglected for computational efficiency. That behavior does not have a significant impact on the flow patterns inside the slurry region in a deep tank [16]. The fluid properties of water were evaluated at room temperature (20°C). The flow conditions for the pump operations are assumed to be fully turbulent since Reynolds numbers for typical operating conditions are in the range of 10^8 based on the pump nozzle conditions. A standard two-equation turbulence model, the k-ε model [17], was used since benchmarking results against literature data [18] showed that the k-ε model predicts turbulent flow evolution in a large stagnant fluid domain with reasonable accuracy. Figure 3 compares predictions for four different two-equation models and the Reynolds stress model (RSM) with test results available in the literature. Although RSM has the potential to give more accurate results for flows in which streamline curvature, swirl, rotation, or rapid changes near the wall boundary might be important, the standard k-ε model is considered a good model for mixing calculations over a large fluid domain such as Tank 18. The results demonstrate that the standard k-ε model combined with standard wall functions generally predicts the test results better than other models. Its predictions agree with the data within about 15%.

This model specifies the turbulent or "eddy" viscosity μ_t by the empirical equation

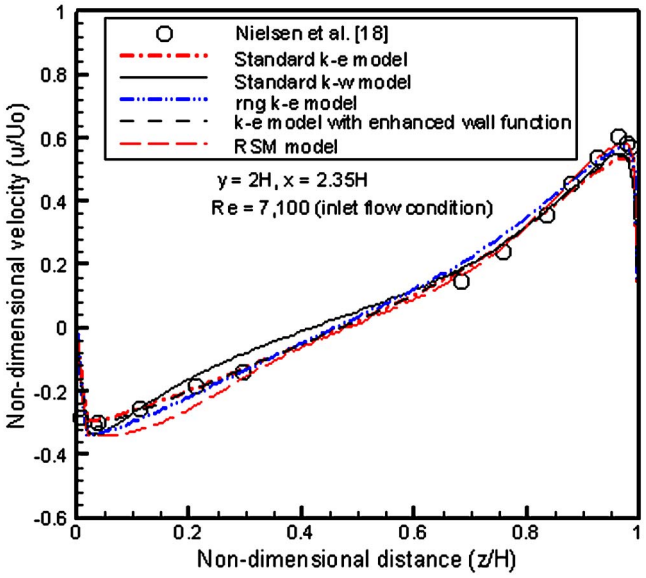

Fig. 3 Comparisons of modeling predictions for different turbulence models against the literature data

$$\mu_t = \left(\frac{C_\mu \rho_f k^2}{\varepsilon} \right) \tag{2}$$

In the present calculations, C_μ is 0.09 [17]. The turbulent viscosity is computed by solving two transport equations for turbulent kinetic energy (k) and dissipation rate of turbulent energy (ε). The governing equations to be solved include one continuity equation, three momentum equations for the three component directions (x, y, and z directions), and two modeled transport equations for the two turbulence quantities, namely, k and ε.

Water was used to simulate the fluid in the tank assuming that it would give an acceptable representation of the flow patterns. Sensitivity studies were performed using other fluid properties for an indexed pump model, i.e., the pump in a fixed radial direction.

2.3 Modeling Results. Three-dimensional flow models were developed and the modeling calculations benchmarked against SRS test results. The benchmarked model was applied to the estimation of flow circulation patterns within Tank 18 and the investigations of steady-state and transient flow responses. Initially, a two-dimensional approach was in an attempt to capture the qualitative flow phenomena associated with the mixing behavior of the jet at a significantly reduced computational time. The results of the two-dimensional calculation were not even qualitatively correct. They overestimated the flow velocity by more than 40% when compared to test results. The flow patterns predicted by the 2D model were different from the 3D modeling results and experimental observations with a stagnation point calculated in an incorrect location. These results stemmed directly from the 2D approximation, partly from neglecting the presence of the tank bottom, partly from the two-dimensional model not having the ability to capture viscous dissipation due to vertical flow rotation, and partly from the requirement that the return flow path be in the plane of the r-θ calculation. The impact of the viscous dissipation term is shown mathematically in the fluid momentum equation,

$$\rho \frac{D\mathbf{v}}{Dt} = -\nabla p - \nabla \cdot \tau + \rho \mathbf{g}$$

from which the viscous term can be expanded as

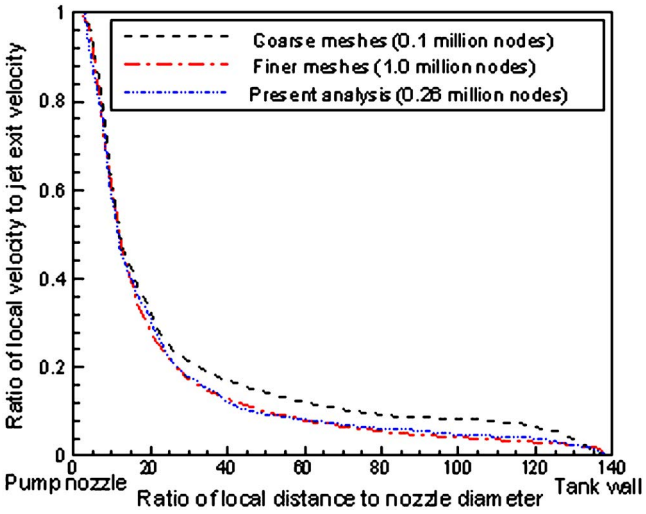

Fig. 4 Mesh sensitivity results of the FTF model

$$(\nabla \cdot \tau)_{\text{shear}} = \mu \nabla \cdot (\nabla \mathbf{v}) = \mu \nabla (\nabla \cdot \mathbf{v}) - \mu \nabla \times (\nabla \times \mathbf{v})$$
$$= \mu \nabla (\nabla \cdot \mathbf{v}) - \mu \nabla \times \boldsymbol{\Omega} \quad (3)$$

In Eq. (3), μ is dynamic viscosity and $\boldsymbol{\Omega}$ is the vorticity related to the fluid rotation. The first term on the right-hand side of Eq. (3) is associated with fluid compressibilty, and the second term is related to the vortex formation generated by the evolution of jet flow. For an incompressible liquid, the first term is zero. In the vorticity term, motion related to Ω_x and Ω_y cannot be captured, since these two components are zero in a two-dimensional model.

A sensitivity analysis for different numbers of mesh nodes was performed to examine numerical uncertainty due to the various spatial discretizations for a range of 1.0×10^5–1×10^6 nodes. From a nodalization study, an optimum number of about 260,000 nodes was established. The optimum number was determined by the criterion that the numerical results be independent of mesh sizes within about 5% uncertainty. In this case, minimum mesh sizes, less than about 5 mm long, were used near the nozzle exit and suction inlet regions to capture the high-velocity gradients in these locations. Sensitivity results for three different meshes along the primary axial direction of jet pump are compared in Fig. 4.

The simulation results showed that jet flows from the two nozzles were dissipated quickly along the principal discharge directions. As soon as the flow exits the nozzle, four main circulation cells are generated in the tank, one on each side of the centerline for each nozzle. Within about 10 s after starting, the nozzle facing the center of the tank created two dominant cells, but after that, all four cells developed to about the same size. Transient flow path lines created using the Lagrangian integral method along the flow direction are shown in Fig. 5. These circulating flow patterns were consistent with the qualitative flow patterns observed by the FTF tests, and this information helped to understand the suspension and removal of waste sludge.

3 Test Description and Model Validation

3.1 Experimental Setup and Data Acquisitions. The full tank facility (FTF) used the ADMP built by Lawrence pumps, Inc. [19] for the sludge mixing test. The ADMP is a 16.764 m long pump, as shown in Fig. 6. The pump is made up of several shaft sections and column sections. Each column section is individually removable and has one thrust bearing, one radial bearing, and one splined shaft. Column sections are bolted together at flanges. Bearings are oil lubricated and fed by the individual bearing housing. Shaft sections connect to each other by flexible couplings. The column was filled with dried filtered air while installed at both FTF and when later installed in the waste tank. Air containment is achieved through mechanical seals, metal o-rings, and graphite gaskets. The ADMP column is made up of 16 and 18 NPS, Schedule 40 pipe. The pump has a 0.9906 m diameter casing, a 0.4572 m diameter mixed flow impeller, and a 300 HP, six-pole induction motor. Figure 6 is a sketch of the pump casing and the two nozzles, which are parts of the casing. Each nozzle is 0.1524 m in diameter and faces an opposing direction. The pump performance is 19.70 m^3/min per nozzle at 1185 rpm and 15.85 m of head. The nozzle discharge velocity is about 17.98 m/s.

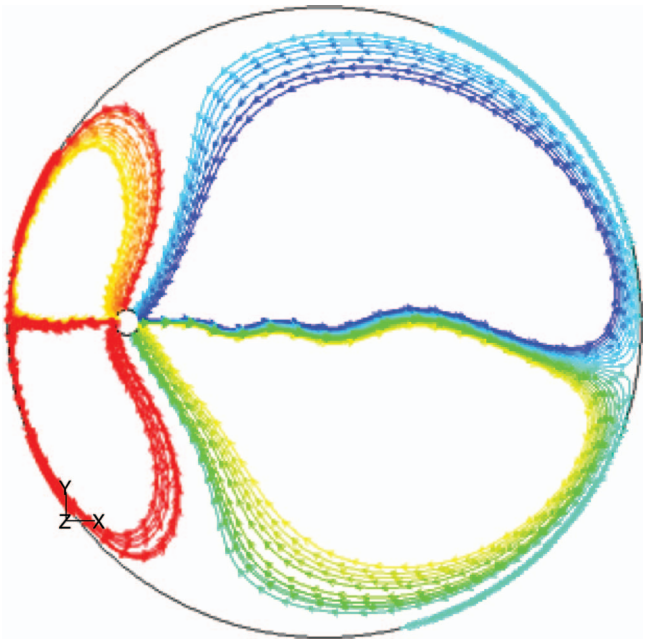

Fig. 5 Flow paths around the tank at 10 s after the start of the pump on the discharge plane of the FTF with stationary pump for the initially quiescent tank

To set up the ADMP for the flow experiment, the pumping system was mounted to an overhead platform at the test facility, as shown in Fig. 6. A turntable supplied with the pump was first mounted to the overhead structural steel platform that spanned the 25.91 m diameter by 2.4384 m deep tank. Two column sections were removed from the pump to shorten the length to meet the structural steel mounting requirements of the FTF, and the ADMP was then bolted to the turntable. The closest horizontal distance between the pump centerline and tank wall was 4.88 m. The nozzle centerline height to the tank floor was 0.6858 m, as shown in Fig. 6.

Fluid velocities were measured using the walkway over the FTF tank, as shown in Fig. 6. The walkway spanned the distance from the tank wall to a pole at the tank center and could be repositioned by rotating the walkway about the tank centerline. Measurements were obtained using a Marsh McBirney model 511 [20] electromagnetic velocity probe. The probe was bolted to a steel rod braced between the walkway and the tank bottom to prevent vibration of the velocity probe.

The calibrated Marsh McBirney equipment [20,21] was used to collect velocity data. The equipment consisted of a transducer probe, cable, and signal processor housed in a portable case. The instrument sensed two-dimensional flows in a plane normal to the longitudinal axis of the electromagnetic sensor, which was parallel to the tank bottom. The panel meters provided visual observation of flow, while the consequent analog output voltages were recorded with a Strawberry Tree data acquisition system [22] at 10 Hz for 3 min. The full scale output range of velocity components is ±0.300 m/s when measured along the orthogonal X and Y axes of the electromagnetic sensor. The probe was positioned to

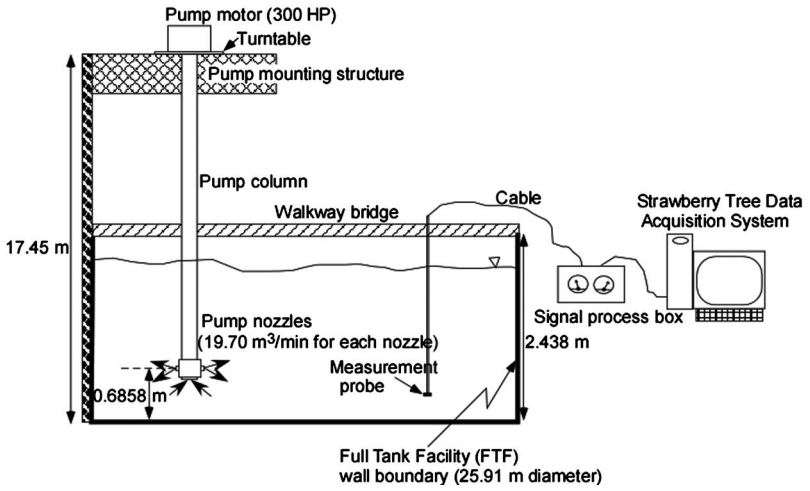

Fig. 6 Schematic of experimental setup for the flow measurement at FTF

ensure that one of the two axes was normal to the pump centerline. The *X* and *Y* velocity vectors were then added to obtain an absolute velocity. 1800 discrete velocity measurements were obtained at each data point over a 3 min time span.

Numerous data locations were selected to capture an array of velocities across the pump discharge jet to assess whether the ADMP could effectively suspend sludge. Velocities were measured on the discharge plane of the pump and close to the tank bottom. The flow measurements were taken with the ADMP operating at its full discharge speed of 17.98 m/s and the test tank filled to a 1.78 m (70 in.) liquid level. The pump was held at a fixed position (i.e., without the turntable moving) throughout the tests. Fluid velocities were measured at both 0.076 m (3 in.) and 0.68 m (27 in.) from the tank bottom at the locations mapped in Fig. 7.

3.2 Flow Test Results. A total of 64 sets of velocity measurements were obtained at the mapped locations, as shown in Fig. 7. All the test results were used for benchmarking the CFD model and they compared favorably. The data reduction techniques are discussed here.

The test data fluctuated sinusoidally, a result of the installed

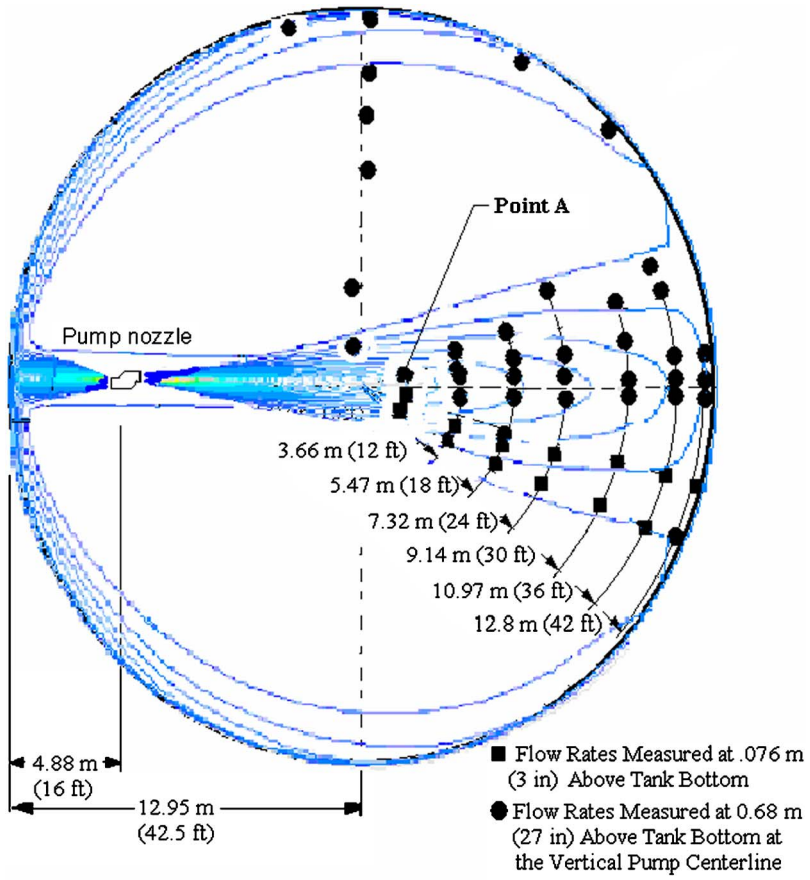

Fig. 7 Velocity measurement data points

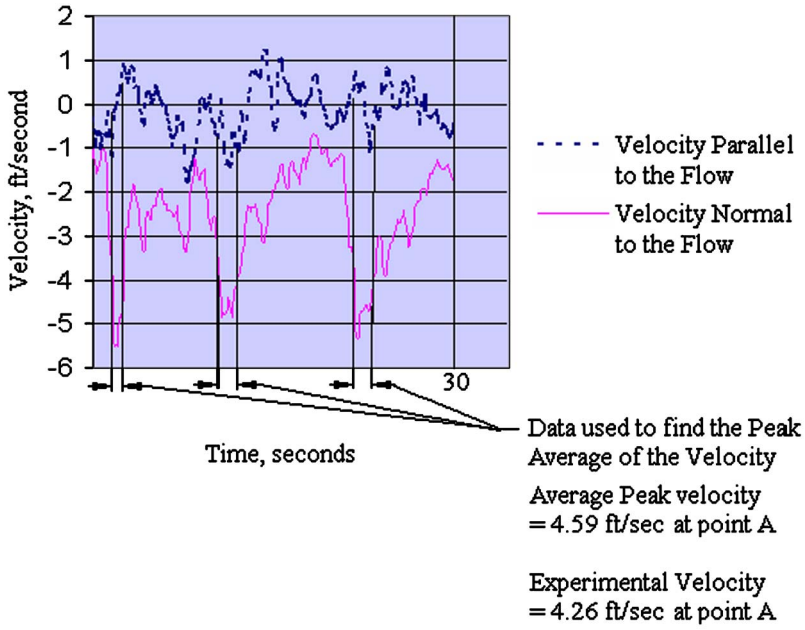

Fig. 8 Velocity data at an arbitrary point in the flow (1 ft/s=0.3048 m/s)

pump oscillating about its axis through a ±10 deg angle with a period of about 10 s. Because of this oscillation, the average of the peak data readings was thought to be a better measure of the actual axial velocity data than the arithmetic average of the data. Point A (Fig. 7) was arbitrarily selected for discussion. The velocity data associated with this point are shown in Fig. 8. The data are observed to reach a well defined maximum every 10 s. This observation corresponded to the situation when the sensor was aligned directly with the primary discharge flow. Consequently, only the data near the peak value were used for the analysis. To obtain a single peak average value, the parallel and normal velocity components were simply added vectorially at each data point and averaged. As noted above, the velocity probe was mounted to a braced steel rod but it still vibrated at approximately 80 Hz. These vibrations had a negligible effect on flow measurements, since they were averaged with respect to the velocity measurement. Similar results for the flow measurements throughout the tank are plotted in Fig. 9 using peak data averages.

As might be expected, the deviations between the peak and arithmetic averages decrease as the distance from the pump increases. Factors such as proximity to the tank bottom and wall, return flow, and distance from the nozzle tend to diminish the effect of oscillations in the nozzle orientation in the far-downstream region. The test results are in agreement with the modeling predictions to within about 25%, as will be shown later. The on-axis measured data are closer in magnitude to the CFD predictions at a distance from the pump than are the off-axis measurements. For example, the experimental velocity for Point A is compared to a least squares fit of the test data along with the predictions in Fig. 9. All the test results obtained along the principal discharge direction in the horizontal plane of the pump nozzle are in agreement with the least squares fit results within about 6%, and with the modeling predictions within about 10%. Flow velocities were also measured at locations less than 25 deg from the pump discharge direction, but the comparisons were not as good.

The effects of the 180 deg pump rotation on the flow patterns at a distance from the pump could not be effectively measured. However, qualitative observations of the jet in the FTF tank clearly indicated that the jet tends to bend slightly during rotation. This bending of the jet causes an asymmetrical flow pattern similar to that predicted in the CFD models. Figure 10 shows the typical effects of pump rotation on the flow patterns. Further details were provided by Lee and Dimenna [3].

3.3 Comparison of Computation Fluid Dynamics Results to Experimental Results. The results of the three-dimensional calculation are compared with the test results near the center of the discharge direction of the nozzle. The combination of all results in both measurement planes are in agreement with the test data to within about 25%. The model predictions were also compared to test data measured at locations less than 25 deg from the discharge direction at the 0.0762 m elevation. The calculated results agree with these data to within about 20%, as shown in Fig. 11. The model results in the discharge plane are also benchmarked against literature data for the high-velocity region not far from the

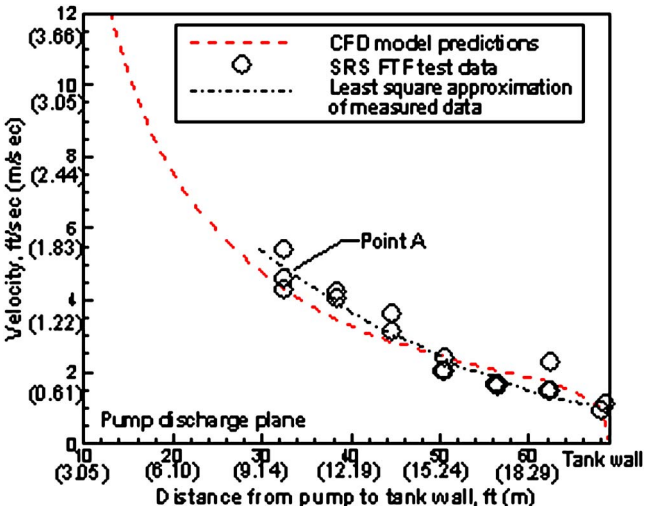

Fig. 9 Comparison of the FTF data to the CFD predictions on the pump discharge plane and velocity measurement location, Point A shown in Fig. 7

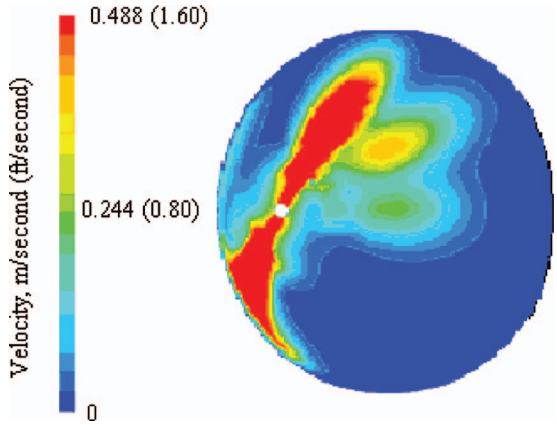

Fig. 10 Flow patterns one minute after the pump starts with the pump rotating counterclockwise

nozzle exit. The predictions of fluid velocity along the axial direction of the jet in this plane agree with the data within about 10%, as shown in Fig. 9.

Figure 12 compares the model predictions with all the test data obtained by FTF. Several data points at remote locations far away from the central axis of the jet flow are significantly higher than the predictions, but the absolute velocities are much smaller than the minimum suspension velocity for zeolite observed in plant operations (~0.4877 m/s). The differences are due to secondary flows created by pump oscillations and flow obstructions neglected in the computational model. The results show that jet velocity decays quickly near the exit of the nozzle due mainly to the turbulent dissipation through the fluid medium. All the test results and modeling predictions are compared quantitatively in Table 2. Figure 13 shows an empirical correlation and test data for free and wall jets available in the literature [5–9]. Test data for the downstream region farther than 40 jet diameters from the pump are not available in the literature. The results in the figure show that the measured velocities along the centerline are about 40% lower than the existing literature correlation in the far field, in agreement with the results predicted by the modeling calculation.

Overall flow patterns for various transient times were computed assuming that the pump was stationary and waste fluid in the FTF

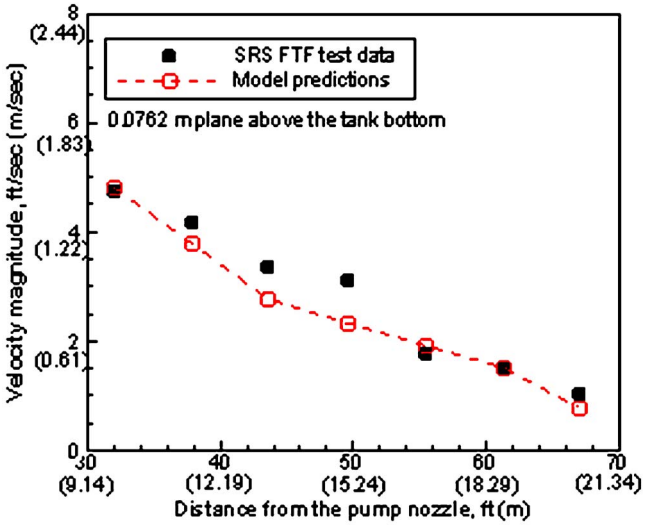

Fig. 11 Comparison of the FTF model predictions of the discharge velocities with the test data near the centerline of the pump discharge direction at the plane 0.0762 m above the tank bottom

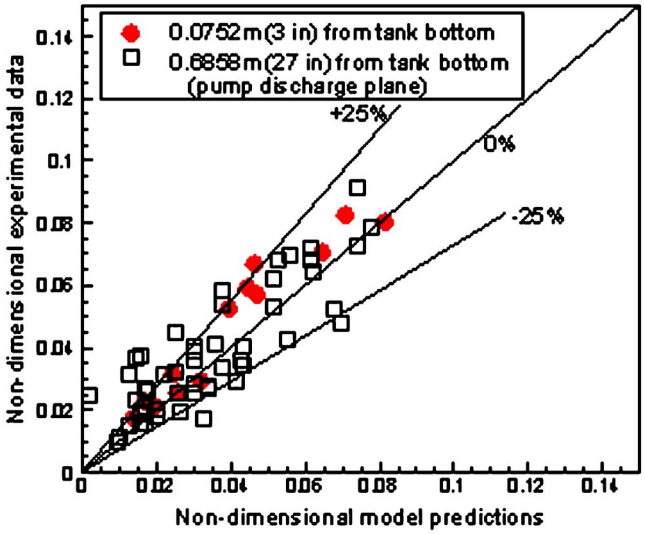

Fig. 12 Comparison of the FTF model predictions with all of the FTF test data in terms of local velocity nondimensionalized with pump exit velocity

tank was initially quiescent. Transient results along the axial flow direction on the pump discharge plane are presented nondimensionally in Fig. 14. The results demonstrated that steady-state flow patterns driven by the ADMP were established in about 2 min. This is consistent with experimental observations.

The verified model was then used to evaluate the hydraulic cleaning capabilities of the ADMP for sludge removal based on the flow evolution of waste slurry under various operating conditions in Tank 18.

3.4 Flow Patterns Following Pump Startup. As shown in Fig. 14, transient flow behavior was examined to evaluate the development of the cleaning distance from a fixed pump. Flow patterns observed at the FTF were simulated by modeling a stepwise 0.25 rpm counterclockwise pump rotation. Transient flow results for the full tank model at the discharge plane were published in SRS technical report [3]. The modeling results showed that the jet flow extended to about 5.8 m from the nozzle within about 2 s, and that it reached the tank wall about 10 s after pump starts in initially quiescent fluid.

Steady-state flow patterns were established within about 2 min. The steady-state flow patterns on the horizontal discharge plane follow a series of parabolic curves similar to that of a free jet, as shown in Fig. 15. The horizontal velocity distributions on the discharge plane of pump nozzle are shown as function of distance from the pump nozzle. Vertical velocity profiles are changed from a bell-shaped curve near the exit of the nozzle to a near-uniform velocity near the tank boundary, as shown in Fig. 16. These are consistent with literature data [9,20]. The results show that when the pump is located 0.6858 m above the tank floor, the local velocity reduces to the 0.70 m/s minimum sludge removal velocity at about 12.19 m distant from the nozzle exit, corresponding to 80 times the nozzle diameter.

4 Tank Model and Analysis

With the validity of the computational model established by comparison with the measured data, the model can now be applied to predict flow behavior in Tank 18.

4.1 Effects of Tank Liquid Level and Pump Nozzle Elevation on Sludge Mixing. Sludge removal capability was evaluated for two different liquid levels as listed in Table 1, 1.778 m and 1.016 m. The results are compared in Fig. 17. The higher liquid level is generally more efficient. The results showed

Table 2 SRS FTF test results compared with the predictions for 0.0762 m and 0.6858 m elevations above the tank bottom

Test No.[a]	Experiments (m/s)	Predictions (m/s)	% Error
03r06t−23.7	1.437	1.463	1.8
03r06t−31.8	1.481	1.270	−14.2
03r12t−18.24	1.267	1.16	−8.4
03r12t−26.34	1.204	0.831	−31
03r18t−18.24	1.018	0.840	−17.5
03r18t−24.58	1.069	0.799	−25.3
03r24t−15.59	0.944	0.710	−24.8
03r24t−23.69	0.565	0.440	−22.1
03r30t−15.05	0.529	0.578	9.3
03r30t−23.15	0.384	0.348	−9.4
03r36t−14.66	0.452	0.457	1.1
03r36t−22.76	0.407	0.297	−27.1
03r42t−14.66	0.315	0.24	−23.7
27r12t+5.34	1.298	1.106	−14.8
27r06t+10.8	1.311	1.335	1.8
27r06t+15.9	0.866	1.25	44.4
27r06t+16.8	0.947	1.219	28.7
27r06t−10.8	1.646	1.335	−18.9
27r06t−5.34	1.409	1.399	−0.7
27r06t−23.7	1.162	1.111	−4.4
27r06t−31.8	1.245	1.000	−19.7
27r06t+97.7	0.566	0.219	−61.2
27r12t+11.34	0.771	0.997	29.3
27r12t+19.44	0.648	0.770	18.8
27r12t−18.24	1.229	0.945	−23.1
27r12t−26.34	1.050	0.674	−35.8
27r12t−5.34	1.230	1.106	−10.1
27r12t+92.24	0.440	0.130	−70.5
27r18t−3.58	0.956	0.924	−3.4
27r18t−24.58	0.805	0.45	−44.1
27r18t−16.48	0.969	0.678	−30.1
27r18t+11.34	0.532	0.747	40.4
27r18t+17.68	0.308	0.482	56.5
27r18t+3.58	1.115	0.924	−17.2
27r24t−2.69	0.619	0.780	26
27r24t+2.69	0.725	0.780	7.6
27r24t+16.79	0.352	0.475	35
27r24t+8.69	0.612	0.670	9.4
27r24t−15.59	0.724	0.540	−25.3
27r24t+89.59	0.468	0.318	−32.1
27r30t−2.15	0.502	0.611	21.6
27r30t+2.15	0.484	0.611	26.2
27r30t+8.69	0.513	0.533	4
27r30t+16.25	0.318	0.357	12.3
27r30t+89.05	0.273	0.219	−19.6
27r30t−23.15	0.662	0.360	−45.6
27r30t−15.05	0.577	0.450	−22
27r36t−1.79	0.699	0.543	−22.3
27r36t+1.76	0.453	0.543	19.7
27r36t+15.86	0.572	0.396	−30.7
27r36t+7.76	0.454	0.463	2
27r36t−14.66	0.357	0.360	0.8
27r36t+88.66	0.383	0.299	−21.9
27r36t+22.76	0.411	0.251	−39.1
27r42t−1.53	0.349	0.282	−19.3
27r42t+1.53	0.338	0.282	−16.7
27r42t+7.76	0.672	0.376	−44
27r42t−14.43	0.485	0.302	−37.8
27r42t−22.56	0.201	0.180	−10.5
27r42t+42.63	0.178	0.169	−5.4
27r42t+69.53	0.280	0.300	7.3
27r42t+88.43	0.649	0.534	−17.6
27r42t+7.53	0.285	0.278	−2.7
27r42t+107.53	0.740	0.644	−13

[a]First two digits are for elevation height in foot, second two digit for radial distance in foot from the tank center, and the last one after the alphabet t stands for clockwise (minus sign) or counter clockwise (addition sign) azimuthal angle from the principal discharge direction of the pump nozzle.

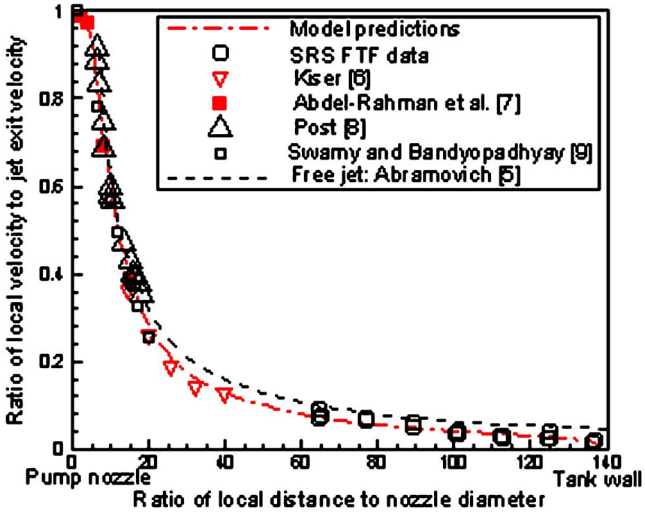

Fig. 13 Benchmarking results of the present model against the SRS FTF test data and literature data

that the sludge removal capability is about the same within about 1.524 m of the pump (corresponding to about ten nozzle diameters), but the velocity difference between the two cases becomes larger as the distance increases from 3.048 m to 12.192 m (near the wall boundary). This is mainly due to the momentum dissipation from the free surface in the case of the lower liquid level, as shown in Figs. 18–21. Sensitivity results [3] show that for a given liquid level, a lower pump elevation provides better mixing performance based on a local velocity requirement for solid suspension. When the ADMP moves down to the tank floor from an elevation of about 0.7 m, the overall hydraulic cleaning capability near the tank bottom increases by about 15%, as shown in Fig. 22.

4.2 Effects of Pump Rotation on Sludge Mixing. Sensitivity results show that rotational effects on flow patterns are negligible for the 1.016 m liquid level. Similar flow behavior is seen at the high liquid level. Graphical comparisons between the cases with and without pump rotation for both the discharge plane and the

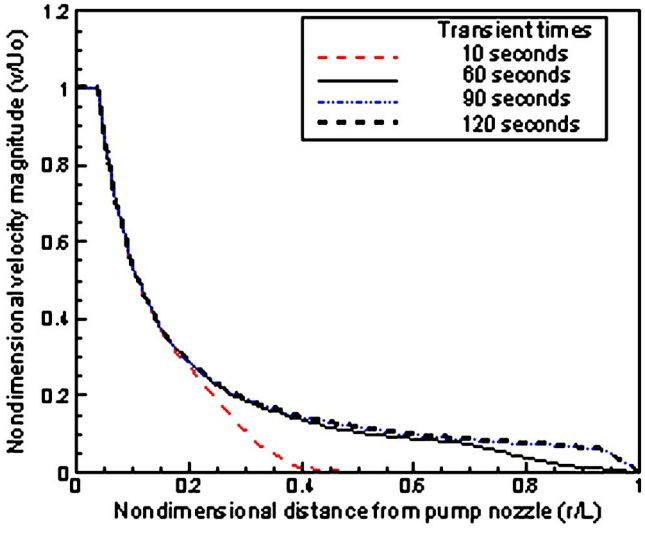

Fig. 14 Transient velocity distributions along the principal discharge direction for various transient times after the start of the pump on the discharge plane of the FTF with stationary pump for the initially quiescent tank

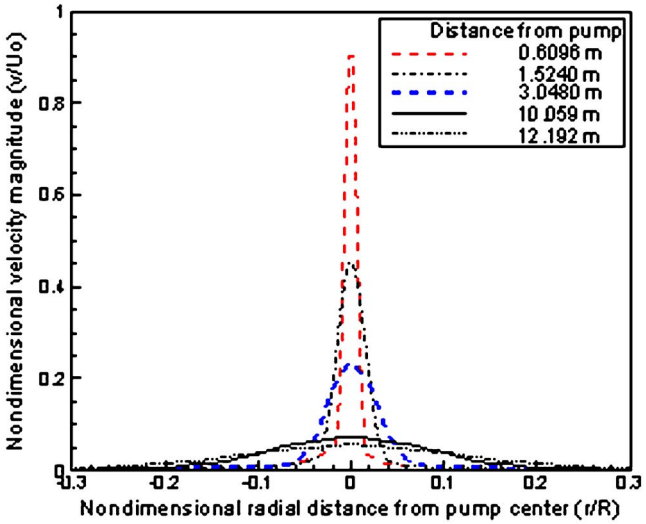

Fig. 15 Steady-state nondimensional horizontal velocity profiles for various distances from the pump at the nozzle discharge plane (0.6858 m above tank bottom): 3D model results for the FTF with 1.778 m liquid level (pump exit velocity U_o =17.98 m/s)

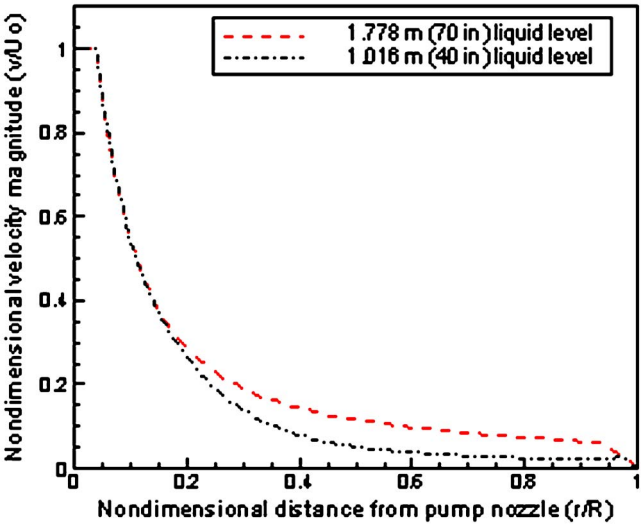

Fig. 17 Nondimensional velocity profiles for various distances from the pump at the nozzle discharge plane located at 0.6858 m above the tank bottom

plane at 0.0762 m above the tank bottom are shown in Fig. 23.

It is important to recognize that local velocity is not the only parameter affecting the ability of the liquid stream to suspend sludge or aggregate materials. Tank sludge properties are equally important, especially when the sludge has a spatially nonuniform structure or is composed of cohesive aggregate. The length of time that the sludge is exposed to the liquid stream is often important in suspending cohesive sludge, and this effect is not captured in the present analysis. A longer exposure time, as would be the case for an indexed pump rather than a rotating pump, could reasonably be expected to result in greater suspension or erosion of the sludge layer at a given location. Exposure time for an indexed pump can be estimated from previous operating experience. Testing in kaolin clay indicated a 3% increase in the ECR when the pump was indexed [12]. Even so, separate quarter-scale pump testing indicated that better mixing was obtained during rotation.

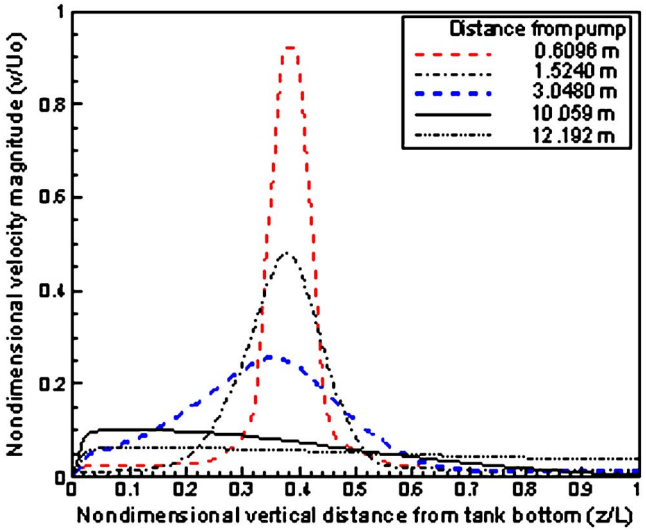

Fig. 16 Steady-state nondimensional vertical velocity profiles for various distances from the pump along the principal discharge direction: 3D model results for the FTF with a given liquid level (L=1.778 m)

4.3 Effects of the Nozzle Diameter on Sludge Mixing. A smaller nozzle diameter was evaluated to examine its effectiveness for sludge removal. A reduced flow rate (9.84 m^3/min per nozzle) and a 0.0762 m nozzle diameter were evaluated. Figure 24 compares velocity distributions for the two nozzle diameters at the plane 0.0762 m (3 in.) above the tank floor with no pump rotation. As shown in the figure, sludge mixing and removal would be improved by about 15% with the smaller nozzle, based solely on local velocity.

Turbulence intensity can be used as an indicator of local mixing to compare the ADMP and the smaller jet flows. The turbulence intensity I is defined as the ratio of the root-mean-square of the velocity fluctuations to mean flow velocity. That is,

$$I = \frac{\sqrt{1/3(u'^2 + v'^2 + w'^2)_{av}}}{V} \approx 0.8165\frac{\sqrt{k}}{V} \tag{4}$$

In Eq. (4), the turbulence intensity is proportional to the square root of the turbulent kinetic energy k for a given mean fluid velocity. A comparison of the turbulence intensity distributions for

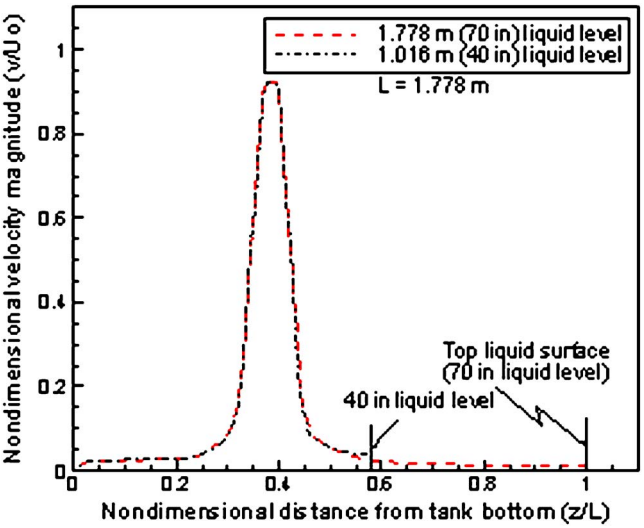

Fig. 18 Comparison of nondimensional velocity profiles for different tank liquid levels at 0.6096 m distance from the pump

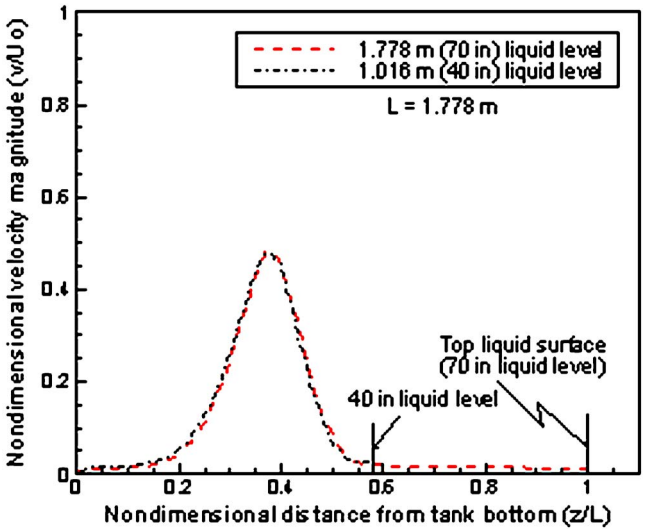

Fig. 19 Comparison of nondimensional velocity profiles for different tank liquid levels at 1.5240 m distance from the pump

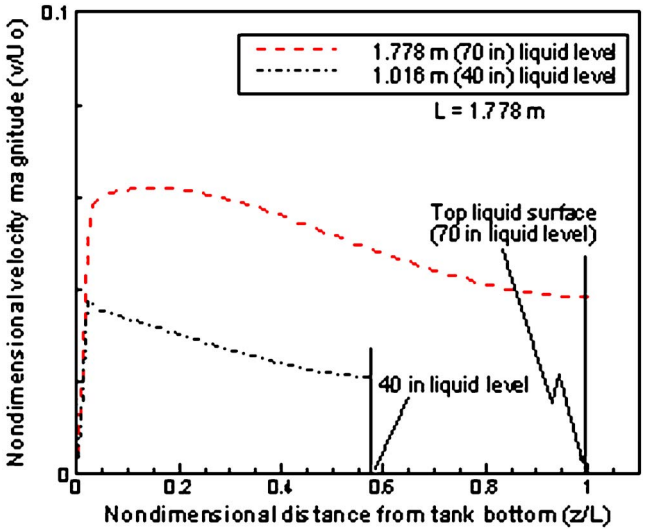

Fig. 21 Comparison of nondimensional velocity profiles for different tank liquid levels at 12.192 m distance from the pump

the two jet mixers is shown in Fig. 25. The results show that the smaller mixer drives higher local velocities, thereby implying better sludge removal capability. The results shown in Figs. 24 and 25 indicate that the velocity reduction rate along the discharge direction increases with increasing turbulence intensity, as shown in Fig. 26. This is mainly related to the increased radial dispersion of fluid momentum, which leads to diminished axial velocity of the nozzle discharge flow. The results clearly show that a smaller mixer has better mixing performance under the same operating conditions in terms of jet flow dissipation into the stagnant fluid domain in tank.

4.4 Effects of Fluid Properties on Sludge Mixing. Most analyses were performed using water at the reference operating conditions. A fluid with a different specific gravity listed in Table 1 was used to examine the sensitivity of the flow patterns to a change in specific gravity. Typically, the fluid above the sludge, known as supernate, has a specific gravity of less than 1.2. The sensitivity study considered ranges of specific gravity from 1 to 1.2 and viscosity from 1 cP to 2 cP. The results show that the flow patterns are not sensitive to this change in specific gravity. At the discharge plane, there are no apparent differences in flow evolution. At the lower elevation 0.0762 m above the tank floor, slurry flow around the horizontal discharge direction of the nozzle dies out slightly more quickly than for water. The radial flow behavior induced by the slurry is larger than that of water because of the increased diffusion in the momentum transport. However, when the ECR is defined as the distance over which the jet velocity exceeds the minimum suspension velocity, differences between water and slurry are negligible for the conditions considered here.

5 Summary and Conclusions

Tank simulation models with ADMP mixers have been developed. Calculations have been performed to benchmark the models with FTF test data and to assess the efficiency of sludge suspension and removal operations during steady-state and transient pump operations. Solid obstructions other than the pump components and free surface motion of the tank liquid were neglected.

A three-dimensional analysis with a two-equation turbulence model was performed with FLUENT™. The computed results were

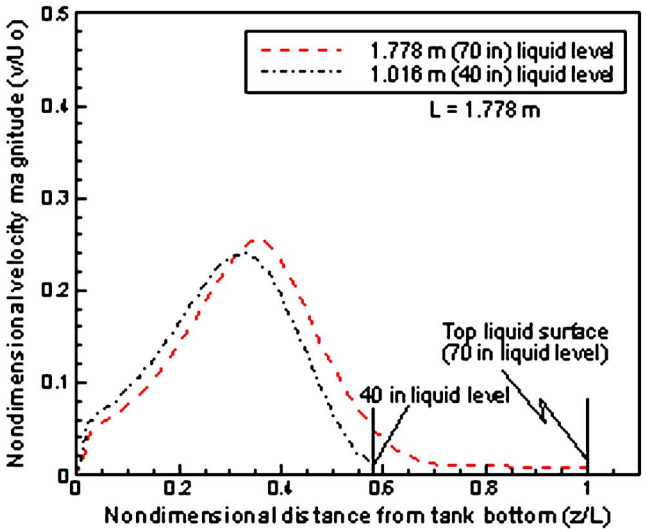

Fig. 20 Comparison of nondimensional velocity profiles for different tank liquid levels at 3.0480 m distance from the pump

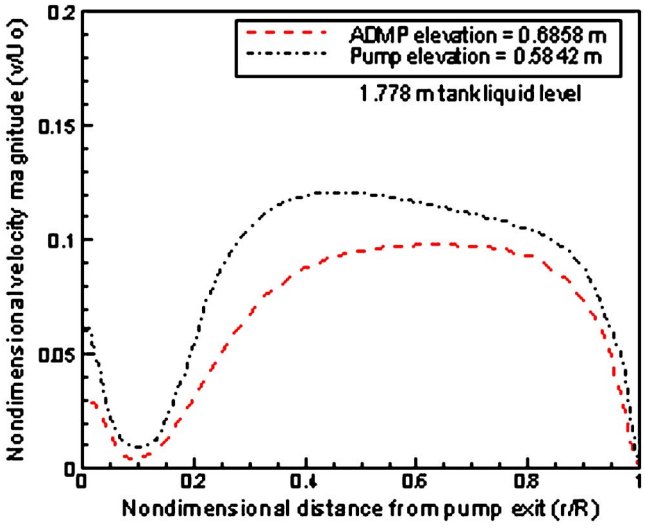

Fig. 22 Comparison of nondimensional velocity profiles along the pump discharge direction for two different pump locations above tank bottom under the 1.778 m liquid level

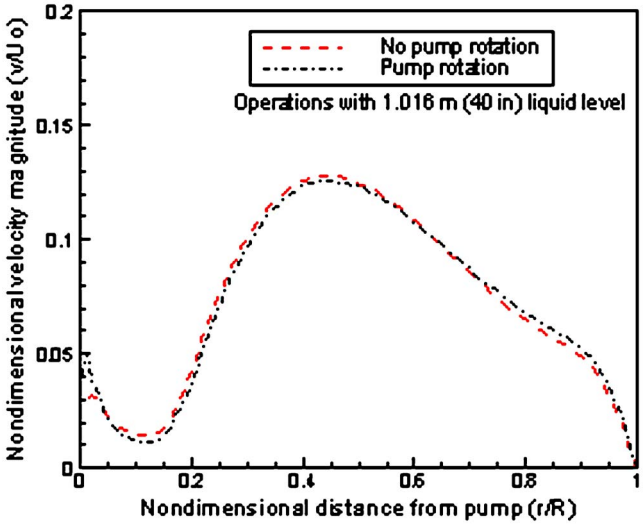

Fig. 23 Downstream evolutions of Tank 18 ADMP with and without pump rotations for 1.016 m tank liquid level at the discharge plane 0.0762 m above the tank bottom

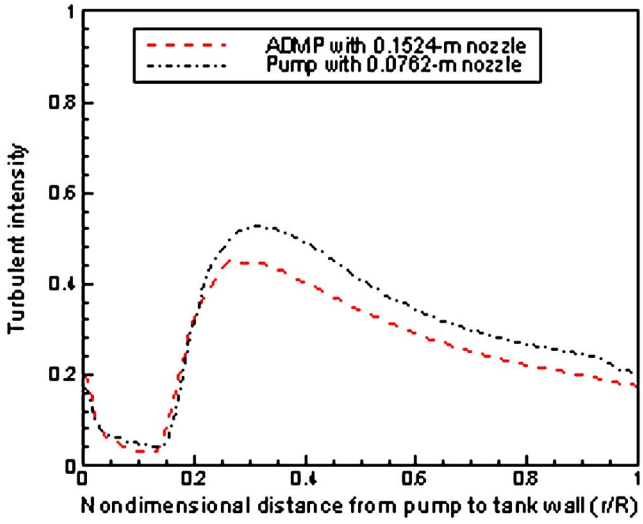

Fig. 25 Comparisons of turbulence intensity profiles for the Tank 18 operations with ADMP and the smaller mixer at the plane 0.0762 m above the tank bottom

validated with FTF test and literature data. Rotational effects of the pump were considered to estimate the impact on sludge suspension and removal assuming that local fluid velocity can be used as a measure of slurrying and mixing efficiency. For a minimum suspension velocity of 0.7 m/s, the results indicated that the existing ADMP mixer would provide adequate sludge removal from the tank with a 1.778 m liquid level except for a wall boundary region of about 0.6096 m.

The CFD simulation results for the ADMP mixer showed that steady-state flow patterns were reached within about 60 s. The results also showed that when the pump was rotated continuously in one direction, the operational time to reach steady-state conditions was much longer. In addition, when the pump is off center, times to reach steady-state flow patterns are much longer than the case with the pump located at the tank center.

The main conclusions are as follows:

- Jet velocity data obtained by FTF are presented for distances greater than 60 diameters from the nozzle.
- Model predictions agree with test data within about 25%. In the velocity ranges where sludge removal is required, the model provides a reasonable estimate when compared to actual test data. The predictions are in good agreement with wall jet data available in the literature.
- The difference between a fixed pump and a rotating pump is small, and is well within the uncertainty of the present calculations. The effect of pump rotation is more pronounced when the pump is located off center and the tank liquid level is lower.
- A higher tank liquid level results in better sludge mixing.
- A smaller nozzle size with an identical $U_o d_o$ has better predicted performance for suspending and removing the sludge.
- The maximum clearing distance is not sensitive to the slurry fluid properties when the ranges of fluid properties for 1 to 1.2 specific gravity and 1–2 cP viscosity are considered.

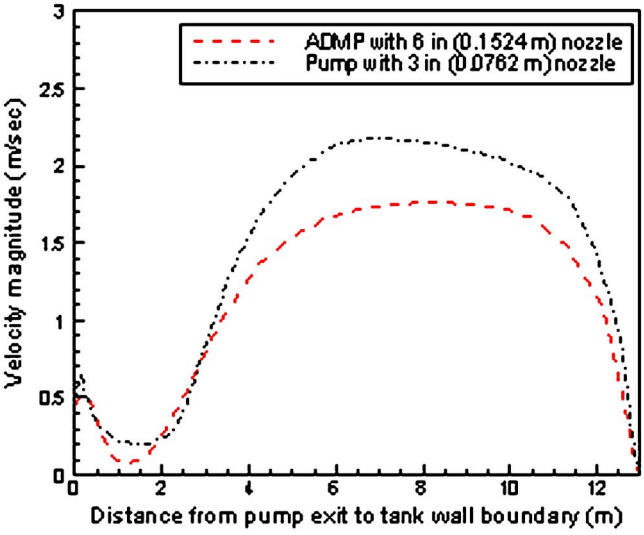

Fig. 24 Comparison of horizontal velocity profiles along the downstream directions of the pump nozzles of Tank 18 with ADMP 0.1524 m mixer and a mixer with a 0.0762 m nozzle at the plane 0.0762 m above the tank bottom

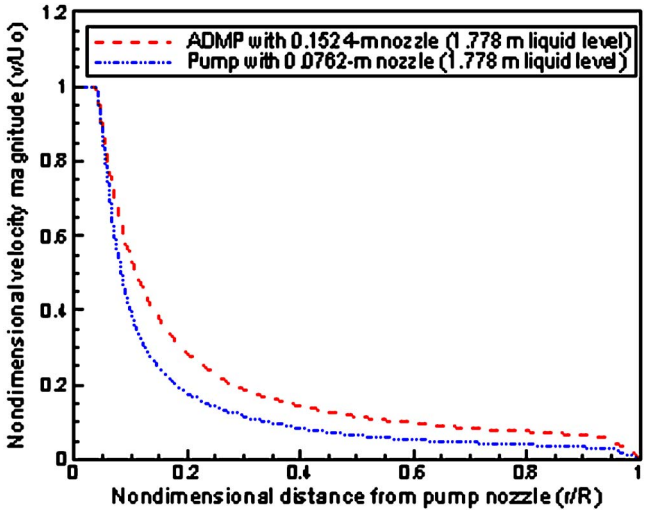

Fig. 26 Comparison of horizontal velocity profiles along the downstream directions of the pump nozzles of Tank 18 with ADMP 0.1524 m mixer and a mixer with a 0.0762 m nozzle at the pump discharge plane 0.6858 m above the tank bottom

- Two dimensional models of the flow are inadequate.

Nomenclature

C_o, C_μ = empirical constants
cP = centipoise (equal to 0.001 kg/m s)
D = tank diameter
d_0 = nozzle diameter
H = height
ft = foot (0.3048 m)
g = gravitational acceleration
I = turbulence intensity
k = turbulent kinetic energy
in. = inch (0.0254 m)
L = total distance
m = meter
p = pressure
R = tank radius
r = radial distance
rpm = revolutions per minute
s = seconds
SG = specific gravity
t = time
x, y, z = local distance from pump nozzle
U_0 = nozzle exit velocity
V = mean velocity magnitude
u, v, w = local velocities in the x, y, and z directions
u', v', w' = local velocity fluctuations in the x, y, and z directions
ε = rate of dissipation of turbulent kinetic energy
φ = nondimensional velocity
η = nondimensional axial distance from nozzle
μ = dynamic viscosity
ρ = density
τ = shear stress
θ = azimuthal angle
Ω = vorticity

References

[1] Lee, S. Y., Dimenna, R. A., Stefanko, D. B., and Leishear, R. A., 2004, "Mixing in Large Scale Tanks—Part I, Flow Modeling of turbulent Mixing Jets," *ASME Heat Transfer/Fluids Engineering Conference*, Charlotte, NC, Jul. 11–15.

[2] Stefanko, D. B., Leishear, R. A., Dimenna, R. A., and Lee, S. Y., 2004, "Mixing in Large Scale Tanks—Part II, Full Scale Pump Testing," *2004 ASME Heat Transfer/Fluids Engineering Summer Conference*, Charlotte, NC, Jul. 11–15.

[3] Lee, S. Y., and Dimenna, R. A., 2001, "Performance Analysis for Mixing Pumps in Tank 18," WSRC-TR-2001-00391.

[4] Augeri, M. J., Hubbard, M., and Thomas, J. L., 2004, "Mixing in Large Scale Tanks—Part IV, Cleaning Nuclear Waste From Tanks," *2004 ASME Heat Transfer/Fluids Engineering Summer Conference*, Charlotte, NC, Jul. 11–15.

[5] Abramovich, G. N., 1963, *The Theory of Turbulent Jets*, MIT, Cambridge, MA.

[6] Kiser, K. M., 1963, "Material and Momentum Transport in Axisymmetric Turbulent Jets of Water," AIChE J., **9**(3), pp. 386–390.

[7] Abdel-Rahman, A., Chakroun, W., and Al-Fahed, S., 1997, "LDA Measurements in the Turbulent Round Jet," Mech. Res. Commun., **24**, pp. 277–288.

[8] Post, S., 1998, "A Computational and Experimental Study of Near-Field Entrainment in Steady Gas Jets," MSME thesis, Purdue University.

[9] Swamy, C. N. V., and Bandyopadhyay, P., 1975, "Mean and Turbulence Characteristics of Three-Dimensional Wall Jets," J. Fluid Mech., **71**(3), pp. 541–562.

[10] Dallavalle, J. M., 1948, *Micromeritics*, 2nd ed., Pitman, New York.

[11] Graf, W. H., 1971, *Hydraulics of Sediment Transport*, McGraw-Hill, New York.

[12] Leishear, R. A., Stefanko, D. B., Dimenna, R. A., and Lee, S. Y., 2004, "Mixing in Large Scale Tanks—Part III, Predicting Slurry Pump Performance," *2004 ASME Heat Transfer/Fluids Engineering Summer Conference*, Charlotte, NC, Jul. 11–15.

[13] Poirier, M. R., Powell, M. R., Gladki, H., and Rodwell, P. O., 1999, "Suspending Zeolite Particles in Tanks," *Seventh International Symposium on Liquid-Solid Flows, Joint ASME-JSME Joint Meeting*, Jul. 18–23.

[14] Leishear, R. A., Stefanko, D. B., Lee, S. Y., Dimenna, R. A., Thomas, J. L., Hubbard, M., and Augeri, M. J., 2004, "ADMP Mixing of Tank 18 Sludge: History, Modeling, Testing, and Results," WSRC-TR-2004-00036.

[15] FLUENT Manual, Fluent, Inc., 1998.

[16] Madina, C. K., and Bernal, L. P., 1994, "Interaction of a Turbulent Round Jet With the Free Surface," J. Fluid Mech., **261**, pp. 305–332.

[17] Jones, W. P., and Launder, P. E., 1972, "The Prediction of Laminarization With a Two-Equation Model of Turbulence," Int. J. Heat Mass Transfer, **15**, pp. 301–314.

[18] Nielsen, P. V., Restivo, A., and Whitelaw, J. H., 1978, "The Velocity Characteristics of Ventilated Rooms," ASME J. Fluids Eng., **100**, pp. 291–298.

[19] VPF 22731, Lawrence Pumps, Inc., Advanced Design Mixer Pump, Vendor drawings for Westinghouse Savannah River Corporation, SC.

[20] Marsh McBirney Inc., 1977, Instruction Manual, Model 511, Electromagnetic Water Current Meter, Frederick, MD.

[21] Private communications with Marsh-McBirney, Inc., Company Address: 4539 Metropolitan Ct., Frederick, MD 21704, Phone: (800) 368-2723, Fax: (301) 874-2172, Website: www.Marsh-McBirney.com

[22] Strawberry Tree Data Acquisition and Control Catalogue, Computer Instrumentation and Controls, Instruction Manual, Strawberry Tree Corp., CA.

Hediye Atik
Research Scientist
The Scientific and Technical Research Council,
Defense Industries Research
and Development Institute,
PK16 Mamak,
Ankara 06261, Turkey
e-mail: hediye.atik@sage.tubitak.gov.tr

Leon van Dommelen[1]
Professor
Department of Mechanical Engineering,
FAMU-FSU College of Engineering,
2525 Pottsdamer Street, Room 229,
Tallahassee, FL 32310-6046
e-mail: dommelen@eng.fsu.edu

Autogenous Suction to Prevent Laminar Boundary-Layer Separation

Boundary-layer separation can be prevented or delayed by sucking part of the boundary layer into the surface, but in a straightforward application the required hydraulics entail significant penalties in terms of weight and cost. By means of computational techniques, this paper explores the possibility of autogenous suction, in which the local pressure differences that lead to separation drive the suction used to prevent it. The chosen examples include steady and unsteady laminar flows around leading edges of thin airfoils. No fundamental theoretical limit to autogenous suction was found in the range of angles of attack that could be studied, but rapidly increasing suction volumes suggest that practical application will become increasingly difficult for more severe adverse pressure gradients. [DOI: 10.1115/1.2813135]

1 Introduction

Control of boundary-layer separation and its effects is a significant area of research in fluid flows. More effective control of separation under varying conditions can offer significant potential benefits in a wide range of applications. One phenomenon of great practical importance caused by boundary-layer separation is stall from wing sections and vanes [1–5]. In recent times dynamic stall has received increasing attention in connection with future designs for helicopters and combat aircraft. Rotorcraft blades are configured to pitch up rapidly as each blade on the main rotor moves in a direction opposite to the forward motion of the helicopter (the retreating side) in order to balance the lift on the advancing side, where a relatively higher mainstream speed is encountered. Although an enhanced lift can be achieved as the blade is pitched above the static stall angle, it has been difficult to exploit the phenomenon due to the severe penalty that must eventually be paid when the stall vortex leaves the upper surface of the blade. For this reason, current helicopters are designed to try to avoid the dynamic stall regime insofar as this is possible. It is likely, however, that future designs of rotorcraft could achieve substantial gains in maneuverability, and much recent work has concerned various ways to control the leading-edge separation [6–10]. Maneuverability is also of critical importance in air-to-air combat, and, typically, the maneuvers that penetrate the unsteady regime are rapid and often of relatively short duration. Hence, practical control measures that inhibit separation from the leading-edge region are of considerable interest in order that the process leading to dynamic stall may be delayed (and potentially suppressed) while still maintaining enhanced levels of lift.

The issue of boundary-layer control at the leading edge is difficult in a practical sense, especially for helicopter blades, where complex mechanical control surfaces do not seem realistic, or for maneuvers in which the requirements for control vary rapidly. In the past, suction has been used for separation control, following the pioneering demonstration of its potential by Prandtl [11]. Since then, significant progress has been made to understand its strengths and problems [6,7,9,12]. There are, however, a number of significant practical issues associated with suction that have historically limited its application, such as the required pumping power; the cost and weight of the pump and hydraulics, mechanical complexity; lost fuel space in the wings; the possibility of pump failure; rain, dirt, and insects; etc. [13]. Autogenous suction could mitigate some of these difficulties.

2 Autogenous Suction

The idea of autogenous suction is to produce the suction that prevents separation using the lower pressure that exists upstream. A sketch of the idea is shown in Fig. 1 for the case of the flow around the leading edge of a wing section. Below the surface of the leading edge, one or more conduits allow boundary-layer fluid in the region where separation must be avoided to be sucked away by the lower pressure upstream. The removed boundary-layer fluid is ejected in the lower pressure area upstream.

Similar ideas have been explored in the past to generate suction behind shocks [14–17]. Nagamatsu et al. [15] credited the idea to Bushnell and Whitcomb in 1979. However, the present study intends to explore what is possible at lower velocities, without shocks to provide a sharp pressure difference. Other sources of low pressure have also been used to drive suction, such as the wing tips and even the other wing in an incipient spin [13]. However, the region immediately upstream of potential separation has the advantages that lower pressures are ensured to exist there and that the air does not have to be ducted over great distances.

The reason that autogenous suction can at least in theory be effective is that the amount of fluid that must be sucked away is small. This initial study will restrict itself to the case of laminar flow around thin airfoils, for which the amount of fluid that must be sucked away is inversely proportional to the square root of the Reynolds number [10]. The higher the Reynolds number, the smaller the amount of fluid involved. Small volumetric flow rates allow small head loss for the fluid flow through the conduits; in other words, they require little pressure difference to drive the flow through the conduits. This is important since the results will show that the available pressure differences are numerically relatively small; laminar boundary layers typically do not penetrate far into regions with adverse pressure gradient. Turbulent boundary layers can, but they are beyond the scope of this study.

Of course, in reality, many effects that are very hard to estimate will play a major part. Transition to turbulence restricts the Reynolds numbers for which the flow can be modeled as laminar, as is done here. Furthermore, it is the practical design of the porous wall and conduits that will eventually determine how large the head losses truly are for a given mass flow. Future studies will be

[1]Corresponding author.

Contributed by the Fluids Engineering Division of ASME for publication in the JOURNAL OF FLUIDS ENGINEERING. Manuscript received February 2, 2006; final manuscript received June 15, 2007; published online December 19, 2007. Review conducted by Joseph Katz.

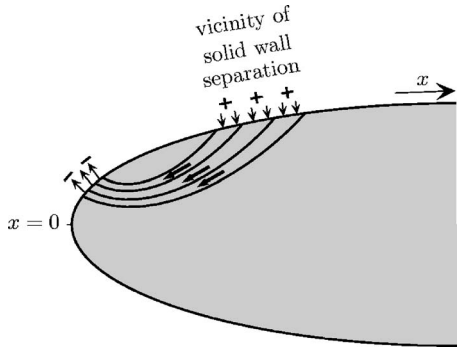

Fig. 1 Separation control using autogenous suction

needed to shed some light on these highly complex issues. The present investigation will restrict itself to the simple question of what the theoretical limits of the procedure are.

In the absence of further refinements or extension to the turbulent case, the most promising area one might look for potential applications of the current results would presumably be low Reynolds numbers (as far as typical applications are concerned, not absolutely low) to avoid having to compete with the effects of turbulent reattachment, or possibly for transient application at higher Reynolds number. For the types of practical applications mentioned in the Introduction, clearly, extension to turbulent and compressible flow will be required. The objective in this first study is not to design an actual system for flight Reynolds numbers, but to examine whether autogenous suction can remove separation within a solidly established fundamental flow model for which the correct equations are known without ambiguities. Much more would need to be done to get a practical procedure, but if it can be achieved, autogenous suction may have some interesting potential advantages: It can be activated and deactivated by the mere opening or closing of valves, the sucked fluid must only be ducted a small distance upstream, and the contour of the wall is unaffected.

3 General Considerations and Notations

The configuration to be studied is the leading-edge stall from an airfoil leading edge shaped as a parabola. This shape provides a valid approximation for the leading edges of conventionally shaped thin airfoils [10,18]; hence, it has a fairly broad applicability. The general concept of autogenous suction is not specific to any particular configuration. As noted in the previous section, it will be assumed that the boundary-layer flow is laminar in the region of interest; the flow will also be assumed to be incompressible. The objective in this study is not to produce high-accuracy quantitative results for a specific airfoil or related flow, but for a generic asymptotic model.

All lengths are scaled with the nose radius, and all velocities with the freestream velocity far from the airfoil. The nondimensional distance from the leading edge, measured along the surface, will be indicated by x (Fig. 1). For thin airfoils at high Reynolds numbers, the flow field near the leading edge depends only on the Reynolds number $\hat{\mathrm{Re}}$ based on the nose radius and on a scaled effective angle of attack a. In the simplest case of an airfoil that is not pitching and in a steady stream, a is defined by

$$a = f(\alpha - \alpha_0)\sqrt{r_{\mathrm{LE}}/2c} \tag{1}$$

where α is the angle of attack in radians, α_0 is the angle of attack for which the leading edge shows a symmetric local flow field, which will depend on the global airfoil shape, especially its camber, r_{LE} is the radius of curvature of the airfoil surface at the leading edge, c is the chord, and f is a factor to correct for an imperfect Kutta condition [7,10,19]. In the flows studied here, a is assumed independent of time.

For a positive scaled angle of attack a, a stagnation point occurs on the lower leading-edge surface, and the flow accelerates around the leading edge toward a pressure minimum on the upper surface. Beyond the pressure minimum, the pressure gradient is adverse, and for $a > 1.2$, this adverse pressure gradient is strong enough to cause boundary-layer separation [20]. The objective in autogenous suction is to apply enough suction in the region of adverse pressure gradient to avoid the separation.

In particular, in steady flow, enough suction must be applied to keep the wall vorticity (or wall shear) from becoming zero. This is needed to prevent the formation of a generalized so-called Goldstein singularity [21], which would imply that an attached boundary layer no longer exists. In the steady computations, this was enforced by application of enough suction to keep the scaled wall vorticity parameter

$$\Omega \equiv -\omega\frac{\delta^*}{U} \tag{2}$$

with ω as the wall vorticity, δ^* the displacement thickness, and U the flow velocity just above the boundary layer, above a selected positive threshold value, typically taken to be 0.1. The upstream ejection distribution was determined from the requirement that its volumetric rate matches that of the suction distribution and that a chosen driving pressure difference ΔC_p exists pointwise between suction and ejection.

To study the transient effects, unsteady simulations were also conducted. Unsteady attached flow can exist even if the vorticity is reversed, and it is the so-called Van Dommelen and Shen singularity that must be avoided instead. This requires that the boundary-layer solution is free of stationary points when viewed in Lagrangian coordinates [22,23]. Note that before the vorticity ω becomes zero, neither the Goldstein nor the Van Dommelen and Shen singularities can occur. Unlike the steady case, in the unsteady simulations, the form of the suction and matching ejection distributions were prescribed a priori rather than chosen adaptively. In particular, the transpiration velocity in the suction region was taken to be of the form

$$v_w = -V_{w_A}\sin^3\left(\pi\frac{x - x_0}{x_1 - x_0}\right) \quad x_0 < x < x_1 \tag{3}$$

with V_{w_A} as the maximum suction strength and x_0 and x_1 the slot boundaries. The transpiration velocity in the ejection region was taken similarly as

$$v_w = V_{w_B}\sin^3\left(\pi\frac{x - x_2}{x_3 - x_2}\right) \quad x_2 < x < x_3 \tag{4}$$

For chosen values of x_2 and x_3, the maximum ejection strength V_{w_B} follows from the requirement that the volumetric ejection rate matches the volumetric suction rate.

The above choice of the suction and ejection distributions was mostly inspired by computational convenience. The large gradients associated with abrupt initiations and terminations of suction and ejection are hard to resolve in an unsteady computation; in the chosen distributions, the edges of the chosen distributions are smoothed so that derivatives up to second order remain continuous at the ends. The objective in this study was not to achieve optimal performance but to establish reliably whether benefits can be obtained in transient situations by simple means and whether the unsteady mechanics would fundamentally differ from the steady case. Even if separation is not actually avoided for all time throughout the flow, delaying separation or reducing its adverse effects can also be of interest.

One important task in the unsteady study was to choose the position and length of the slots in a systematic way. In order for the device to work, the slots should be chosen such that the suction slot is at higher pressure than the ejection slot to achieve a passive suction process. In the unsteady calculations, it was assumed that if a pressure difference exists between the midpoints

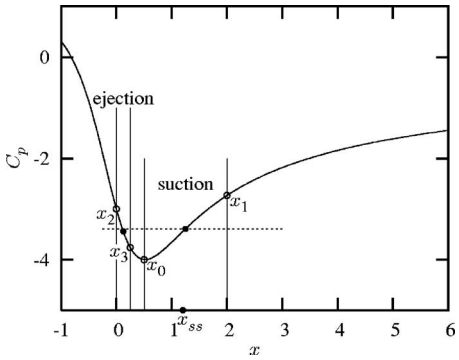

Fig. 2 Pressure distribution at scaled angle of attack $a=2$

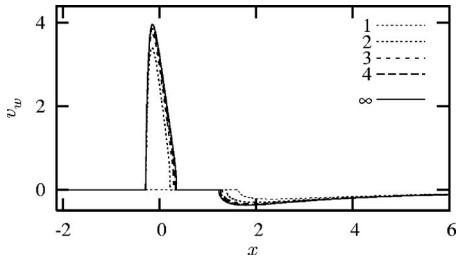

Fig. 3 Wall transpiration velocity at successive iterations; $a=1.6$, $\Delta C_p=0.05$, $\Omega_{min}=0.1$

of the slots, then this was sufficient to produce suction and to create the velocity distributions given in Eqs. (3) and (4). In particular, all distributions satisfy the essential constraint that the total, mass-flow weighted, head loss is positive, which is needed whatever the detailed mechanics in the ducting may be [24] (p. 128).

The pressure distribution at an example scaled angle of attack $a=2$ is shown in Fig. 2. The pressure reaches a minimum value at $x=0.52$. The pressure then increases gradually from $x=0.52$ in the downstream direction, but the steepest rate of increase occurs just after $x=0.52$. It is evident from Fig. 2 that the ejection slot should be placed near $x=0.52$ but upstream of the minimum. This is because the suction slot must also extend as close as possible to the nose in order to be effective in inhibiting separation [10]. However, the leading edge of the ejection slot cannot be pushed a significant distance upstream since the pressure rises rapidly as one moves along the surface toward the vertex and beyond. In view of these considerations, the ejection slot must be fairly narrow, and there is a very limited range in which it can be placed. In the current calculations, the upstream edge of ejection slot was fixed at the vertex at $x=0$ (after an amount of experimentation). The suction slot should at least bracket the separation point location x_{ss} for a solid wall. It is further generally desirable to extend the suction slot over some distance, or separation will quickly appear at a nearby location after it is prevented at x_{ss}. Lengthening the suction slot in the downstream direction is also beneficial for the device since the pressure increases downstream. Such arguments still leave a number of parameters to be chosen: (1) the ejection slot width, (2) the suction slot position and width, and (3) the suction strength V_{w_A}; this will be done based on numerical experimentation in Sec. 6.

4 Computational Procedures

The computational schemes used in this study are essentially the same ones used in Ref. [10]; so here we will restrict ourselves to the issues specific to the present study. For the steady computations of Sec. 5, the boundary-layer equations were solved in vorticity form; a minor change from that study is the use of *A*-stable backward streamwise differences rather than Crank–Nicholson. The real difference in this study is that in the region of ejection, the transpiration velocity through the wall is not known a priori; it must match the as yet unknown suction velocities downstream. An iterative procedure was therefore used, as illustrated in Fig. 3. Starting from the front stagnation point, the flow is computed ignoring any ejection. When in the region of adverse pressure gradient, the scaled wall vorticity threatens to fall below the selected threshold value (Eq. (2)), just enough suction is applied to keep it at the threshold. The required suction velocity distribution is shown in Fig. 3 as the dotted line marked 1. However, in an autogenous suction scheme, the fluid flux removed in the adverse pressure region must be ejected upstream at, in this example, a pressure coefficient 0.05 lower. The ejection velocity can be computed from the mass flux and pressure difference, and in the second iteration, the flow is recomputed using these values. However, the ejection has a negative effect on the downstream boundary layer, and the required suction velocity will now be somewhat higher. Hence, further iterations are needed until the required suction velocity exactly matches the ejection velocity upstream.

For angles of attack just above the one for solid-wall separation, this converges very fast, but at larger values, it becomes desirable to speed it up, especially since each iteration requires a full boundary solution. Initially, we added over-relaxation by simply magnifying the changes in ejection velocity by an empirically found factor (ranging from not much more than 1 at small angles to about 2 at the larger angles.) At still larger angles, this simple procedure started to become too slow to converge, and we added Aitken extrapolation of the differences in ejection velocity at empirically determined intervals. Full convergence was achieved in all cases: The ejection velocities actually used in the computations were equal to the ones computed from the suction velocities to an error of no more than about $10^{-7}\%$ of the maximum ejection velocity, the worst case being $4\times10^{-7}\%$ for the largest scaled angle of attack $a=2.6$ that was computed.

To estimate the numerical accuracy, computations were conducted at three mesh sizes: (A) 2048×512 mesh points iterated out to a maximum difference in ejection velocity of no more than $10^{-1}\%$, (B) 4096×1024 points iterated out to $10^{-4}\%$, and (C) 8192×2048 points iterated out until no further improvement occurred, about $10^{-7}\%$ as above. Table 1 gives the differences in results for transpiration velocity v_w and wall vorticity ω, both expressed as percentages of their maximum value, and the abso-

Table 1 Maximum (top) and root mean square (bottom) differences in the steady results due to variations in mesh size

	Δv_w (%)		$\Delta\omega$ (%)		$\Delta\delta^*$	
a	A,B	B,C	A,B	B,C	A,B	B,C
1.4–2.2	1.54	0.49	0.92	0.23	0.13	0.043
2.4–2.6	—	0.47	—	0.61	—	0.058
1.4–2.2	0.153	0.029	0.075	0.014	0.0095	0.0020
2.4–2.6	—	0.079	—	0.060	—	0.0064

Table 2 Relative maximum differences in the unsteady results for u due to variations in mesh size and time step

t	1,2	2,3	4,5	5,6
1.0	0.0014	0.0005	0.0090	0.00085
2.0	0.0014	0.0005	0.0014	0.00017
4.0	0.0015	0.0005	0.0011	0.00012
6.0	0.0015	0.0005	0.0022	0.00028
6.5	0.0076	0.0043	0.0034	0.00004
7.0	0.067	0.050	0.083	0.0015

lute errors in displacement thickness, which may be compared to a displacement thickness of about 1.5 at the front stagnation point (though the maximum errors actually occur at asymptotically large displacement thicknesses far downstream; see Fig. 5(*c*)). The estimated errors are one-third of the differences between meshes B and C.

It is seen that the differences in results between the computations are small. The reason that the rms errors are smaller by an order of magnitude than the maximum errors is that the largest errors are restricted to the small regions of steep gradients where transpiration starts or ends. For scaled angles of attack $a=2.4$ and $a=2.6$, the errors in the coarsest, A, computation are large enough to produce slightly negative vorticity right where suction starts, something the program will not accept. However, the differences between the finer two meshes B and C remain acceptably small, and the results show no evidence of numerical problems, so these angles of attacks are also believed to be accurate.

The unsteady simulations require the initial unsteady separation process to be accurately resolved, and it is surprisingly difficult to do so in a conventional Eulerian computation [25]. Lagrangian computations in which the mesh points are allowed to drift with the flow have little problem with resolving the separation process [22], but for more complicated flows, Lagrangian computations suffer from mesh degradation over time. The compromise adapted here, as developed by Walker and co-workers [10,26,27], is to start the computation out in Eulerian coordinates until a time at which sharp, separation-related gradients start to become significant, and from then on to allow the mesh points to move with the flow. When mesh points move apart and cause skewness in the grid, a remeshing algorithm is used to locate new mesh points. Again, we refer to Ref. [10] and restrict the discussion to issues specific to this investigation.

The computations assumed an impulsive start of the motion from rest, and autogenous suction was turned on shortly after that at a time indicated by t_v. The time at which the computations were switched into Lagrangian mode is indicated by t_0, and this time it must be chosen well into advance of the time t_f at which a full Eulerian computation actually fails due to separation-related problems.

The computations were conducted at various mesh sizes and time steps to ensure that the results are mesh independent [10,28]; all results presented in Sec. 6 were computed using a final 601×301 mesh and time steps ranging from 0.001 to 0.0001.

A more formal convergence study for a typical example ($a=2$, $t_v=0.5$, $t_0=6$, $V_{w_A}=0.5$, $x_0=0.5$, $x_1=2.0$, $x_2=0$, and $x_3=0.25$, as defined in Sec. 3) is shown in Tables 2 and 3. Three meshes were used to estimate the spatial resolution, with (1) 401×201, (2) 601×301, and (3) 801×401 mesh points, respectively, all with a time step of 0.001. Figure 4 shows a detail of meshes (1) and (3) and their streamlines near the leading edge as a graphical illustration of the resolution of these meshes. As shown, the mesh is either Eulerian or Lagrangian immediately after a mesh regenera-

Table 3 Time and location of unsteady separation for various mesh sizes and time steps

	1	2	3	p	e_a^{23}	e_{ext}^{23}	GCI_{fine}	4	5	6
t_s	7.482	7.237	7.170	2.7	0.93%	0.81%	1.0%	7.237	7.223	7.223
x_s	1.687	1.702	1.705	3.5	0.18%	0.10%	0.12%	1.702	1.701	1.701

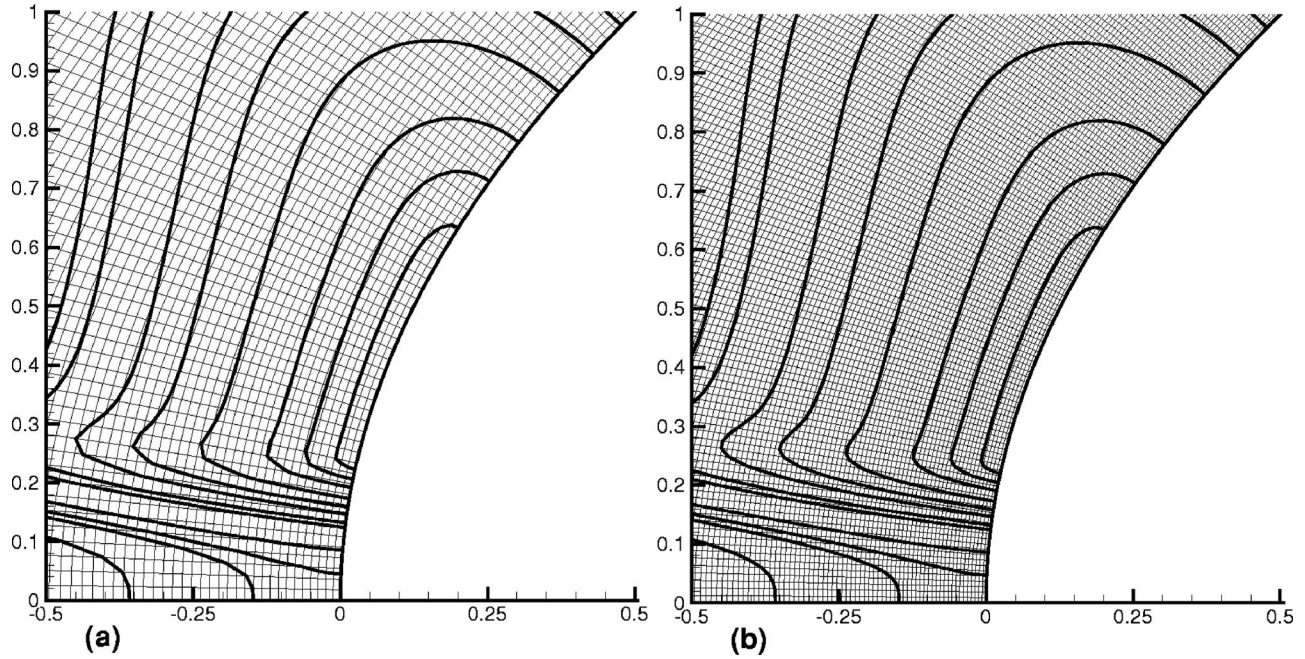

Fig. 4 Detail of the computational grids near the leading edge in physical coordinates, but blown-up boundary-layer thickness, for $a=2$ and $V_{w_A}=0.5$ at time $t=7$. (*a*) Mesh 1; (*b*) mesh 3.

tion. To estimate the effect of the time step, the 601×301 mesh size was computed at time steps (4) 0.01 and 0.001, (5) 0.001 and 0.0001, and (6) 0.0001 and 0.00001 in the Eulerian and Lagrangian ranges, respectively. The remeshing criteria were specified such that the penetration of the injection slot boundary has to exceed 0.2 in the Lagrangian computational space. Table 2 shows the maximum differences in the streamwise velocity component u between these various computations, as a fraction of the maximum velocity. Note that in the last two columns, the Lagrangian computations start from the same solution (5) at time 6, and the remeshing algorithm allowed four remeshings until the separation singularity, so that the differences show only the Lagrangian effect with the remeshing process. In the first two columns, the Eulerian and Lagrangian errors are cumulative. In Table 3, errors in the finest mesh estimated using Richardson extrapolation are also shown. Note, however, that the presented computations use the 601×301, rather than the 801×401, mesh, so the estimated error in separation time should be taken to be 1.5% rather than 0.8%.

When the suction strength V_{w_A} in Eq. (3) was increased, eventually small high frequency oscillations appeared in the numerical solution near the ejection slot. To some extent, such numerical issues are to be expected since the ejection slot is narrow, and, consequently, the ejection strength is significantly larger than the suction one; additionally, the streamwise velocity gradients are also large in this region. In fact, a value $V_{w_A}=0.5$ of the peak suction velocity appeared to be the maximum that could be used without encountering significant oscillations. Even for the case $V_{w_A}=0.5$, a corrective action had to be taken in order to get results that were free of oscillations. First, the mesh was clustered more near the vertex of the parabola instead of near the middle of the suction slot, as done in computations at lower suction. Secondly, instead of applying suction and ejection abruptly at $t=t_v$, the suction and ejection were increased linearly from zero at time $t=0$ until the full values were achieved at $t=t_v=0.5$. For the case of $V_{w_A}=0.5$, these modifications were successful in removing the oscillations from the numerical solution. (Tables 2 and 3 use this nonabrupt initiation of suction.) However, when suction was further increased to still larger values such as $V_{w_A}=2$, the oscillations appeared again and could not be completely suppressed at the used mesh sizes, though they could be reduced greatly by increasing streamwise resolution. There is growth in the extent of these oscillations once they appear, but the amplitude increases, if any, are not dramatic and, in fact, the computation can be continued on to the formation of a separation singularity.

5 Steady Results

Figure 5(a) shows the scaled transpiration velocity through the wall for a typical steady example of an autogenous suction; the physical transpiration velocities are smaller by a factor of $1/\sqrt{\mathrm{Re}}$. Ejection corresponds to $v_w>0$ and occurs upstream of the pressure minima, which are indicated in Fig. 5(a) by the vertical line segments extending up from zero. Note that the pressure minima move upstream when the angle of attack increases. Suction, $v_w<0$, occurs farther downstream. In the computations, a uniform head loss through the conduits was assumed corresponding to a pressure difference $\Delta C_p=0.05$ between the suction and ejection ends. This pressure difference becomes first available at the vertical line segments extending downward. Note that for $a=2$, suction must be started as soon as the required pressure difference is available; for larger angles of attack, separation cannot be avoided with a head loss $\Delta C_p=0.05$, at least not if it is uniform. It may also be noted that when the ejection distribution gets close to the pressure minimum, its slope reduces; this is a consequence of the fact that the derivative of the pressure is zero at the minimum.

Figure 5(b) shows the wall vorticity. For a given angle of attack, when the ejection starts at the point indicated by a triangle, it causes the wall vorticity to plunge. Separation, however, will not occur in the region of favorable pressure gradient, as can be seen

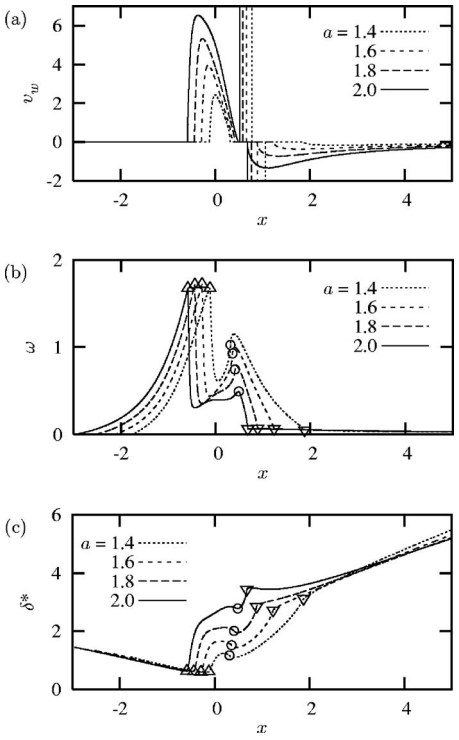

Fig. 5 Scaled wall transpiration velocity, wall vorticity (or wall shear), and boundary-layer displacement thickness for various scaled angles of attack a; $\Delta C_p=0.05$, $\Omega_{\min}=0.1$

from a straightforward extension of Ref. [29]. Farther downstream, where the ejection velocity rapidly falls to zero, the wall vorticity recovers significantly under the rapidly improving wall boundary condition. However, after this effect terminates at the end of ejection, indicated by a circle, the wall vorticity reverts to the downward trend expected in this region, and to prevent separation, suction must then be started at the point indicated by an inverted triangle. Just enough suction was applied to keep the value of the nondimensional wall vorticity parameter Ω (Eq. (2)), above 0.1. The effect of the minimum value of Ω is not large, so 0.1 is used in all results presented here. Suction slots that keep the vorticity just above zero tend to extend quite far downstream [10]; suction terminated at x values ranging from 14.6 at $a=1.4$ to 33.9 at $a=2$.

Figure 5(c) shows how suction terminates the steepening up of the scaled boundary-layer displacement thickness distribution as it evolves toward separation. Far downstream, the boundary layer approximates a Blasius flow, with a displacement thickness that continues to grow proportional to $\sqrt{x}$.

To avoid separation for scaled angles of attack a greater than 2, the head loss through the conduits has to be reduced. The ideal is zero head loss; the transpiration velocity at various angles of attack for that case is shown in Fig. 6. Angles of attack up to $a=2.6$ proved now possible; in fact, the limitation to proceed to still higher angles of attack was not separation but the fact that the convergence of the present iterative procedure becomes prohibitively slow. In addition, the strong singular gradients at the start and end of the ejection and suction regions become hard to resolve accurately even at 4096×1024 mesh points, as shown by increasing differences from the results at 8192×2048 mesh points (Table 1)

Figure 7 shows the suction coefficient or the nondimensional volumetric flow rate that must be sucked away, scaled up with the square root of the Reynolds number. For comparison, the corresponding coefficient for pure suction is also shown. The volumetric flow rate for pure suction increases fairly linearly with the

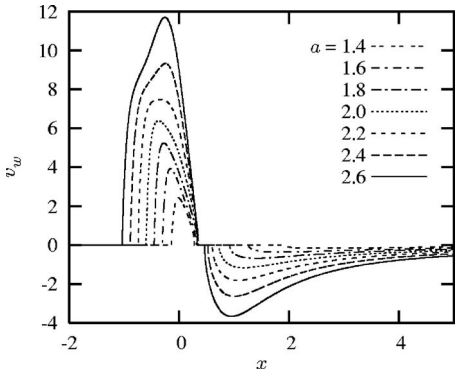

Fig. 6 Wall transpiration velocity for various scaled angles of attack a; $\Delta C_p=0$, $\Omega_{min}=0.1$

scaled angle of attack a; however, for autogenous suction the adverse effects of ejecting the removed fluid upstream causes the volumetric flow rate in autogenous suction to grow much more rapidly. It can be concluded that it becomes increasingly difficult to prevent separation using autogenous suction when the angle of attack increases: A rapidly increasing suction volume must be ducted with a decreasing allowable head loss.

6 Transient Evolution

This section examines the effectiveness of autogenous suction for unsteady flow, using the simpler implementation described in Sec. 3, in which the suction and ejection distributions are prescribed in terms of a few parameters, rather than computed.

For the lowest scaled angle of attack computed, $a=2$, the pressure at the solid-wall separation location $x_{ss}=1.2$ was evaluated, and then the middle of the ejection slot was selected so that the pressure was just below this value. The need for a driving pressure difference determines the downstream edge of the ejection slot, and it leads to the selection of an ejection slot that extended between $x_2=0$ and $x_3=0.25$ (Fig. 2). It is desirable to move the smoothed upstream edge of the suction region as close to the pressure minimum as possible to prevent separation before the smoothed distribution has gained some strength. Numerical results for two possible positions of the upstream edge, and using $V_{w_A}=0.2$, are given in Table 4. It was found that the suction is somewhat more effective when the slot is extended upstream toward the vertex. However, the effect is not large, and it must be noted that practical considerations suggest that the distance between the end of ejection and the start of suction should not be made too small. The upstream edge was therefore chosen at $x_0=0.5$ in the remaining computations at $a=2$. The effect of extending the suction slot farther downstream is also shown in Table 4. Separation at longer slots occurs earlier, and the location of separation is closer to the vertex. This reflects the fact that the suction peak is shifted downstream through the use of the longer slots, and with weakened suction near the vertex, separation then occurs in that region. However, the separation time with the slot extending to $x_1=3$ is not much affected, and this case has a much larger average pressure difference between suction and ejection.

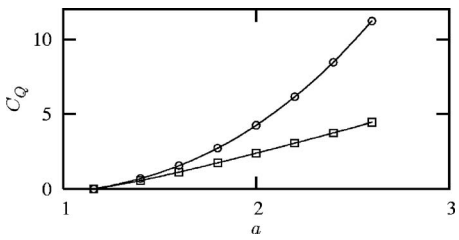

Fig. 7 Scaled suction coefficient for autogenous suction (circles) and pure suction (squares); $\Delta C_p=0$, $\Omega_{min}=0.1$

Table 4 The effect of the suction slot boundaries for $a=2$, $V_{w_A}=0.2$, $x_2=0$, and $x_3=0.25$

x_0-x_1	0.35–3.0	0.5–3.0	0.5–2.0	0.5–4.0
t_f	7.3	6.9	7.0	6.0
t_0	6.2	6.0	6.0	5.0
t_s	7.5	7.0	7.1	6.2
x_s	1.23	1.20	1.41	1.16

In Table 5, the effect of suction strength on separation time and location is given for two slot widths. It is seen that an increase in suction strength results in an increase in separation times. In addition, the separation point moves toward the downstream edge of the shorter suction slot, making the longer slot more beneficial at higher suction volumes. It is evident that when the suction strength V_{w_A} is increased for the longer suction slot, separation can be delayed significantly, as seen from the separation times. Note that in the case $V_{w_A}=0.4$, the separation point x_s has moved slightly upstream compared to the case $V_{w_A}=0.2$. An increase in the suction strength implies an increase in the ejection strength, and these results suggest that increasing the ejection strength has a negative effect such that separation point moves toward the upstream direction.

For $a=2$, the most effective situation was obtained with $V_{w_A}=0.5$, the ejection slot between $x_2=0$ and $x_3=0.25$ and the suction slot between $x_0=0.35$ and $x_1=3.0$. The suction was initiated at $t=0$ and was increased linearly in strength from zero to V_{w_A} in the time range from zero until $t_v=0.5$. A separation singularity now occurred at $t_s=10.8$ and $x_s=2.23$. In this case, the separation took around 1.9 times longer to appear with autogenous suction than for a solid wall. Instantaneous streamlines around the parabola, using an artificial stretched transverse scale, are shown in Fig. 8. It may be seen that the process of normal ejection produced a substantial perturbation to the boundary-layer flow causing the streamlines, even at relatively large scaled distances from the wall, to be deflected sharply away from the surface and then back again. With increasing ejection strength, it is evident that this disturbance in the streamlines will become progressively more severe.

Table 5 The effect of suction strength on separation times and locations for two suction slot lengths; $a=2$, $x_2=0$, and $x_3=0.25$

x_0-x_1		0.5–2.0			0.5–3.0	
V_{w_A}	0	0.1	0.2	0.5	0.2	0.4
t_f	—	6.6	7.0	7.0	6.9	7.8
t_0	4.5	5.7	6.0	6.0	6.0	6.5
t_s	5.82	6.7	7.1	7.2	7.0	8.5
x_s	1.20	1.27	1.41	1.71	1.20	1.16

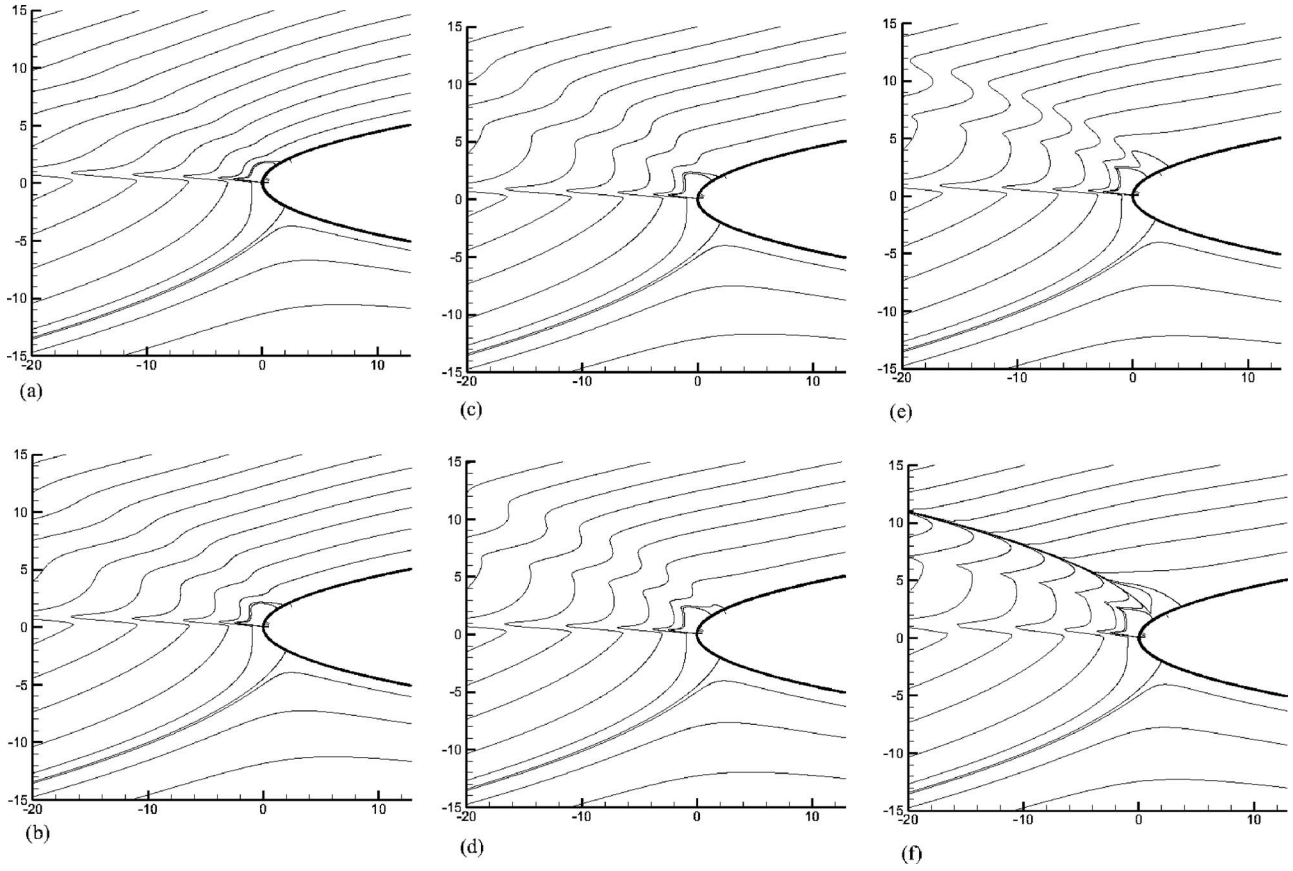

Fig. 8 Temporal development of the instantaneous streamlines for $a=2$ and $V_{w_A}=0.5$ in physical coordinates, but blown-up boundary-layer thickness, at times (*a*) $t=1.0$, (*b*) $t=3.0$, (*c*) $t=5.0$, (*d*) $t=7.0$, (*e*) $t=9.0$, and (*f*) $t_s=10.8$

As noted in Sec. 4, in increasing the suction strength, the present computations are limited by the appearance of numerical oscillations above the ejection slot, suggesting the possibility of a flow instability (though the oscillations seem to disappear when the streamwise mesh resolution is increased [28]). In Fig. 9, streamwise velocity profiles above the ejection and suction slots are shown. The velocity profiles are (1) at the vertex of the parabola, (2) in the middle of the ejection slot, (3) at the end of the ejection slot, (4) at the beginning of the suction slot, and (5) in the middle of the suction slot. Note that the profiles become increasingly distorted and inflectional above the ejection slot.

Higher angle-of-attack cases, i.e., $a=3$ and $a=4$, were also considered [28]. For $a=3$, with $x_0=0.2$, $x_1=1.6$, $x_2=-0.1$, $x_3=0.1$, and $V_{w_A}=1$, separation was delayed from $t_{ss}=2.55$ and $x_{ss}=0.789$ to $t_s=3.16$ and at $x_s=1.281$. For $a=4$, with $x_0=0.15$, $x_1=1.4$, $x_2=-0.15$, $x_3=0.05$, and $V_{w_A}=1$, separation was delayed from $t_{ss}=1.62$ and $x_{ss}=0.637$ to $t_s=1.93$ and $x_s=1.02$. It therefore appears that the benefits tend to decrease significantly at larger angles of attack.

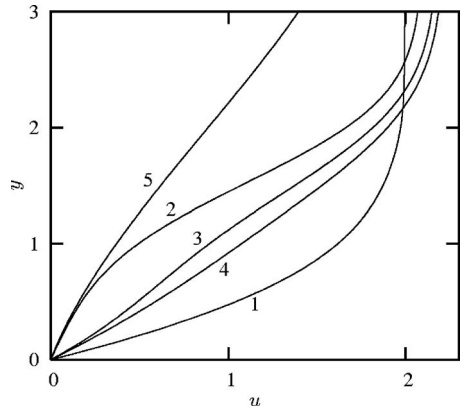

Fig. 9 Streamwise velocity profiles for $a=2$ at $t=5$

On the other hand, it appears that the device may be effective at lower angles. A number of calculations were carried out for smaller values of a [28], and it was found that separation above the suction slot could be suppressed for values of $a \leqslant 1.5$. For example, with $a=1.5$ and $x_0=1$, $x_1=4$, $x_2=0$, $x_3=0.6$, and $V_{w_A}=0.2$, it was found that the Eulerian computation continued until $t_f=33.3$, and separation was then expected downstream of the slot. Lengthening the slot would presumably push the separation farther downstream; however, lengthening it too much will produce separation at the upstream end. It seems likely that this effect may be mitigated using a more sophisticated suction distribution, with the suction more concentrated near the upstream end, as in the steady computations, rather than the symmetric distribution assumed here. In its present form, the device produced reasonable gains in a moderate range of angles of attack above the critical value $a=1.2$.

7 Conclusion

The results obtained in this study show that autogenous suction can, in principle, be effective. Laminar separation at high Reynolds numbers can theoretically be eliminated for scaled angles of attack well beyond the maximum no-suction value of 1.2. In fact, there was no fundamental limit to the scaled angle of attack evident in the range that the present steady numerical procedures were able to compute, which was up to 2.6.

However, prospects that seem attractive in theory may be difficult in actual practice [13]. In our present highly idealized study, finite Reynolds number and conduit size effects were not directly addressed, and the chosen strategy used to determine the suction velocities in the steady case may not be the easiest to implement practically. Clearly, creating suitable permeable surfaces and conduits with specified head loss is a significant technical problem, and the technical difficulties multiply for problems with variable angle of attack. It should also be noted that it took us some time to develop suction algorithms that allowed the demonstrated angle of attack to be gradually pushed up to 2.6 for steady calculations. This seems to suggest that the latitude in transpiration velocity distributions may be relatively narrow; in particular, we found that the suction distributions must be sufficiently weighted toward their upstream end, or the upstream ejection will cause separation there before suction has picked up enough to prevent it.

Yet, what has been established here is that there are no fundamental theoretical objections against autogenous suction. There is a rapid increase in what can be done technically, and history shows that what may seem prohibitively difficult at one time can become routine subsequently.

Acknowledgment

The authors would like to acknowledge significant contributions of Professor J.D.A. Walker, formerly of Lehigh University, to the research reported in this paper. Dr. Walker unexpectedly passed away before this paper could be written. However, as thesis advisor of one of the authors (H.A.), he directed significant parts of the efforts reported here.

This material is based on work supported by the U.S. Army Research Laboratory and the U.S. Army Research Office under Grant Nos. DAAD19-99-1-0244 and W911NF-05-1-0295.

Nomenclature

a = scaled angle of attack (1)
α = angle of attack
c = chord length
C_p = pressure coefficient
C_Q = suction coefficient times $\sqrt{\mathrm{Re}}$
Re = leading-edge radius Reynolds number
t = time
t_0 = time of the switch to Lagrangian coordinates
t_f = time at which a Eulerian computation fails
t_s = separation time (ss, steady separation)
t_v = time at which suction starts
v_w = surface transpiration velocity times $\sqrt{\mathrm{Re}}$
V_w = peak suction (A)/ejection (B) velocity, (3)/(4)
x = distance along the airfoil surface, Fig. 1
x_i = ($i=0,1,2,3$) transient-case transpiration slot boundaries, (3) and (4)
x_s = position of separation (ss, steady separation)
δ^* = displacement thickness times $\sqrt{\mathrm{Re}}$
ω = wall vorticity divided by $\sqrt{\mathrm{Re}}$
$\Omega_{\min}$ = allowed minimum wall vorticity parameter (2)

References

[1] McAlister, K. W., and Carr, L. W., 1979, "Water Tunnel Visualizations of Dynamic Stall," ASME J. Fluids Eng., **101**, pp. 367–380.
[2] Francis, M. S., and Keesee, J. E., 1985, "Airfoil Dynamic Stall Performance With Large Amplitude Motions," AIAA J., **23**, pp. 1653–1659.
[3] Acharya, M., and Metwally, M. H., 1992, "Unsteady Pressure Field and Vorticity Production Over a Pitching Airfoil," AIAA J., **30**, pp. 403–411.
[4] Currier, J. M., and Fung, K.-Y., 1992, "Analysis of the Onset of Dynamic Stall," AIAA J., **30**, pp. 2469–2477.
[5] Shih, C., Lourenco, L. M., Van Dommelen, L. L., and Krothapalli, A., 1992, "Unsteady Flow Past an Airfoil Pitching at Constant Rate," AIAA J., **30**, pp. 1153–1161.
[6] Karim, M. A., and Acharya, M., 1994, "Suppression of Dynamic Stall Vortices Over Pitching Airfoils by Leading-Edge Suction," AIAA J., **32**, pp. 1647–1655.
[7] Wang, S.-C., 1995, "Control of Dynamic Stall," Ph.D. thesis, Florida State University, Tallahassee, FL.
[8] Yu, Y. H., Lee, S., McAlister, K. W., Tung, C., and Wang, C. M., 1995, "Dynamic Stall Control for Advanced Rotorcraft Application," AIAA J., **33**, pp. 289–295.
[9] Alrefai, M., and Acharya, M., 1996, "Controlled Leading-Edge Suction for Management of Unsteady Separation Pitching Airfoils," AIAA J., **34**, pp. 2327–2336.
[10] Atik, H., Kim, C.-Y., Van Dommelen, L., and Walker, J., 2005, "Boundary-Layer Separation Control on a Thin Airfoil Using Local Suction," J. Fluid Mech., **535**, pp. 415–443.
[11] Prandtl, L., 1961, "Über Flüssigkeitsbewegung bei sehr kleiner Reibung," *Ludwig Prandtl gesammelte Abhandlüngen*, Springer-Verlag, Berlin, Vol. 2, pp. 575–584.
[12] Poppleton, E. D., 1955, "Boundary Layer Control for High Lift by Suction of the Leading-Edge of a 40 Degree Swept-Back Wing," ARC, UK, Technical Report No. RM 2897.
[13] 1961, *Boundary Layer and Flow Control*, G. Lachmann, ed., Pergamon, London, Vols. I and II.
[14] Bahi, L., Ross, J., and Nagamatsu, H., 1983, "Passive Shock Wave/Boundary Layer Control for Transonic Airfoil Drag Reduction," AIAA Paper No. 83-0137.
[15] Nagamatsu, H., Dyer, R., and Ficarra, R., 1985, "Supercritical Airfoil Drag Reduction by Passive Shock Wave/Boundary Layer Control in the Mach Number Range .75 to .9," AIAA Paper No. 85-0207.
[16] Nagamatsu, H., Trilling, T., and Bossard, J., 1987, "Passive Drag Reduction on a Complete NACA 0012 Airfoil at Transonic Mach Numbers," AIAA Paper No. 87-1263.
[17] Koval'nogov, S., Fomin, V., and Shapovalov, G., 1987, "Experimental Study of the Possibility of Passive Control of Shock-Boundary Layer Interactions," Uch. Zap. TsAGI, **18**, pp. 112–116.
[18] Van Dyke, M., 1964, *Perturbation Methods in Fluid Mechanics*, Academic, New York.
[19] Zalutsky, K., 2000, "Unsteady Boundary-Layer Separation," Ph.D. thesis, Lehigh University, Lehigh, PA.
[20] Werle, M. J., and Davis, R. T., 1972, "Incompressible Laminar Boundary Layers on a Parabola at Angle of Attack: A Study of the Separation Point," ASME J. Appl. Mech., **39**, pp. 7–12.
[21] Terrill, R. M., 1960, "Laminar Boundary Layer Flow Near Separation With and Without Suction," Philos. Trans. R. Soc. London, Ser. A, **253**, pp. 55–100.
[22] Van Dommelen, L. L., and Shen, S. F., 1980, "The Spontaneous Generation of a Singularity in a Separating Boundary Layer," J. Comput. Phys., **38**, pp. 125–140.
[23] Van Dommelen, L. L., and Cowley, S. J., 1990, "On the Lagrangian Description of Unsteady Boundary-Layer Separation. Part 1. General Theory," J. Fluid Mech., **210**, pp. 593–626.
[24] Panton, R., 2005, *Incompressible Flow*, 3rd ed., Wiley, Hoboken, NJ.
[25] Doligalski, T. L., and Walker, J. D. A., 1984, "The Boundary Layer Induced by a Convected Vortex," J. Fluid Mech., **139**, pp. 1–28.
[26] Peridier, V. J., Smith, F. T., and Walker, J. D. A., 1991, "Vortex-Induced Boundary-Layer Separation. Part 1. The Unsteady Limit Problem $Re\rightarrow\infty$," J. Fluid Mech., **232**, pp. 99–131.
[27] Degani, A. T., Li, Q., and Walker, J. D. A., 1996, "Unsteady Separation From the Leading Edge of a Thin Airfoil," Phys. Fluids, **8**, pp. 704–714.
[28] Atik, H., 2002, "Boundary-Layer Separation and Control," Ph.D. thesis, Lehigh University, Lehigh, PA.
[29] Lighthill, M. J., 1963, "Introduction. Boundary Layer Theory," *Laminar Boundary Layers*, L. Rosenhead, ed., Oxford University Press, Oxford, UK, pp. 46–72.

Analysis of Coherent Structures in the Far-Field Region of an Axisymmetric Free Jet Identified Using Particle Image Velocimetry and Proper Orthogonal Decomposition

A.-M. Shinneeb
e-mail: shinneeb@uwindsor.ca

R. Balachandar
e-mail: rambala@uwindsor.ca

Department of Civil and Environmental Engineering,
University of Windsor,
401 Sunset Avenue,
Windsor, ON, N9B 3P4, Canada

J. D. Bugg
Department of Mechanical Engineering,
University of Saskatchewan,
57 Campus Drive,
Saskatoon, SK, S7N 5A9, Canada
e-mail: jim.bugg@usask.ca

This paper investigates an isothermal free water jet discharging horizontally from a circular nozzle (9 mm) *into a stationary body of water. The jet exit velocity was* 2.5 m/s *and the exit Reynolds number was 22,500. The large-scale structures in the far field were investigated by performing a proper orthogonal decomposition (POD) analysis of the velocity field obtained using a particle image velocimetry system. The number of modes used for the POD reconstruction of the velocity fields was selected to recover 40% of the turbulent kinetic energy. A vortex identification algorithm was then employed to quantify the size, circulation, and direction of rotation of the exposed vortices. A statistical analysis of the distribution of number, size, and strength of the identified vortices was carried out to explore the characteristics of the coherent structures. The results clearly reveal that a substantial number of vortical structures of both rotational directions exist in the far-field region of the jet. The number of vortices decreases in the axial direction, while their size increases. The mean circulation magnitude is preserved in the axial direction. The results also indicate that the circulation magnitude is directly proportional to the square of the vortex radius and the constant of proportionality is a function of the axial location.* [DOI: 10.1115/1.2813137]

Keywords: axisymmetric turbulent free jet, coherent structures, PIV, POD

1 Introduction

The turbulent free round jet has received the attention of many researchers because of its fundamental significance as a basic flow in turbulence research (see, for example, Refs. [1,2] for comprehensive reviews). Many previous studies have focused on the evolution and dynamics of coherent structures in turbulent jets. This is motivated by the role of coherent structures in processes of practical interest such as entrainment and mixing. The coherent vortical structures in the far field of a round turbulent jet have received little attention compared to those in the near-exit region. The reason may be attributed to the measurement techniques used, which were inappropriate in the fully developed region. The development of quantitative techniques such as particle image velocimetry (PIV) provides new possibilities for studying these structures because they provide instantaneous global velocity fields, which are not possible with pointwise techniques. The purpose of this study is to gain more insight into the dynamics of these structures in the far field of a round turbulent jet using the capability of the PIV technique.

The existence of coherent motions in the fully developed turbulent axisymmetric jet has been suspected by researchers ever since coherent motion became a major focus of experimental turbulence research. Tso et al. [3] reported two-point correlation measurements of streamwise velocities using hot wires. They inferred passage of similar large-scale structures periodically in the fully developed region whose size was of the same order of magnitude as the local jet diameter. Tso and Hussain [4] reported an experimental investigation of large-scale coherent vortical motions in an air jet with exit Reynolds number of 69,000 by employing a radial rake of X wires. They found that the helical mode was the most preferred and occurred 12% of the time, while the double helical mode was found to occur only 3% of the time. The ring mode was observed in the jet far field but was considered to be dynamically unimportant. Dahm and Dimotakis [5] investigated the organizational modes in a jet and suggested the presence of ring and helical modes with the jet continually switching between them. Agrawal and Prasad [6] examined the organizational modes of large vortices occurring in the axial plane of a self-similar round turbulent jet. The jet exit Reynolds number was 3000. These large vortices were deduced by means of a Galilean transformation and the analysis was performed by the linear stochastic estimation (LSE) technique. It was found that both ring and helical modes occurred prominently in jets, with the helical mode being the more frequent. In another study, Agrawal and Prasad [7] used high-pass filtering of PIV measurements to educe small vortices occurring in the self-similar region of an axisymmetric turbulent jet. An automated method was developed to identify vortex centers, rotational sense, size, circulation, vorticity, and energy. Then, a statistical study of the vortex properties was performed, which revealed the existence of an almost equal number of vortices of each rotational sense close to the jet axis.

Since the discovery of coherent structures, describing and identifying these structures in a turbulent flow have been a challenge. However, some methods of analysis such as the proper orthogonal

Contributed by the Fluids Engineering Division of ASME for publication in the JOURNAL OF FLUIDS ENGINEERING. Manuscript received December 19, 2006; final manuscript received July 10, 2007; published online December 19, 2007. Review conducted by Juergen Kompenhans.

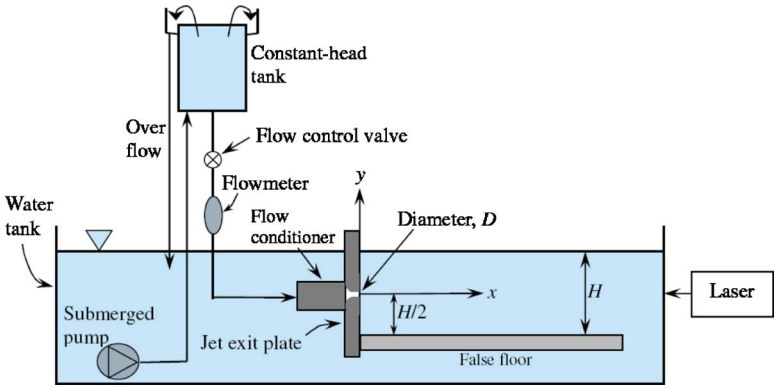

Fig. 1 Schematic description of the apparatus

decomposition (POD) technique have been employed to obtain useful information about the characteristics of these structures. This technique was introduced by Lumley in 1967 (see Holmes et al. [8]) as an unbiased method for extracting structures in a turbulent flow. The POD is the most efficient way of extracting the most energetic components of an infinite-dimensional process with only few modes [8,9]. POD requires measurement of the spatial cross correlation of the velocities in a turbulent flow field. The high spatial resolution of the PIV data makes it an ideal experimental technique for use with POD [10,11].

This paper reports PIV measurements of an isothermal round water jet discharging horizontally from a vertical wall into a stationary body of water of large extent. The objective of this paper is to quantify large-scale structures in the far field of the free jet. This is done by performing a POD analysis on the fluctuating velocity fields and using the vortex identification algorithm of Agrawal and Prasad [7] to quantify their size, circulation, and direction of rotation.

2 Apparatus

The experiments were performed in a long, glass-walled water tank shown in Fig. 1. The water tank has nominal interior dimensions of 0.7 m depth, 1 m width, and 4 m length. The experimental setup consists of an insert placed in the water tank and a water supply system. The insert, which consists of a false floor and a vertical jet exit plate, was placed inside the water tank as shown schematically in Fig. 1. The false floor formed the bottom boundary, while the top boundary was the free surface. In order to generate a free jet, the false floor was positioned near the bottom of the water tank so that the maximum water depth ($H \approx 540$ mm) could be achieved. Water was discharged through an orifice of diameter $D=9$ mm into the water tank. The discharge nozzle was located at the center of the vertical jet exit plate.

The water supply system consisted of a submersible pump, a constant head tank, a flow control valve, a turbine flowmeter, a flow conditioner, and the jet exit itself. The submersible pump supplied water from the water tank to the constant head tank. The head tank provided a constant head of 5 m. The flow conditioner was attached directly to the jet exit plate and consisted of a 160 mm long, 112 mm diameter section, which contained three wire screens and a set of flow straightening vanes. This flow conditioner was successful in producing a top-hat velocity profile (see Refs. [12,13]). Following the flow conditioner, the jet was formed by a circular arc exit with a radius equal to the exit diameter (9 mm). The exit plane of the jet was flush with the jet exit plate. The jet flow was generated by the hydrostatic pressure difference between the head tank and the water tank. The jet exit velocity was 2.5 m/s, yielding a Reynolds number of 22,500. The origin of the coordinate system used in this paper is at the jet exit and the x axis extends in the axial direction (see Fig. 1).

3 Particle Image Velocimetry System and Data Analysis

The PIV system used for the present measurements incorporated 50 mJ/pulse dual Nd:YAG lasers. The light sheet was formed through a 1000 mm focal length spherical lens and a 12.7 mm focal length cylindrical lens. The light sheet was oriented vertically and included the axis of the jet. The light sheet entered the end of the water tank (as shown in Fig. 1), while the optical axis of the camera was positioned perpendicular to it at the side of the tank. After carefully filtering the water through a 1 μm filter, 10 μm diameter hollow glass bead seed particles were introduced. These particles have a specific gravity of 1.1 and a mean diameter of 10 μm. They are expected to follow the flow faithfully in this application since their density is very close to that of water and they are very small (see Shinneeb [13] for a complete analysis).

The field of view was imaged with a 2048×2048 pixel Redlake ES4.0/E Megaplus camera operating in dual capture mode. The camera was fitted with a 60 mm Micro-Nikkor lens and the object distance was adjusted to give the required field of view (FOV). A Berkeley Nucleonics 500B digital delay generator was used to trigger the lasers and provide synchronization with the camera. The frame grabber was an EDT PCI DVC-Link. Images were acquired at a sampling rate of 1 Hz. This rate is low enough for the images to be uncorrelated. Image calibration was achieved by taking a picture of a steel ruler with 1 mm divisions. Using this ruler, it was confirmed that there was negligible distortion over the FOV. Measurements will be reported only on the x-y plane, which includes the jet axis (x axis). All FOVs were positioned at an axial location between $10 < x/D < 65$. Table 1 summarizes the number, location, size, and spatial resolution of the four FOVs reported in this paper. Note that the third column in this table gives the distance from the jet exit to the left edge of each FOV (see Fig. 1).

Image analysis was performed with a correlation analysis software developed in-house. The images were first analyzed with 64×64 interrogation areas using a fast Fourier transform (FFT)-based cross correlation between successive images. The correlation-based correction (CBC) method proposed by Hart [14]

Table 1 Summary of the characteristics of the velocity fields

FOV	No. of images	Distance from jet exit (mm)	Image size (mm × mm)	Spatial resolution (mm)
1	1000	0.0	67.3 × 67.3	0.526
2	2000	96.0	168.5 × 168.5	0.658
3	2000	259.0	160.7 × 160.7	0.628
4	2000	416.0	167.9 × 167.9	0.656

was used to improve the signal-to-noise ratio and limit the number of spurious vectors. Then, using the displacement results from this rather coarse grid to determine a local interrogation area offset, the image was reanalyzed with 32×32 pixel interrogation areas. This offset is achieved by shifting the interrogation window symmetrically around the central grid point in the first and second images. This analysis process was repeated one more time to complete a three-pass analysis and yield a final interrogation area size of 16×16 pixels. The interrogation areas were overlapped by 50%. The actual spatial resolution that this procedure yielded was dependent on the size of the measurement plane and is reported in Table 1.

After the correlation analysis was complete, outliers were rejected using the cellular neural network (CNN) method [15] with a variable threshold technique proposed by Shinneeb et al. [16]. The main theme of this technique is to use information from the local velocity gradient in the flow to make a more local choice for the threshold. The percentage of vectors rejected varied from 4% to 12%. Rejected vectors were replaced using a Gaussian-weighted mean of their neighbors.

The PIV image analysis software used in this paper has been thoroughly tested using the "Series A" data set of the 2003 PIV Challenge (Stanislas et al. [17]). This data set is also for a self-similar turbulent jet and so closely resembles the flow conditions of the present paper. All of the rather extensive flow parameters used to assess the groups participating in the original Challenge were predicted well by the software used in this paper. These include the rate of the jet centerline velocity decay, the jet spread rate, the normalized profiles of velocity and axial rms velocity, the peak locking parameter, the number of outliers, and the entrainment velocity. On this basis, the analysis software used in this paper appears sound.

Smoothing of the PIV data is commonly used to remove high-frequency noise. In order to avoid removing real high-frequency data, a simple convolution of the data with a rather narrow smoothing kernel is generally used. A Gaussian kernel with a narrow width equal to two grid units ($2\Delta x$) was employed in this study (see Shinneeb [13] for more details).

4 Identification of Vortical Structures

The PIV data were analyzed using the POD technique to identify the main energy-containing structures. This was done by first averaging the velocity fields and calculating the fluctuating velocities. Then, the fluctuating velocity fields were processed using the POD via the method of snapshots [18] (see also Shinneeb [13] for more details). In order to maintain a common ground for comparison, the analysis was performed by fixing the energy content of the exposed structures. Since turbulence has a wide spectrum of eddy sizes and since there is no demarcation that clearly separates large eddies from smaller ones, the definition of large-scale structures adopted in this paper is based on the range of the largest exposed structures that contain a specified amount of energy. The number of modes used for the POD reconstruction was selected based on a target of 40% energy content. These reconstructed fields were used as a basis to search for vortical structures using the vortex identification algorithm described by Agrawal and Prasad [7].

The vortex identification algorithm of Agrawal and Prasad [7] is based on the concept of using *closed streamlines* to identify vortices [19]. This technique involves searching the POD reconstructed field for circular streamlines by monitoring the change in direction of the measured velocity vectors along expanding circular paths surrounding candidate vortex centers. The largest such path for which the change in direction is monotonic for 75% of the vectors defines the size of the vortex. The circulation Γ of a structure is calculated by integrating along its outermost path. In discrete data, it is calculated by integrating along a polygon path as follows:

$$\Gamma = \sum (u_{\mathrm{POD}} \Delta x + v_{\mathrm{POD}} \Delta y) \tag{1}$$

where u_{POD} and v_{POD} represent the velocity components of the reconstructed field and Δx and Δy are the axial and vertical (radial) grid intervals, respectively. Due to the discrete nature of the data, the path was approximated by the polygon that best describes a circle. This technique of vortex identification was chosen over the alternative of considering regions of concentrated vorticity because vorticity identifies not only vortex cores but also any shearing motion present in the flow. This often makes the vorticity contours ambiguous even when there was closed streamlines apparent in the vector fields. This difficulty is also discussed by Adrian et al. [9] and Ganapathisubramani et al. [20].

5 Uncertainty Analysis

The uncertainty in the PIV data is influenced by a number of factors, such as particle image size, nonuniform illumination, interrogation area size, particle seeding density, computational effects, and flow properties such as velocity gradients, curvature of the particle trajectories, and three-dimensional (out of plane) motion. This makes the task of error assessment rather difficult. Since measurements of a steel ruler at various locations within the FOV confirmed negligible optical distortion, the uncertainty analysis concentrates on the image analysis process. The uncertainty analysis was performed by generating synthetic images with characteristics similar to the real images. In this way, the exact values of the particle displacements are known so that the uncertainty analysis can be performed. The characteristics of the simulated images were quantified by the following parameters: background noise, number of paired particles, number of spurious particles, particle diameter, particle intensity, and displacement magnitude. This method is fully described by Bugg and Rezkallah [21]. These characteristics were obtained from the real images using MATROX INSPECTOR® software. The size of the simulated images was 2048×2048 pixels, the same as the real images. After a set of simulated images was generated, they were analyzed using the same procedures applied to the real images. Then, the outliers were detected and replaced using the same techniques as the real data. Finally, both systematic and random uncertainties were determined by comparing the known and measured particle displacements.

A complete discussion of the uncertainty analysis may be found from Shinneeb [13] and a summary of the findings is given below. The characteristic velocity scale in the present flow (the centerline velocity) corresponds to a displacement of about eight to ten pixels. The relative uncertainty in the characteristic instantaneous (smoothed) velocity measurement is about 1.7%. Including the uncertainty in the jet exit velocity (1.25%), the relative uncertainty for the normalized velocity fields becomes 2.1%. The characteristic velocity of the fluctuating velocity component is about one order of magnitude smaller than the instantaneous velocity component; therefore, the relative error of the fluctuating velocity field is amplified to about 21%.

The definition of the circulation Γ (see Eq. (1)) indicates that uncertainties in measuring velocity and vortex radius R will contribute to the uncertainty in Γ (Agrawal and Prasad [22]). The measurement of R is affected by the fact that the vortex center may not lie exactly on a grid point. In addition, not all closed streamlines are perfectly circular or even perfectly closed due to the nature of the identification process and the threshold employed therein. Furthermore, due to the discrete nature of the data, the true vortex radius may be slightly smaller or larger than the measured value. These effects can produce an additional random uncertainty in the value of Γ. Unfortunately, these uncertainties cannot be quantified accurately without extensive investigations. However, the uncertainty in R is estimated to be equal to one grid unit ($\sim$0.6 mm). The relative uncertainty then varies according to the vortex size, which is roughly estimated to be 10–30%. Moreover, the uncertainty in Γ around a perfect circle is equal to the

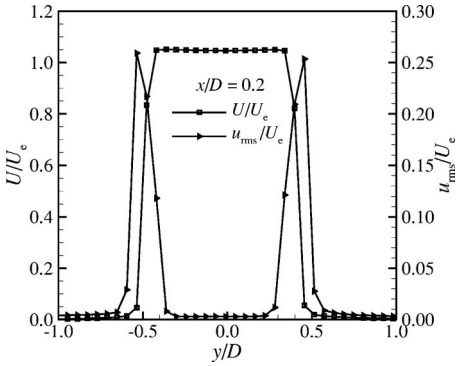

Fig. 2 Axial mean velocity and turbulence intensity profiles near the jet exit ($x/D=0.2$). Velocities are normalized by the exit velocity (2.5 m/s) and distances by the jet exit diameter (9 mm).

uncertainty of a single fluctuating velocity uncertainty (21%). Thus, the cumulative measurement error in Γ is estimated to be 23–37% (see also Agrawal and Prasad [22] for a similar analysis).

6 Results

The purpose of the present investigation is to increase our understanding of the turbulent structure of a round free jet in the far-field region. The jet exit diameter and velocity were 9 mm and 2.5 m/s, respectively, yielding a Reynolds number of 22,500. PIV measurements are reported at several distances from the jet exit.

6.1 Jet Exit. The purpose of taking measurements at the jet exit is to document the initial condition of the jet since the flow at downstream locations is dependent on it. The number, size, and spatial resolution of this FOV (FOV1) are given in Table 1.

Figure 2 shows the mean axial velocity component U just downstream the exit plane ($x/D=0.2$). This profile was extracted from the average of 1000 PIV velocity fields and shows that the profile is very close to uniform. The velocity in the core of the jet at this location reached 2.62 m/s, which may be explained by the formation of a very thin boundary layer at the jet exit. The maximum deviation of the velocity from the core velocity over the jet exit was 0.46%. Figure 2 also shows the axial turbulence intensity normalized by the jet exit velocity U_e and confirms that the high-shear regions at the edges of the jet produce the highest turbulence intensity. The axial turbulence intensity in the core of the jet exit was only 0.3%. These data indicate clearly that the flow is uniform at the jet exit with low turbulence intensity.

6.2 Coherent Structures. The objective of this study is to quantitatively investigate large-scale structures in the far-field region of an axisymmetric free jet. For this purpose, 2000 images were acquired at three adjacent locations in the far field of the jet (see Table 1) in order to extract reliable statistical information about the behavior of the flow. These structures were exposed using the POD technique. The size of the correlation matrix for the POD analysis was 2000×2000. To focus on large-scale structures, the number of modes used in the POD reconstruction was selected to contain 40% of the turbulent kinetic energy. Then, a vortex identification algorithm of Agrawal and Prasad [7] was employed to identify the center, radius, and strength (circulation) of vortices. Table 2 lists the total number of structures identified by this technique and the number of POD modes used for the reconstruction of the velocity fields. This step was followed by a statistical study of the distribution of vortex size and circulation. It should be noted that vortical structures with a radius smaller than three grid units ($\sim0.2D$) or a circulation less than 0.1 cm^2/s were eliminated. It should also be noted that all the results presented in this work correspond to vortices whose axes are approximately perpendicular to the x-y plane.

Table 2 Properties of the educed vortical structures

FOV	No. of vortices	No. of POD modes	Energy contained in the modes (%)	Ratio of positive to negative vortices
2	30,257	25	40.13	0.962
3	13,725	15	40.22	0.974
4	7,150	10	39.74	0.981

Selected examples of POD reconstructed velocity fluctuation fields for the free jet representing three adjacent FOVs in the far-field region are shown in Fig. 3 as plots $(a)-(c)$. In these plots, only every fifth vector is shown in both directions to avoid cluttering. These velocity fields contain $\sim40\%$ of the fluctuating velocity energy. Locations are normalized by the jet exit diameter D. Note that $y/D=0$ represents the center of the jet. These figures show several vortical structures of different sizes. Dark and light circles in these plots represent positive and negative rotational senses, respectively.

The plots confirm the existence of both positive and negative vortices in the free jet flow. It is clear in plot (a) that the jet flow contains several vortices and their size increases in the axial direction. It also shows that the vortices located at the sides of the jet penetrate the surrounding fluid, which sheds light on the process of entraining the fluid from the surroundings. Plots (b) and (c) illustrate that the size of the vortices becomes even larger at downstream locations compared to plot (a). In addition, this increase in size is accompanied by a reduction in the number of vortices. This observation suggests the occurrence of vortex pairing.

The observations drawn from Fig. 3 reflect the general behavior of the vortices. A complete analysis of this behavior will now be presented in the form of a statistical study that is based on all the identified vortices from all the velocity fields. This will provide deeper insight into the vortex characteristics in the flow.

Figure 4 shows the variation of the number of vortices in the axial direction x. In this figure, the horizontal axis represents the axial direction x normalized by the jet exit diameter D and the vertical axis represents the number of vortical structures N_v normalized by the number of velocity frames N_f. Each point on this curve represents the normalized number of structures contained in a 16-grid-unit interval ($\sim1.1D$) of the axial distance x. This figure shows that the number of vortices decreases quite quickly in the axial direction.

The distribution of vortex radius R and rotational sense with axial position x is illustrated in Fig. 5. Both R and x are normalized by the jet exit diameter D. Note that the sign of R/D corresponds to the rotational sense of the vortex, where positive R/D represents positive rotational sense. This figure shows three plots representing three adjacent FOVs. Each plot is obtained from a set of data containing 2000 velocity fields. It should be pointed out that the data at the edges of each plot were removed because large vortical structures cannot be identified near the right and left edges of the velocity field. Also, the band near $R/D=0$ corresponds to the minimum resolvable vortex size of $R/D<0.21$. To help perceive the size of the vortices, the half-width $r_{1/2}$ of the present jet is also shown in Fig. 5 as gray lines. Note that $r_{1/2}$ represents the radial location where the mean axial velocity equals one-half of the centerline value. $r_{1/2}$ varies linearly in the axial direction with a rate equal to 0.096 for the present data. This rate was determined by fitting the mean axial velocity profiles to the Gaussian distribution using the Levenberg–Marquardt algorithm [23]. Figure 5 clearly shows that the jet has a wide spectrum of vortex sizes at each axial location. Moreover, the distribution of positive vortical structures is a mirror image of the negative ones.

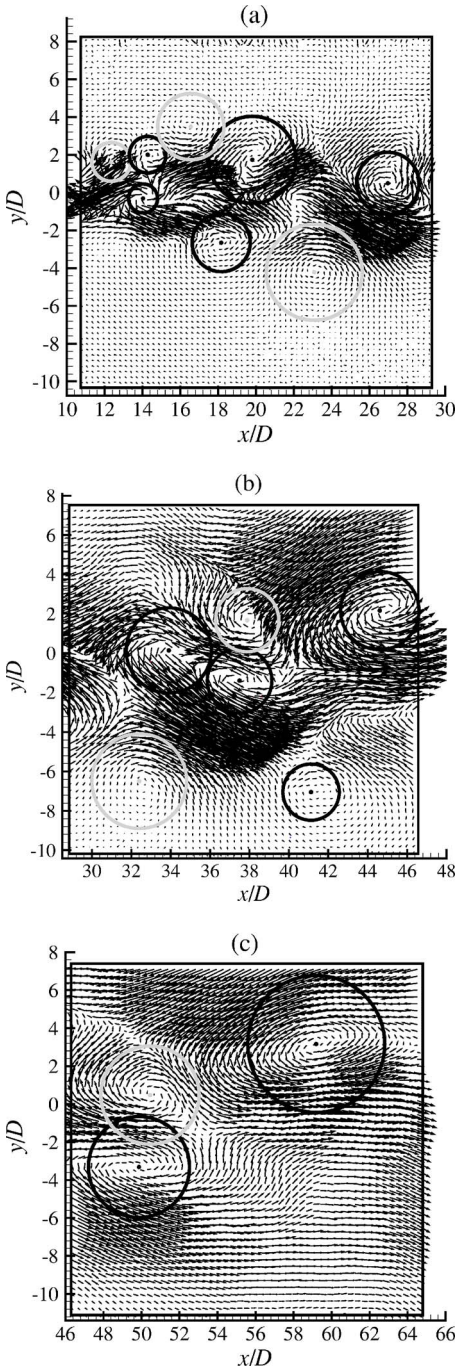

Fig. 3 ((*a*)–(*c*)) Examples of POD reconstructed velocity fluctuation fields for the free jet representing three adjacent FOVs. The circles represent the size of identified vortices. Dark and light circles represent positive and negative rotational senses, respectively.

All plots in Fig. 5 clearly show that the range of vortex size increases in the axial direction and large vortices have sizes comparable to the local jet width $r_{1/2}$.

More information may be extracted from the data shown in Fig. 5 by sorting the vortical structures on the basis of size and rotational sense. Figure 6 shows the percentage of vortical structures as a function of vortex radius R and rotational sense. In this figure, the sign of R corresponds to the rotational sense of the vortex, where positive R indicates that the vortex is turning counterclockwise. Figure 6 consists of three plots, which show the percentage of vortices for the free jet extracted from three adjacent FOVs.

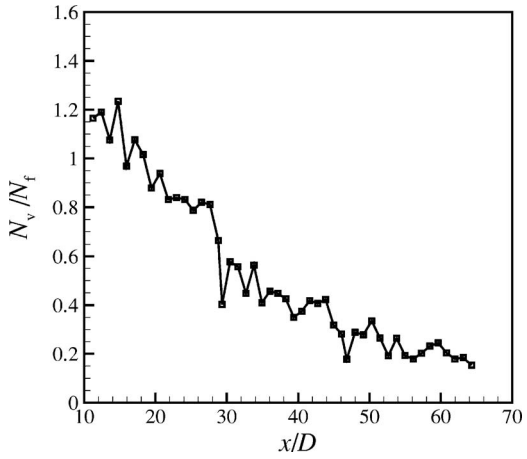

Fig. 4 Variation of the normalized number of vortices N_v/N_f in the axial direction x/D

The purpose of plotting these profiles is to show the effect of the axial distance on the size distribution of the vortical structures. It should be noted that these plots were obtained by separately counting vortices of opposite signs in a velocity field and dividing by the total number of vortices. The bin size of the vortex radius R used to construct all profiles was $\sim 0.07D$. It should be also noted that these profiles were obtained by using only the data in the range of x/D indicated on each plot and removing the data at the left and right edges of the FOVs. This is because large vortices cannot be identified near the edges of the velocity fields and, therefore, the results would have been biased toward small values of R/D.

Figures 6(*a*)–6(*c*) reveal that the population of structures of either sign is almost identical for all radii and their number decreases as the size increases. The ratio between the number of positive and negative vortices for plots (*a*), (*b*), and (*c*) is 0.96, 0.97, and 0.98, respectively. These ratios are so close to 1 that it can be concluded that the jet contains almost identical numbers of vortices of both signs. It is also clear that small vortices have generally higher population in all profiles. By comparing the three profiles, it is apparent that the number of small vortices decreases slightly with increasing axial distance and there is a corresponding increase in the number of bigger vortices. Furthermore, the range of the vortex size increases with axial distance. Note that the largest identified vortices shown in plots (*a*), (*b*), and (*c*) have sizes $|R/D| \approx 4$, 6, and 8, respectively. Generally, the high percentage of small vortices in all the velocity fields indicates the occurrence of the tearing process besides the pairing process.

Figure 7 shows the distribution of circulation Γ associated with the vortices in the axial direction x. In these figures, the circulation Γ is normalized by DU_e. This figure also consists of three plots. Figure 7 indicates that the circulation magnitude varies from a weak to a relatively larger circulation at each axial location. Figure 7 illustrates that the range of the circulation magnitude does not change significantly in the axial direction where $|\Gamma/DU_e|$ is generally less than 1.2. However, the number of the points representing vortex circulations is clearly smaller at downstream locations. This observation is consistent with the reduction of the number of vortices shown in Fig. 4.

Additional insight is gained by plotting the behavior of mean vortex radius R_{mean} and circulation Γ_{mean} in the axial direction x (Fig. 8). In this figure, the axial location x and the mean vortex size R_{mean} are normalized by the jet exit diameter D, while the circulation is normalized by DU_e. These mean values were calculated from the vortices that exist in 16-grid-unit intervals ($\sim 1.1D$) of the axial distance x. It should be noted that these mean quantities are calculated from the resolved vortices (R/D

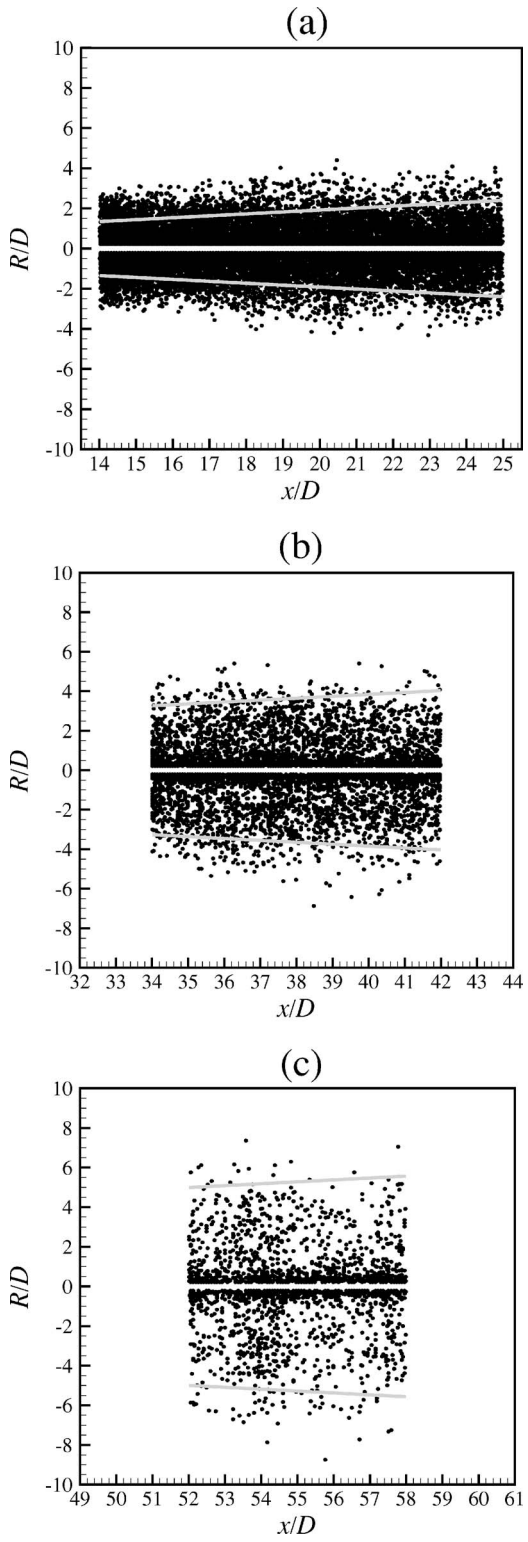

Fig. 5 ((*a*)–(*c*)) The distribution of vortex size *R* in the axial direction *x* at three adjacent locations. Each plot represents data extracted from 2000 velocity fields. Note that positive *R*/*D* represents positive rotational sense and the gray lines represent the half-width of the jet.

≥ 0.2). Since the number of vortices is inversely proportional to the vortex size, these mean quantities are expected to be biased toward the high side because the smallest vortices ($R/D < 0.2$) are not included in the average.

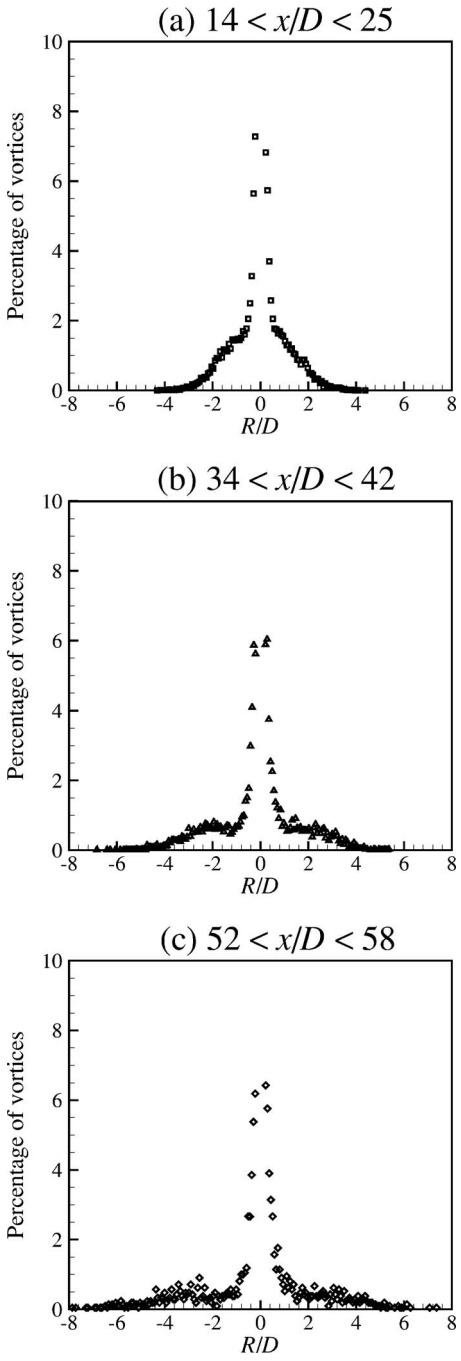

Fig. 6 Percentage of vortices for the free jet at axial locations: (*a*) 14< *x*/*D*<25, (*b*) 34< *x*/*D*<42, and (*c*) 52< *x*/*D*<58

Figure 8 shows that the mean size of the vortices generally increases in the axial direction, which is consistent with Figs. 5 and 6. It should be noted that these curves were extracted from three adjacent FOVs. Several points near the left and right edges of each field were removed as indicated earlier. It is also apparent from this figure that the mean vortex circulation Γ_{mean}/DU_e of the free jet fluctuates within a small range in the axial direction. It is interesting to observe that the mean circulation seems to be conserved in the downstream direction ($\Gamma_{mean}/DU_e \approx 0.115$) although the mean size increases. The constant mean circulation can be interpreted in terms of the flow scales. Since the quantity used for normalizing the mean circulation (DU_e) is equivalent to the jet half-width $r_{1/2}$ times the local centerline velocity U_c, this indicates that the linear growth in the length scale of the vortices is com-

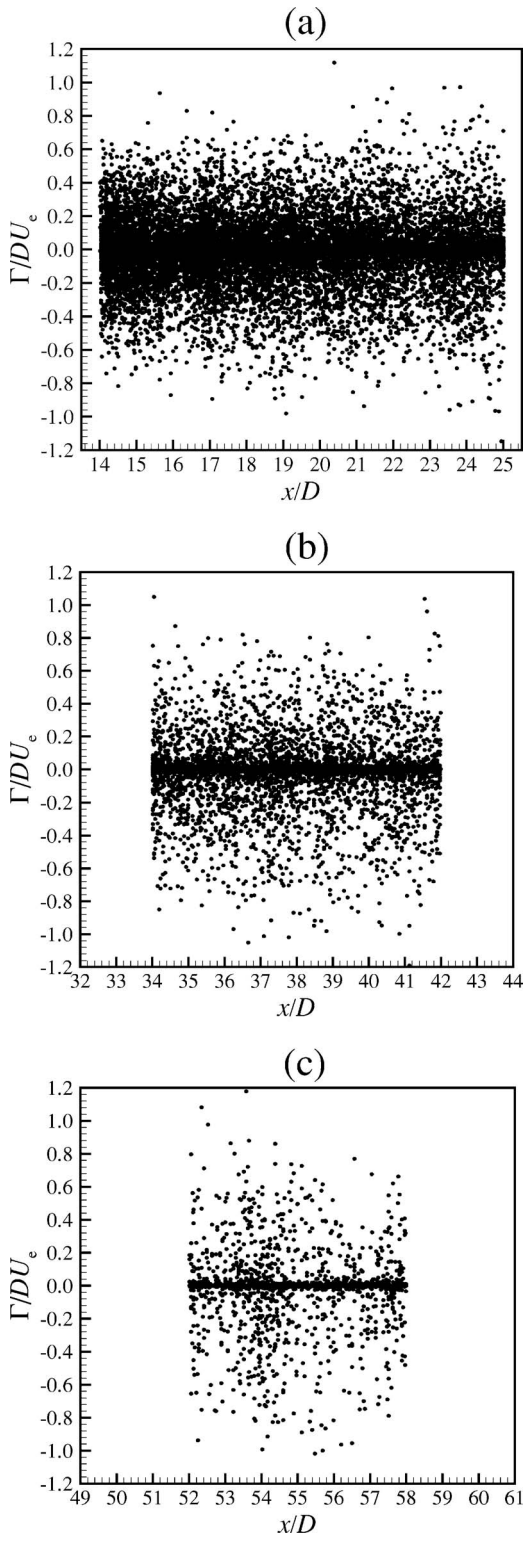

Fig. 7 ((*a*)–(*c*)) Distribution of vortex circulation Γ of the free jet in the axial direction *x* extracted from 2000 velocity fields of three adjacent FOVs. Note that positive Γ/DU_e represents positive rotational sense.

pensated by the linear decrease in their local velocity. Consistent with this interpretation, this behavior may also be explained by the balance between the pairing and tearing processes. Otherwise, the mean circulation would increase significantly if the pairing process, for example, was dominant. This phenomenon was observed in the horizontal plane of shallow water jets (parallel to a plane solid wall and free surface boundaries) because of the vertical confinement [13].

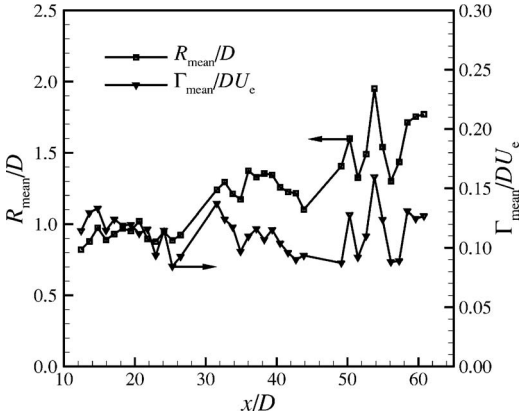

Fig. 8 Variation of the normalized mean radius *R*/*D* and circulation Γ_{mean}/DU_e of vortices in the normalized axial direction *x*/*D*

The circulation associated with vortical structures of different sizes is shown in Fig. 9. In this figure, the horizontal axis represents a normalized vortex radius R/D and the vertical axis represents the normalized circulation Γ/DU_e. Note that the sign of the vortex radius R corresponds to the rotational sense of the vortices. The purpose of this plot is to show the variation of the vortex strength with vortex size. Once again, these results should be interpreted in light of the size of vortices resolved in this study ($R/D \geq 0.2$) since the smaller vortices are not included in the calculations.

Figures similar to Fig. 9 (not shown) but at different axial locations clearly illustrate that the vortices increase in size with the downstream location although the range of vortex strengths seems to be preserved. The maximum circulation magnitude $|\Gamma/DU_e|$ in these plots reaches 1.2 although most of them are below 1.0. Generally speaking, these results indicate that larger vortices have a higher value of circulation, while smaller values of circulation are associated with smaller eddies. The relationship between the vortex circulation Γ and radius R may be modeled by

$$\left|\frac{\Gamma}{DU_e}\right| = K\left(\frac{R}{D}\right)^2 \tag{2}$$

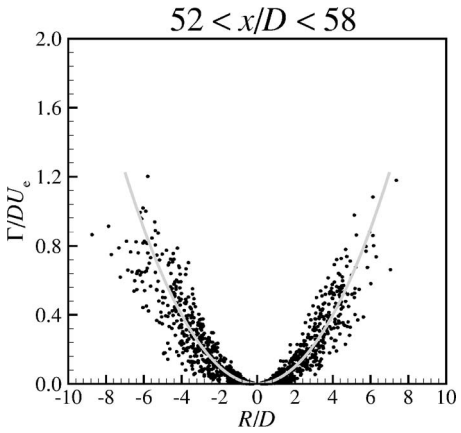

Fig. 9 Distribution of normalized circulation Γ/DU_e associated with the identified vortices of different sizes in the range $52 < x/D < 58$. The gray line represents the model values.

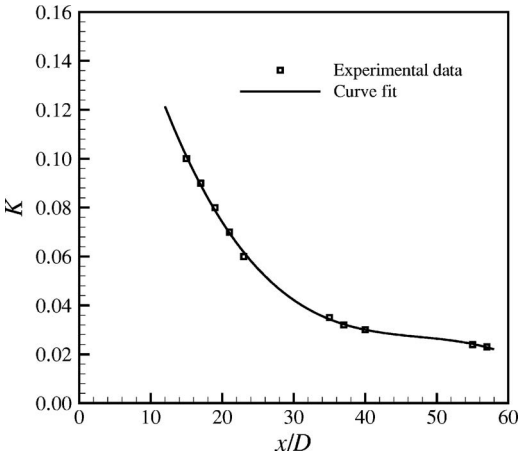

Fig. 10 Variation of the *K* value in Eq. (2) with the axial location *x/D*. Each point on this curve represents the *K* value obtained from a range of 2*D* to 3*D* in *x*.

where K represents the constant of proportionality.

In order to illustrate the dependence of K on the axial location x/D, K values were determined for $2D$ to $3D$ ranges of x from all three FOVs. The results are presented in Fig. 10 and they clearly show the decrease in K with increasing distance. Equation (3) represents a curve fit for the data in Fig. 10,

$$K = 0.242 - 1.30 \times 10^{-2}\left(\frac{x}{D}\right) + 2.68 \times 10^{-4}\left(\frac{x}{D}\right)^2 - 1.88 \times 10^{-6}\left(\frac{x}{D}\right)^3 \quad (3)$$

The relationship between Γ and R^2, which is obtained from this large number of vortices, raises an important question about the nature of the variation of the circulation Γ within the vortices. Since the tangential velocity of a vortex may be calculated by dividing Γ by πR [22], it can be concluded that the tangential velocity varies linearly with the vortex size R. This result suggests the similarity between the real vortices and the Rankine vortex, which assumes solid-body rotation within the vortex core.

7 Conclusions

PIV measurements have been made in the far field of a free round jet. The POD technique was applied to the data to expose vortical structures in the far field. The velocity fields were reconstructed using enough modes to recover 40% of the turbulent kinetic energy. The following is a summary of the statistical investigation:

1. The free jet has a large number of structures and the number of resolved structures decreases rapidly in the axial direction.
2. The population of resolved vortical structures of either rotational sense is almost identical for all radii. Moreover, small vortices are more common in all fields and the number of resolved vortices decreases as the vortex size increases. Generally, the percentage of small resolved vortices decreases slightly at downstream locations, while the percentage of larger vortices and the range of vortex size increase. This is an indication that pairing is occurring. Also, the existence of small vortices in all cases indicates the occurrence of the tearing process.
3. The resolved vortices increase in size in the downstream direction, while the range of vortex strengths is preserved. This observation is supported by the mean vortex size and circulation results. The maximum circulation magnitude $|\Gamma/DU_e|$ reaches 1.2 although most of the circulation values are below 1.0. Generally, the distribution of the resolved vortices in all cases indicates that larger vortices have a higher value of circulation, while smaller values of circulation are associated with smaller eddies.
4. The constant value of the mean circulation in the axial direction indicates that the linear growth in the length scale of the vortices is compensated by the linear decrease in their local velocity. In addition, it is an indication of a balance in the occurrence of the pairing and tearing processes. Otherwise, the dominance of one process would change the result significantly.
5. It is found that the circulation magnitude $|\Gamma/DU_e|$ is directly proportional to $(R/D)^2$ and the constant of proportionality is a function of the axial location x/D.

Acknowledgment

The support of the Natural Sciences and Engineering Research Council of Canada is gratefully acknowledged. The assistance of the Bioinformatics Research Laboratory at the University of Saskatchewan with processing the PIV images is also gratefully acknowledged.

Nomenclature

- D = jet exit diameter
- FOV = field of view
- H = water depth
- K = constant of proportionality
- N = number of vortices
- PIV = particle image velocimetry
- POD = proper orthogonal decomposition
- R = vortex radius
- Re = Reynolds number
- u_{rms} = axial turbulence intensity
- U = mean axial velocity
- U_e = jet exit velocity
- x, y = Cartesian coordinate system
- Γ = vortex circulation

References

[1] Abramovich, G. N., 1963, *The Theory of Turbulent Jets*, MIT, Cambridge.
[2] Rajaratnam, N., 1976, *Turbulent Jets*, Elsevier Scientific, Amsterdam.
[3] Tso, J., Kovasznay, L. S. G., and Hussain, A. K. M. F., 1981, "Search for Large-Scale Coherent Structures in the Nearly Self-Preserving Region of a Turbulent Axisymmetric Jet," ASME Trans. J. Fluids Eng., **103**, pp. 503–508.
[4] Tso, J., and Hussain, F., 1989, "Organized Motions in Fully Developed Turbulent Axisymmetric Jet," J. Fluid Mech., **203**, pp. 425–448.
[5] Dahm, W. J. A., and Dimotakis, P. E., 1990, "Mixing a Large Schmidt Number in the Self-Similar Far Field of Turbulent Jets," J. Fluid Mech., **217**, pp. 299–330.
[6] Agrawal, A., and Prasad, A. K., 2002, "Organizational Modes of Large-Scale Vortices in an Axisymmetric Turbulent Jet Flow," Flow, Turbul. Combust., **86**(4), pp. 359–377.
[7] Agrawal, A., and Prasad, A. K., 2002, "Properties of Vortices in the Self-Similar Turbulent Jet," Exp. Fluids, **33**(4), pp. 565–577.
[8] Holmes, P., Lumley, J. L., and Berkooz, G., 1996, *Turbulence, Coherent Structures, Dynamical Systems and Symmetry*, Cambridge University Press, New York.
[9] Adrian, R. J., Christensen, K. T., and Liu, Z.-C., 2000, "Analysis and Interpretation of Instantaneous Turbulent Velocity Fields," Exp. Fluids, **29**, pp. 275–290.
[10] Bi, W., Sugii, Y., Okamoto, K., and Madarame, H., 2003, "Time-Resolved Proper Orthogonal Decomposition of the Near-Field Flow of a Round Jet Measured by Dynamic Particle Image Velocimetry," Meas. Sci. Technol., **14**, pp. L1–L5.
[11] Barker, J. M., 1998, "Flow Structure Dynamics of an Impinging Elliptic Jet," Ph.D. thesis, Clemson University, Clemson, South Carolina.
[12] Shinneeb, A.-M., Bugg, J. D., and Balachandar, R., 2002, "PIV Measurements in a Confined Jet," *In American Society of Mechanical Engineering Fluids Engineering Division Summer Meeting*, Vol. 257(2A), pp. 87–93.
[13] Shinneeb, A.-M., 2006, "Confinement Effects in Shallow Water Jets," Ph.D. thesis, University of Saskatchewan, Canada.
[14] Hart, D., 2000, "PIV Error Correction," Exp. Fluids, **29**, pp. 13–22.
[15] Liang, D., Jiang, C., and Li, Y., 2003, "Cellular Neural Network to Detect

Spurious Vectors in PIV Data," Exp. Fluids, **34**(1), pp. 52–62.
[16] Shinneeb, A.-M., Bugg, J. D., and Balachandar, R., 2004, "Variable Threshold Outlier Identification in PIV Data," Meas. Sci. Technol., **15**, pp. 1722–1732.
[17] Stanislas, M., Okamoto, K., Kähler, C. J., and Westerweel, J., 2005, "Main Results of the Second International PIV Challenge," Exp. Fluids, **39**, pp. 170–191.
[18] Sirovich, L., 1987, "Turbulence and the Dynamics of Coherent Structures. Part I: Coherent Structures," Q. Appl. Math., **45**(3), 561–571.
[19] Robinson, S. K., 1991, "Coherent Motions in the Turbulent Boundary Layer," Annu. Rev. Fluid Mech., **23**, pp. 601–639.
[20] Ganapathhisubramani, B., Longmire, E. K., and Marusic, I., 2002, "Investigation of Three Dimensionality in the Near Field of a Round Jet Using Stereo PIV," J. Turbul., **3**, pp. 1–10.
[21] Bugg, J. D., and Rezkallah, K. S., 1998, "An Analysis of Noise in PIV Images," J. Visualization, **1**(2), pp. 217–226.
[22] Agrawal, A., and Prasad, A. K., 2003, "Measurements Within Vortex Cores in a Turbulent Jet," ASME Trans. J. Fluids Eng., **125**(3), pp. 561–568.
[23] Press, W. H., Teukolosky, S. A., Vetterling, W. T., and Flannery, B. P., 1998, *Numerical Recipes in C*, 2nd ed., Cambridge University Press, Cambridge, NY.

Destabilization of Laminar Wall Jet Flow and Relaminarization of the Turbulent Confined Jet Flow in Axially Rotating Circular Pipe

Snehamoy Majumder[1]

Dipankar Sanyal
e-mail: srg_maj@yahoo.com

Department of Mechanical Engineering,
Jadavpur University,
Kolkata 700 032, India

Destabilization and relaminarization phenomena have been investigated in an axially rotating circular duct. Standard k-ε model with modification for streamline curvature has been used in the numerical study. The laminar and turbulent velocity distributions at inlet have been observed to become turbulent and laminar, respectively, toward the exit of the pipe. A local velocity profile with parabolic or nearly uniform variation has been considered as the characteristic of laminarlike or turbulent flow, respectively, and changeover of flow from former to the later variation or vice versa has been taken to characterize destabilization and relaminarization, respectively. The predicted azimuthal velocity component was found to be reasonably accurate near the wall and not so encouraging in the core region of the swirling flow. The recirculation bubble generated by a central jet flow at the wall has been observed to reduce in size due to rotation of the pipe confirming the relaminarization phenomenon, whereas with laminar wall jet waspredicted recirculation bubble growing with rotation rate manifesting the destabilization effects.
[DOI: 10.1115/1.2813068]

Keywords: rotation, turbulent model, streamline curvature, re-laminarization, recirculation bubble

1 Introduction

The analysis of the turbulent flow through circular duct is important since it is encountered in many industrial appliances and natural phenomena. Laufer [1] carried out in detail the first experimentation on the fully developed turbulent flow in a stationary circular duct. The initial efforts [2,3] to investigate the swirling flow were on laminar flow in the presence of swirl at the inlet. Talbot [2] investigated the effect of swirl on an otherwise Poiseuille flow in a stationary circular duct. Later Kiya et al. [3] analyzed the effect of the inlet swirl in the entrance region of a stationary circular pipe and observed increment in the entrance length due to the presence of inlet swirl. Quite obviously, they have observed that the swirl decays exponentially. Kreith and Sonju [4] conducted the theoretical and experimental analyses of the decay of the turbulent swirling flow in the stationary circular pipe. Their results showed mixed success; good agreement occurred between theory and experiment in the upstream side, while disagreement was evident at the far downstream stations. Nevertheless, their work was of enormous importance since it was one of the initial attempts to bridge the gap between the theory and experimentation of the turbulent swirling flow through stationary circular pipe.

Benton [5] tried to analyze the effect of spanwise rotation on the laminar pipe flow, an attempt to estimate the effect of rotation of earth on the internal flow through ducts. Faghri et al. [6,7] are among the other contributors of the laminar flow analysis through rotating circular ducts. The numerical investigation they have conducted includes the side mass injection and heat transfer conjugate problem with different wall boundary conditions.

Majumder et al. [8] and Howard et al. [9] theoretically analyzed the turbulent flow through rotating noncircular duct. Speizale et al. [10] concluded that the special algebraic model is the most accurate turbulence model having drawbacks significantly lesser than other models for the analysis of the rotating circular duct flow. However, the standard *k-ε* model with particular modification to take care of the effect of flow swirl is much simpler.

Launder [11] and Jones and Launder [16], Patel and Head [13] were among the first to predict the possibility of laminarization of turbulent flow. Later, Narashima and Sreenivasan [14] and Sreenivasan [15] reported the relaminarization in accelerated flows. They have forecasted the possible relaminarization due to the rotation of the bounding flow geometry. Murakami and Kikuyama [16], Imao et al. [17], Reich and Beer [18], Kikuyama et al. [19], Imao et al. [20] have shown that simple rotating turbulent flow becomes laminar-like and vice-versa at the exit of the duct.

The numerical investigation of destabilization and relaminarization phenomenon in a circular duct predicted by using the modification of standard *k-ε* model for streamline curvature [21,22] forms the core of the study reported here. The wall and confined jet flows were selected for studying destabilization and relaminarization phenomenon, respectively. A low Reynolds number flow in the presence of a wall jet may be considered laminar [23–30], while a confined jet is essentially a turbulent flow due to the presence of shear layer. The increase or decrease of the size of the recirculation bubble has been captured as manifestation of the destabilization and relaminarization, respectively, with the change in rotation rate. In this connection, it is worthwhile to mention that the jet flows have been observed by several researchers [26–32]. However, neither the destabilization of wall jet nor the relaminarization of confined jet has been reported in these studies.

[1]Corresponding author.

Contributed by the Fluids Engineering Division of ASME for publication in the JOURNAL OF FLUIDS ENGINEERING. Manuscript received September 7, 2006; final manuscript received June 27, 2007; published online January 16, 2008. Review conducted by Joseph Katz.

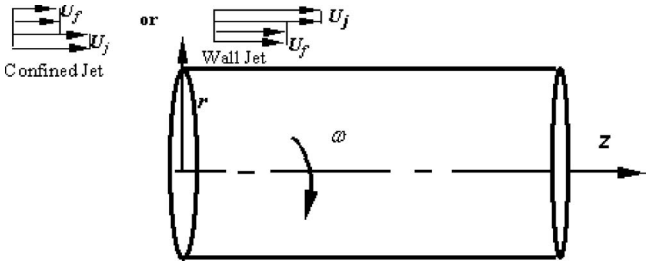

Fig. 1 Flow geometry with rotation and inlet conditions

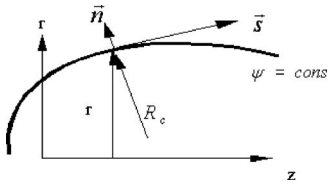

Fig. 2 Streamline coordinate system

2 Physical Description and Mathematical Model of the Flow

The problems considered here are (a) simple ducted flow with inlet swirl and rotation about the axis and (b) jet flows (both wall jet and central jet flow) with rotation about the axis.

The physical geometry in the cylindrical coordinate *r*-z and the flow conditions are shown in the Fig. 1. Here, the velocity of the flow outside the region of jet at the inlet is shown as U_f and the jet velocity is U_j and ω represents the rotational speed of the duct. The governing equations for a rotating pipe have been considered here as those of Refs. [6,7] in the Newtonian inertial reference frame. The flow conditions of Refs. [6,7] are laminar, while the present study deals with the laminar and turbulent flows, both axially rotating. This is in contrast to that of Refs. [10], where the governing equations have been written in rotating frame of coordinate, with no-slip boundary conditions incorporated for all of the components of the velocity. In the present numerical study, the equations have been presented with the pipe rotating in a stationary co-ordinate system as considered in Refs. [6,7]. Thus, the conditions of wall rotation have been specified by no-slip boundary condition for azimuthal component. The mass and momentum conservation equations in axisymmetric cylindrical coordinates for the turbulent mean flow with eddy viscosity model is given as follows:

(a) continuity equation,

$$\frac{\partial(\rho\bar{u})}{\partial z}+\frac{1}{r}\frac{\partial(\rho r\bar{v})}{\partial r}=0 \tag{1}$$

axial component (z component),

$$\rho\left[\bar{v}\frac{\partial\bar{u}}{\partial r}+\bar{u}\frac{\partial\bar{u}}{\partial z}\right]=-\frac{\partial\bar{p}}{\partial z}+\frac{\partial}{\partial z}\left(\mu_{\text{eff}}\frac{\partial\bar{u}}{\partial z}\right)+\frac{1}{r}\frac{\partial}{\partial r}\left(r\mu_{\text{eff}}\frac{\partial\bar{u}}{\partial r}\right)+\left[\frac{\partial}{\partial z}\left(\mu_{\text{eff}}\frac{\partial\bar{u}}{\partial z}\right)+\frac{1}{r}\frac{\partial}{\partial r}\left(r\mu_{\text{eff}}\frac{\partial\bar{v}}{\partial z}\right)\right] \tag{2}$$

radial component (r component),

$$\rho\left[\bar{v}\frac{\partial\bar{v}}{\partial r}+\bar{u}\frac{\partial\bar{v}}{\partial z}\right]=-\frac{\partial\bar{p}}{\partial r}+\frac{\partial}{\partial z}\left(\mu_{\text{eff}}\frac{\partial\bar{v}}{\partial z}\right)+\frac{1}{r}\frac{\partial}{\partial r}\left(r\mu_{\text{eff}}\frac{\partial\bar{v}}{\partial r}\right)+\left[\frac{\partial}{\partial z}\left(\mu_{\text{eff}}\frac{\partial\bar{u}}{\partial r}\right)+\frac{1}{r}\frac{\partial}{\partial r}\left(r\mu_{\text{eff}}\frac{\partial\bar{v}}{\partial r}\right)\right]-2\mu_{\text{eff}}\frac{\bar{v}}{r^2}+\rho\frac{\bar{w}^2}{r} \tag{3}$$

azimuthal component (θ component)

$$\rho\left[\bar{v}\frac{\partial\phi}{\partial r}+\bar{u}\frac{\partial\phi}{\partial z}\right]=\frac{\partial}{\partial z}\left(\mu_{\text{eff}}\frac{\partial\phi}{\partial z}\right)+\frac{1}{r}\frac{\partial}{\partial r}\left(r\mu_{\text{eff}}\frac{\partial\phi}{\partial r}\right)-\frac{2}{r}\frac{\partial}{\partial r}(\mu_{\text{eff}}\phi) \tag{4}$$

where $\bar{u}$, $\bar{v}$, *and* $\bar{w}$ are the mean velocity components along z, r, *and* θ directions, respectively, and the variable $\phi=r\bar{w}$. The additional Coriolis components are $2\omega\bar{w}\rho$ and $-2\omega r\bar{v}\rho$, which should be added in Eqs. (3) and (4), respectively, to get the governing equations of the noninertial reference frame [10]. However, the present authors found identical results using both inertial Refs. [6,7] and noninertial [10] reference frame implementing respective boundary conditions and opted for the form of equations of Refs. [6,7]. The effective viscosity is,

$$\text{The eddy viscosity is } \mu_{\text{eff}}=\mu_l+\mu_t \tag{5}$$

where μ_l and μ_t stand for molecular or laminar viscosity and eddy or turbulent viscosity, respectively. The eddy viscosity is given by

$$\mu_t=\rho C_\mu k^2/\varepsilon \tag{6}$$

where C_μ is given by [11]

$$C_\mu=\frac{-K_1K_2}{\left[1+8K_1^2\frac{k^2}{\varepsilon^2}(\partial U_S/\partial n+(U_S/R_C))\frac{U_S}{R_c}\right]} \tag{7}$$

Here $U_s=\sqrt{\bar{u}^2+\bar{v}^2}$, R_c=radius of curvature of the streamline concerned (ψ=const) as explained in the Fig. 2. The detail of Equation (7) is given in [11], with K_1 and K_2 equal to 0.27 and 0.3334, respectively. Also, depending on the numerator the value of C_μ may be negative, which is unwanted. Actually the correction adopted for $C\mu$ in Eq. (7) leads to significant reduction of its value around the separation streamline [21], with a corresponding recommendation to limit the lower bound. This is based on their observations regarding loosing on local equilibrium between the turbulent stresses and energy, if C_μ is very low or negative. In fact, the truncated lower value of 0.025 has been invoked only in the zone where the streamline curvature is severe in the vicinity of flow separation zone. The upper value of 0.09 is limited for the compatibility with the standard eddy viscosity. Hence, to preserve the physical realism and compatibility with the standard eddy viscosity, its value is arbitrarily kept constrained between 0.025 and 0.09. These have been found effective to provide realistic solutions in the conditions of severe streamline curvature, such as rotation of the geometry.

The k-ε equations are given by the following:

k-equation,

$$\rho\left[\bar{u}\frac{\partial k}{\partial z}+\bar{v}\frac{\partial k}{\partial r}\right]=\frac{\partial}{\partial z}\left[\left(\mu_l+\frac{\mu_t}{\sigma_k}\right)\frac{\partial k}{\partial z}\right]+\frac{1}{r}\frac{\partial}{\partial r}\left[r\left(\mu_l+\frac{\mu_t}{\sigma_k}\right)\frac{\partial k}{\partial r}\right]+\rho G-\rho\varepsilon \tag{8}$$

where G is the production term and given by

$$G=\mu_t\left[2\left\{\left(\frac{\partial\bar{v}}{\partial r}\right)^2+\left(\frac{\partial\bar{u}}{\partial z}\right)^2+\left(\frac{\bar{v}}{r}\right)^2\right\}+\left(\frac{\partial\bar{u}}{\partial r}+\frac{\partial\bar{v}}{\partial z}\right)^2+\left(\frac{\partial\bar{w}}{\partial r}-\frac{\bar{w}}{r}\right)^2+\left(\frac{\partial\bar{w}}{\partial z}\right)^2\right]$$

ε-equation,

$$\rho\left[\bar{u}\frac{\partial\varepsilon}{\partial z}+\bar{v}\frac{\partial\varepsilon}{\partial r}\right]=\frac{\partial}{\partial z}\left[\left(\mu_l+\frac{\mu_t}{\sigma_\varepsilon}\right)\frac{\partial\varepsilon}{\partial z}\right]+\frac{1}{r}\frac{\partial}{\partial r}\left[r\left(\mu_l+\frac{\mu_t}{\sigma_\varepsilon}\right)\frac{\partial\varepsilon}{\partial r}\right]+C_{\varepsilon1}G\frac{\varepsilon}{k}-C_{\varepsilon2}\frac{\varepsilon^2}{k} \tag{9}$$

Here, $C_{\varepsilon1}$, $C_{\varepsilon2}$, σ_k, and σ_ε are the empirical turbulence constants,

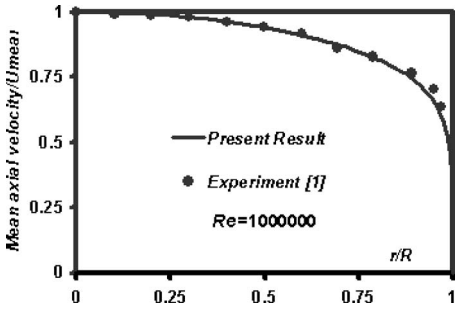

Fig. 3 Validation of the present method with the stationary pipe flow

the values of which are given in the table given below according to Ref. [22].

$c_{\varepsilon 1}$	$C_{\varepsilon 2}$	σ_k	σ_ε
1.44	1.92	1.0	1.3

The wall function of Ref. [22] has been adopted for the solution of the k-ε equations.

3 Results and Discussions

The geometry is shown in Fig. 1. The axial length and diameter of the duct are L_d=9 m and D=0.1534 m, respectively, and the fluid is assumed as air with density ρ=1.235 kg/m^3 and molecular viscosity $\mu_l=1.853\times10^{-5}$ kg/m s. The later three values along with the inlet flow velocity outside the jet region have been used to define the Reynolds number, $\mathrm{Re}=(\rho U_{\mathrm{mean}}D)/\mu_l$.

The wall function of Launder and Spalding [22] has been considered. For the simple ducted flow the inlet flow, considered is the one-seventh power law that is accepted as standard for modeling fully developed turbulent flow. The Newtonian frame of reference has been adopted as that of Refs. [6,7] for the mathematical equations and the boundary conditions are the no-slip condition for streamwise and radial velocities while a slip condition is taken for the azimuthal component of the velocity to take care of the rotation of the pipe.

The control volume formulation of Patankar [33] with SIMPLER algorithm with power-law scheme has been adopted in an axisymmetric condition while the boundary conditions adopted by Faghri et al. [6,7] have been considered for the numerical analysis as already mentioned. The present results have been matched with the benchmark results for the validation and later the test problems and results are presented. Two arrays of 251×101 and 501×201 grid points in axial and radial directions, respectively, were found to provide *total turbulent energy flux* variations at N=1.0 with maximum percentage difference of 0.001%. However, for the sake of accuracy and complexities expected at higher rotation rates, the finer grid array of 501×201 has been used for all subsequent results reported here.

3.1 Validation of the Present Results With Benchmark Solutions. Figure 3 presents the first validation exercise for the turbulent model used here using the experimental results of Laufer [1] for a turbulent flow through a stationary pipe as the basis. The exact matching of the two results qualifies the present computational scheme as applicable for stationary pipe flow analysis. In Fig. 4, the experimental results of Kreith and Sonju [4] have been compared for swirling flow in a straight stationary pipe. Good agreement between the numerical prediction and experimental results, except in the region near wall, establishes the validity of the present method for the swirling duct flow. It is understandable that the presence of inlet swirl and rotation of the duct impart similar streamline curvature. Another very important validation has been presented later in Fig. 10 in the context of flow relaminarization in a rotating duct, where the numerical predictions have been compared with the results of Ref. [18]. The close agreement observed clearly validates the numerical scheme employed here to study flow in an axially rotating duct.

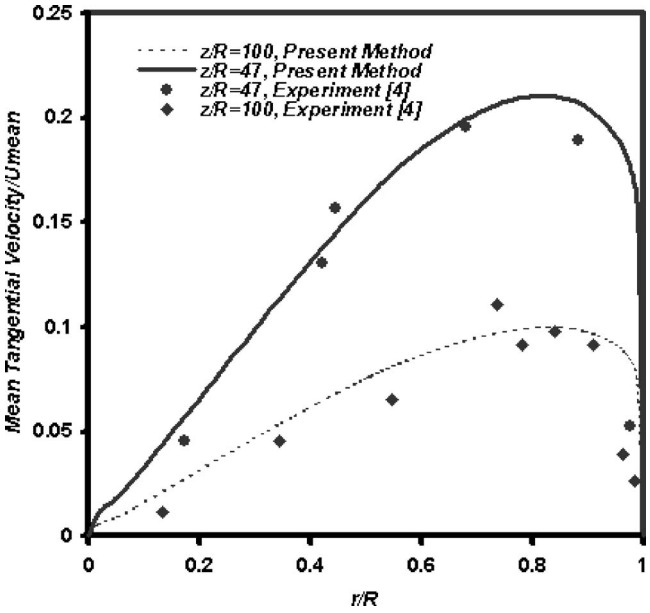

Fig. 4 Validation of the present results with swirling pipe flow (Re=48,000)

3.2 Destabilization. The rotation of a duct about its axis could have both stabilizing and destabilizing effects depending on the type of the inlet flow. Rotation of the duct imparts tangential forces to the fluid that is intense in the vicinity of the pipe wall. Such swirling flow situations are encountered in the inlet part of turbomachines, rotating heat exchangers, and cooling systems. In the case of laminar flow at the inlet, the centrifugal force due to the rotation generates instabilities leading to turbulent flow in the later portion of the duct. The higher is the rotational speed, the intense is the destabilization effects.

The streamline contour plots of Figs. 5 and 6 correspond to laminar wall jet with Re=1000, jet velocity ratio U_j/U_f=12.5, existing from the radial position r=0.06222–0.0767 m at the inlet. Two recirculations have been observed in the flow field, one near the central zone adjacent to the axis and another near to the wall. For nonrotating flow, however, only the central recirculation bubble exists in the presence of the laminar wall jet. The jet entrains flow from the surrounding, thereby creating a reverse flow at the central core region. The rotation of the duct induces destabilization to the flow due to centrifugal force, thereby generate a tortuous curving streamline pattern. With sufficiently high rotation rate an additional recirculation bubble is observed in Fig. 6 in the outer region. This flow is marked by opposite rotation with respect to the central bubble that is partially enveloped by the outer bubble. With gradual increase in rotation rate, the inner bubble first reduces in size, disintegrates thereafter forming small vortices near the axis, and finally all disappear.

During the entire regime of increasing rotation, the outer recirculation bubble keeps growing. This growth is maintained by the increasing supply of energy from wall rotation. Usually wall jet flow is dominated by small scales, which are viscous in nature. The gradual increase in the wall rotation results in an increase in the length scales, which are less viscous in nature. The increase in the recirculation bubbles with gradual increase in the rotation rate is associated with the increase in length scales. Gradually the flow becomes more and more turbulentlike. The above phenomenon is

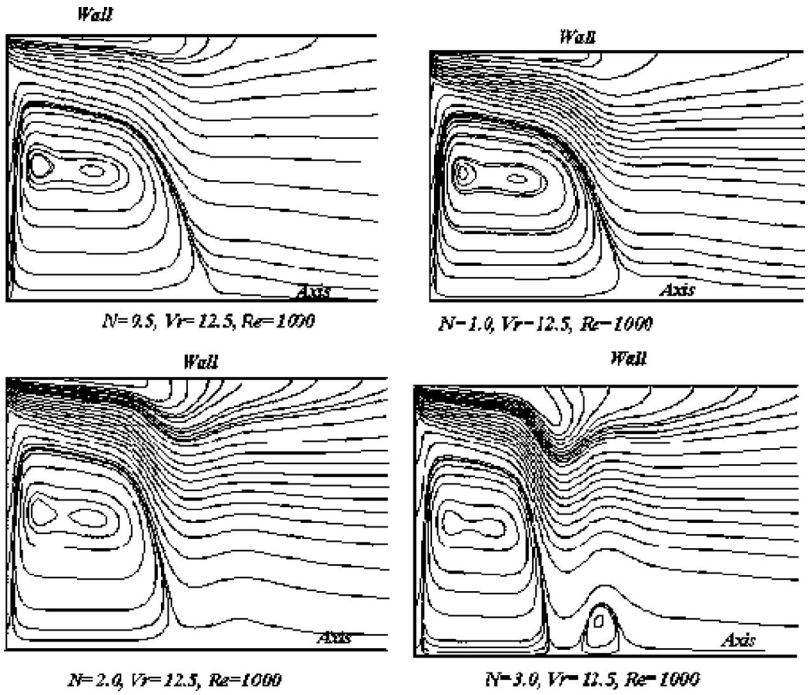

Fig. 5 Destabilization of the laminar wall jet flow due to rotation

described in terms of the variation of bubble sizes L and W shown in Fig. 7 that is normalized by duct radius and plotted against rotation rate in Figs. 8 and 9.

3.3 Relaminarization. Several researchers have reported the relaminarization phenomenon for different flow conditions, particularly in accelerated boundary layer and in axially rotating duct with fully developed turbulent flow at the inlet. There are basically three types of physical mechanism [15], which are responsible separately or in some combination responsible for relaminarization phenomenon. The first mechanism is excited by external body force such as buoyancy that either destroys or absorbs the turbulent energy. The second mechanism becomes significant, when molecular parameterlike viscosity dissipates the turbulent stresses. In the third mechanism, the boundary layer relaminarizes in the presence of a strong acceleration or rotation. In these cases, a new inner viscous dominated layer develops in which the turbulence inherited from initial conditions decays gradually. For the

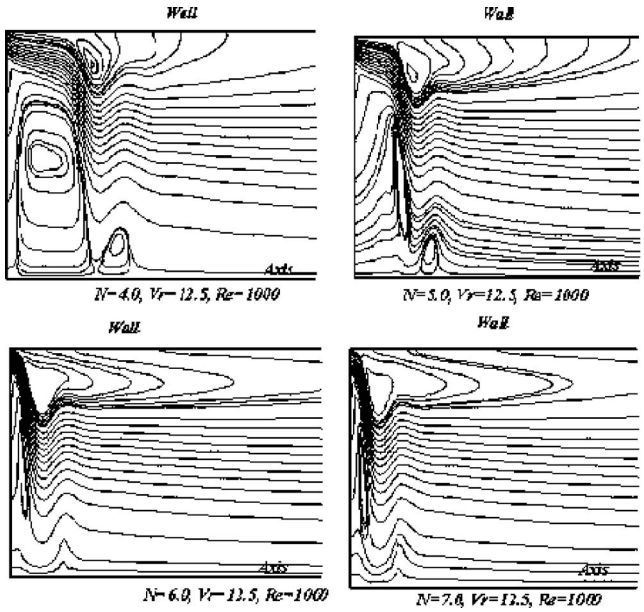

Fig. 6 Destabilization of the laminar wall jet flow due to rotation

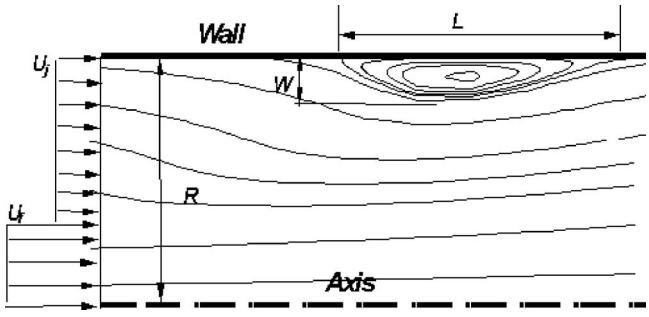

Fig. 7 Nomenclature of the wall recirculation of a jet flow

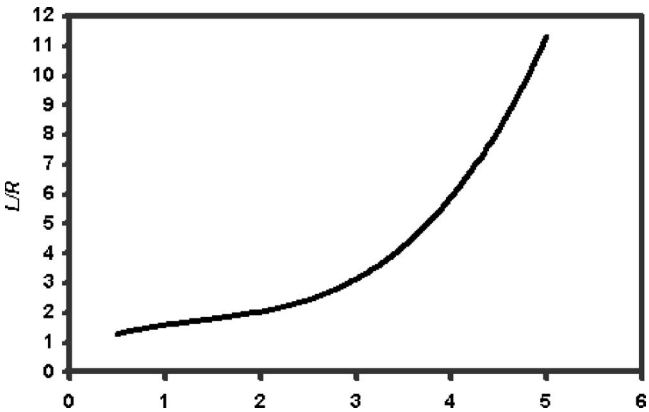

Fig. 8 Increase of recirculation length of the laminar wall jet due to rotation

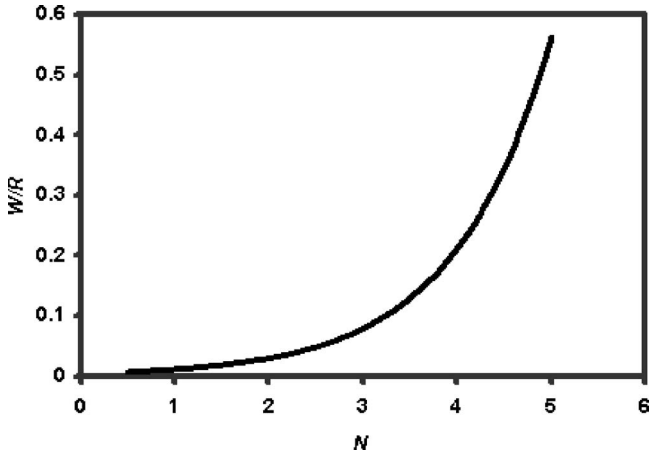

Fig. 9 Increase of recirculation breadth of the laminar wall jet due to rotation

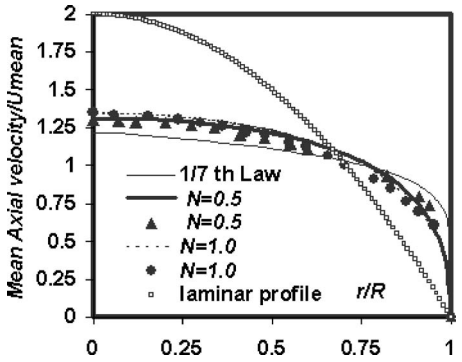

Fig. 10 Relaminarization of the pipe flow (compared with Ref. [18], Re=20,000)

case of rotating duct, the centrifugal force generated reduces the fluctuations and acts as a relaminarization agent transforming the initial turbulent flow to a laminarlike flow gradually. This is in contrast to the destabilization process where the centrifugal force due to rotation enhances the generation of the large scales transforming the laminarlike flow to the turbulentlike one.

The present work represents the relaminarization of a turbulent flow in an axially rotating circular duct with fully developed initial turbulent flow at the inlet and in an axially rotating circular duct confining a jet flowing in the vicinity of the axis, the later being shown in the Fig. 1.

In Fig. 10 the result corresponding to the inlet velocity profile that can be described by the (1/7)th power law characterizing a fully developed turbulent flow is presented. However, with increasing rotation rate N the exit ($L/D=120$), velocity profile is seen to deviate gradually away from the power-law profile and approach a laminarlike configuration, since a fully laminar flow is characterized by a parabolic distribution with axial velocity at the axis equal to twice the average velocity.

Results in Fig. 11 corresponding to Re=40,223 and rotating duct indicate a decrease of recirculation bubble size with increase in rotation rate. This indicates that the flow is transforming from the turbulent state to laminarlike state, since turbulent and fully laminarized flows are marked, respectively, by the presence and absence of recirculation bubble or vortex. This is also clear from Fig. 12, which predicts that with increase in rotation rate, the recirculation bubble decreases in volume. At $N=3$ it is imperceptible in Fig. 12, whereas very precise calculations in Fig. 11 tends to indicate a higher value of rotation rate. Indeed, Imao et al. [20] and Imao [34] has experimentally demonstrated that in the case of axially rotating circular pipe of identical dimension used in this numerical study, the rotation rate value of 3 is critical above and below which, respectively, relaminarization and destabilization take place. The notable difference in the earlier experimental studies was their use of fully developed velocity profile at the inlet as opposed to the use of inlet jet-flow structure in the numerical results of Fig. 12.

Figures 13 and 14 show the predicted variation of shear stress at $z/R=236$ for Re=40,223. As the rotation rate increases, the turbulent shear stresses decreases gradually, indicating the suppression of turbulence intensity and promotion of laminarlike flow. In Fig. 15, similar changes in the structure parameter, which is ratio of shear stress to the twice of turbulent kinetic energy, have been shown. Naturally the variation is like the shear stress in the plane parallel to the pipe axis, only differing in scale.

The decrease of turbulent shear stress $\overline{u'v'}$ in radial direction outside the core region and near the axis, as seen in Figs. 13 and 15, is consistent with earlier observations with wall swirl and fully developed turbulent flow at inlet [17]. In fact, like the present prediction, Kitoh [35] observed the shear stress to become nega-

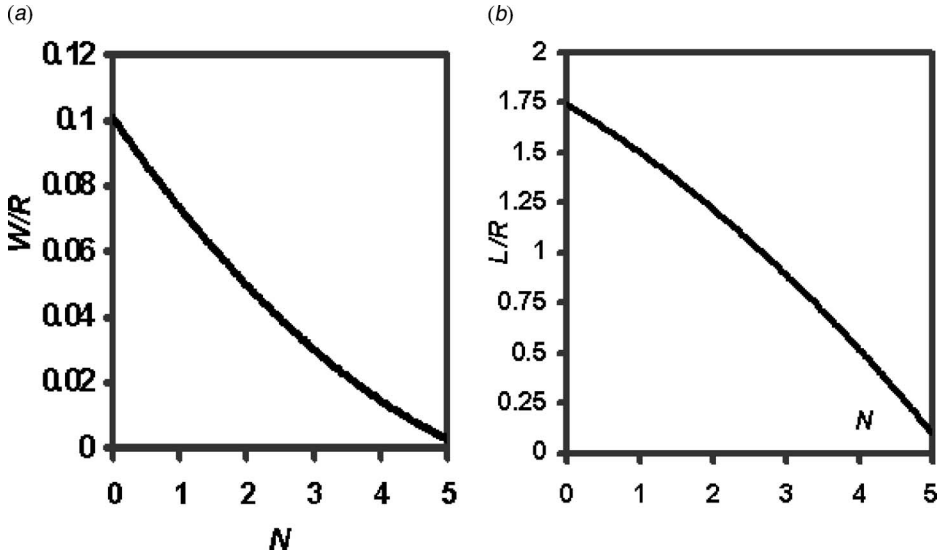

Fig. 11 Effect of rotation rate on recirculation (*a*) width and (*b*) length

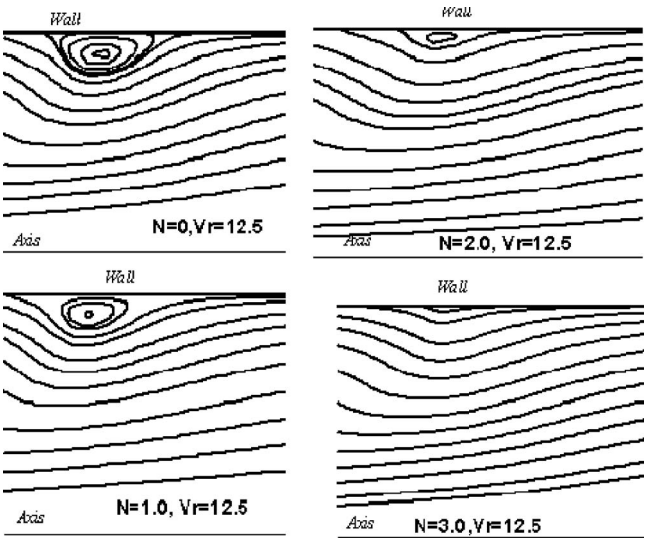

Fig. 12 Decrement of recirculation size with increase in rotation rate at Re=40,223

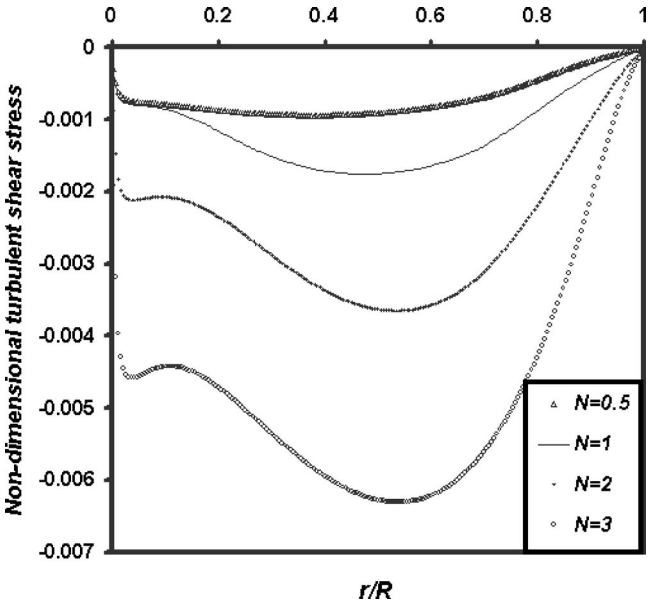

Fig. 14 Radial distribution of turbulent shear stress $(\overline{u'w'}/U^2_{mean})$

tive near the wall in the presence of its rotation. However, the notable feature of the present prediction pertaining to confined jet is that of negative shear stress near the wall region even in the absence of wall rotation.

It can be seen from Fig. 12 that in the absence of wall rotation and inlet confined jet, there is a prominent recirculation bubble on the wall inside the duct. As the bulk flow crosses the bubble, it turns radially outward making the flow accelerate in the axial direction. Thus, the radial variation of axial velocity approaches the no-slip condition on the wall with a maximum not far away from the wall. The region of turbulent shear stress in Figs. 13 and 15 correspond to this region near the wall where the radial gradient of axial velocity is positive so that a positive $\overline{v'}$ indicating a flow in the mean approaching the wall moves from a region of higher to lower axial velocity that makes the $\overline{u'}$ negative. The region between the maximum velocity location toward the wall and the wall is so thin that this region with positive cross correlation usual for duct flow could not be discerned in Figs. 13 and 15.

In fact, in Fig. 15 that uses the normalization by the total turbulent intensity that is much lower than the mean square average axial velocity used for normalization in Fig. 13, only the trend of diminishing negative value toward the wall is visible. In fact, increased wall rotation rate induces increased radially outward motion of the bulk flow during its passage through the duct. This in turn increases the negative peak in the cross-correlation term near the duct wall, as evidenced by Figs. 13 and 15.

Figures 16 and 17 correspond to variations predicted at $z/R=236$ for Re=40,223 and inlet confined jet flow. Figure 16 depicts

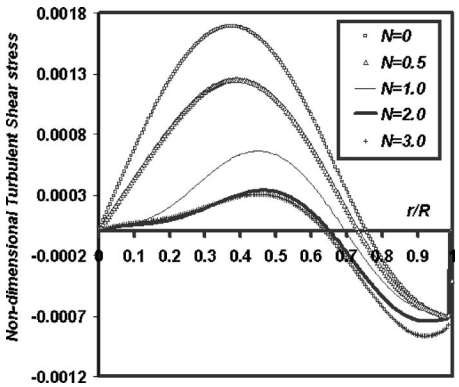

Fig. 13 Radial distribution of turbulent shear stress $(\overline{u'v'}/U^2_{mean})$

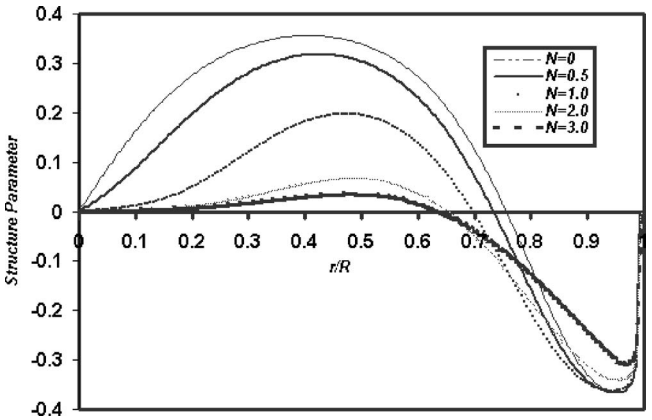

Fig. 15 Radial distribution of structure parameter $(\overline{u'v'}/q^2)$

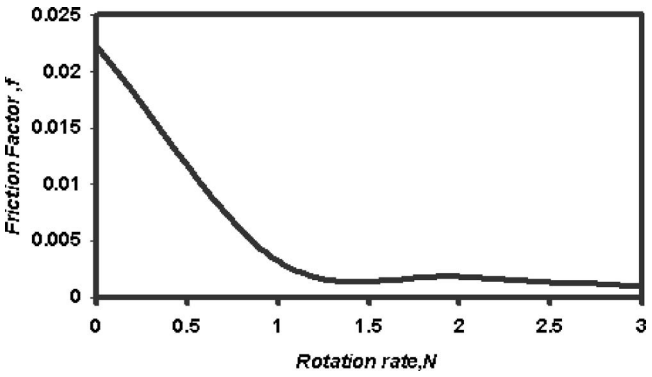

Fig. 16 Variation of friction factor with rotational rate

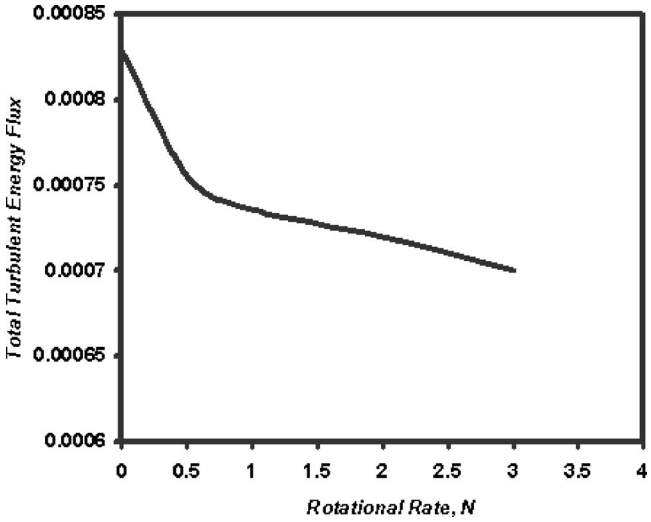

Fig. 17 Variation of total turbulent energy flux with rotational rate

the numerical prediction of friction factor to decrease gradually with rotation rate. The friction factor has been computed [36] using

$$f = \left[\int_0^L \int_0^{2\pi} \left(-\mu \frac{\partial \bar{u}}{\partial r} \right)_{r=R} R d\theta dz \right] \Bigg/ \left[(2\pi RL) \left(\frac{1}{2} \rho U_m^2 \right) \right]$$

The observed decrease in friction factor with increase in N is another evidence of flow relaminarization.

The nondimensional total energy flux T_e is given by

$$T_e = \int_0^R \frac{0.5\rho q^2 \bar{u} 2\pi r dr}{\rho U_{\text{mean}}^3 \pi R^2}$$

The variation of nondimensional total energy flux for turbulent flow is shown in Fig. 17 against rotation rate. The flux is seen to decrease gradually with increase in rotation rate. It means the rate of turbulent energy transport reduces considerably with increase in rotation. The rate of the decrement is rapid up to $N=0.5$ and slow thereafter. Imao et al. [17] observed similar tendency in their experiment in the downstream direction of a duct with fully developed turbulent flow at the inlet. At very high rotation rate, the friction factor and the total turbulent energy flux are expected to have opposite impact on destabilizing, and the domination of a particular mechanism should govern the outcome [37].

4 Conclusion

The rotation of the circular tube manifests destabilization or laminarization effect at the downstream depending upon the type of flow at the inlet. The flow with wall jet transfers to turbulent-like while the confined jet gradually changes to laminarlike as the rotation rate increases. There has been considerable decrement in the turbulent shear stress and structure parameters with the increase of rotation rate, indicating substantial suppression of turbulence intensity due to the stabilizing effects of the centrifugal force. The total turbulent energy and friction factor decrease gradually with the rise in rotation rate indicating occurrence of relaminarization phenomenon.

Nomenclature

B = breadth of the recirculation bubble, m
D = diameter of the duct, m
f = friction factor
K_1 = constant
K_2 = constant
k = turbulent kinetic energy
L = length of the recirculation bubble, m
L_d = length of the duct, m
N = rotation rate $= W_m / U_{\text{mean}}$
$\mathbf{n}$ = unit normal vector
$q^2/2$ = kinetic energy of turbulent fluctuations, $\overline{u'^2} + \overline{v'^2} + \overline{w'^2}/2$
r = radial coordinate across the duct
R = maximum radius of the duct, m
Re = reynolds number
$\mathbf{s}$ = unit tangential vector
T_e = nondimensional total turbulent energy flux
U_{mean} = mean axial velocity, m
U_j = jet velocity as shown in Fig. 1, m/s
U_f = fluid velocity as shown in Fig. 1, m/s
V_r = velocity ratio $= U_j / U_f$
W_m = maximum tangential velocity, m/s
$\bar{u}$ = time mean velocity along z axis, m/s
$\bar{v}$ = time mean velocity along r direction, m/s
$\bar{w}$ = time mean velocity along θ direction, m/s
u', v', w' = fluctuating velocity components in z, r, and θ coordinates
z = axial coordinate along the duct
θ = tangential coordinate along the duct periphery
ε = turbulent dissipation rate
ρ = density of air, kg/m^3
μ = viscosity of the air, kg/m s
ψ = stream function, m^2/s

References

[1] Laufer, J., 1954, "The Structure of Turbulence in Fully-Developed Pipe Flow," NACA Report No. 1174.
[2] Talbot, L., 1954, "Laminar Swirling Pipe Flow," ASME J. Appl. Mech., pp. 1–7.
[3] Kiya, M., Fukusako, S., and Arie, M., 1971, "Laminar Swirling Flow in the Entrance Region of a Circular Pipe," JSME, **14**(73), pp. 659–670.
[4] Kreith, F., and Sonju, O. K., 1965, "The Decay of a Turbulent Swirl in a Pipe," J. Fluid Mech., **22**, pp. 257–271.
[5] Benton, G. S., 1956, "The Effect of the Earth's Rotation on Laminar Flow in Pipes," ASME J. Appl. Mech., **23**, pp. 123–127.
[6] Faghri, A., Gogineni, S., and Thomas, S., 1993, "Vapor Flow Analysis of an Axially Rotating Heat Pipe," Int. J. Heat Mass Transfer, **36**(9), pp. 2293–2303.
[7] Faghri, A., Gogineni, S., and Cao, Y., 1995, "Fluid Flow Analysis in an Axially Rotating Porous Pipe With Mass Injection at the Wall," Numer. Heat Transfer, Part A, **28**, pp. 723–737.
[8] Majumder, A. K., Pratap, V. S., and Spalding, D. B., 1977, "Numerical Computation of Flow in Rotating Ducts," ASME Trans. J. Fluids Eng., **99**, pp. 148–153.
[9] Howard, J. H., Patankar, S. V., and Bordynuik, R. M., 1980, "Flow Prediction in Rotating Ducts Using Coriolis Modified Turbulence Models," ASME Trans. J. Fluids Eng., **102**, pp. 456–461.
[10] Speizale, C. G., Younis, B. A., and Berger, S. A., 2000, "Analysis and Modeling of Turbulent Flow in an Axially Rotating Pipe," J. Fluid Mech., **407**, pp. 1–26.
[11] Launder, B. E., 1964, "Laminarisation of the Turbulent Boundary Layer by Acceleration," MIT Gas Turbines Laboratory Report No. 77.
[12] Jones, W. P., and Launder, B. E., 1972, "The Prediction of Laminarization With a Two-Equation Model of Turbulence," Int. J. Heat Mass Transfer, **15**, pp. 301–314.
[13] Patel, V. C., and Head, M. R., 1968, "Reversion of Turbulent to Laminar Flow," Aero. Res. Counc. **29 859-F.M.** pp. 3929.
[14] Narashima, R., and Sreenivasan, K. R., 1973, "Re-Laminarization in Highly Accelerated Turbulent Boundary Layers," J. Fluid Mech., **61**, pp. 417–447.
[15] Sreenivasan, K. R., 1982, "Laminarescent, Relaminarizing and Retransitional Flows," Acta Mech., **44**, pp. 1–48.
[16] Murakami, M., and Kikuyama, K., 1980, "Turbulent Flow in Axially Rotating Pipes," ASME Trans. J. Fluids Eng., **102**, pp. 97–103.
[17] Imao, S., Itoh, M., and Harada, T., 1996, "Turbulent Characteristics of the Flow in an Axially Rotating Pipe," Int. J. Heat Fluid Flow, **17**(5), pp. 444–451.
[18] Reich, G., and Beer, H., 1989, "Fluid Flow and Heat Transfer in an Axially Rotating Pipe—I. Effect of Rotation on Turbulent Pipe Flow," Int. J. Heat Mass Transfer, **32**(3), pp. 551–562.
[19] Kikuyama, K., Murakami, M., Nishibori, K., and Maeda, K., 1983, "Flow in an Axially Rotating Pipe," JSME, **26**(214), pp. 506–513.
[20] Imao, S., Zhang, Q., and Yamada, Y., 1989, "The Laminar Flow in the Devel-

oping Region of a Rotating Pipe," JSME Int. J., Ser. II, **32**(3), pp. 317–323.
[21] Leschziner, M. A., and Rodi, W., 1981, "Calculation of Annular and Twin Parallel Jets Using Various Discretization Schemes and Turbulence-Model Variations," ASME Trans. J. Fluids Eng., **103**, pp. 352–360.
[22] Launder, B. E., and Spalding, D. B., 1974, "The Numerical Computation of Turbulent Flows," Comput. Methods Appl. Mech. Eng., **3**, pp. 269–289.
[23] Tumin, A., 1998, "Subharmonic Resonance in a Laminar Wall Jet," Phys. Fluids, 10(7).
[24] Riley, N., 1958, "Effects of Compressibility on a Laminar Wall Jet," J. Fluid Mech., **4**, pp. 615–628.
[25] Das, M. K., and Badjatiya, S., 2002, "Conjugate Heat Transfer Study of Plane Laminar Wall Jet Flow," *12th International Comference*, Grenoble, France, Aug. Vol. 2, p. 315.
[26] Badjatiya, S., and Das, M. K., 2003, "Comparison of Heat Transfer Coefficient Correlation for Laminar Plane Wall Jet," *Sixth ASME JSME Thermal Engineering Joint Conference*, Mar. 16–20, HI.
[27] Kanna, P. R., and Das, M. K., 2004, "Conjugate Forced Convection Heat Transfer From a Laminar Plane Wall Jet Flow," presented in *17th National Heat & Mass Transfer Conference; Sixth ISHMT—ASME Heat & Mass Transfer Conference*, Kalpakkam, India, Jan. 5–7.
[28] Bajura, R. A., and Szewezyk, A. A., 1970, "Experimental Investigation of a Two-Dimensional Plane Wall-Jet," Phys. Fluids, **13**, pp. 1653–1664.
[29] Mele, P., Morganti, M., Scibilia, M. F., and Lasek, A., 1986, "Behaviour of Wall Jet in Laminar-to-Turbulent Transition," AIAA J., **24**, pp. 938–939.
[30] Likachev, O., and Tumin, A., 1996, "Stability of a Compressible Laminar Wall Jet With Heat Transfer," ASME Trans. J. Fluids Eng., **118**, pp. 824–828.
[31] Elghobashi, E. E., Pun, W. N., and Spalding, D. B., 1977, "Concentration Fluctuation in Isothermal Turbulent Confined Coaxial Jets," Chem. Eng. Sci., **32**, pp. 161–166.
[32] Quintana, D. L., Amitay, M., Ortega, A., and Wygnanski, I. J., 1997, "Heat Transfer in the Forced Laminar Wall Jet," J. Heat Transfer, **119**, pp. 451–459.
[33] Patankar, S. V., 1981, *Numerical Heat Transfer and Fluid Flow*, McGraw-Hill, New York.
[34] Imao, S., 1981, "Retransition Phenomenon of the Flow in an Axially Rotating Pipe," Bull. Nagoya Inst. Tech., **33**, pp. 153–159, in Japanese.
[35] Kitoh, O., 1991, "Experimental Study of Turbulent Swirling Flow in a Straight Pipe," J. Fluid Mech., **225**, pp. 445–479.
[36] Bird, R. B., Stewart, W. E., and Lightfoot, N. L., 1960, *Transport Phenomena*, Wiley, New York.
[37] Hirai, S., Tagaki, T., and Matsumoto, M., 1988, "Predictions of the Laminarisation Phenomenon in an Axially Rotating Pipe Flow," ASME Trans. J. Fluids Eng., **110**, pp. 424–430.

PIV Study of Turbulent Flow in Asymmetric Converging and Diverging Channels

M. K. Shah

M. F. Tachie
e-mail: tachiemf@cc.umanitoba.ca

Department of Mechanical and Manufacturing Engineering,
University of Manitoba,
Winnipeg MB, R3T 5V6, Canada

An experimental investigation of turbulent flow subjected to variable adverse and favorable pressure gradients in two-dimensional asymmetric channels is reported. The floors of the diverging and converging channels were flat while the roofs of the channels were curved. Adverse pressure gradient flows at $Re_h=27{,}050$ and 12,450 and favorable pressure gradient flow at $Re_h=19{,}280$ were studied. A particle image velocimetry was used to conduct detailed measurements at several planes upstream, within the variable section and within the downstream sections. The boundary layer parameters were obtained in the upper and lower boundary layers to study the effects of pressure gradients on the development of the mean flow on the floor and roof of the channels. The profiles of the mean velocities, turbulence intensities, Reynolds shear stress, mixing length, eddy viscosity, and turbulence production were also obtained to document the salient features of pressure gradient turbulent flows in asymmetric converging and diverging channels.
[DOI: 10.1115/1.2829590]

1 Introduction

Turbulent flows with pressure gradient are often encountered in engineering designs. A considerable amount of research has been dedicated to such flows since the early works of Dönch [1] and Nikuradse [2] in diverging and converging channel flows. The motivation for studying these flows is their application and significant impact on the performance of engineering designs. In real flow situations, an adverse pressure gradient (APG) exists in draft tubes of hydroelectric power plants, near the trailing edges of airfoils or at the termination of the streamlined bodies such as submarines or ships, and often plays a critical role in the performance of these devices. Favorable pressure gradients (FPGs) are of great interest to researchers as well. FPG is also encountered widely in engineering, for example, at the leading edge of the high lift systems. The flow in wind tunnel contractions and turbine cascades are among some of the applications of the turbulent boundary layers in a FPG.

Pressure gradients greatly affect the structure of the turbulent boundary layers. Decelerating flows subjected to an APG thicken the boundary layer and complicate the flow characteristics whereas accelerating flows stabilize the boundary layer (Kim et al. [3]). APG occurs when the static pressure increases in the direction of the flow, i.e., in the case where a solid surface turns away from the mean flow direction (diffuser, diverging channel, etc.). This is significant since increasing the fluid pressure is akin to increasing the potential energy of the fluid, leading to a reduced kinetic energy and a deceleration of the fluid. Since the fluid in the inner part of the boundary layer is moving slower than the outer region, it is more greatly affected by the increasing pressure gradient. For a large enough pressure increase, this fluid may slow to zero velocity or even become reversed. When flow reversal occurs, the flow is said to be separated from the surface. This may have practical consequences in aerodynamics since flow separation significantly modifies the pressure distribution along the surface and hence the lift and drag. FPG occurs whenever a solid surface turns into the mean flow direction (e.g., converging channel). The effect of FPG on drag has fueled a lot of studies in this field. In the presence of large enough FPG, laminarization occurs. FPG is associated with a decrease in both turbulence intensity and drag force.

Turbulent flows in zero pressure gradient (ZPG) as well as mild and strong APG and FPG have been studied experimentally and numerically. A summary of some selected previous experimental and numerical studies is provided in Table 1. The flow quantities reported in these studies include the streamwise mean velocity (U), turbulence intensities (u, v, and w), Reynolds shear stress ($-uv$), skewness (S), flatness (F), production (P), diffusion (Diff) and dissipation rate (ε) of the turbulent kinetic energy, eddy viscosity (ν_t), and mixing length (l_m) distributions. The complete terms in the transport equation for the turbulent kinetic energy equation (TKE) are reported in a few studies. In the experimental studies, velocity measurements were obtained using Pitot tube, hot wires, laser Doppler anemometry (LDA), and particle image velocimetry (PIV). Direct numerical simulation (DNS) was employed in the numerical work. Where available, either the acceleration parameter K, or the pressure gradient parameter β, or the gradient of pressure coefficient dc_p/dx are provided.

Recently, Ichimiya et al. [14] studied relaminarization of turbulent boundary layers under strong FPG. The pressure gradient was created by a curved plate, preceded and followed by parallel plates. The maximum value of turbulence intensity (u) decreased in the converging section and then increased in the downstream section. Blackwelder and Kovasznay [15,16] obtained detailed measurements in a converging channel with a curved lower wall. They found that the absolute values of the mean velocities and stresses were approximately constant along a mean streamline except in the immediate vicinity of the wall. However, the values of u/U_e, v/U_e, and $-uv/U_e^2$ decrease as the flow accelerates along the channel. Their results also indicate that the displacement and momentum thicknesses and the Reynolds number based on momentum thickness decrease in the region prior to lamanarization. They found that the log region disappeared in the region of maximum acceleration ($K=4.8\times10^6$). However, at the location of lower acceleration ($K\approx1.0\times10^6$), friction velocity obtained from the log law was within 1% of values obtained by measuring the velocity gradient in the viscous sublayer. The skin friction was observed to decrease in the converging section followed by an increase in the section downstream of convergence. Cardoso et al. [12] were among the few to study the characteristics of accelerat-

Contributed by the Fluids Engineering Division of ASME for publication in the JOURNAL OF FLUIDS ENGINEERING. Manuscript received September 11, 2006; final manuscript received September 20, 2007; published online January 18, 2008. Review conducted by Hamid Johari.

ing turbulent flow in an open channel. In their study, the bottom wall of the open channel was tilted at various angles ($\alpha=3$ deg, 5 deg, 7 deg) to produce axial FPG. They found that the mean velocity profiles become "more full" and the relative turbulence intensities decrease as flow acceleration increases.

Turbulent boundary layers subjected to mild APG created over a 4 deg ramp preceded by FPG was studied by Aubertine and Eaton [4]. The mean velocity profiles become "less full" in the diverging section. The velocity profiles exhibit a substantial log region but as the flow evolves downstream, the wake region occupies an increasing portion of the boundary layer thickness. In this flow, values of the pressure gradient parameter were in the range of $-1.40<\beta<2.31$. Their results also indicate that the displacement and momentum thicknesses and the Reynolds number based on momentum thickness increase in the diverging section. The Reynolds stresses were found to be similar in the inner layer to ZPG profiles but higher in the outer layer. Spalart and Watmuff [10] reported experimental and numerical studies of turbulent boundary layer in APG preceded by FPG. Skin friction measurements were obtained using Preston tubes. The DNS results showed that the velocity profile in the buffer and lower log layer shifts up in FPG ($\beta=-0.3$) and down in APG ($0<\beta<2$). A similar but weaker trend in the same direction is also reported for the experimental data. Samuel and Joubert [8] studied boundary layer developing in an increasingly APG. They obtained skin friction values from the log law that were in good agreement with values obtained from the Preston tubes and floating point element meter. Skåre and Krogstad [9] conducted measurements in an equilibrium boundary layer in a strong APG ($12<\beta<22$). The log law and Preston tubes were found to produce similar values of the skin friction. Due to strong APG, the Reynolds shear stress ($-\rho uv$) reaches values considerably higher than the wall shear stress (τ_w). The measurements showed that the stress ratios are similar to those measured in ZPG turbulent boundary layers, indicating that the distribution of kinetic energy between the different stresses is unaffected by the pressure gradient. Angele and Muhammad-Klingmann [6] reported PIV and LDA measurements in APG with weak separation. The mean velocity profiles demonstrated an overlap with the log law for the flow where $\beta\leqslant 4.9$. The log law region vanished near the separation bubble.

In this paper, a PIV is used to study the characteristics of turbulent flows in mild APG and FPG produced, respectively, in asymmetric diverging and converging channels. Measurements of mean velocities and turbulent quantities on the curved upper wall and flat lower wall of the channels are used to document the interaction between the lower and upper boundary layers under the influence of the variable adverse and FPG. The comprehensive data set reported in this paper will be valuable for developing and validating turbulence models for adverse and FPG turbulent flows in asymmetric channels.

2 Experimental Setup and Measurement Procedure

2.1 Test Facility. The experiments were conducted in a closed recirculation type water channel. The test section of the main channel is 2500 mm long, 200 mm wide, and 200 mm deep. A 6:1 contraction, with a symmetrical cross section, is used prior to the working section to reduce the turbulence intensity by accelerating the mean flow. The test section was fabricated using clear acrylic to facilitate optical access and flow visualization.

A variable pressure gradient channel made of 3 mm thick acrylic plates was inserted into the main channel. For the FPG, the flow encounters an asymmetric converging channel (Fig. 1(a)) while an asymmetric diverging channel (Fig. 1(b)) is used to produce the APG flow. As indicated in both figures, the first 750 mm of channel (OA) and the last 750 mm of channel (BC) have straight parallel walls. The 1000 mm section of channel (AB) located between these parallel sections diverges nonlinearly from a height of 54 mm to 84 mm for the APG case, and converges from 84 mm to 54 mm for the FPG case. The zero location for x coordinate is taken at the start of convergence/divergence (A) and $y=0$ on the lower wall. The heights of the variable channel for APG and FPG are, respectively, given by

$$2h(x) = 54 - 7.39\times 10^{-4}x + 5.73\times 10^{-5}x^2 - 3.12\times 10^{-9}x^3 - 5.09\times 10^{-11}x^4 + 2.78\times 10^{-14}x^5 \quad (1a)$$

$$2h(x) = 84 - 4.01\times 10^{-2}x + 2.09\times 10^{-5}x^2 - 7.17\times 10^{-8}x^3 + 8.83\times 10^{-11}x^4 - 2.78\times 10^{-14}x^5 \quad (1b)$$

where x is measured in millimeters and the relationship is valid between $0\leqslant x\leqslant 1000$. The converging and diverging channels described above have been employed previously by Tachie [17]. The choice of the above profiles was partly constrained by the test section of the existing main water channel and the need to obtain two-dimensional mean flow at the midplane of the converging and diverging channels. A number of curved profiles were then tried and the pressure gradient along the channel was analytically calculated assuming inviscid flow. The profiles described above (Eqs. (1a) and (1b)) were chosen because they produced pressure gradients that were not too severe to cause flow separation (in the diverging channel) or relaminarization (in the converging channel), yet high enough to noticeably modify the flow field compared with that in channel with parallel walls. In this paper, mean velocities will be denoted by upper cases (e.g., U, V) while fluctuating quantities will be denoted by lower-case letters (e.g., u, v, $-uv$ etc.).

2.2 Particle Image Velocimetry System and Measurement Procedure. In this study, the PIV technique was adopted to measure the velocity field. The flow was seeded with 5 μm polyamide seeding particles having a specific gravity of approximately 1.03. A Nd-YAG (yttrium aluminum garnet) laser (120 mJ/pulse) of 532 nm wavelength was employed to illuminate the flow field. The laser sheet was located at the midplane of the channel. A 12 bit HiSense 4M camera (2048 pixels $\times$ 2048 pixels charge-coupled device (CCD) array size and a 7.4 μm pixel pitch) was coupled to a 60 mm AF Micro Nikkor lens. The camera's field of view was maintained to be approximately 96×96 mm^2, for all measurement fields. The particle image diameter was estimated to be $d_p=15.4$ μm (2.2 pixels) which is close to a value of 2.0 pixels recommended by Raffel et al. [18] to minimize peak locking. During the image acquisition, the PIV parameters were optimized to satisfy the condition that the maximum particle displacement is less than one-quarter of interrogation area (IA). The digital images were postprocessed by the adaptive-correlation option of the commercial software developed by Dantec Dynamics (Flow Manager 4.50.17). Following a convergence test, it was decided to use 2000 instantaneous images for the computation of the mean velocity and turbulent statistics reported subsequently.

A 42 mm wide trip made of four 6 mm wide rectangular bars, 6 mm apart, were used at the upper and lower walls of the channel entrance to ensure a rapid development of the turbulent boundary layer. For each test condition (Test D1, Test D2, and Test C), measurements were obtained at five x-y planes: upstream of the convergence/divergence (denoted as P1), three planes within the converging/diverging section (P2, P3, and P4) and a plane downstream of convergence/divergence (P5). The data set extracted from P1 is referred to as L1, from P2 as L2, and so on (see Fig. 1(c)). The section before convergence/divergence will be referred to as the upstream section, the converging/diverging section will also be referred to as the variable section, and the remaining of the channel will be referred to as the downstream section.

Measurements were made in APG at Reynolds number based on the upstream half channel height h (at $x<0$) and approach velocity, $\mathrm{Re}_h=27,050$ and 12,450, which are denoted as Test D1 and Test D2, respectively. Measurements were also obtained in the FPG at $\mathrm{Re}_h=19,280$ and is denoted as Test C. The complete test

Table 1 Summary of relevant studies

Authors	Flow	Technique	Quantities	K or β or dc_p/dx
Abertine and Eaton [4,5]	APG, FPG	LDA, FISF	U, u, v, P, TKE	$-1.4<\beta<2.31$
Angele, Muhammad-Klingmann [6][a]	APG	PIV, LDA	U, C_f, u, v, uv	$0.1<dc_p/dx<0.7$
Ruetenik and Corrison [7]	APG	Hot wire	U, u, v, w, uv	
Samuel and Joubert [8][a]	APG	Hot wire, Pitot tube	U, u, v, w, uv	$0.06<dc_p/dx<0.3$
Skåre and Krogstad [9][a]	APG	Hot wire, Pitot tube	U, u, v, w, uv, l_m, P, Diff, ε	$12<\beta<21.4$
Spalart and Watmuff [10][a]	APG, FPG	Hot wire, DNS, Preston tube	U, u, v, w, C_f, ε	$-0.30<\beta<2$
Kline et al. [11][a]	ZPG, FPG, APG	Hot wire,	U, others	$0.21<K\times10^6<3.85$ $-2<K\times10^6<-0.25$
Cardoso et al. [12]	FPG	Hot wire	U, C_f, u	$-3.73<\beta<-0.35$
Finnicum and Hanratty [13]	FPG	DNS	U, C_f, u, v, w, uv, TKE, P	$K\times10^6=2.8$, 2.03
Ichimiya et al. [14][a]	FPG	Hot wire	U, u, S, F	$0<K\times10^6<1$
Blackwelder and Kovasznay [15][a]	FPG	Hot wire	U, u, v, uv	$0<K\times10^6<4.8$

[a]Curved wall used to create the pressure gradient.

conditions, various streamwise locations for which detailed data sets will be presented, and the pertinent boundary layer parameters are summarized in Table 2. For a given test condition (Test D1, Test D2, and Test C), at each location (L1, L2, L3, L4, and L5), x is the corresponding streamwise distance from the beginning of the variable section, U_e is the local maximum velocity, $y_{\max}$ is the wall normal distance from the lower wall to the location of maximum streamwise velocity U_e, Re_θ is the Reynolds number based on local maximum streamwise velocity U_e and momentum thickness θ, and U_τ is the friction velocity obtained from the Clauser technique. Because of the asymmetric nature of the channels, the boundary layer on the upper wall develops at a different rate compared to the boundary layer on the lower wall. Therefore, both the upper and lower wall parameters are reported. The term "lower boundary layer" is used to describe the profile formed on the lower wall up to the $y_{\max}$ location, while the "upper boundary layer" is from the upper wall to the $y_{\max}$ location. Subscripts U and L are used, respectively, for a parameter obtained from the upper and lower boundary layers. The values of friction velocity and its validity are discussed in Sec. 3.3.

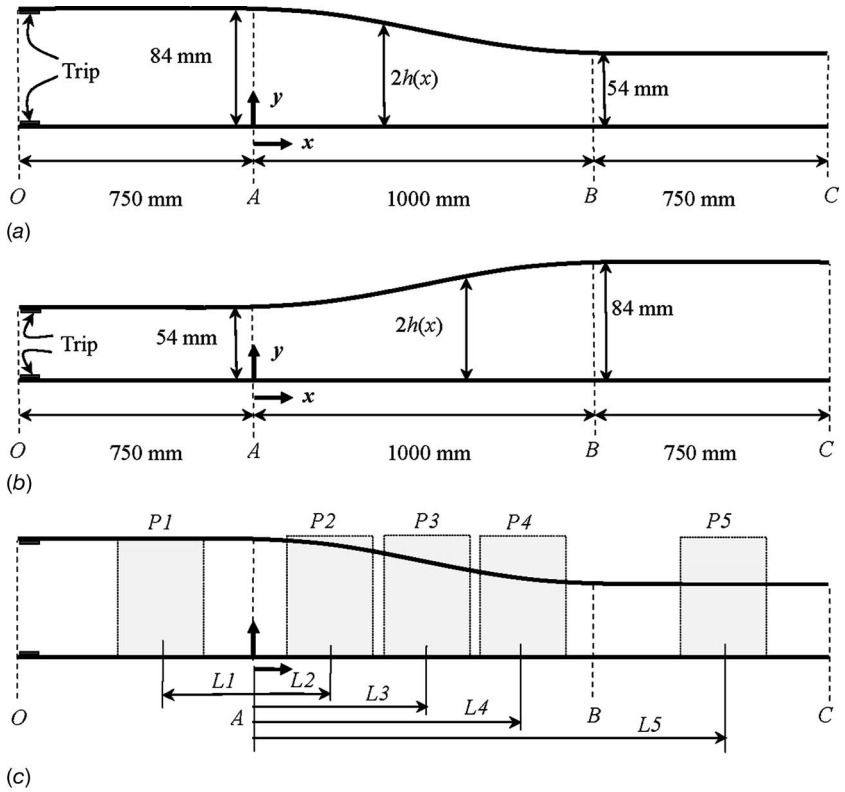

Fig. 1 Experimental setup: (*a*) converging channel, (*b*) diverging channel, and (*c*) P1 to P5 denoted *x-y* planes in which PIV measurements were made. L1 to L5 correspond to locations where detailed data analysis was performed.

Table 2 Summary of test conditions and pertinent boundary layer parameters

Test	Location	x (mm)	U_e (m/s)	$y_{max}/2h$	$Re_{\theta,L}$	$Re_{\theta,U}$	$U_{\tau,L}$	$U_{\tau,U}$
D1	L1	−85	1.002	0.46	1150	1070	0.0480	0.0495
Re_h=27,050	L2	310	0.950	0.58	2270	1360	0.0415	0.0448
	L3	580	0.843	0.65	3930	1930	0.0329	0.0370
	L4	840	0.738	0.60	4150	2100	0.0283	0.0330
	L5	1190	0.735	0.65	4170	1780	0.0300	0.0343
D2	L1	−39	0.461	0.45	550	740	0.0242	0.0235
Re_h=12,450	L2	324	0.427	0.51	960	850	0.0207	0.0211
	L3	585	0.389	0.59	1540	1040	0.0175	0.0185
	L4	845	0.308	0.69	2080	670	0.0127	0.0156
	L5	1228	0.300	0.67	1840	560	0.0132	0.0158
C	L1	−98	0.459	0.40	750	1630	0.0238	0.0218
Re_h=19,280	L2	205	0.476	0.47	720	990	0.0252	0.0242
	L3	526	0.630	0.64	680	640	0.0323	0.0328
	L4	738	0.694	0.49	700	720	0.0352	0.0358
	L5	1342	0.731	0.48	1150	1380	0.0347	0.0344

Previous experiments showed that a relatively low spatial resolution can underestimate the true values of the turbulent quantities in the wall region (Piirto et al. [19]). The PIV images were processed using two IAs, 32 pixels × 32 pixels with 50% overlap (Δx=0.750 mm × Δy=0.750 mm) and 32 pixels × 16 pixels with 50% overlap (Δx=0.750 mm × Δy=0.375 mm) to evaluate any effects of spatial resolution on the flow statistics. Based on maximum friction velocity for a given test, Δy^+_{max}=18.6, 9.1, and 13.2, respectively, for Test D1, Test D2, and Test C. This resolution is better than in many previous PIV studies. For example, a recent PIV study of APG by Angele and Muhammad-Klingmann [6] reported spatial resolution of 2.2 × 2.2 mm^2 corresponding to Δy^+ =149. Figure 2 shows profiles of the mean velocity and turbulent quantities obtained using the two IAs at L1 of Test D2. It is evident that the profiles of the mean velocity, turbulence intensities, and Reynolds shear stress obtained from the two IAs are nearly indistinguishable. This implies that both IAs provide spatial resolutions that are adequate for these quantities. The data presented subsequently are those obtained from the IA of 32 pixels × 16 pixels with 50% overlap. Saikrishnan et al. [20] studied the effects of spatial resolution on turbulence intensity and Reynolds shear stress by comparing measurements obtained from various PIV IA sides with DNS results. They found that the near-wall or buffer region was most sensitive to the size of the IA and as the resolution increased, the PIV values approached the DNS values. Their results show that in the buffer region, PIV IA of Δy^+=20 gave values of u^+, v^+ and $-u^+ v^+$ that are, respectively, 96%, 92%, and 95% of the corresponding DNS values. Hence, even the lowest resolution is expected to yield reasonably accurate results.

In PIV technique, the accuracy of velocity measurement is limited by the accuracy of the subpixel interpolation of the displacement correlation peak. The particle response to fluid motion, light sheet positioning, light pulse timing, and size of IA are among the other sources of measurement uncertainties. According to studies

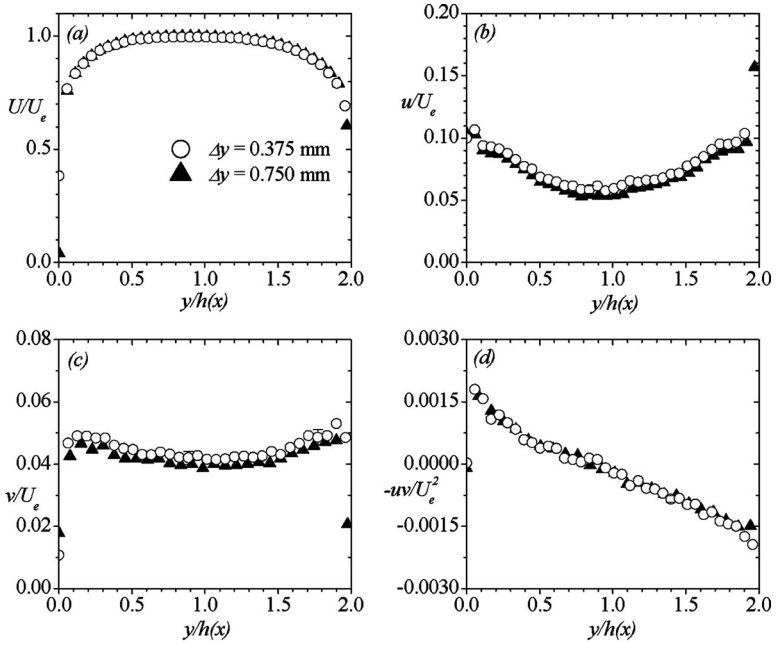

Fig. 2 Profiles of the mean velocity and turbulent quantities obtained using the two IAs at the L2 of Test D2: (*a*) *U*, (*b*) *u*, (*c*) *v*, and (*d*) −*uv*. Error bars in this and subsequent figures denote measurement uncertainty at 95% confidence level.

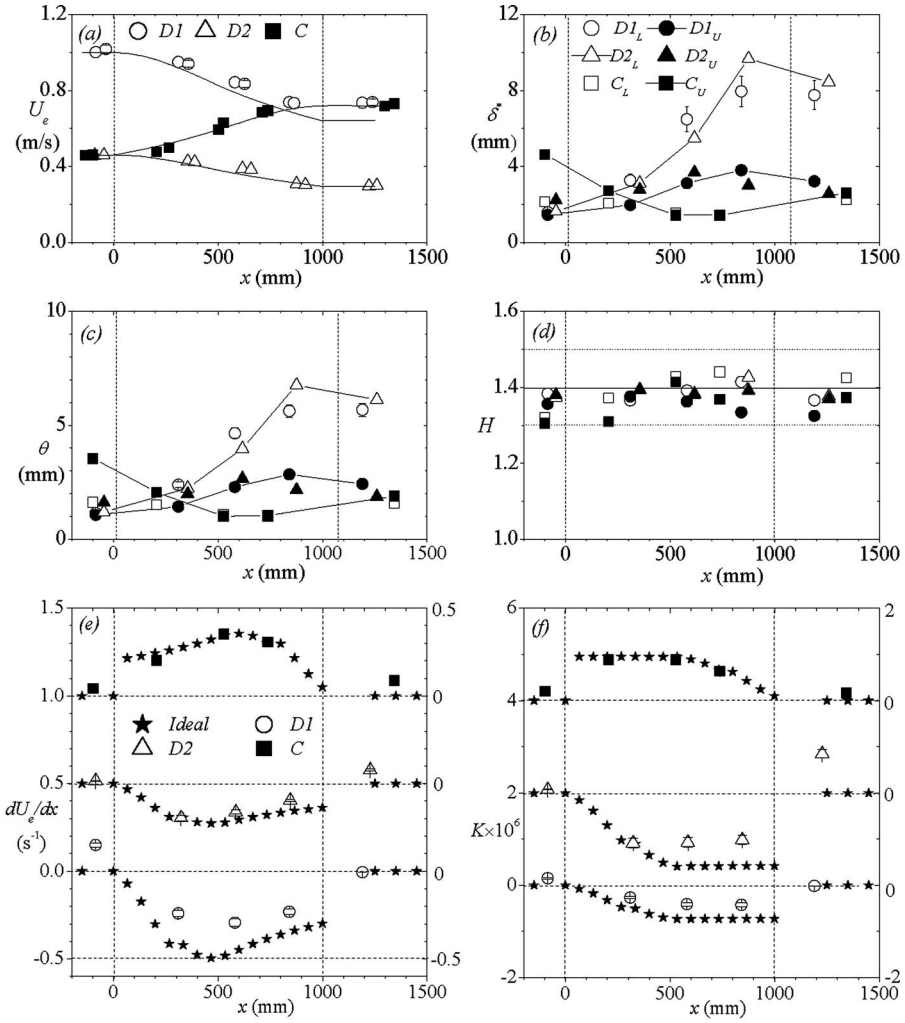

Fig. 3 Various mean flow parameters: (*a*) local freestream velocity, (*b*) displacement thickness, (*c*) momentum thickness, (*d*) shape factor, (*e*) velocity gradient, and (*f*) acceleration parameter.

such as Forliti et al. [21], a Gaussian peak-fitting algorithm is found to have the lowest bias and precision errors. The velocity gradients within the interrogation window tend to broaden the displacement peak and reduce the amplitude. For a cross-correlation technique (which is used in the present study), Keane and Adrian [22] suggested that to achieve an acceptable valid detection probability of 95%, the gradients should follow the expression

$$\frac{M\Delta U_y \Delta t}{d} < 0.03$$

where M is the magnification factor, $\Delta U_y = (\partial U/\partial y)(d/2)$, Δt is the time between the two laser pulses, and d is the length of the IA side. This condition was met in all the experiments. On basis of the size of IA and curve fitting algorithm used to calculate the instantaneous vector maps, and the large number of instantaneous vector maps used to calculate the mean velocity and turbulence quantities, the uncertainties in the mean velocity at 95% confidence level were estimated to be $\pm 2\%$ of the local value while those in the mean momentum flux and vorticity are $\pm 5\%$. The uncertainties in turbulence intensities and Reynolds shear stress are $\pm 5\%$ and $\pm 10\%$, respectively, whereas those in the mixing length, eddy viscosity, and production terms are $\pm 15\%$. The relatively larger uncertainties in the mixing length, eddy viscosity, and production terms are due to additional uncertainties in the values of $\partial U/\partial y$, which were estimated using second-order central differencing scheme.

3 Results and Discussion

3.1 Boundary Layer Characteristics. The local maximum mean velocity U_e obtained at selected x locations within the various planes of measurement are shown in Fig. 3(*a*). The dashed vertical lines at $x=0$ and $x=1000$ represent the start and end of the variable section. For the APG case (Test D1 and Test D2), U_e decreases monotonically and plateaus outside the diverging section, that is, where the top and bottom walls of the channel become parallel. Downstream of the divergence section, the values of U_e are 25% and 35% lower for Test D1 and Test D2, respectively, than the corresponding upstream value. As expected, for the FPG case (Test C), U_e increases monotonically and remains constant outside the converging section. Downstream of the converging section, U_e is almost 60% higher than the upstream value. As noted earlier, the profiles for the diverging and converging channels (Eqs. (1*a*) and (1*b*)) were chosen by assuming an inviscid (ideal) flow through the channels. These ideal velocity distributions in the channels are plotted as solid lines in Fig. 3(*a*). In spite of the boundary layer growth on the walls of the channel, the measured values (symbols) are only $\pm 7\%$ different from the

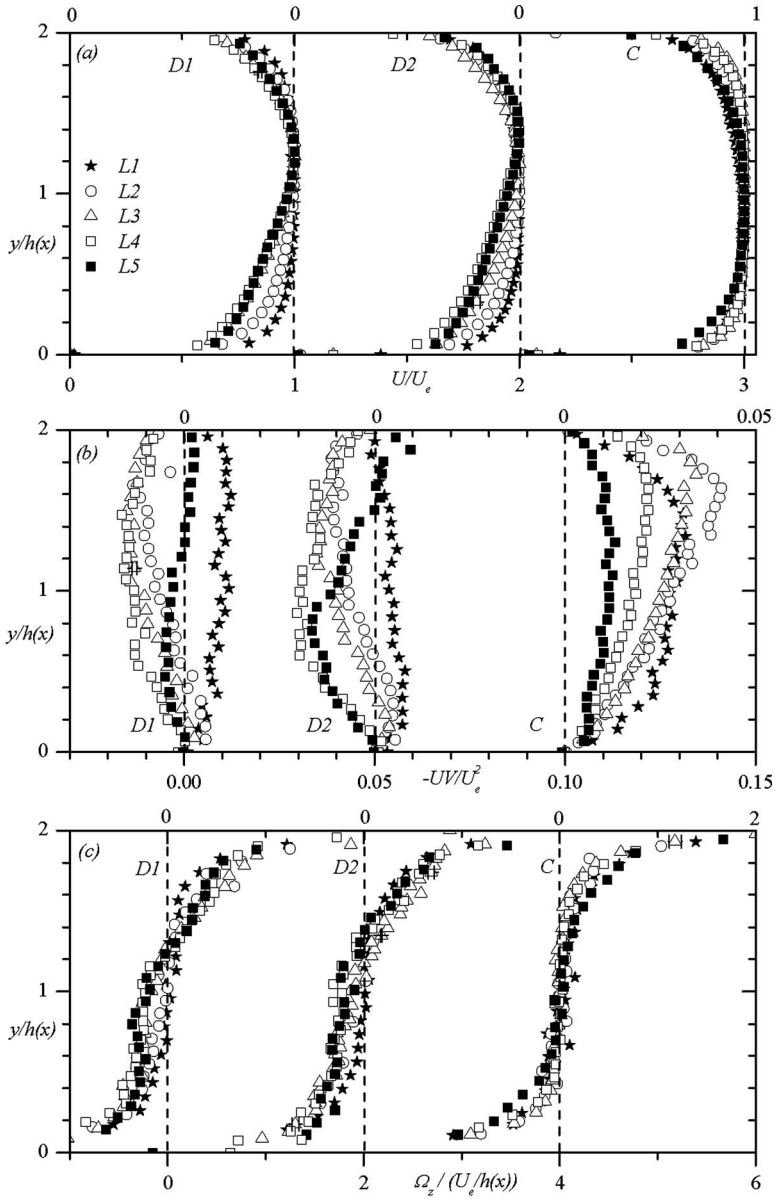

Fig. 4 Mean quantities in outer coordinates: (*a*) mean velocity, (*b*) mean momentum flux, and (*c*) mean vorticity.

ideal values except at L5 for Test D1 where the difference is about 13%.

The displacement thickness δ^* and momentum thickness θ for the upper and lower boundary layers are plotted in Figs. 3(*b*) and 3(*c*), respectively. In the case of APG (Tests D1 and Test D2), values of δ^* and θ obtained from the lower and upper boundary layers increase monotonically in the diverging section and decrease slightly at the downstream location L5. The increase in δ^* and θ within the diverging section is indicative of the characteristic higher mass and momentum flux deficit associated with APG. A similar trend was observed in the APG studies reported by Spalart and Watmuff [10] and Aubertine and Eaton [4]. The values of δ^* and θ obtained from the lower boundary layer are higher than those from the upper boundary layer, an indication that the impact of the APG is greater on the lower boundary layer than on the upper boundary layer. The maximum increase in δ^* (the lower boundary layer) when compared with the upstream value is approximately 500% for Test D1 and Test D2. Corresponding increase in θ is about 450% for Test D1 and Test D2. Spalart and Watmuff [10] observed an increase of 250% in δ^* and 190% in θ for their boundary layer flow in APG. Boundary layer thinning associated with FPG resulted in a decrease of δ^* and θ in the converging section. For Test C, a decrease of 50% in δ^* and 57% in θ is observed. The shape parameter, $H=\delta^*/\theta$, for the three test cases is plotted in Fig. 3(*d*). In spite of the large differences found among values of δ^* and θ for the various test conditions and measurement locations, the values of H remain nearly constant at 1.4 ± 0.1. The H values reported by Escudier et al. [23] for FPG flow where $K<3\times10^6$ were in the range of $1.3\leqslant H\leqslant1.4$.

The increase in U_e along the converging section is not exactly linear. However, in estimating the gradient dU_e/dx from the measured data in each measurement plane, a linear variation of U_e with x was assumed and dU_e/dx was evaluated as the slope of a least squares linear fit to U_e versus x. The values of dU_e/dx and $K=(\nu/U_e^2)(dU_e/dx)$ calculated from measured values are plotted in Figs. 3(*e*) and 3(*f*). Corresponding values of dU_e/dx and K obtained from the ideal velocity distributions shown in Fig. 3(*a*)

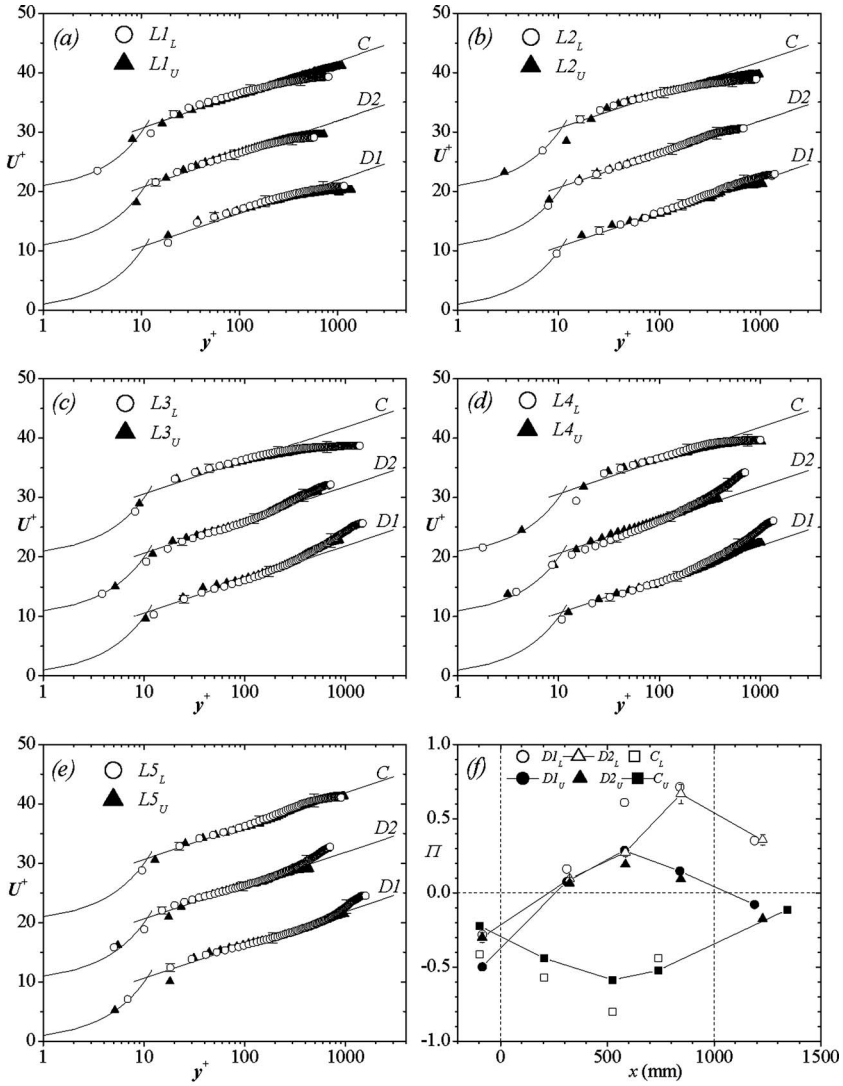

Fig. 5 Mean velocity profiles in inner coordinates: (*a*) L1, (*b*) L2, (*c*) L3, (*d*) L4, (*e*) L5, and (*f*) Wake parameter.

are denoted by star symbol in Figs. 3(*e*) and 3(*f*). Note that values of dU_e/dx and K vary from 0 to 0.5 and 0 to 2, respectively, and the vertical axis is staggered. The absolute value of the acceleration parameter increases dramatically from L1 to L2, remains nearly constant up to L4, and then decreases downstream of the variable section. The absolute values of K for Test D2 are generally higher than those obtained in Test D1.

3.2 Profiles of the Mean Velocities, Momentum Flux and Spanwise Vorticity. The development of the mean streamwise velocity profiles in the APG and FPG is shown in Fig. 4(*a*) using outer scaling (U_e and $h(x)$). The velocity profiles and other profiles to be presented subsequently contain 255 data points. However, appropriate number of data points is skipped to minimize data congestion. In Fig. 4(*a*), the five profiles obtained in the upstream (L1), variable (L2, L3, and L4), and downstream sections (L5) are plotted together for each of the three test cases. It is clear from the velocity profiles that the flow does not separate in the diverging channel. As suggested by Smits and Wood [24], the major influence of pressure gradient is felt in the near-wall region.

It can be seen that close to the walls, the deviation from the upstream profile increases progressively up to L4 and then begin to recover back to the upstream profile at L5. The profiles at L5 and L1 nearly collapse for the upper boundary layer in case of Test D2. Aubertine and Eaton [4] also observed a similar increase in deviation from the upstream profiles in APG. Their profile at the last measurement location in parallel section (at $x/L_r=1.67$, L_r=length of the ramp) was significantly less full compared with the upstream profile. One of the important observations is that APG produced in an asymmetric channel has more profound effects on the mean flow on the flat bottom wall than on the curved top wall. Because of the asymmetric nature of the channel, there was a tendency of the flow to "spread" upwards to fill the additional space created by the diverging upper curved wall. As a result the flow close to the flat lower wall within the diverging section is slowed substantially in comparison with values that would be obtained if both walls of the channel were to remain parallel. This caused a greater deviation among the profiles in the lower boundary layer of Test D1 and Test D2 and increased the thickness of the boundary layer considerably. As for the FPG, the upper boundary layer is affected slightly more than the lower boundary layer. In the upper boundary layer, the profiles for FPG become "more full" from L1 to L3 and those obtained at L4 and L5 appear to be recovering back to L1. The mean velocity deviation from the upstream profile in FPG and subsequent recovery toward upstream profile is also reported by Ichimiya et al. [14].

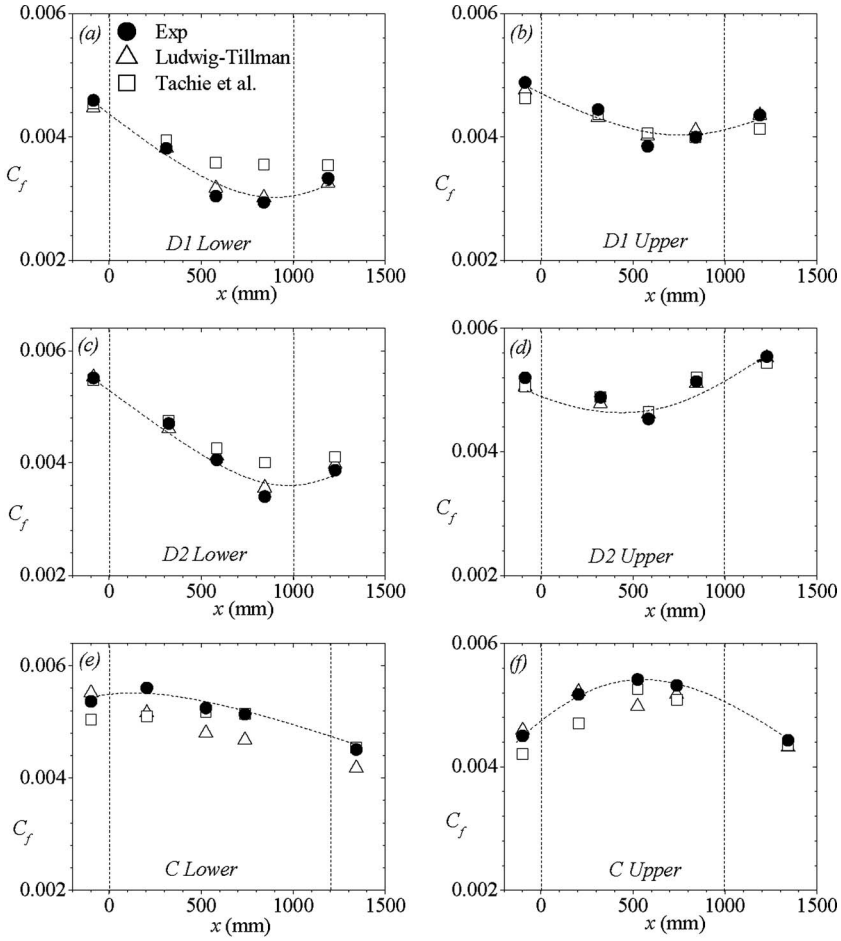

Fig. 6 Skin friction distribution: (*a*) Test D1, lower; (*b*) Test D1, upper; (*c*) Test D2, lower; (*d*) Test D2, upper; (*e*) Test C, lower; (*f*) Test C, upper. Trend lines are for visual aid only.

They observed that their profiles in the region of $0.4 < y/\delta < 1.5$ were indistinguishable.

The mean momentum flux ($-UV$) is related to the momentum transport across the channel. In a fully developed two-dimensional channel, $-UV$ is identically zero. Figure 4(*b*) shows that the absolute values of $-UV/U_e^2$ at all five locations are less than 5%. It is not clear why the profiles at L1, for example, are not antisymmetric about midheight, as should be expected. The mean vorticity ($\Omega = \partial V/\partial x - \partial U/\partial y$) profiles are shown in Fig. 4(*c*). In all three cases, the voriticity is negative close to the lower wall indicating that $\partial U/\partial y > \partial V/\partial x$. For Test D1 and Test D2, the profiles exhibit a modest increase in magnitude across the flow whereas at L5, the profile is returning toward the upstream profile. The upstream profile exhibits zero Ω in the region of $0.6 < y/h(x) < 1.2$. However, under the influence of APG, the location where $\Omega = 0$ shifts to $y/h(x) = 1.2$ and 1.4 at L4 for Test D1 and Test D2, respectively. For Test C, a slight decreasing trend is observed under the influence of FPG for profiles at L1 to L4. For the FPG, the mean vorticity is nearly zero in the region, $0.4 < y/h(x) < 1.6$, which is substantially wider compared with APG.

3.3 Friction Velocity and Mean Velocity Profiles in Inner Coordinates. The friction velocity U_τ was determined using the Clauser chart technique, that is, by fitting the measured mean velocity to the classical log law:

$$U^+ = \kappa^{-1} \ln y^+ + 5.0 \tag{2}$$

where $U^+ = U/U_\tau$, $y^+ = yU_\tau/\nu$, κ (=0.41) is the von Karman constant, and ν is the kinematic viscosity. Previous studies showed that the log law is valid for mild and moderate APG (Samuel and Joubert [8]; Cutler and Johnston [25]; and Aubertine and Eaton [4,5]). As the APG increases so does the strength of the wake and in the case of strong APG the logarithmic region disappears. The log law has also been applied to moderate and mild FPG (Fernholz and Warnack [26]) but reported to disappear as the acceleration becomes very strong (Blackwelder and Kovasznay [15]), i.e., at $K = 4.8 \times 10^{-6}$.

The velocity profiles obtained from the upper and lower boundary layers are plotted in Figs. 5(*a*)–5(*e*) using inner coordinates. The profiles exhibit substantial log region in all cases. Most of the profiles have data points below $y^+ = 10$. The strength of the wake is varying as the flow develops along the converging and diverging channels. The values of the wake parameter Π were estimated from the relation: $\Delta U^+_{\max} = 2\Pi/\kappa$ (where $\Delta U^+_{\max}$ is the maximum deviation of the measured data in Fig. 5 from the log law) and are plotted in Fig. 5(*f*). The wake parameter is known to depend on both pressure gradient and Reynolds number. It increases in APG and decreases in FPG (White [27]). The strength of wake increases for Test D1 and Test D2 in the variable section and subsequently decreases in the downstream section. The wake strength decreased within the converging section (for the FPG) but increased as the flow evolved into the downstream parallel section.

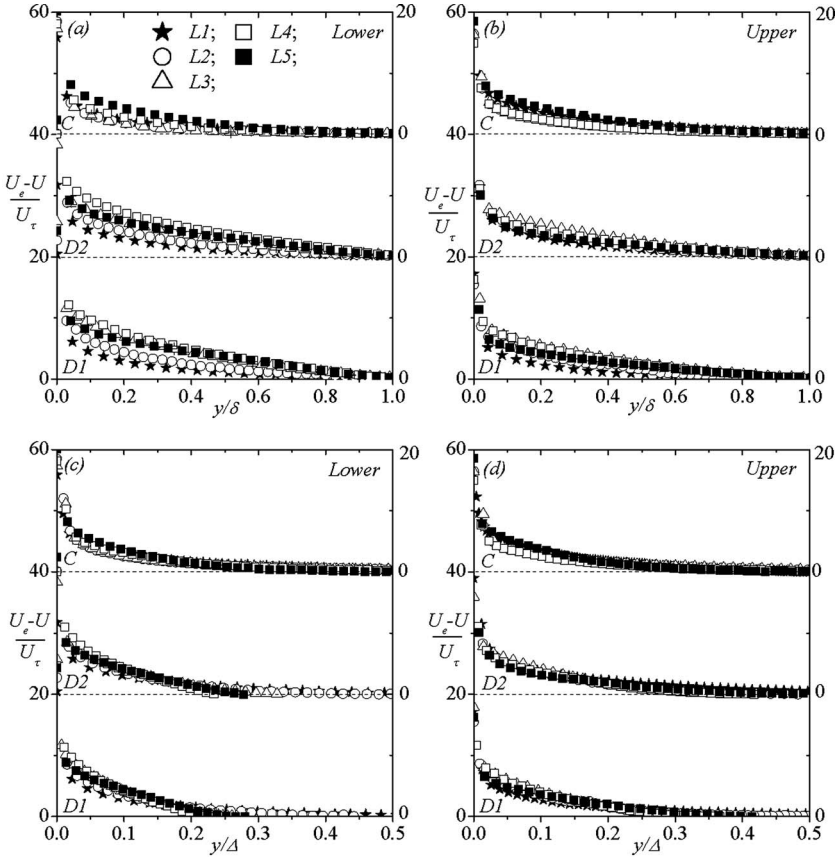

Fig. 7 Mean velocity defect profiles normalized by friction velocity. Note that in (*a*) and (*b*) *y* by δ; in (*c*) and (*d*) *y* by Δ.

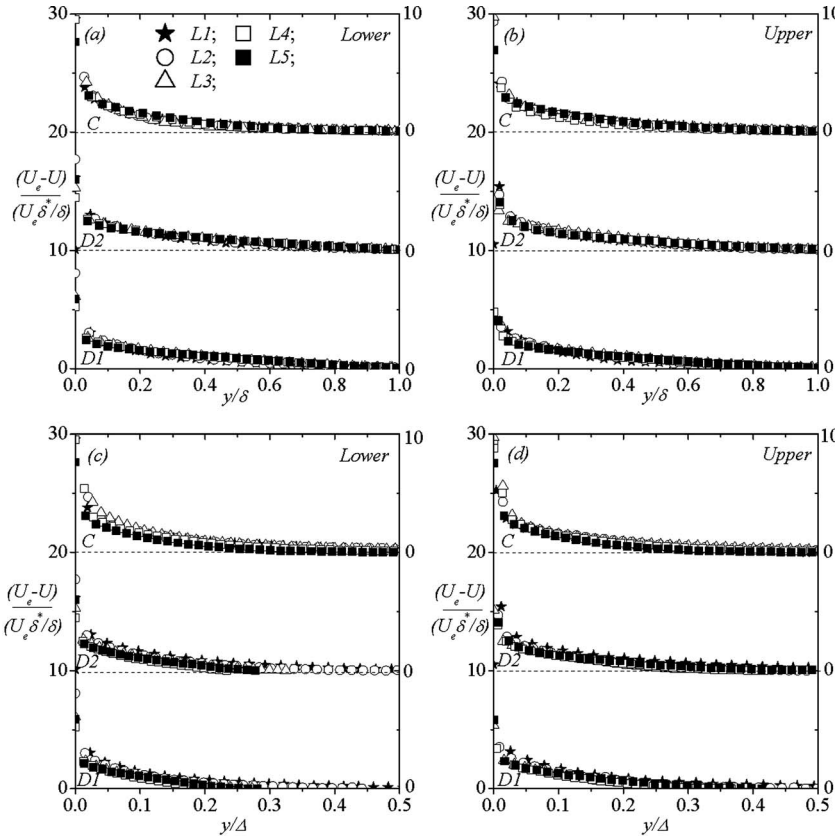

Fig. 8 Mean velocity defect profiles normalized by mixed scaling proposed by Zagarola and Smits (1998). Note that in (*a*) and (*b*) *y* by δ; in (*c*) and (*d*) *y* by Δ.

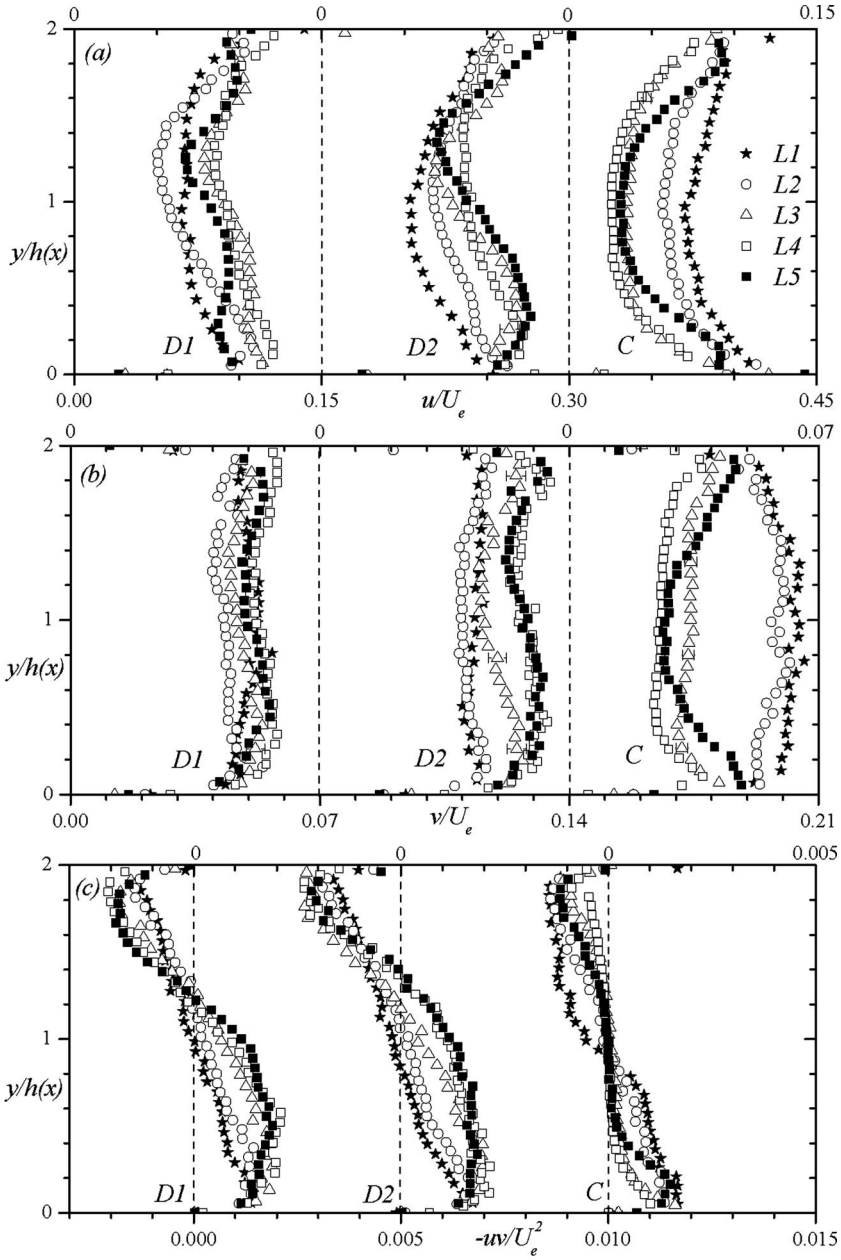

Fig. 9 Profiles of turbulence intensities and Reynolds shear stress in outer coordinates: (*a*) streamwise turbulent intensity, (*b*) transverse turbulent intensity, and (*c*) Reynolds shear stress.

This confirms the finding of Perry et al. [28] that the pressure gradient does not distort the logarithmic profile but it simply controls its y range of applicability.

The optimized U_τ values obtained from the log law are summarized in Table 2. The skin friction ($C_f = 2[U_\tau/U_e]^2$) distribution for the lower and the upper boundary layers are plotted in Fig. 6. For Test D1 and Test D2, the C_f values in the diverging section were lower than at L1 but began to increase at L5 for the lower boundary layer and at L4 for the upper boundary layer. The maximum reduction was found to be approximately 40% for both Test D1 and Test D2. In both cases, the maximum reduction was attained in the lower boundary layer. A decrease in skin friction values has been reported in many studies (Aubertine and Eaton [4]; and Skåre and Krogstad [9]). As for the FPG, the skin friction for the lower boundary layer increases at L2 and then decreases from there on. However, for the upper boundary layer, the skin friction continues to increase until L3 and then starts to decrease at L4 and L5. Blackwelder and Kovasznay [15] observed an increase in skin friction value in FPG upstream of the convergence but it dropped toward its laminar value as it entered the converging channel. The skin friction values were compared with values obtained from the following correlation proposed by Tachie et al. [29]:

$$C_f = 4.13 \times 10^{-2} - 2.68 \times 10^{-2}(\log \mathrm{Re}_\theta) + 6.528 \times 10^{-3}(\log \mathrm{Re}_\theta)^2 - 5.54 \times 10^{-4}(\log \mathrm{Re}_\theta)^3 \quad (3)$$

The data used to develop the correlation were obtained in open and closed water channels, and the Re_θ ranged from 150 to 15,000. For the APG, the values obtained from the correlation (Eq. (3)) are typically within $\pm 7\%$ (except in the lower boundary layer at L3 and L4 for Test D1 and at L4 for Test D2). The

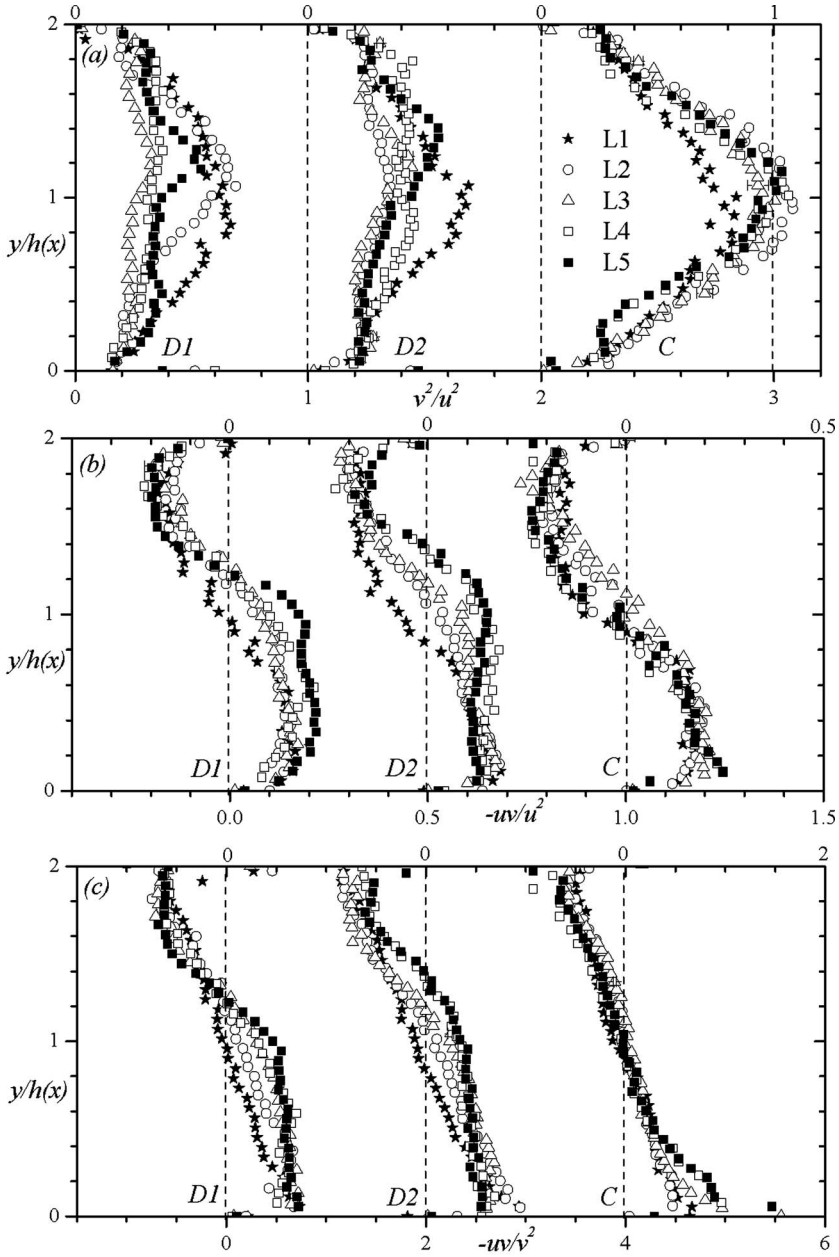

Fig. 10 Stress ratio profiles: (*a*) v^2/u^2, (*b*) $-uv/u^2$, and (*c*) uv/v^2.

difference was relatively higher for Test D2 at L3 and L4 (17% and 20%, respectively) and for Test D2 at L3 (17%). The correlation seems to do a good job of predicting skin friction values at locations where the APG is not very strong. For Test C, the skin friction values were obtained within ±10%. The skin friction values were also estimated using the Ludweig–Tillman correlation (White [27]):

$$C_f = 0.256\,\mathrm{Re}_\theta^{-0.268} 10^{-0.678H} \tag{4}$$

This correlation has been previously used in channel flows and flows with pressure gradients (Bradshaw and Wong [30] and Cutler and Johnston [25]) to estimate the skin friction. The correlation depends on the values of δ^* and θ for its accuracy. The values of δ^* and θ are expected to be reliable since almost all data sets have measurements starting in the region, $2 \leqslant y^+ \leqslant 10$. In determining the displacement and momentum thicknesses, the measured data were extrapolated to the wall using $U=0$ at $y=0$. For APG case (Test D1 and Test D2), the skin friction values are found to be within ±5% of values obtained from the log law. For the FPG case (Test C), the difference between the two values is found to be within ±10%.

3.4 Mean Velocity Defect Profiles. Different velocity and length scales have been proposed to interpret the mean velocity defect profiles. Therefore, a comparison of different velocity and length scales to plot the mean velocity defect profiles is provided in the present study. The velocity scales include U_τ proposed by classical theory, and the mixed velocity scale $(U_e\delta^*/\delta)$ proposed by Zagarola and Smits [31]. The mixed velocity scale $(U_e\delta^*/\delta)$ was later extended to turbulent boundary layers with pressure gradients by Castillo [32]. The boundary layer thickness δ is commonly used to normalize y but it appears that a more useful characteristic length scale for pressure gradient turbulent boundary layers is the defect thickness $(\Delta=\delta^* U_e/U_\tau)$ proposed by Clauser. The mean velocity defect profiles normalized by U_τ are plotted in Fig. 7. The values of y are normalized by δ in Figs. 7(*a*) and 7(*b*),

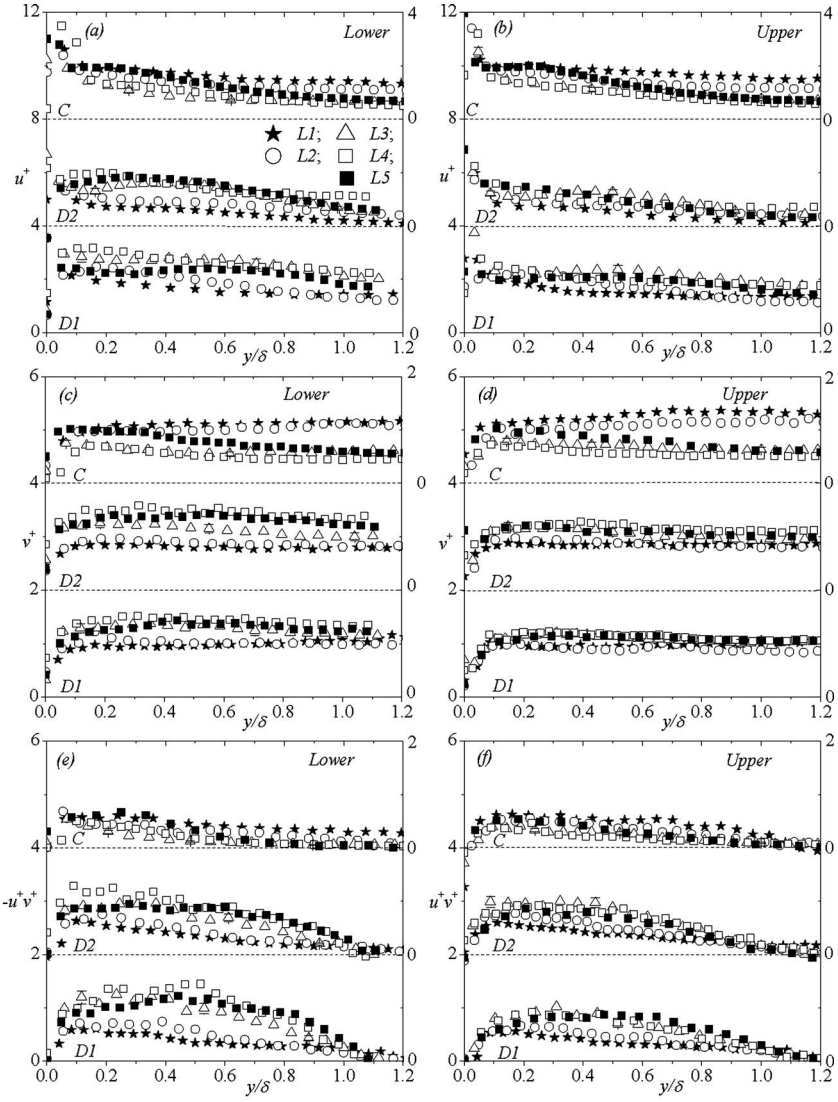

Fig. 11 Profiles of turbulence intensities and Reynolds shear stress normalized by friction velocity: (*a*) streamwise turbulence intensity, lower; (*b*) streamwise turbulence intensity, upper; (*c*) trasnverse turbulence intensity, lower; (*d*) transverse turbulence intensity, upper; (*e*) Reynolds shear stress, lower; (*f*) Reynolds shear stress, upper.

while Δ is used to normalize y in Figs. 7(c) and 7(d). A distinct pressure gradient effect can be seen among the defect profiles at various locations for a given test when δ is used to normalize y. For the APG, an increasing upward deviation from the L1 profile is observed in the diverging section whereas the profile at L5 relaxes toward the upstream profile. Similar to the mean velocity profiles (Fig. 4(a)), the pressure gradient effect is greater for the lower boundary layer. For FPG, the profiles within the converging section tend to move downwards and subsequently relax toward the upstream profile. It can be seen from Figs. 7(c) and 7(d) that for $y/\Delta > 0.1$, the profiles are nearly indistinguishable at all the locations for a given test. In Fig. 8, $U_e\delta^*/\delta$ is used to plot the defect profiles; δ is used to normalize y in Figs. 8(a) and 8(b), while y is normalized by Δ in Figs. 8(c) and 8(d). It is evident that the mixed scaling does a better job in collapsing the profiles onto a single curve compared to U_τ. (Figs. 7(a) and 7(b)). Figures 8(c) and 8(d) show that Δ provides a reasonable collapse among the profiles and for $y/\Delta > 0.1$, the profiles are nearly indistinguishable. Comparing all the combinations of velocity and length scales used in Figs. 7 and 8, it can be concluded that when the mean velocity defect is normalized by $U_e\delta^*/\delta$ and y by δ the best overall collapse among the profiles is achieved for a given test.

3.5 Turbulence Intensities and Reynolds Shear Stress. The streamwise turbulence intensity u normalized by U_e and y by $h(x)$ is shown in Fig. 9(a). For the APG, the peak value $(u/U_e)_{\max}$ occurs very close to the wall and decays rapidly away from the wall. As the flow develops though the diverging section, the peak value increases and its location moves farther away from the wall. The effect of APG is more dramatic in Test D2, which has greater magnitude of K. For this test, $(u/U_e)_{\max}$ at L4 occurred at $y/h(x)=0.23$. This corresponds to $y/\delta=0.18$ compared with $(u/U_e)_{\max}$ at $y/\delta=0.45$ for Skåre and Krogstad [9]. The $(u/U_e)_{\max}$ values obtained at L4 for Test DI and Test D2 are 22% and 36%, respectively, higher than the upstream value. As the flow returns to the parallel walls, L5, the turbulence intensity begins to decay but it is still higher than the upstream profile. The acceleration of the flow results in a progressive decay of the streamwise turbulence intensity for Test C, an opposite trend compared with the

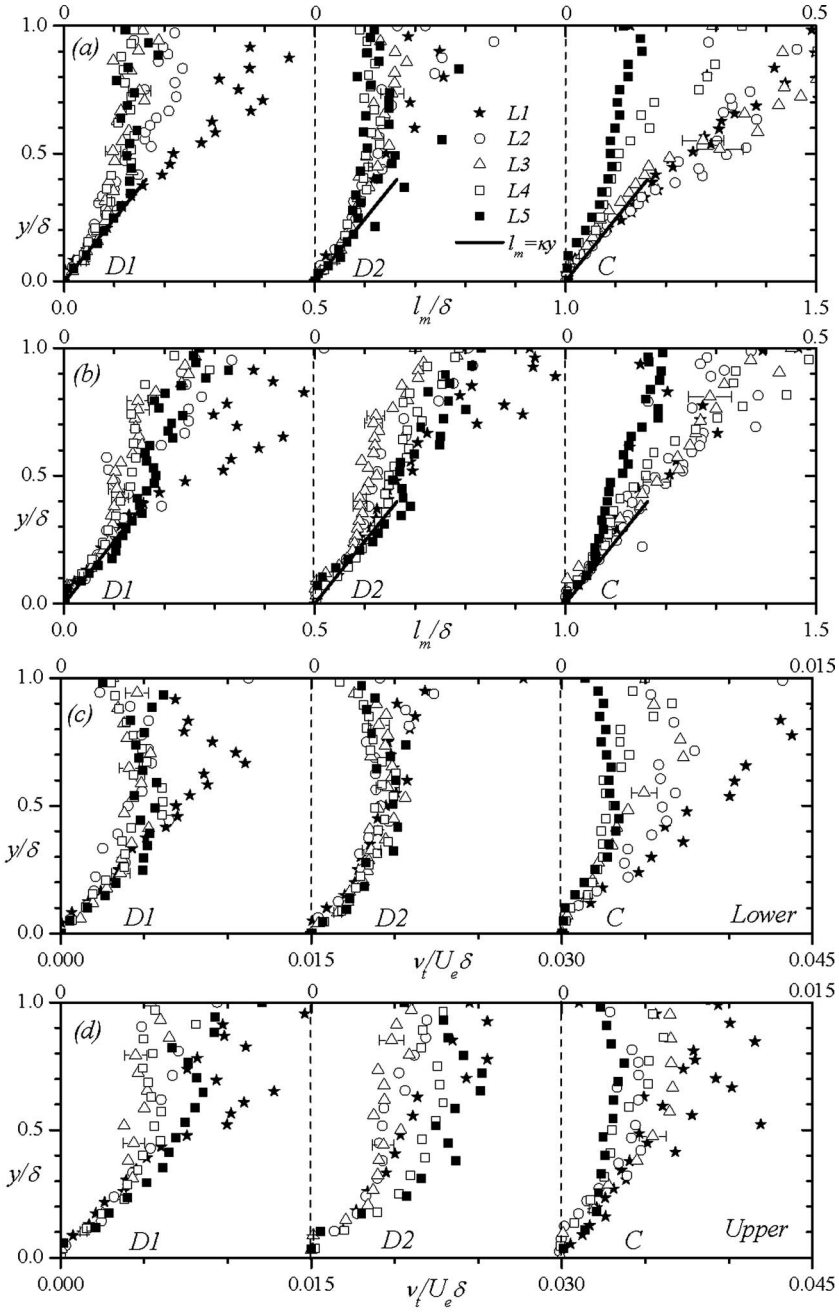

Fig. 12 Profiles of mixing length and eddy viscosity in outer coordinates (*a*) mixing length, lower; (*b*) mixing length, upper; (*c*) eddy viscosity, lower; (*d*) eddy viscosity, upper.

APG. Here, $(u/U_e)_{\max}$ at L4 decreased by 64% compared with the upstream value. Unlike the APG profiles, these profiles remain nearly symmetric at all locations.

Figures 9(*b*) and 9(*c*) show that the development of transverse turbulence intensity v and Reynolds shear stress are qualitatively similar to the streamwise turbulence intensity. $(v/U_e)_{\max}$ at L4 is 45% higher than L1 for Test D2 but $(v/U_e)_{\max}$ at L4 for Test D1 is nearly similar to the corresponding upstream value. The most significant effects of pressure gradient on transverse turbulence intensity can be seen in Test C where $(v/U_e)_{\max}$ at L4 is 61% lower than L1. Similar to the turbulence intensities, the magnitude of $(-uv/U_e^2)_{\max}$ is increasing in the APG and its location is moving away from the walls. At the lower wall, the value of $(-uv/U_e^2)_{\max}$ at L4 is 45% higher for Test D1 and 30% higher for Test D2 compared to the upstream profile. The shear stress is decaying in magnitude under the effect of FPG. In the region $0.5<y/h(x)<1.25$, the shear stress is nearly zero at L3 and L4. For a two-dimensional flow, positive $\partial U/\partial x$ (FPG) is associated with negative $\partial V/\partial y$ and Townsend [33] suggested that negative $\partial V/\partial y$ tends to flatten the large eddies and reduces the contribution to Reynolds stresses. For APG, the y location where $-uv=0$ corresponds to $y_{\max}$ (i.e., the y location of U_e) with maximum deviation of 6%. However, for FPG, the difference between the two locations is as high as 13% (at L3 and L4).

The stress ratios v^2/u^2, $-uv/u^2$, and $-uv/v^2$ are shown in Fig. 10. Near the upper and lower walls, no systematic pressure gradient effects are observed for the APG and FPG profiles. However, away from the walls, there is a considerable decay and flattening

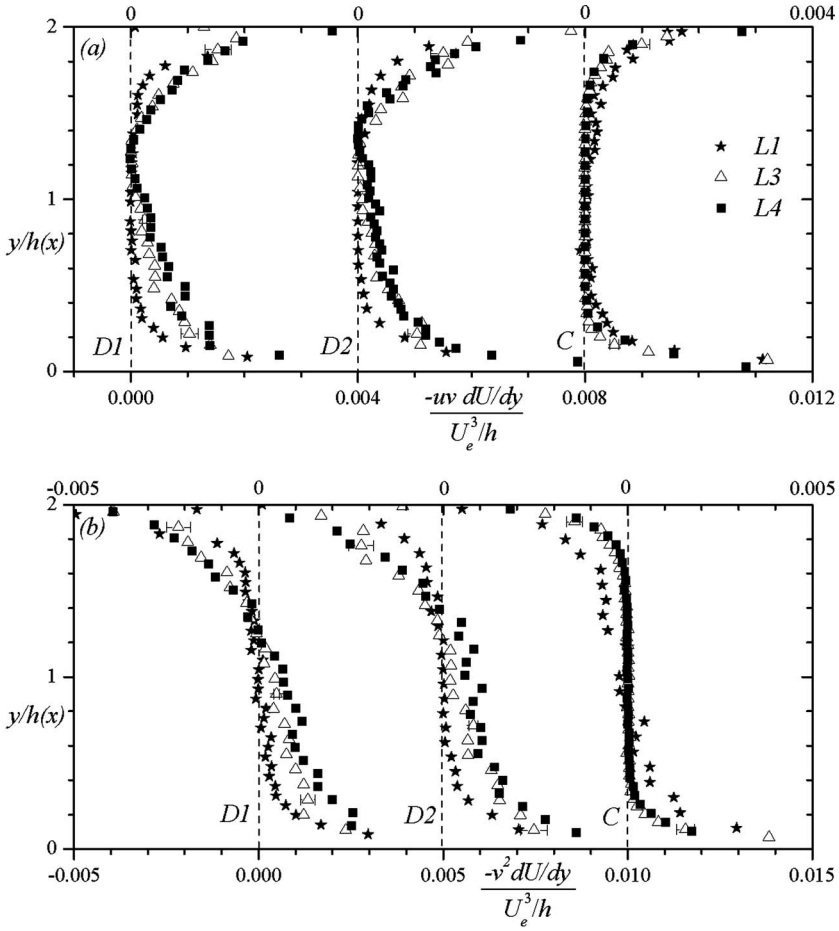

Fig. 13 Profiles of turbulence production: (*a*) $-uvdU/dy$ and (*b*) $-v^2dU/dy$

of the stress ratio within the diverging section. For Test D2, for example, the maximum value of v^2/u^2 in the diverging section is about 0.3–0.4 compared with 0.65 at the upstream location. This can be attributed to a more rapid increase in u^2 due to APG compared with v^2. Skåre and Krogstad [9] reported that the mechanism for redistributing the turbulent energy between the different normal stresses is independent of the mean flow pressure gradient. Their stress ratio profiles were similar throughout the boundary layer. Their finding may be attributed to the APG turbulent boundary being maintained in equilibrium. For FPG, on the other hand, away from the walls, profiles of v^2/u^2 in the converging section are higher than the upstream profile. This implies that FPG attenuates u^2 more significantly than v^2 is. It is also evident that v^2/u^2 profiles are significantly higher in FPG than in APG. The peak values at L2 to L4 for the FPG case, for example, are about twice as high as in the APG case. Figures 10(*b*) and 10(*c*) show that pressure gradient does not have any significant effects on $-uv/u^2$ and $-uv/v^2$ in the near-wall region. However, in APG $-uv/u^2$ and $-uv/v^2$ show an increasing trend away from the walls. This trend can be attributed to a greater rate of increase of $-uv$ compared to u^2 and v^2. The location where $-uv/u^2$ and $-uv/v^2$ changes sign moves closer to the upper wall. In FPG case, $-uv/u^2$ shows a decreasing trend implying that u^2 decays faster than $-uv$. However, no systematic effects of FPG are observed in case of $-uv/v^2$.

The streamwise and transverse turbulence intensities normalized by the friction velocity are shown in Fig. 11. Close to the walls, the values of u^+ and v^+ are significantly higher at all the locations than at L1 for APG (Fig. 11(*a*) to Fig. 11(*d*)) and remain high to the edge of the boundary layer. For FPG, L1 profile is higher than the rest of turbulence intensities profiles. The Reynolds shear stress in inner coordinates can be seen in Figs. 11(*e*) and 11(*f*). To facilitate visual comparison, the Reynolds shear stress in the upper boundary layer is plotted as positive values in Fig. 11(*f*). The variation of the shear stress is essentially the same as in the case of turbulence intensities. In the lower boundary layer at L4, $(-u^+v^+)_{\max}$ increases to 1.45 and 1.30 for Test D1 and Test D2, respectively. Under the influence of FPG, in lower boundary layer of L4, $(-u^+v^+)_{\max}$ reduces to 0.65.

3.6 Mixing Length and Eddy Viscosity and Turbulence Production. The distribution of the mixing length $l_m = (-uv)^{0.5}/(\partial U/\partial y)$ normalized by δ is shown in Figs. 12(*a*) and 12(*b*), respectively. Even though l_m lacks physical meaning, they are used as the basis of data correlations in turbulence models for calculating slowly evolving flows (Jovic [34]). In the inner region $(y/\delta < 0.1)$, the mixing length distribution for all cases follow the universal linear relation $l_m = \kappa y$, where $\kappa = 0.41$. The mixing length profiles exhibit a greater decay in the lower boundary layers. In case of Test D1 and Test D2, for $y/\delta > 0.1$, the profiles exhibit a slope of $\kappa < 0.15$ for the lower boundary layer (Fig. 12(*a*)). Skåre and Krogstad [9] reported a reduction in slope from $\kappa = 0.41$ to 0.07 for the data between $0.15 > y/\delta > 0.9$ in APG flow. The APG mixing length is decaying in the outer region due to its characteristic higher values of $\partial U/\partial y$ in the outer region. For FPG, the L1 to L3 profiles are similar but decay at L4 and L5 in the lower boundary layer. In the upper boundary layer, L5 exhibits a slight decay while the other profiles are quite similar.

The profiles of the eddy viscosity, $\nu_t = -uv/(\partial U/\partial y)$, normalized by $U_e\delta$ for lower and upper boundary layers are shown in Figs. 12(*c*) and 12(*d*), respectively. It is observed that the eddy

viscosity is self-similar in the region $y/\delta < 0.2$. A steady increase in profiles is seen as the distance from the wall increases followed by a slight decrease near the edge of the boundary layer thickness.

For a two-dimensional turbulent flow, the production terms in u^2 and $-uv$ are, respectively, $P_{uu} = [-u^2 \partial U/\partial x - uv\partial U/\partial y]$ and $P_{uv} = [-u^2 \partial V/\partial x - v^2 \partial U/\partial y]$. Similarly, the production term in turbulent kinetic energy is $P_k = [-uv(\partial U/\partial y + \partial V/\partial x)] - [(u^2 \partial U/\partial x + v^2 \partial V/\partial y\ ]$. It was found that $\partial U/\partial y \gg \partial V/\partial x$ so that $-uv\partial U/\partial y$ becomes the dominant production term in P_{uu} and P_k, while $-v^2 \partial U/\partial y$ is the major contributor to P_{uv}. Typical profiles of $-uv\partial U/\partial y$, and $-v^2 \partial U/\partial y$ for the various tests at L3 and L4 are compared with the upstream profile in Figs. 13(*a*) and 13(*b*), respectively. The effect of the APG is to enhance the production term, $-uv\partial U/\partial y$ (Fig. 13(*a*)). The term remains high away from the wall due to high magnitude of $-uv$ and $\partial U/\partial y$ over most of the channel. In FPG, the production term peaks very close to the wall and rapidly decays. The term is nearly zero in the region $0.5 < y/h(x) < 1.4$. The magnitude of the production term, $-v^2 \partial U/\partial y$ (Fig. 13(*b*)), behaves in qualitatively similar manner as the previous term. This term is also enhanced in APG and attenuated in FPG.

4 Conclusion

An experimental study has been conducted in variable APG and FPG flows. The mean velocity profiles become "more full" in FPG and "less full" in APG. It was observed that for APG the lower boundary layer is affected more significantly compared to the upper boundary layer. However, the effect of FPG on the upper and the lower boundary layers was found to be nearly similar. APG enhances production of turbulent kinetic energy and Reynolds shear stress while these quantities are attenuated by FPG. As a result, the turbulence intensities and Reynolds shear stress are increased in APG and decreased in FPG. The location of $-uv = 0$ was observed to shift toward the upper wall under the influence of APG; however, in FPG, the Reynolds shear stress remained fairly symmetric about midchannel height. Many different scales were used to plot the velocity defect profiles. The scale $(U_e \delta^*/\delta, \delta)$ provided the best collapse of the profiles onto a single curve. In the region $y/\delta < 0.1$, the mixing length distribution for all cases follow the universal linear relation $l_m = \kappa y$. The data in the outer region exhibit a much smaller slope. The eddy viscosity profiles show a greater pressure gradient effect in the lower boundary layer.

Acknowledgment

The second author gratefully acknowledged the financial support provided by Canada Foundation for Innovation, Natural Sciences and Engineering Research Council of Canada (Discovery Grant) and Manitoba Hydro.

References

[1] Dönch, F., 1926, "Divergente und Konvergente Turbulente Strömungen mit Kleinen Öffnungs-Winkeln," Forsch. Geb. Ingenieurwes., **282**, pp. 1–58.
[2] Nikuradse, J., 1929, "Untersuchungen über die Strömungen des Wassers in Konvergenten un Divergenten Kanälen," Forsch. Geb. Ingenieurwes., **289**, pp. 1–49.
[3] Kim, D. S., White, B. R., Ayala, A., and Bagheri, N., 1999, "Higher-Order Turbulence Products of Velocity and Temperature for Adverse Pressure Gradient Boundary Layer Flows," *Proceedings of Heat Transfer and Fluid Mechanics Institute*, pp. 125–132.
[4] Aubertine, C. D., and Eaton, J. K., 2005, "Turbulence Development in a Non-Equilibrium Turbulent Boundary Layer With Mild Adverse Pressure Gradient," J. Fluid Mech., **532**, pp. 345–364.
[5] Aubertine, C. D., and Eaton, J. K., 2006, "Reynolds Number Scaling in a Non-Equilibrium Turbulent Boundary Layer With Mild Adverse Pressure Gradient," Int. J. Heat Fluid Flow, **27**, pp. 566–575.
[6] Angele, K. P., and Muhammad-Klingmann, B., 2006, "PIV Measurements in a Weakly Separating and Reattaching Turbulent Boundary Layer," Eur. J. Mech. B/Fluids, **25**, pp. 204–222.
[7] Ruetenik, J. R., and Corrison, S., 1955, "Equilibrium Turbulent Flow in a Slightly Divergent Channel," 50 Jahre Grenzschichtforschung, Friedr. Vieweg and Son. Braunschweig, 446.
[8] Samuel, A. E., and Joubert, P. N., 1974, "A Boundary Layer Developing in an Increasingly Adverse Pressure Gradient," J. Fluid Mech., **66**, pp. 481–505.
[9] Skåre, P. E., and Krogstad, P.-Å., 1994, "A Turbulent Equilibrium Boundary Layer Near Separation," J. Fluid Mech., **272**, pp. 319–348.
[10] Spalart, P. R., and Watmuff, J. H., 1993, "Experimental and Numerical Study of a Turbulent Boundary Layer With Pressure Gradients," J. Fluid Mech., **249**, pp. 337–371.
[11] Kline, S. J., Reynolds, W. C., Schraub, F. A., and Runstadler, P. W., 1967, "The Structure of Turbulent Boundary Layers," J. Fluid Mech., **30**, pp. 741–773.
[12] Cardoso, A. H., Graf, W. H., and Gust, G., 1991, "Steady Gradually Accelerating Flow in a Smooth Open Channel," J. Hydraul. Res., **29**, pp. 525–543.
[13] Finnicum, D. S., and Hanratty, T. J., 1998, "Effect of Favorable Pressure Gradients on Turbulent Boundary Layers," AIChE J., **34**, pp. 529–540.
[14] Ichimiya, M., Nakamura, I., and Yamashita, S., 1998, "Properties of a Relaminarizing Turbulent Boundary Layer Under a Favorable Pressure Gradient," Exp. Therm. Fluid Sci., **17**, pp. 37–48.
[15] Blackwelder, R. F., and Kovasznay, L. S. G., 1972, "Large-Scale Motion of a Turbulent Boundary Layer during Relaminarization," J. Fluid Mech., **53**, pp. 61–83.
[16] Blackwelder, R. F., and Kovasznay, L. S. G., 1970, "Large-Scale Motion of a Turbulent Boundary Layer With a Zero and a Favorable Pressure Gradient," Department of Mechanical Engineering, The Johns Hopkins University, Report No. 2.
[17] Tachie, M. F., 2007, "Particle Image Velocimetry Study of Turbulent Flow Over Transverse Square Ribs in Asymmetric Diffuser," Phys. Fluids, **19**, p. 065106.
[18] Raffel, M., Willert, C. E., and Kompenhaus, J., 1998, *Particle Image Velocimetry: A Practical Guide*, Springer, New York.
[19] Piirto, M., Saarenrinne, P., Eloranta, H., and Karvinen, R., 2003, "Measuring Turbulence Energy With PIV in Backward-Facing Step Flow," Exp. Fluids, **35**, pp. 219–236.
[20] Saikrishnan, N., Marusic, I., and Longmire, E. K., 2006, "Assessment of Dual Plane PIV Measurements in Wall Turbulence using DNS Data," Exp. Fluids, **46**, pp. 265–278.
[21] Forliti, D. J., Strykowski, P. J., and Debatin, K., 2000, "Bias and Precision Errors of Digital Particle Image Velocimetry," Exp. Fluids, **28**, pp. 436–447.
[22] Keane, D. J., and Adrian, R. J., 1992, "Theory of Cross-Correlation of PIV Images," Appl. Sci. Res., **49**, pp. 191–215.
[23] Escudier, M. P., and Abdel-Hameed, A., Johnson, M. W., and Sutcliffe, C. J., 1998, "Laminarisation and Re-Transition of a Turbulent Boundary Layer Subjected to Favorable Pressure Gradient," Exp. Fluids, **25**, pp. 491–502.
[24] Smits, A. J., and Wood, D. H., 1985, "The Response of Turbulent Boundary Layers to Sudden Perturbations," Annu. Rev. Fluid Mech., **17**, pp. 321–358.
[25] Cutler, A. D., and Johnston, J. P., 1989, "The Relaxation of a Turbulent Boundary Layer in an Adverse Pressure Gradient," J. Fluid Mech., **200**, pp. 367–387.
[26] Fernholz, H. H., and Warnack, D., 1998, "The Effects of a Favorable Pressure Gradient and of the Reynolds Number on an Incompressible Axisymmetric Turbulent Boundary Layer. Part 1. The Turbulent Boundary Layer," J. Fluid Mech., **359**, pp. 329–356.
[27] White, F. M., 1974, *Viscous Fluid Flow*, McGraw-Hill, New York.
[28] Perry, A., Bell, J. B., and Joubert, P. N., 1966, "Velocity and Temperature Profiles in Adverse Pressure Gradient Turbulent Boundary Layers," J. Fluid Mech., **25**, pp. 299–320.
[29] Tachie, M. F., Bergstrom, D. J., Balachandar, R., and Ramachandran, S., 2001, "Skin Friciton Correlation in Open Channel Boundary Layers," ASME J. Fluids Eng., **123**, pp. 953–956.
[30] Bradshaw, P., and Wong, F. Y. F., 1972, "The Reattachment and Relaxation of a Turbulent Shear Layer," J. Fluid Mech., **52**, pp. 113–135.
[31] Zagarola, M. V., and Smits, A. J., 1998, "Mean-Flow Scaling of Turbulent Pipe Flow," J. Fluid Mech., **373**, pp. 33–79.
[32] Castillo, A. L., 2000, "Application of Zagarola/Smits Scaling in Turbulent Boundary Layers With Pressure Gradient," *Advances in Fluid Mechanics III*, WIT, Montreal, Canada, pp. 275–288.
[33] Townsend, A. A., 1961, "Equilibrium Layers and Wall Turbulence," J. Fluid Mech., **11**, pp. 97–120.
[34] Jovic, S., 1996, "An Experimental Study of a Separated/Reattached Flow Behind a Backward-Facing Step. $Re_h = 37{,}000$," NASA TM 110384.

Simulation of Shallow Flows in Nonuniform Open Channels

Qiuhua Liang
Lecturer in Hydraulic Engineering,
School of Civil Engineering
and Geosciences,
Newcastle University,
Newcastle Upon Tyne NE1 7RU, UK
e-mail: qiuhua.liang@ncl.ac.uk

This paper presents a new formulation of the 2D shallow water equations, based on which a numerical model (referred to as NewChan) is developed for simulating complex flows in nonuniform open channels. The new shallow water equations mathematically balance the flux and source terms and can be directly applied to predict flows over irregular bed topography without any necessity for a special numerical treatment of source terms. The balanced governing equations are solved on uniform Cartesian grids using a finite-volume Godunov-type scheme, enabling automatic capture of transcritical flows. A high-order numerical scheme is achieved using a second-order Runge–Kutta integration method. A very simple immersed boundary approach is used to deal with an irregular domain geometry. This method can be easily implemented in a Cartesian model and does not have any influence on computational efficiency. The numerical model is validated against several benchmark tests. The computed results are compared with analytical solutions, previously published predictions, and experimental measurements and excellent agreements are achieved. [DOI: 10.1115/1.2829593]

Keywords: open channel flow, shallow water equations, Godunov-type scheme, Riemann solver, boundary treatment, source term balancing

1 Introduction

In most engineering practice, open channel flows can normally be assumed to be hydrostatic in pressure distribution. Fluid particles move on depth-averaged velocity, with the vertical acceleration component neglected. Under these assumptions, a flow can be described using the 1D St Venant or 2D shallow water equations. Many numerical models for simulating open channel flows have been published based on these equations [1–7].

In practice, open channel flows can be very complicated when interacting with domain geometry, bed topography, and/or structures. Complex flow patterns, such as supercritical flow, transitional flow, subcritical flow, hydraulic jump, and hydraulic drop, can appear instantaneously in a considered channel reach. Currently, a popular way to deal with these complex flow processes is to use a Godunov-type scheme [5,7]. The advantage of a Godunov-type scheme is its capability to automatically capture different flow types, including shock-type flow discontinuity (e.g., hydraulic jump). This approach is adopted in the present model.

When simulating a flow in a domain with irregular boundaries, a popular approach is to solve the governing equations on a boundary-fitted curvilinear grid [2,5,7]. In order to obtain numerical solutions, the governing equations are transformed from Cartesian to a new curvilinear coordinate system. An important drawback of this method is that the governing equations will become much more complicated in the new coordinate system, which unfortunately increases discretization errors and numerical instability. Furthermore, to generate a good quality boundary-fitted grid is not a straightforward task in certain cases when the boundary becomes extremely irregular and complicated. An alternative way to deal with the curved boundary problem is to use the Cartesian cut cell technique [8–10], in which the unwanted regions outside the computational domain are cut out of the background mesh, so that the curved boundaries are approximated by a series of line segments. Using cut cells, the flow equations are directly solved on a Cartesian grid system. However, the main disadvantage of this technique is its effect on computational efficiency of an explicit numerical scheme. When a small cut cell (with area less than half of that of the original uncut cell) is met, a correspondingly small time step has to be used in order to maintain numerical stability. To overcome this problem, a conventional way is to merge the small cut cells with a neighboring cell to form a "large cut cell." However, this method is considered to lose accuracy. Actually, even for those cut cells larger than half of a normal fluid cell, there is still a constraint on the time step as the worst case is to perform the calculation on a cut cell with half of its original area. This means that whenever a Cartesian cut cell method is implemented, the computational efficiency of a model will become at most half of its counterpart without using cut cells if no local time step method is considered. Therefore, it would be desirable to have a Cartesian grid based model with boundary fitting, but without any effect on computational efficiency.

Another difficulty in modeling open channel flows is to deal with the source terms in the governing equations, i.e., bed slope and friction. As the bed topography and friction have great influence on open channel flows (or even determine the flow patterns), it is extremely important to evaluate these terms properly in a numerical model. In the last two decades, efforts have been made to develop well-balanced schemes for simulating free surface flow hydrodynamics [11–17]. In particular, Rogers et al. [17] derived a new formulation of shallow water equations with flux and source terms balanced mathematically; hence, the balancing property is independent of the numerical process. In this paper, a new formulation of shallow water equations is derived in a similar way to that proposed by Rogers et al., but it is more general and applicable to a problem involving wetting and drying.

This work presents a novel numerical model that deals with these problems simultaneously. The governing 2D shallow water equations will be reformulated in a new balanced form in Sec. 2. In Sec. 3, the new equation set is solved using an explicit finite-volume Godunov-type scheme incorporated with the Harten, Lax and van Leer with contact wave restored (HLLC) approximate Riemann solver. A Runge–Kutta time stepping scheme is used to achieve a second-order accuracy. For the irregular boundary problem, a simple local boundary modification method is implemented. Then, in Sec 4, this new model is validated against four benchmark tests. Brief conclusions are drawn in Sec. 5.

Contributed by the Fluids Engineering Division of ASME for publication in the JOURNAL OF FLUIDS ENGINEERING. Manuscript received March 9, 2007; final manuscript received August 20, 2007; published online January 18, 2008. Review conducted by Rajat Mittal.

2 Governing Equations

The 2D shallow water equations can be derived by vertically integrating the 3D Reynolds averaged Navier–Stokes equations. Traditionally, the hyperbolic conservation law of the 2D shallow water equations are expressed as [18,19]

$$\frac{\partial \mathbf{u}}{\partial t} + \frac{\partial \mathbf{f}}{\partial x} + \frac{\partial \mathbf{g}}{\partial y} = \mathbf{s} \tag{1}$$

where t denotes time, x and y are the Cartesian coordinates, and $\mathbf{u}$, $\mathbf{f}$, $\mathbf{g}$, and $\mathbf{s}$ are the vectors representing the conserved variables, fluxes in the x and y directions, and source terms, respectively. The vectors are given by

$$\mathbf{u} = \begin{bmatrix} h \\ uh \\ vh \end{bmatrix} \quad \mathbf{f} = \begin{bmatrix} uh \\ u^2h + \frac{1}{2}gh^2 \\ uvh \end{bmatrix}$$
$$\mathbf{g} = \begin{bmatrix} vh \\ uvh \\ v^2h + \frac{1}{2}gh^2 \end{bmatrix} \quad \mathbf{s} = \begin{bmatrix} 0 \\ -\frac{\tau_{bx}}{\rho} - gh\frac{\partial z_b}{\partial x} \\ -\frac{\tau_{by}}{\rho} - gh\frac{\partial z_b}{\partial y} \end{bmatrix} \tag{2}$$

where h is the total water depth; u and v are depth-averaged velocity components in the x and y directions, respectively; g is the gravity acceleration; ρ is the density of water; z_b is the bed elevation above the datum; $\partial z_b/\partial x$ and $\partial z_b/\partial y$ represent the bed slope in the two Cartesian directions; and τ_{bx} and τ_{by} are the bed friction stresses, representing the effect of bed roughness on the flow and may be estimated by using the following empirical formulas:

$$\tau_{bx} = \rho C_f u\sqrt{u^2+v^2} \quad \text{and} \quad \tau_{by} = \rho C_f v\sqrt{u^2+v^2} \tag{3}$$

in which the bed roughness coefficient C_f can be evaluated using $C_f = gn^2/h^{1/3}$, where n is the Manning coefficient.

Even though they are widely used, however, Rogers et al. [17] demonstrated that the above formulation of the shallow water equations (Eqs. (1) and (2)) may not preserve a still water state of $u=0$ and $v=0$, but $h\neq 0$ in a domain with a nonuniform bed profile when they are solved using a finite-volume Godunov-type method incorporated with Roe's approximate Riemann solver. The proof can be extended to other approximate Riemann solvers (e.g., HLLC).

In order to cope with the problem, the vector terms in Eq. (2) are reformulated as follows:

$$\mathbf{u} = \begin{bmatrix} \eta \\ uh \\ vh \end{bmatrix} \quad \mathbf{f} = \begin{bmatrix} uh \\ u^2h + \frac{1}{2}g(\eta^2 - 2\eta z_b) \\ uvh \end{bmatrix}$$
$$\mathbf{g} = \begin{bmatrix} vh \\ uvh \\ v^2h + \frac{1}{2}g(\eta^2 - 2\eta z_b) \end{bmatrix} \quad \mathbf{s} = \begin{bmatrix} 0 \\ -\frac{\tau_{bx}}{\rho} - g\eta\frac{\partial z_b}{\partial x} \\ -\frac{\tau_{by}}{\rho} - g\eta\frac{\partial z_b}{\partial y} \end{bmatrix} \tag{4}$$

Taking the x-direction momentum equation as an example, the new formulation is essentially derived from the following relationship:

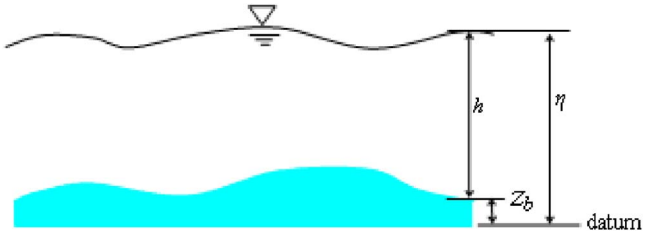

Fig. 1 Definition sketch of bed topography for the shallow water equations

$$\frac{g}{2}\frac{\partial h^2}{\partial x} + gh\frac{\partial z_b}{\partial x} = \frac{g}{2}\frac{\partial(\eta^2 - 2z_b\eta)}{\partial x} + g\eta\frac{\partial z_b}{\partial x} \tag{5}$$

In the above formulations, as shown in Fig. 1, η is defined as the surface elevation above the datum; the water depth is then evaluated by $h=\eta - z_b$.

The hyperbolic property of the new conservation law consisting of shallow water equations (Eqs. (1) and (4)) can be confirmed by examining the eigenstructures of the flux Jacobian. The new shallow water equations are mathematically balanced for the flux and source terms so that still water state can be automatically maintained. This can be easily demonstrated by considering a general case of motionless steady state of fluid with $u=0$ and $v=0$, but $h\neq 0$ in a domain with spatially varying bed bathymetry. The continuity equation is directly satisfied as $u=0$ and $v=0$. The x-direction momentum equation reduces to $(g/2)[\partial(\eta^2 - 2\eta z_b)/\partial x] = -g\eta(\partial z_b/\partial x)$ after eliminating all of the zero terms caused by the zero velocities. Under the wet-bed conditions ($h\neq 0$), η is a constant at a still steady state; hence, the x-direction momentum equation can be further simplified to $-g\eta(\partial z_b/\partial x) = -g\eta(\partial z_b/\partial x)$. This means that the equation is balanced and the initial steady state will be unconditionally conserved without any necessity to use special numerical techniques for treating source terms, provided that the bed slope term $\partial z_b/\partial x$ in both sides are discretized as $(z_{b_{i+1/2,j}} - z_{b_{i-1/2,j}})/\Delta x$, which is the case in the current numerical model. Herein, Δx is the grid size in the x direction, and $z_{bi+1/2,j}$ and $z_{bi-1/2,j}$ are the bed elevations at the right and left interfaces of a grid cell, respectively. A similar analysis can be applied to the y-direction momentum equation.

3 Numerical Models

The shallow water equations (Eqs. (1) and (4)) are solved using a finite-volume Godunov-type scheme. High resolution is achieved using a second-order Runge–Kutta integrating method. A finite-volume numerical scheme solves the integral form of the governing equations, resulting in the following explicit time-marching formula:

$$\mathbf{u}_{i,j}^{n+1} = \mathbf{u}_{i,j}^{n} - \frac{\Delta t}{\Delta x}(\mathbf{f}_{i+1/2,j}^{n} - \mathbf{f}_{i-1/2,j}^{n}) - \frac{\Delta t}{\Delta y}(\mathbf{g}_{i,j+1/2}^{n} - \mathbf{g}_{i,j-1/2}^{n}) + \Delta t\mathbf{s}_{i,j}^{n} \tag{6}$$

where the superscript n represents the time level; subscripts i and j are the cell indices in the x and y directions, respectively; Δt is the time step; Δy is the cell dimension in the y direction; $\mathbf{f}_{i+1/2,j}^{n}$, $\mathbf{f}_{i-1/2,j}^{n}$, $\mathbf{g}_{i,j+1/2}^{n}$, and $\mathbf{g}_{i,j-1/2}^{n}$ are the fluxes through the west, east, south and north cell interfaces, respectively.

Applying a second-order Runge–Kutta method, the time-marching formula (Eq. (6)) is rearranged to

$$\mathbf{u}_{i,j}^{n+1} = \mathbf{u}_{i,j}^{n} + \frac{1}{2}\Delta t(\mathbf{K}_{i,j}(\mathbf{u}^{n}) + \mathbf{K}_{i,j}(\mathbf{u}^{*})) \tag{7}$$

where $\mathbf{K}_{i,j}$ is defined by

$$\mathbf{K}_{i,j} = -\frac{\mathbf{f}_{i+1/2,j} - \mathbf{f}_{i-1/2,j}}{\Delta x} - \frac{\mathbf{g}_{i,j+1/2} - \mathbf{g}_{i,j-1/2}}{\Delta y} + \mathbf{s}_{i,j} \tag{8}$$

The intermediate flow variables are calculated, using a first-order scheme, from

$$\mathbf{u}^*_{i,j} = \mathbf{u}^n_{i,j} + \Delta t \mathbf{K}_{i,j}(\mathbf{u}^n) \tag{9}$$

In order to calculate $\mathbf{K}_{i,j}(\mathbf{u}^n)$ and $\mathbf{K}_{i,j}(\mathbf{u}^*)$, hence to update the flow variables at each time step, it is necessary to correctly evaluate the interface fluxes $\mathbf{f}_{i-1/2,j}$, $\mathbf{f}_{i+1/2,j}$, $\mathbf{g}_{i,j-1/2}$, and $\mathbf{g}_{i,j+1/2}$, which involves solving local Riemann problems in the context of a Godunov-type scheme. In this work, the HLLC approximate Riemann solver is adopted as it automatically accommodates a proper prediction of a wet-dry interface and is easy to implement. The implement of the HLLC approximate Riemann solver in a Godunov-type scheme is well documented in the literature (see, e.g., Refs. [20,21]).

When updating the flow variables in a new time step using the second-order Runge-Kutta method, we firstly compute $\mathbf{K}_{i,j}(\mathbf{u}^n)$ and then use Eq. (9) to predict the intermediate flow variables. Calculation of $\mathbf{K}_{i,j}(\mathbf{u}^n)$ involves applying the HLLC approximate Riemann solver to evaluate fluxes through all four cell interfaces and properly calculating the source terms, as indicated in Eq. (8). To solve a local Riemann problem at a cell interface, Riemann states at both sides of the interface are required. In the present numerical scheme, the flow variables are stored at the cell centers at each time step; therefore, a proper reconstruction approach is needed to establish the face values (Riemann states). Because a first-order accurate scheme is used when calculating the intermediate flow variables, the Riemann states are considered to be the same as the corresponding cell-centered values. For example, at the cell interface $i+1/2$, $\mathbf{u}_L = \mathbf{u}^n_{i,j}$ and $\mathbf{u}_R = \mathbf{u}^n_{i+1,j}$.

As the shallow water equations (Eqs. (1) and (4) are mathematically balanced, source terms are directly calculated at each cell center, and there is no need for any special numerical treatment. The bed slope terms $\partial z_b/\partial x$ and $\partial z_b/\partial y$ are evaluated using a central difference (second-order accurate). For example, the source terms in the x direction are calculated by

$$-\frac{\tau_{bx}}{\rho} - g\eta\frac{\partial z_b}{\partial x} = -\left(\frac{\tau_{bx}}{\rho}\right)^n_{i,j} - g\eta^n_{i,j}\left(\frac{z_{bi+1/2,j} - z_{bi-1/2,j}}{\Delta x}\right) \tag{10}$$

Once the interface fluxes and source terms are properly evaluated, the intermediate flow variables $\mathbf{u}^*_{i,j}$ can then be predicted using Eq. (9). It is noted that a first-order accurate Godunov-type scheme can be obtained if the flow variables in Eq. (9) are directly updated to the new time step. Therefore, a useful feature of the current shallow flow model is that a switch between first-order and second-order accurate schemes is straightforward.

$\mathbf{K}_{i,j}(\mathbf{u}^*)$ is evaluated based on intermediate flow variables $\mathbf{u}^*$, in a similar way to that used for calculating $\mathbf{K}_{i,j}(\mathbf{u}^n)$. The only difference is that a spatially second-order accurate scheme is used when estimating the Riemann states at each cell interface. In a finite-volume method, this can be realized by using a linear interpolation to reconstruct the face values from the cell-centered flow variables. In order to prevent spurious oscillations that would occur near discontinuous solutions (steep gradient) in a second- or higher-order accurate numerical scheme, a minmod slope limiter is used together with the linear reconstruction to compute the Riemann states (see, e.g., Ref. [21]). Then the interface fluxes can again be evaluated using the HLLC approximate Riemann solver. Together with a proper computation of source terms (based on $\mathbf{u}^*$), $\mathbf{K}_{i,j}(\mathbf{u}^*)$ can be calculated using Eq. (8), and the flow variables can be updated to a new time step using Eq. (7).

The current numerical scheme is explicit, and its stability property is controlled by the Courant–Friedrichs–Lewy (CFL) criterion, which can be used for predicting an appropriate time step Δt for a new iteration,

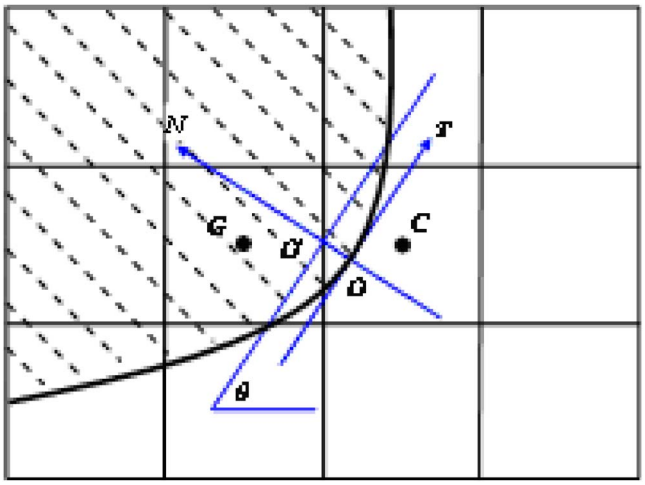

Fig. 2 Local boundary modification method for a Cartesian grid model. (*a*) Free surface elevation. (*b*) Velocity.

$$\Delta t = C \min(\Delta t_x, \Delta t_y) \tag{11}$$

with

$$\Delta t_x = \min_{i,j}\left(\frac{\Delta x_{i,j}}{|u_{i,j}| + \sqrt{g h_{i,j}}}\right) \text{ and } \Delta t_y = \min_{i,j}\left(\frac{\Delta y_{i,j}}{|v_{i,j}| + \sqrt{g h_{i,j}}}\right)$$

where C is the Courant number specified in the range $0 < C \leqslant 1$ and is set to 0.8 for all of the test cases in this work to ensure stability.

In this work, two types of boundary conditions are used, i.e., transmissive and reflective (slip) boundary conditions. For a normal transmissive boundary, including inflow and outflow, fictional values of flow variables at a ghost cell are given by

$$h_B = h_I \quad \hat{u}_B = \hat{u}_I \quad \hat{v}_B = \hat{v}_I \tag{12}$$

where $\hat{u}$ and $\hat{v}$ are the depth-averaged velocity components normal and tangential to the boundary. Subscripts B and I denote the values of flow variables at the ghost and inner boundary cells, respectively.

In the case of slip boundary conditions, if the boundary happens to align with the cell face, the flow values at the ghost cell are directly given by

$$h_B = h_I \quad \hat{u}_B = -\hat{u}_I \quad \hat{v}_B = \hat{v}_I \tag{13}$$

which predicts a zero normal velocity component through the boundary. However, in a general situation, a computational domain could be complicated, and the boundary curves may not align with cell faces. A Cartesian grid can only provide a "staircase" approximation to such boundaries. The staircases compromise the accuracy of numerical predictions. Even worse, they may locally produce spurious flow circulations and ruin the results.

In order to provide better numerical solutions near a nonaligned boundary, a simple local boundary modification method is implemented in the current model. This method can be classified as an immersed boundary approach (e.g., Refs. [22,23]). In the ghost-cell immersed boundary method introduced by Tseng and Ferziger [23], the value of a flow variable in a ghost cell is interpolated from those values in neighbor cells in conjunction with appropriate boundary conditions. Using the current simple method for a boundary treatment, the flow values in a ghost cell are calculated directly from those flow variables in the boundary cell under consideration. As shown in Fig. 2 a boundary curve cuts the Cartesian computational grid into two parts, where the shadowed part is the solid area outside of the computational domain and the other part is the fluid area. A cell with its center located in the solid area is called a solid cell. Otherwise, a cell is defined as a fluid cell (with

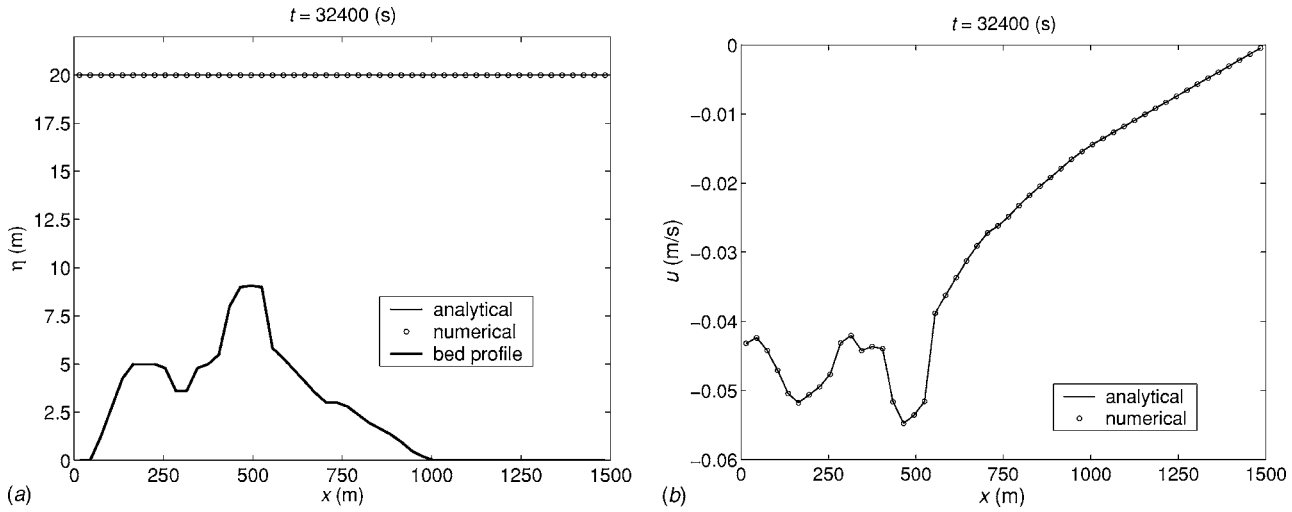

Fig. 3 Tidal wave propagating in a channel with an irregular bed profile

cell center inside the fluid area). The computational domain consists of all the fluid cells. Those fluid cells neighboring one or more solid cells are defined as boundary fluid cells (e.g., Cell C in Fig. 2). The local boundary modification method applies to all the boundary fluid cells whenever ghost values are required. Taking Cell C in Fig. 2 as an example, slip boundary conditions require a zero normal velocity component on the boundary. In practical computation on a Cartesian grid without a special boundary treatment, the boundary point is assumed to be at the midpoint (O') of a cell face next to the boundary curve. Flow variable values are directly given by Eq. (13), which would cause inaccuracy. Herein, a simple method is proposed, where the first step is to find the boundary point (O) that is closest to O'. The angle θ is identified to define the tangential at point O. Then, it is assumed that the boundary point O migrates to O', and slip boundary conditions require a velocity component normal to the tangential equal to zero. After decomposing the velocity components at the tangential and normal directions, slip boundary conditions can be expressed as

Normal direction:

$$-u_C \sin\theta + v_C \cos\theta = -(-u_G \sin\theta + v_G \cos\theta) \tag{14}$$

Tangential direction:

$$u_C \cos\theta + v_C \sin\theta = u_G \cos\theta + v_G \sin\theta$$

Solving these simple equations gives the Cartesian velocity components at the ghost cell, and the slip boundary conditions are now given by

$$\zeta_G = \zeta_C \quad u_G = u_C - 2(u_C \sin\theta - v_C \cos\theta)\sin\theta$$
$$v_G = v_C + 2(u_C \sin\theta - v_C \cos\theta)\cos\theta \tag{15}$$

Despite its simplicity, it will be demonstrated that this local boundary modification method is effective and accurate. Another important feature is that the method has no effect on computational efficiency.

4 Results and Discussion

In this section, the high-resolution shallow water equation solver described above is validated against four benchmark test cases, and numerical predictions are compared with analytical solutions, alternative numerical results, and experimental measurements, where available. In all of the simulations, $g=9.81\ \mathrm{m/s^2}$ and $\rho=1000\ \mathrm{kg/m^3}$.

4.1 Wave Propagating in a Channel With an Irregular Bed Profile. The first test is about an analytical wave propagating in a channel with an irregular bed profile, which was proposed at a workshop on dam-break simulations [24] and reconsidered by Zhou et al. [16]. This case can be considered as an idealization of a coastal tidal wave traveling upstream through a river mouth.

This is actually a 1D problem occurring in a frictionless channel of $L=1500$ m long, with the wave defined by

$$h(x,t) = 20 - z_b(x) - 4\sin\left[\pi\left(\frac{4t}{86{,}400} + \frac{1}{2}\right)\right]$$
$$u(x,t) = \frac{(x-L)\pi}{5400h(x,t)}\cos\left[\pi\left(\frac{4t}{86{,}400} + \frac{1}{2}\right)\right] \tag{16}$$

The present 2D model is directly applied to simulate this tidal flow on a 50×5 uniform grid with $\Delta x=\Delta y=30$ m. The water is initially still with a surface elevation $\eta=20$ m. $h(0,t)$ and $u(0,t)$ are imposed at the western inflow boundary. At the eastern outflow boundary, $u(L,t)=0$, which leads to a no flow boundary. Figure 3 presents the comparison of predicted water surface elevation and velocity with analytical solutions at $t=32{,}400$ s. The irregular bed profile $z_b(x)$ is also indicated in Fig. 3(a). Both the surface elevation and velocity profiles agree very well with the analytical solutions. This confirms the capability of the current balanced governing equations and the corresponding numerical scheme in simulating unsteady flow over a complex bed topography.

4.2 Oblique Hydraulic Jump. The second test is to simulate a steady hydraulic jump developed when a unidirectional supercritical flow in an open channel is contracted by an inclined solid wall. In a $40\times30\ \mathrm{m^2}$ frictionless channel with a flat bed, a uniform flow occurs with water depth and velocity being 1 m and 8.57 m/s, respectively, which give a supercritical flow with a Froude number of 2.74. Now the southern channel wall is modified so that, starting from $x=10$ m, it inclines inward with an angle of 8.95 deg to the x direction. Under the new channel configuration, the fast moving supercritical flow reflects from the southern inclined wall and forms an oblique hydraulic jump. Theoretically, the jump starts from $x=10$ m and crosses the channel at an angle of 30 deg to the x direction. Water depth changes abruptly from 1.0 m to 1.5 m after the jump.

Because the southern channel wall is not aligned with the cell face, this case actually validates the simple local boundary modification method for treating the nonaligned boundary problem.

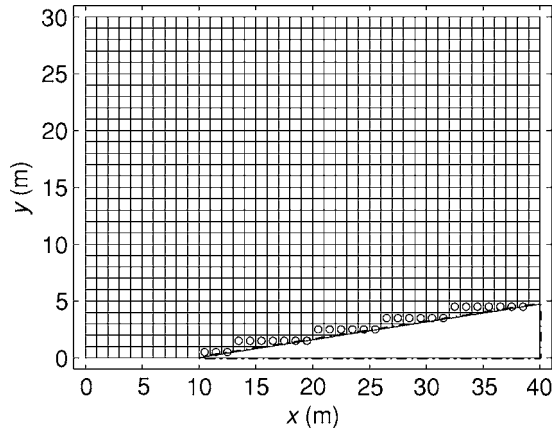

Fig. 4 Oblique hydraulic jump: sample computational grid

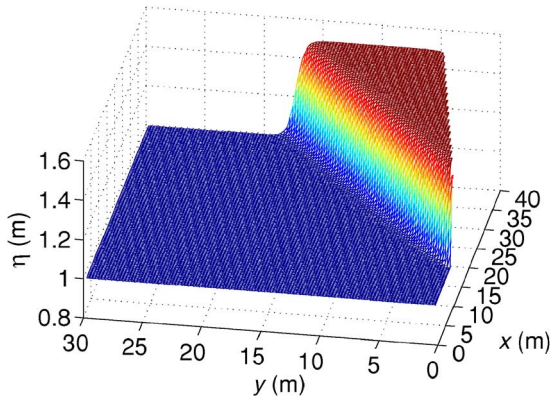

Fig. 6 Oblique hydraulic jump: 3D water surface predicted on a 160×120 grid

Rogers et al. [25] suggested that a Cartesian grid method with a staircase approximation of the inclined boundary wall could not reproduce accurately the steady hydraulic jump in this case. In the current simulation, a sample grid, consisting of 40×30 cells, is illustrated in Fig. 4, in which the boundary fluid cells are marked by small circles; the simple local boundary modification method is applied to these cells. Slip boundary conditions are imposed on the southern boundary wall. The northern channel wall is assumed to be open. Inflow boundary conditions assume $u=8.57$ m/s and $h=1$ m at the western end of the channel. The eastern boundary is set to be outflow without specifying any flow condition. Starting from the initial flow with uniform depth and velocity, the model is run until a steady state is reached. The steady state is indicated by a global relative error R defined by

$$R=\sqrt{\sum_{i,j}\left(\frac{h_{i,j}^{n}-h_{i,j}^{n-1}}{h_{i,j}^{n}}\right)^{2}} \tag{17}$$

where $h_{i,j}^{n}$ and $h_{i,j}^{n-1}$ are the water depth of the current and previous time steps at cell (i,j). The solution is considered to be steady state if $R<1\times10^{-8}$.

Simulation is firstly carried out on a 160×120 grid. Figure 5 shows the convergence history, in which numerical solution takes about 15 s to converge to a steady state. Figure 6 presents the predicted 3D water surface elevation. A steady hydraulic jump is observed to be properly predicted, across which the water depth changes suddenly from 1 m to 1.5 m. The numerical solution near the inclined wall is smooth and gives a correct water depth of 1.5 m, implying the effectiveness and accuracy of the local boundary modification method. Figure 7 shows the velocity vectors near the inclined boundary wall. The velocities occupy the tangential direction while maintaining their magnitude when they come close to the wall, which is physically correct according to the slip boundary conditions. Figure 8 illustrates the depth contours and the water surface profiles along the central line of the domain, predicted on three different grids with 40×30, 80×60, and 160×120 cells, respectively. The correct position of the jump (indicated by the dashed line in the graphs of depth contours) is accurately predicted on all three grids. The sharp-fronted water surface caused by the hydraulic jump appears to converge to a discontinuous solution as the grid becomes finer.

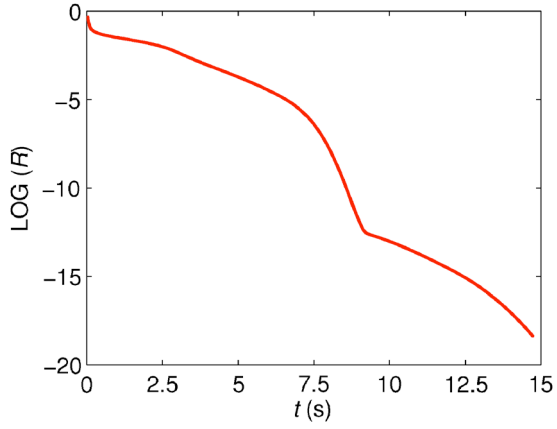

Fig. 5 Oblique hydraulic jump: convergence history

For the purpose of comparison, simulation is also run on a 160×120 grid without implementing the local boundary modification method; i.e., the inclined boundary wall is approximated by staircases. The convergence history is illustrated in Fig. 9. Obviously, it takes a much longer time (more than twice as long) to achieve a steady state. Figure 10 presents the 3D water surface and depth contours. The solution near the inclined wall is obviously smashed, and "spikes" are predicted. The location of the jump is also wrongly predicted. Similar results were presented by Rogers et al. [25] using an adaptive quadtree grid based shallow water equation solver with a fine mesh used near the inclined boundary wall. Figure 11 presents those velocity vectors near the inclined channel wall. Velocities significantly decrease in magnitude at those boundary cells. Numerical viscosity is apparently introduced into the solution and causes the flow to "wiggle," resulting in an unreliable prediction. Therefore, without a proper boundary treatment, a numerical model based on a Cartesian grid may not be applicable to certain cases in practice. This again validates the local boundary modification method and confirms that, despite its simplicity, the method is accurate and robust. This simple method is directly applicable to a general case with a more complicated geometry.

4.3 Hydraulic Jump and Drop. This case, also considered by Zhou and Stansby [6], is a useful test to validate a numerical scheme's capability to deal with complex flow situations with source terms. The test occurs in a channel 30.5 m long, with a

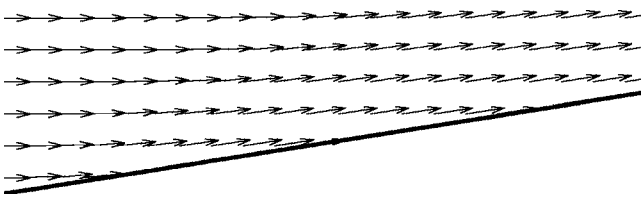

Fig. 7 Oblique hydraulic jump: velocity vectors near the inclined wall. (*a*) 40×30 grid, (*b*) 80×60 grid, and (*c*) 160×120 grid.

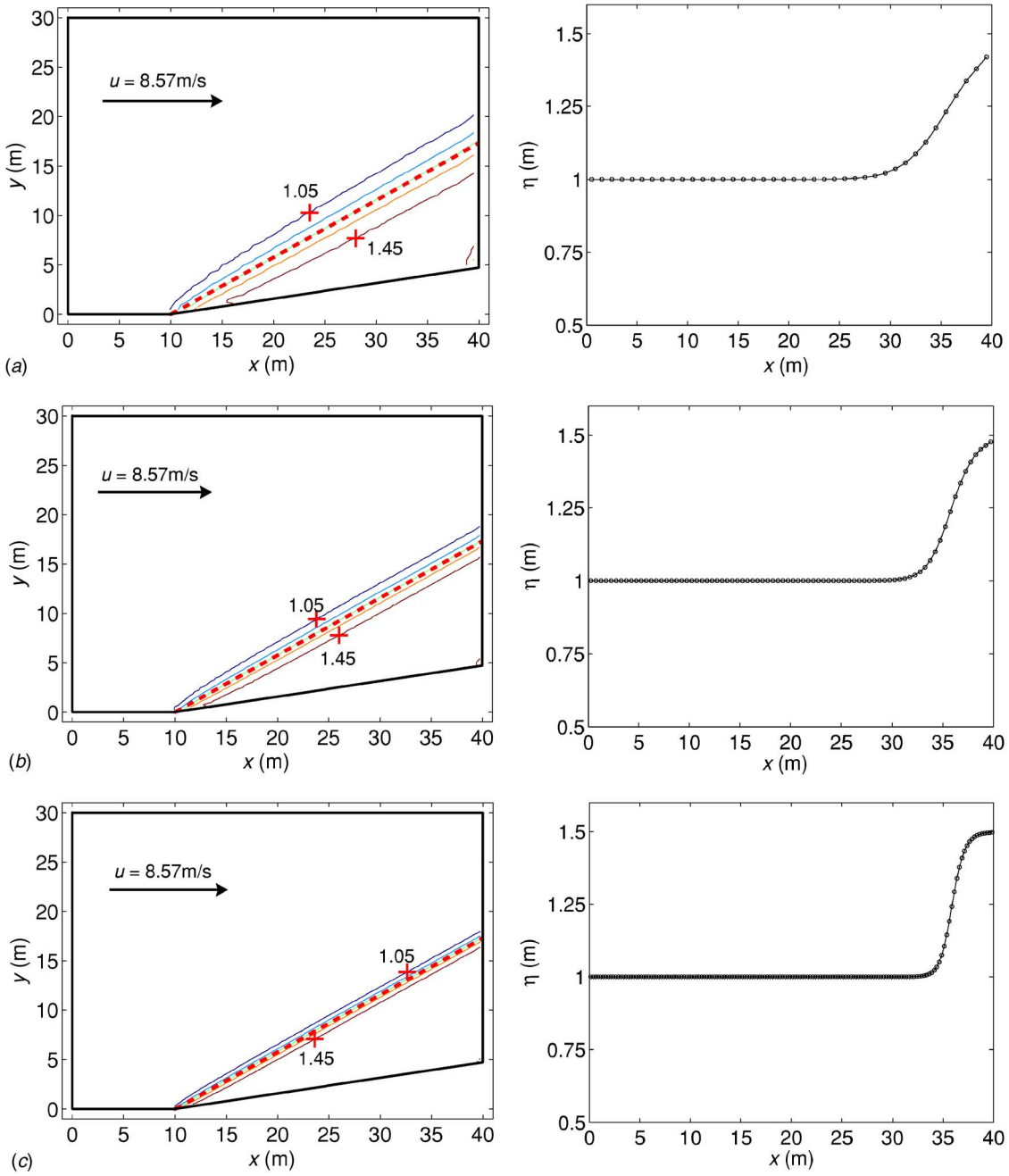

Fig. 8 Oblique hydraulic jump: depth contours and central water surface profiles on different grids

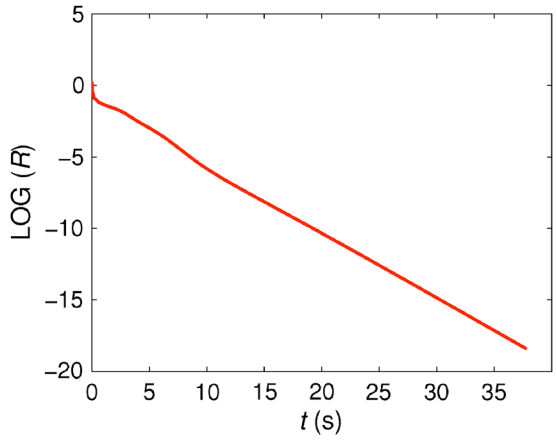

Fig. 9 Oblique hydraulic jump: convergence history for the case without a boundary treatment

nonuniform bed profile in the longitudinal direction. The upstream section of 14.5 m long is horizontal, and the downstream part 16 m long has a bed slope of $S=0.03$. The inflow conditions at the western end of the channel are $u=3.571$ m/s and $h=0.06$ m, which give a Froude number of Fr=4.65. The Manning's coefficient is $n=0.019$ $m^{1/3}$ s^{-1}. A highly complex flow profile is developed under these conditions. The incoming supercritical flow joins the subcritical flow developed in the horizontal reach through a hydraulic jump. As the bed slope changes from horizontal to $S=0.03$ (steep slope under the current conditions), the flow will eventually develop into a supercritical flow. The only way to connect the subcritical flow in the horizontal reach and the downstream supercritical flow is through a hydraulic drop. Reproducing these complex flow features could be a crucial task for a numerical model.

Numerical simulation is carried out on a 61×5 uniform grid with $\Delta x=\Delta y=0.5$ m. This gives a channel width of 2.5 m. The

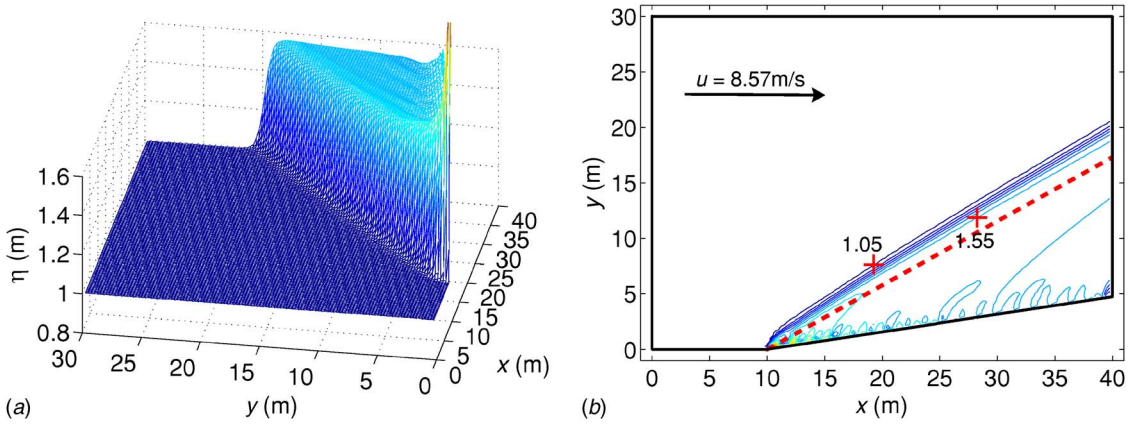

Fig. 10 Oblique hydraulic jump: results without a boundary treatment

dimension in the y direction does not affect the numerical results as this is actually a 1D problem. No specific conditions are needed at the eastern outflow boundary as the flow automatically evolves into a supercritical flow after the hydraulic drop. Slip boundary conditions are assumed at the northern and southern channel walls. Initially, the water depth and velocity in the entire domain are assumed to be the same as those prescribed at the inflow boundary.

The numerical model is run until $t=270$ s after the steady-state solution is achieved, again defined by $R<1\times10^{-8}$. Figure 12 illustrates the convergence history. Figure 13 shows the water surface profile along the central line of the channel, comparing with an analytical solution obtained by numerically integrating the general equation of gradually varied flow incorporated with the hydraulic jump formula [26]. The surface profile is characterized mainly by a hydraulic jump in the horizontal channel reach and a hydraulic drop around the turning point where the bed slope changes from horizontal to steep. Before the jump, the inflow depth increases through an H3 profile until the first sequent depth of the jump is reached. After the jump and before the drop, an H2 profile is developed. After the drop, an S2 curve transits the flow to the supercritical flow depth corresponding to the prescribed flow conditions. The resulting profile is as expected and agrees well with the analytical approximation.

4.4 Dam Break in a Channel With a Local Constriction. The current numerical model is used to reproduce an experimental dam-break wave through a channel with a local constriction, proposed by the CADAM workshop [24]. The experimental setup is illustrated in Fig. 14, in which a 0.5 m wide horizontal channel is separated into a reservoir and floodplain by a gate (dam) at 6.1 m downstream of the western boundary. A channel constriction of 1.0 m long and 0.1 m wide is installed at 7.9 m downstream of the gate. After the constriction, the channel returns back to the original width. All the transition walls are in 45 deg with the channel walls.

Initially, still water is 0.3 m deep upstream of the gate, and the floodplain downstream of the gate is wetted by 0.003 m deep still water. Western, northern, and southern boundaries are assumed to be reflective walls. Transmissive boundary conditions are imposed at the eastern boundary. The Manning's coefficient is set to

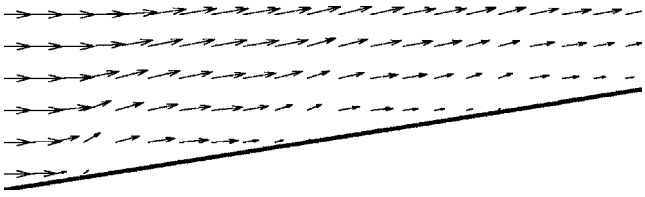

Fig. 11 Oblique hydraulic jump: velocity vectors near the inclined wall without a boundary treatment

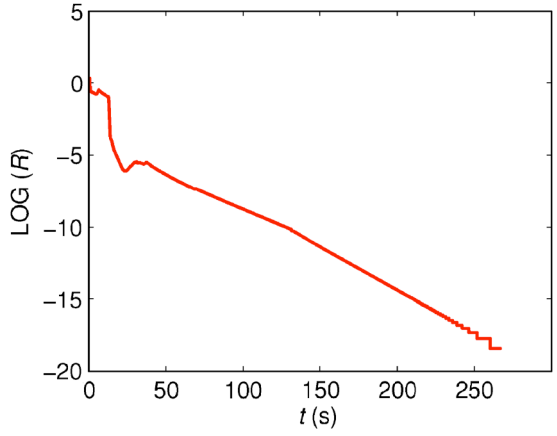

Fig. 12 Hydraulic jump and drop: convergence history

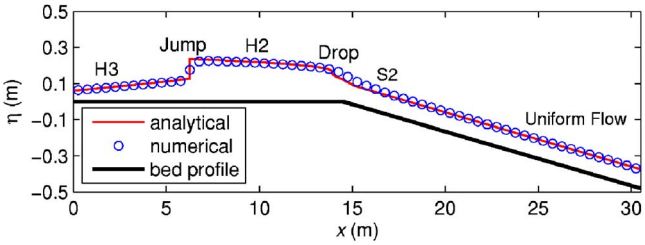

Fig. 13 Hydraulic jump and drop: surface profile

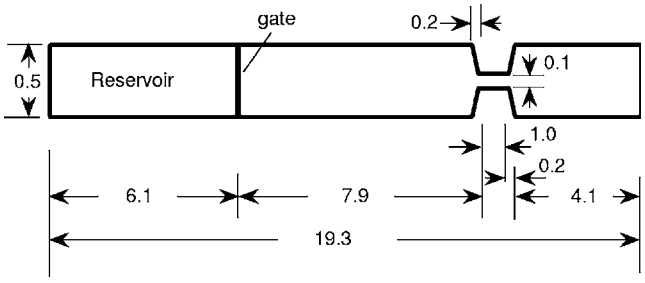

Fig. 14 Dam break: experimental setup

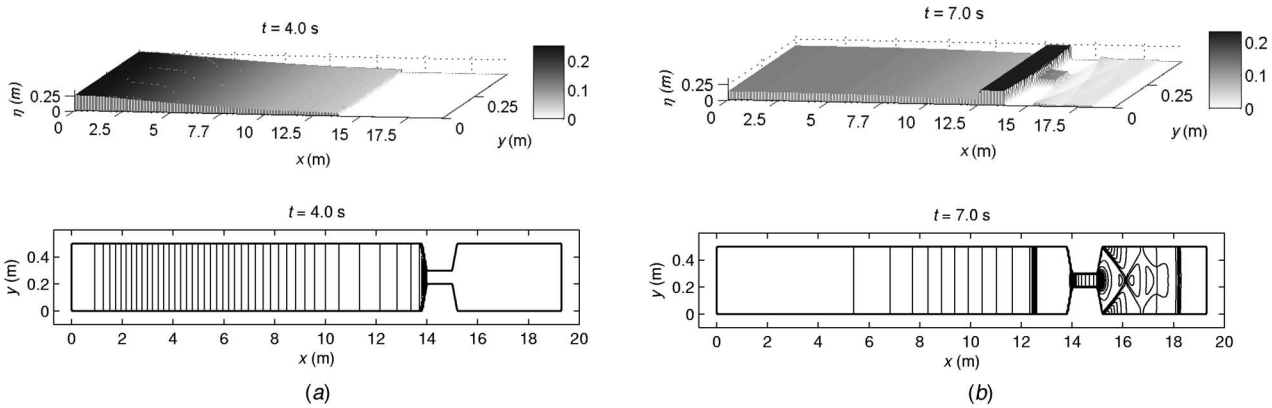

Fig. 15 Dam break: 3D surface elevation and depth contours at different output times. (*a*) *t*=4.0 s and (*b*) *t*=7.0 s.

0.01 $m^{1/3}$ s^{-1} in the entire domain. The gate is removed entirely at $t=0$.

Numerical simulation of the dam-break waves is carried out on a uniform grid with $\Delta x=0.05$ m and $\Delta y=0.0125$ m. The predicted 3D water surface elevation and corresponding depth contours are presented in Fig. 15 at sample output times. After a sudden collapse of the dam, a wall of water rapidly propagates downstream as a shock-type wave. Associated with the shock front, a rarefaction is formed and travels upstream. The shock front reaches the channel constriction at $t=4$ s and a reflected shock is immediately developed and starts to propagate upstream. Part of the original shock front passes through the constriction and continues to travel downstream toward the eastern boundary. Complicated wave patterns are formed due to wave diffraction and interactions. The time history of water surface elevation is recorded at four gauge points located at 1.0 m upstream the gate, 6.1 m, 8.6 m, and 10.5 m downstream the gate, respectively, along the central line of the channel. Figure 16 shows the comparison of predicted time histories and experimental measurements. The arrival time of shock front is accurately predicted, which is essential for dam-break wave simulation [27]. The numerical predictions generally

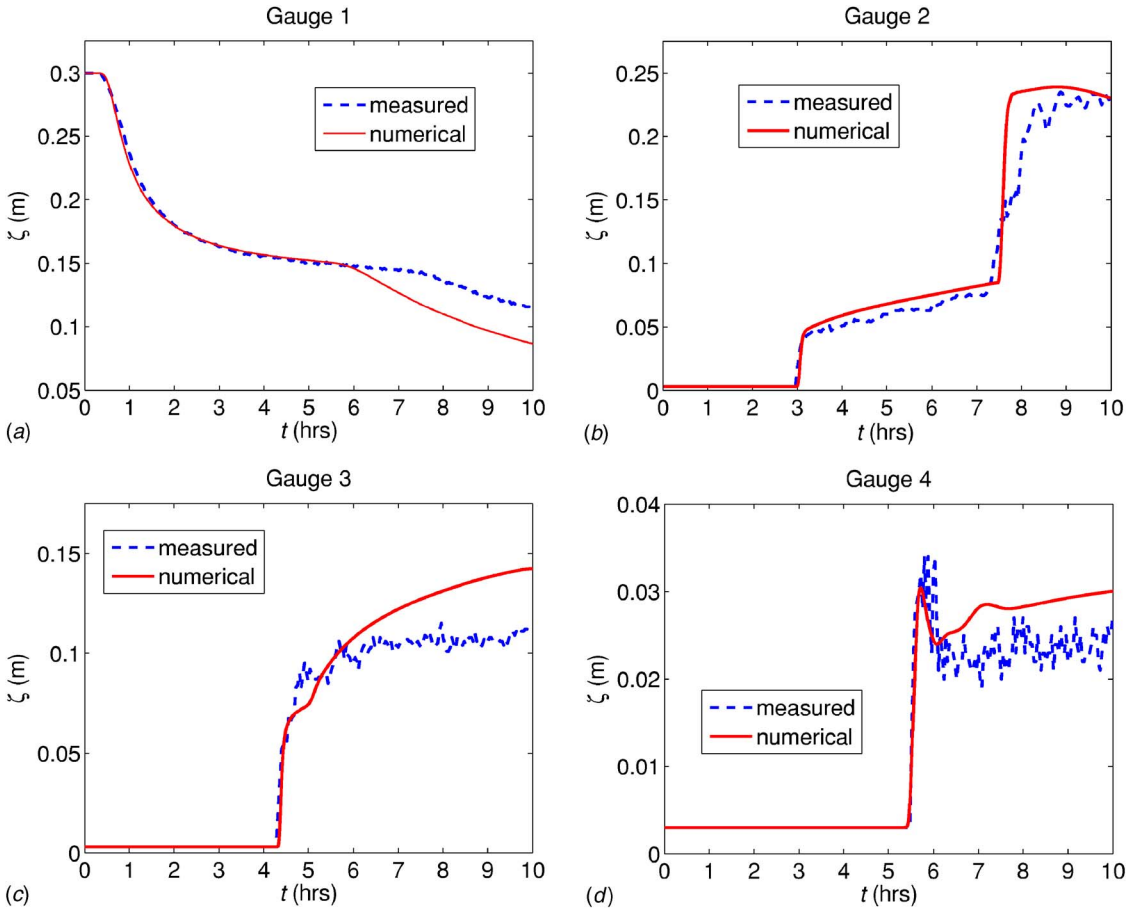

Fig. 16 Dam break: comparison between the predicted time history of water surface elevation and experimental measurements at four gauge points. (*a*) Gauge 1. (*b*) Gauge 2. (*c*) Gauge 3. (*d*) Gauge 4.

agree with the numerical data. Certain discrepancies are also predicted by Goutal and Maurel [27] using a different numerical approach.

5 Conclusions

This paper has presented a shallow flow model, NewChan, developed for simulating complex open channel flows. Herein, we highlight two new features of the model, which are the new flux and source term balanced shallow water equations for simulations on domains with irregular bed topography and the simple local modification method for treating curved boundary problems. The new hyperbolic formulation of the balanced shallow water equations is solved using a high-resolution finite-volume Godunov-type method incorporated with the HLLC approximate Riemann solver on Cartesian uniform grids. Second-order accuracy of the numerical scheme is achieved by a Runge–Kutta time integrating approach. The model is validated against several benchmark tests, and the results compare very well with theoretical, alternative numerical solutions and/or experimental measurements. Even though the model is designed for simulating complex open channel flows, it is a robust, efficient, and accurate numerical tool directly applicable to predict shallow flow hydrodynamics in more general cases, e.g., flows in the rivers, lakes, estuaries, etc. In the future, upon proper implementation of a numerical technique for wetting and drying, NewChan can also be used for flood simulation, e.g., predicting flood flows onto floodplains through a breach of a flood defense.

References

[1] Glaister, P., 1993, "Flux Difference Splitting for Open-Channel Flows," Int. J. Numer. Methods Fluids, **16**, pp. 629–654.

[2] Molls, T., and Chaudhry, M. H., 1995, "Depth-Averaged Open-Channel Flow Model," J. Hydraul. Eng., **121**(6), pp. 453–465.

[3] Meselhe, E. A., Sotiropoulos, F., and Holly, F. M., Jr., 1997, "Numerical Simulation of Transcritical Flow in Open Channels," J. Hydraul. Eng., **123**(9), pp. 774–783.

[4] Delis, A. I., and Skeels, C. P., 1998, "TVD Schemes for Open Channel Flow," Int. J. Numer. Methods Fluids, **26**, pp. 791–809.

[5] Hu, K., Mingham, C. G., and Causon, D. M., 1998, "A Bore-Capturing Finite Volume Method for Open-Channel Flows," Int. J. Numer. Methods Fluids, **28**, pp. 1241–1261.

[6] Zhou, J. G., and Stansby, P. K., 1999, "2D Shallow Water Flow Model for the Hydraulic Jump," Int. J. Numer. Methods Fluids, **29**, pp. 375–387.

[7] Causon, D. M., Mingham, C. G., and Ingram, D. M., 1999, "Advances in Calculation Methods for Supercritical Flow in Spillway Channels," J. Hydraul. Eng., **125**(10), pp. 1039–1050.

[8] Yang, G., Causon, D. M., Ingram, D. M., Saunders, R., and Batten, P., 1997, "A Cartesian Cut Cell Method for Compressible Flows Part A: Static Body Problems," Aeronaut. J., **101**(1002), pp. 47–56.

[9] Causon, D. M., Ingram, D. M., Mingham, C. G., Yang, G., and Pearson, R. V., 2000, "Calculation of Shallow Water Flows Using a Cartesian Cut Cell Approach," Adv. Water Resour., **23**, pp. 545–562.

[10] Liang, Q., Zang, J., Borthwick, A. G. L., and Taylor, P. H., 2007, "Shallow Flow Simulation on Dynamically Adaptive Cut-Cell Quadtree Grids," Int. J. Numer. Methods Fluids, **53**(12), pp. 1777–1799.

[11] Bermudez, A., and Vázquez, M. E., 1994, "Upwind Methods for Hyperbolic Conservation Laws With Source Terms," Comput. Fluids, **23**(8), pp. 1049–1071.

[12] LeVeque, R. J., 1998, "Balancing Source Terms and Flux Gradients in High-Resolution Godunov Methods: The Quasi-Steady Wave-Propagation Algorithm," J. Comput. Phys., **146**(1), pp. 346–365.

[13] Vázquez-Cendón, M. E., 1999, "Improved Treatment of Source Terms in Upwind Schemes for the Shallow Water Equations in Channels With Irregular Geometry," J. Comput. Phys., **148**(2), pp. 497–526.

[14] Hubbard, M. E., and García-Navarro, P., 2000, "Flux Difference Splitting and the Balancing of Source Terms and Flux Gradients," J. Comput. Phys., **165**(1), pp. 89–125.

[15] García-Navarro, P., and Vázquez-Cendón, M. E., 2000, "On Numerical Treatment of the Source Terms in the Shallow Water Equations," Comput. Fluids, **29**, pp. 951–979.

[16] Zhou, J. G., Causon, D. M., Mingham, C. G., and Ingram, D. M., 2001, "The Surface Gradient Method for the Treatment of Source Terms in the Shallow-Water Equations," J. Comput. Phys., **168**(1), pp. 1–25.

[17] Rogers, B. D., Borthwick, A. G. L., and Taylor, P. H., 2003, "Mathematical Balancing of Flux Gradient and Source Terms Prior to Using Roe'S Approximate Riemann Solver," J. Comput. Phys., **192**(2), pp. 422–451.

[18] Brufau, P., García-Navarro, P., and Vázquez-Cendón, M. E., 2002, "A Numerical Model for the Flooding and Drying of Irregular Domains," Int. J. Numer. Methods Fluids, **39**, pp. 247–275.

[19] Begnudelli, L., and Sanders, B. F., 2006, "Unstructured Grid Finite-Volume Algorithm for Shallow-Water Flow and Scalar Transport With Wetting and Drying," J. Hydraul. Eng., **132**(4), pp. 371–384.

[20] Toro, E. F., 2001, *Shock-Capturing Methods for Free-Surface Shallow Flows*, Wiley, Chichester.

[21] Liang, Q., Borthwick, A. G. L., and Stelling, G., 2004, "Simulation of Dam- and Dyke-Break Hydrodynamics on Dynamically Adaptive Quadtree Grids," Int. J. Numer. Methods Fluids, **46**(2), pp. 127–162.

[22] Ye, T., Mittal, R., Udaykumar, H. S., and Shyy, W., 1999, "An Accurate Cartesian Grid Method for Viscous Incompressible Flows With Complex Immersed Boundaries," J. Comput. Phys., **156**(2), pp. 209–240.

[23] Tseng, Y.-H., and Ferziger, J. H., 2003, "A Ghost-Cell Immersed Boundary Method for Flow in Complex Geometry," J. Comput. Phys., **92**, pp. 593–623.

[24] 1997, *Proceedings of the Second Workshop on Dam-Break Wave Simulation*, edited by N. Goutal and F. Maurel, Département Laboratoire National d'Hydraulique, Groupe Hydraulique Fluviale Electricité de France, France, Paper No. HE 43/97/016/B.

[25] Rogers, B. D., Fujihara, M., and Borthwick, A. G. L., 2001, "Adaptive Q-Tree Godunov-Type Scheme for Shallow Water Equations," Int. J. Numer. Methods Fluids, **35**, pp. 247–280.

[26] Chow, V. T., 1959, *Open Channel Hydraulics*, McGraw-Hill, New York.

[27] Goutal, N., and Maurel, F., 2002, "A Finite Volume Solver for 1D Shallow-Water Equations Applied to an Actual River," Int. J. Numer. Methods Fluids, **38**, pp. 1–19.

Incipience of Liquid Entrainment From a Stratified Gas-Liquid Region in Multiple Discharging Branches

R. C. Bowden

I. G. Hassan[1]
e-mail: ibrahimh@alcor.concordia.ca

Department of Mechanical
and Industrial Engineering,
Concordia University,
Montreal, QC, H3G 2W1, Canada

The onset of liquid entrainment in discharging branches, from a stratified gas-liquid region, has implications in industrial applications where safety is of concern. The onset criterion was characterized by the critical height, the vertical distance from the discharge inlet to the gas-liquid interface, and was shown to be a function of the Froude number. The critical height signified a transition in the discharging flow quality from a single phase gas to a two-phase gas-liquid mixture. The onset of liquid entrainment with multiple discharging branches, and a stratified gas-liquid region, was experimentally investigated using air and water. A test section with a semicircular cross section and three discharging branches at 0 deg*,* 45 deg*, and* 90 deg *was used. The critical height was recorded using both increasing and decreasing liquid level methods, thereby demonstrating surface tension and wetness effects. A total of eight cases were investigated for single, dual, and triple discharges, with onset occurring in the branch closest to and above the gas-liquid interface. Wall curvature effects were discussed through comparison with previous flat wall studies. Agreement between previously developed analytical models and the decreasing liquid level results was found.* [DOI: 10.1115/1.2813138]

Keywords: onset of liquid entrainment, multiple discharges, stratified gas-liquid

1 Introduction

A two-phase fluid flowing through a device intended for single phase flow—which includes pumps, compressors, turbines, and heat exchangers—can have alarmingly detrimental effects. The performance and reliability of these devices can be affected by two-phase flow. Reservoirs are commonly used to store fluid between the various devices in a pressurized system. An engineer may, for example, design a reservoir that both receives and supplies fluid to the devices within the system. The reservoir maintains a designed inlet condition for the device, for example, a single phase fluid. In certain instances, the designed inlet condition can be compromised by an unforeseen failure in the system, causing two phases to be present in the reservoir, and potentially the device. An industrial example where this can occur is the Canada deuterium and uranium (CANDU) nuclear reactor. The CANDU reactor incorporates a fluid distribution system whereby coolant flows from a large reservoir (known as the header) through a network of pipes (known as feeders) to the reactor fuel channels. A break in the distribution network, or a pump failure, can cause a two-phase environment to occur within the header. This, in turn, can lead to the gas phase entraining into the feeder branches, where liquid flows under normal operation, resulting in a two-phase mixture to flow into the fuel channels. The two-phase flow impacts the designed cooling effectiveness, and can lead to an increase in the reactor core temperature. Not too surprisingly, a rise in core temperature poses serious safety concerns. Such potentially catastrophic scenarios are known as loss-of-coolant accidents (LOCAs), and considerable efforts have been made to understand and prevent them.

1.1 Single Discharge Studies. Zuber [1] studied the presence of two phases in reservoirs, with a single discharging flow, and revealed two occurring phenomena. If the gas-liquid interface was above the discharge inlet, gas was entrained into the discharge flow at a critical height, called the onset of gas entrainment (OGE). If the interface was below the discharge inlet, liquid was entrained into the discharge flow at a critical height, called the onset of liquid entrainment (OLE). Following Ref. [1], several authors investigated the OLE in a single discharging branch with a variety of geometries, fluids, and flow conditions.

Smoglie and Reimann [2] experimented with a single discharging branch located on the side of a horizontal pipe. The pipe flow was stratified using water and air at an operating pressure of 0.5 MPa. They demonstrated a relationship between the critical height and the discharge Froude number. Following this, several authors performed similar single discharge experiments under a variety of conditions, fluids, discharge branch diameters, and orientations [3–5]. Their correlated results demonstrated a similar relationship between the critical height and the Froude number, but with slightly varying coefficients. Of interest, Hassan et al. [5] used two methods to record the critical height at the OLE. They found that the critical height was affected by whether the interface was increasing or decreasing. They reported that the critical height was always slightly higher with a decreasing liquid level.

1.2 Dual Discharge Studies. The impact of a second simultaneously discharging branch on the critical height was investigated by several authors. These studies were carried out with two discharges located on a flat wall exposed to a smooth-stratified two-phase environment. Armstrong et al. [6] investigated experimentally, and theoretically, two discharging branches aligned vertically on a flat wall. They studied the effects of the branch centerline separating distance and discharge Froude number. In their experiments, they used water and air at an operating pressure of 310 kPa, with the interface located below both branches. The OLE was found to occur in the branch closest to the gas-liquid interface. Their analytical model was derived by considering both

[1]Corresponding author.

Contributed by the Fluids Engineering Division of ASME for publication in the JOURNAL OF FLUIDS ENGINEERING. Manuscript received December 29, 2005; final manuscript received July 17, 2007; published online December 19, 2007. Review conducted by Timothy J. O'Hern.

discharges as point sinks in a potential flow field. They demonstrated reasonable agreement between their model and experimental results in the ranges considered. Following, experimental investigations were performed with two discharging branches, in various orientations on a flat vertical wall [7–9]. A theoretical model was also established by Hassan et al. [10] for two branches on a flat inclined wall, and Maier et al. [11] for two branches on a flat vertical wall. Both considered the branches to have a finite diameter and showed improved accuracy over the point-sink model at lower Froude numbers as the physical limits were approached.

1.3 Triple Discharge Studies. An experimental investigation of discharge quality and mass flow rate with multiple discharging branches on a curved surface, from a stratified environment, was performed by Hassan et al. [12]. Following, Ahmad and Hassan [13] experimentally investigated the critical height at the OLE with multiple discharging branches on a curved surface with similar geometry and flow conditions. In both these studies single, dual, and triple discharge cases were investigated for branches located on the semi-circular surface at 0 deg, 45 deg, and 90 deg, down from horizontal. In both these studies, the scaled down test section was modeled from a typical CANDU header-feeder bank's geometry.

1.4 Scope of the Present Study. From the literature survey, experimental evidence pertaining to multiple discharges on curved surfaces is limited where liquid entrainment is concerned. This experimental study, therefore, presents a thorough investigation of the critical height in single, dual, and triple discharge scenarios. A scaled model of the CANDU header-feeder geometry was used; however, this study is relevant to other applications of similar geometry and flow conditions. Previous dual discharge investigations had considered a gas-liquid interface below both discharges. In this study, the second discharges were both above and below the interface. The effects of the recording method on the critical height were also investigated by performing experiments using both the increasing and decreasing liquid level methods. This study found that the differences in critical height, recorded using the two methods, became more pronounced at low discharge flow rates. Comparison of the critical height recorded from both methods demonstrated the effects of surface wetness. Surface tension effects were suspect in the increasing liquid level method results, with the discharge Froude ≤ 1. The dual and triple discharge cases were compared with the single discharge cases, thereby demonstrating the effects of discharge location and strength on the critical height. The effects of wall curvature were isolated by comparing the current curved wall results with those of previous flat wall studies.

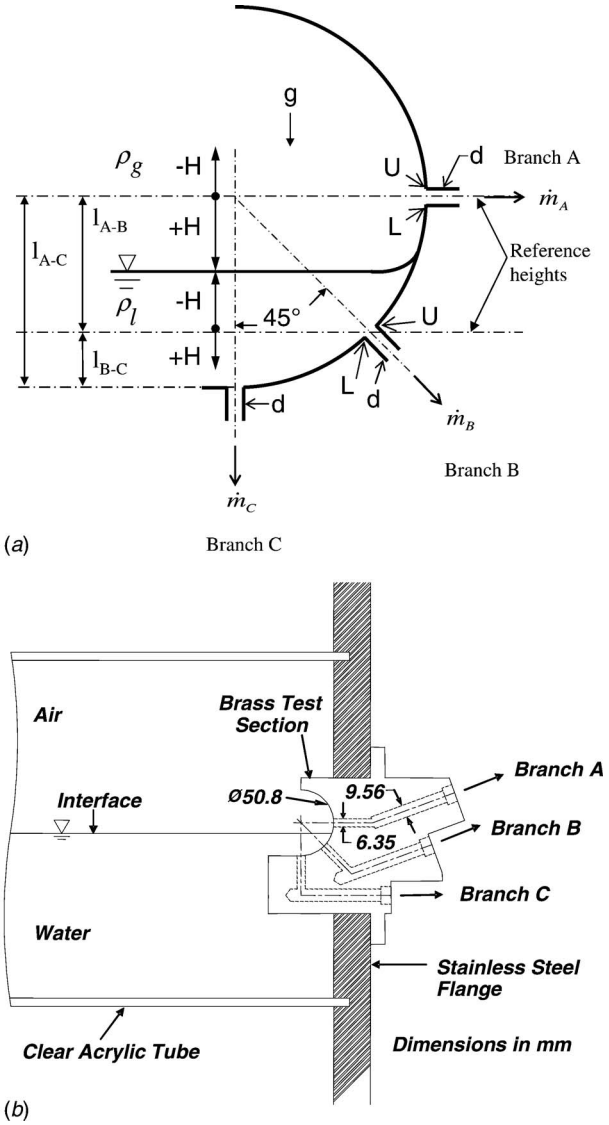

Fig. 1 (*a*) **Modeled geometry and parameters and** (*b*) **test section installed in the two-phase reservoir**

2 Problem Description

2.1 Prototype. A typical CANDU header has a circular cross section, measures approximately 6 m long, has an inside diameter between 0.356 m and 0.406 m, and is closed on both ends. The header is oriented horizontally along its axis. Flow enters through two turrets located on either end of the header, and exits through a network of feeder banks. These feeder banks are distributed along the length of the header. Each feeder bank consists of five 50.8 mm diameter openings located circumferentially at 0 deg, 45 deg, 90 deg, 135 deg, and 180 deg down from horizontal. It was found that a semicircular test section, with three discharging branches, had several experimental advantages and provided reasonable dynamic similarity to a header-feeder bank with five discharges [12].

2.2 Dimensional Analysis. A model of the semicircular geometry was developed using dimensional analysis. The relevant parameters considered in the analysis are shown in Fig. 1(*a*). The dimensional analysis, with up to three simultaneous discharges and a smooth-stratified two-phase regime, neglected viscous and surface tension effects and considered both fluids to be incompressible and irrotational. The following relationship was found:

$$\frac{H}{d} = f\left(\frac{l_{1-2,3}}{d}, \mathrm{Fr}_1, \mathrm{Fr}_2, \mathrm{Fr}_3\right) \tag{1}$$

The critical height H at the OLE is the vertical distance between the primary branch centerline and the gas-liquid interface. Subscript 1 and "primary branch" denote the discharge where the OLE occurs. The primary branch is the discharge located closest to and above the gas-liquid interface. Subscripts 2 and 3 denote the secondary discharges where OLE does not occur. The coordinate system is shown in Fig. 1(*a*) for primary Branches A and B. The critical height is positive, $+H$, when the interface is below the branch centerline, and negative, $-H$, when the interface is above the centerline. The three discharging branches are of diameter d. With two and three simultaneous discharges, the center-to-center vertical distance between the primary and secondary branches is l. The branch discharge Froude number Fr is defined as

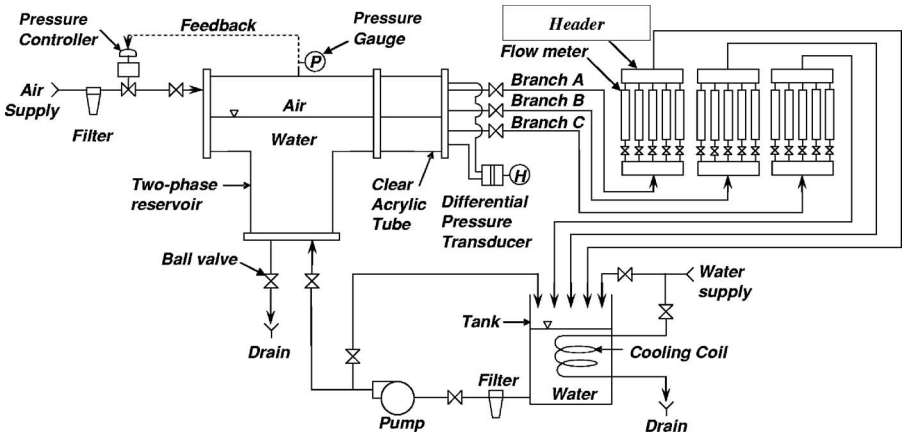

Fig. 2 Experimental test facility schematic

$$\mathrm{Fr} = \frac{4\dot{m}}{\pi\sqrt{(gd^5\rho\Delta\rho)}} \tag{2}$$

The mass flow rate of the single phase fluid, of density ρ, flowing in the branch, prior to onset of two-phase flow, is $\dot{m}$. Gravitational acceleration is g. This dimensionless number indicates that the physics of the problem are governed by a ratio of the inertial and gravitational forces. The density ratio of the two fluid phases appears in Eq. (2) as $\rho\Delta\rho$. The density difference between the heavier, ρ_l, and lighter, ρ_g, fluid phases is defined as $\Delta\rho=\rho_l-\rho_g$.

3 Experimental Investigation

An experimental test facility at Concordia University in Montreal was established recently by Ahmad and Hassan [13]. It was used in the present study. A brief discussion is presented regarding its components, namely, the test section and flow distribution system. In addition, the experimental procedure, test matrix, and uncertainty of the present study are presented.

3.1 Test Section. The test section, modeled from a header-feeder bank's geometry, had a semicircular cross section with three branches. The branches were located at 0 deg, 45 deg, and 90 deg, from the horizontal axis, and are referred to as Branches A, B, and C, respectively, throughout this text. The test section was installed in the two-phase reservoir, as shown in Fig. 1(*b*). Its curved surface was exposed to a smooth-stratified gas-liquid environment. The test section was designed to enhance flow visualization conducive to the OLE measurements. A 50.8 mm diameter hole, 50.8 mm in length, was machined into the end of a solid brass rod to form the semicircular surface. Three holes, 6.35 mm in diameter, were drilled 30.4 mm deep into the semicircular surface at 0 deg, 45 deg, and 90 deg and then enlarged to 9.56 mm in diameter for a remaining 90.4 mm depth.

3.2 Test Facility and Instrumentation. The test facility is presented in Fig. 2. The two-phase reservoir was made from two stainless steel pipes welded together in a T shape; flanges were welded onto the three ends. Two of the flanges were capped with stainless steel covers. On the third flanged end, a clear acrylic tube was fastened and its open end capped with a stainless steel cover. The test section was installed through a hole machined at the center of this cover. The test section was bolted to the cover and an O-ring provided adequate sealing. The three test section discharges, Branches A, B, and C, were controlled by downstream ball valves installed at their outlets. Downstream of the ball valve, each discharge was connected to a flow meter that was regulated with an inline needle valve. Five air flow meters, with overlapping ranges up to a maximum of 2.83 m^3/min, and four water flow meters, with overlapping flow rates up to a maximum of 75 l/min, were used. The flow meters were selected to provide different orders of magnitude of the discharge Froude number ($0.001 \leqslant \mathrm{Fr} \leqslant 30$). The flow meters were connected together in parallel, by inlet and outlet headers, which allowed easy adjustment of the flow rate within the various ranges.

Regulated air was supplied to the two-phase reservoir by a Fisher pressure controller. The discharge air was released to atmosphere downstream of the flow meters. The air pressure in the two-phase reservoir was monitored by a Rosemount liquid crystal display (LCD) pressure transducer with a factory calibrated range of 0–830 kPa. Water was stored in a 208 l tank and supplied to the two-phase reservoir by a 3 hp eight-stage vertical pump. The discharged water downstream of the flow meters was circulated back to the tank. The water height was measured by a Rosemount LCD differential pressure transducer with a factory calibrated range of 0–255 mm H_2O. Plumbing between the two-phase reservoir and all other devices—which include the pump, pressure regulator, pressure transducer, differential pressure transducer, and flow meters—was established using flexible polyvinyl chloride (PVC) tubing. The hydraulic resistance of tubing and valves downstream of the test section was equal for each branch.

3.3 Experimental Procedure. The critical height H at the OLE was recorded using the increasing liquid level (ILL) and the decreasing liquid level (DLL) methods. First, water was supplied to the two-phase reservoir, keeping the air-water interface below the primary branch. This prevented the test section surface between the interface and primary branch inlet from being wetted prematurely. Initial placement of the interface below the primary branch was also necessary to ensure that OLE did not occur immediately upon activating ($\dot{m}_1 > 0$) the primary branch. Branches were activated when the ball valve and flow meter valve were opened, thereby allowing fluid to flow from the reservoir into the branch. The reservoir was then pressurized to the desired set point. The primary branch was activated and the flow rate set to the desired value. Since the primary branch was located above the air-water interface, air was initially flowing into the branch upon activation. For dual and triple discharge cases, the additional branches were also activated ($\dot{m}_{2,3} > 0$) and their flow rates adjusted to the desired values. The water level in the reservoir was then steadily increased at a rate of approximately 1 mm/min. As the air-water interface approached the primary branch inlet, a deformation of the interface was observed. Increasing the water level further caused a stream of water to be pulled into the primary branch. The progression of these events is shown in the three images in Fig. 3 (see also Appendix A, Fig. 17). The height of water was then recorded from the differential pressure transducer. The recorded water height was then subtracted from a known reference height to determine the critical height H at the

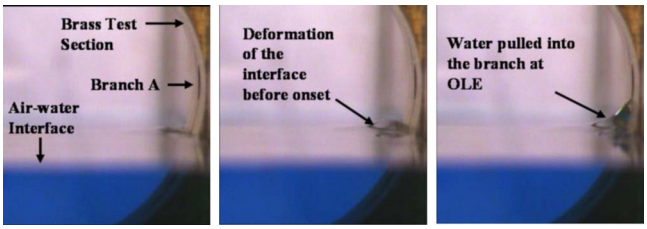

Fig. 3 The OLE using the ILL method

OLE using the ILL method. The reference height was the primary branch centerline (see Fig. 1(*a*)). At low Froude numbers, using the ILL method, care was taken to observe the air-water interface near the branch inlet—as will be seen later on, the effects of surface tension are of increasing importance at low Froude numbers (see also Appendix A, Fig. 18). The water level in the reservoir was then slowly decreased, at a rate of approximately 1 mm/min, until the stream of water ceased to flow into the primary branch. The water height was again recorded and subtracted from the same reference height used previously. The resulting value corresponded to the critical height H at the OLE using the DLL method (see also Appendix A, Fig. 19.) The brass test section surface was then dried and the procedure was repeated for the next primary branch flow rate. In dual and triple discharge cases, the secondary discharge flow rates were also adjusted. Routine cleaning of the test section surface was performed to maintain surface integrity.

3.3.1 Test Matrix. The test matrix for the single, dual, and triple discharge cases is shown in Table 1. The heavier fluid used was water, and its temperature was maintained constant by a cooling coil installed in the water tank. Air was the lighter fluid and was maintained at a pressure of 413.6 kPa inside the reservoir. This pressure was used because it was within the safety limits of the experimental test facility, and higher Froude numbers could be achieved in multiple discharge cases. Experiments were performed at room temperature. A data reduction method, outlined by Maier et al. [9], was used to find the value of air density at the inlet of the branch. The method consisted of applying an energy balance between the stagnation conditions and the branch inlet, and assuming air to be an ideal gas.

3.3.2 Measurement Uncertainty. All measurement devices were calibrated by the manufacturer as per component specifications. The maximum uncertainty in the calculation of the Froude number Fr where air was the working fluid was estimated to be ±11%. The maximum uncertainty in the calculation of the Froude number, where water was the working fluid, was estimated to be ±5%. The instrument uncertainty in measuring P_0 was ±0.83 kPa, and an acceptable range during experimentation was 413.6±6.8 kPa. The instrument uncertainty in measuring H, using the differential pressure transducer, was found to be ±0.165 mm H_2O.

4 Results and Discussion

4.1 Overview. The critical height H at the OLE was recorded for single, dual, and triple discharge cases. As seen from the de-

Table 1 Test matrix, single, dual, and triple discharge cases

Data set	Primary branch	Secondary branches	l/d	Recording method	Fr_A	Fr_B	Fr_C
1-1	A	—	—	ILL	0.004–20	—	—
1-2				DLL			
2-1	B	—	—	ILL	—	0.004–20	—
2-2				DLL			
3-1	A	B	2.83	ILL	0.004–20	5.1	—
3-2				DLL			
3-3				ILL		15.9	
3-4				DLL			
3-5				ILL		26.4	
3-6				DLL			
4-1		C	4	ILL		—	5.1
4-2				DLL			
4-3				ILL			15.9
4-4				DLL			
4-5				ILL			26.4
4-6				DLL			
5-1	B	A	2.83	ILL	1.15	0.004–20	—
5-2				DLL			
5-3				ILL	6.13		
5-4				DLL			
5-5				ILL	Fr_B		
5-6				DLL			
6-1		C	1.17	ILL	—		0.14
6-2				DLL			
6-3				ILL			0.38
6-4				DLL			
7-1	A	B,C	2.83, 4	ILL	0.004–20	5.1	5.1
7-2				DLL			
8-1	B	A, C	2.83,	ILL	1.15	0.004–20	0.14
8-2			1.17	DLL			
8-3				ILL			0.38
8-4				DLL			
8-5				ILL	13.8		
8-6				DLL			

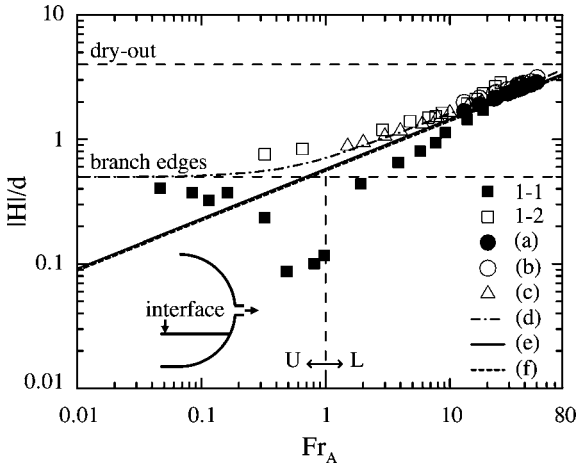

Fig. 4 OLE in side branch with comparison to Hassan et al. [5] for (*a*) ILL method, (*b*) DLL method, and (*c*) Maier et al. [9] for ILL method. Analytical models by (*d*) Maier et al. [11], (*e*) Armstrong et al. [6], and (*f*) Yonomoto and Tasaka [3].

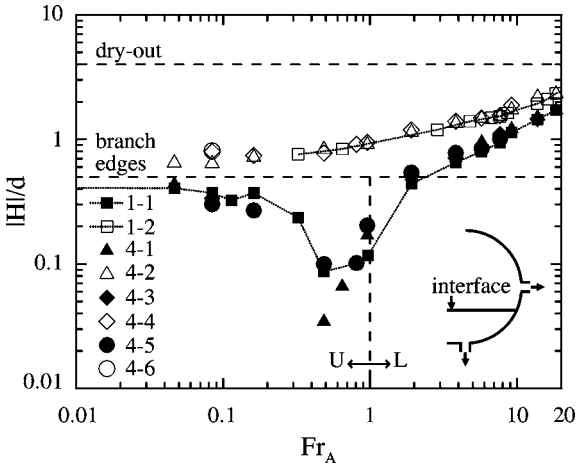

Fig. 6 OLE in Branch A with secondary Branch C. Comparison with single discharge cases demonstrating the effect of varying Fr_C.

tails of the experimental test matrix listed in Table 1, Cases 1 and 2 were single discharge, Cases 3–6 were dual discharge, and Cases 7 and 8 were triple discharge. The critical height, in all cases, was presented as a function of the primary branch Froude number in Figs. 4–14. The absolute value of the dimensionless critical height, $|H|/d$, is plotted along the ordinate with the primary branch Froude number along the abscissa. A negative value of H resulted when the air-water interface was above the reference height when OLE occurred, requiring the absolute value to be taken to present the result on a log-log plot. Some features of Figs. 4–14 are consistent and are discussed below in Secs. 4.1.1, 4.1.2, and 4.1.3. In each figure, the critical height obtained from both methods was presented (ILL data point symbols are filled). Sketches of each case, showing active discharges and interface location, were provided in each of the figures.

4.1.1 Physical Limits: Dry-Out and Branch Edges. Two horizontal lines, constant values of $|H|/d$, are presented in each of the figures. These lines, designated as "dry-out" and "branch edges," represent the physical limits of the test section. The critical height has maximum and minimum values at these physical limits. The dry-out line represented the vertical distance between the primary branch centerline and the bottom of the test section. Dry-out will occur at high primary branch Froude numbers. For primary Branch A, the value of $|H|/d$ at dry-out is 4. For primary Branch B, the value of $|H|/d$ at dry-out is 1.17. The definition of branch edges depends on the method used to record the critical height. The term refers to the vertical distance from the primary branch centerline, at its inlet, to its upper (U) and lower (L) edges (see also Fig. 1(*b*) and Appendix A, Figs. 17–19). In the case of primary Branch A, the top and bottom edges were defined at $|H|/d = 0.5$. For primary Branch B, both edges were defined at $|H|/d = 0.35$. A critical height equivalent to the branch edge line means that the air-water interface was at either the upper or lower edge of the branch when OLE occurred. For the DLL method, the branch edge line was the lower edge in all cases.

The upper and lower edges, using the ILL method, are defined by a vertical line passing through $Fr_1 = 1$. This line represents an asymptote at $|H|/d = 0$ and $Fr_1 = 1$. With $Fr_1 > 1$, the branch edge line is the lower edge. (In this region, the air-water interface is below the primary branch centerline when OLE occurs.) With $Fr_1 < 1$, the branch edge line is the upper edge. (In this region, the air-water interface is above the primary branch centerline when OLE occurs.) The terms U and L were included in Figs. 4–14 to distinguish the side of the vertical line where the upper and lower edges were defined for the ILL results.

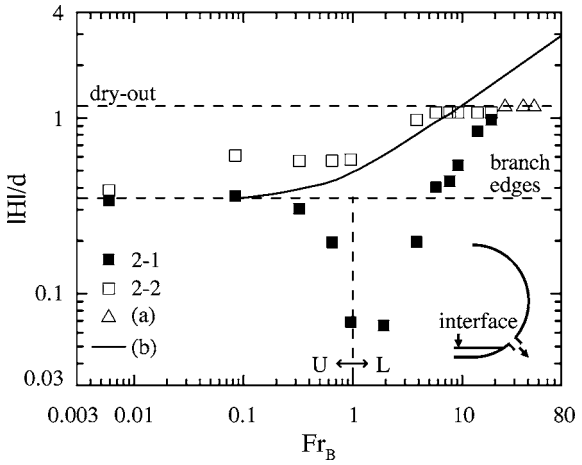

Fig. 5 OLE in side Branch B with comparison to (*a*) Hassan et al. [12] (DLL) and (*b*) flat wall analytical model by Hassan et al. [10]

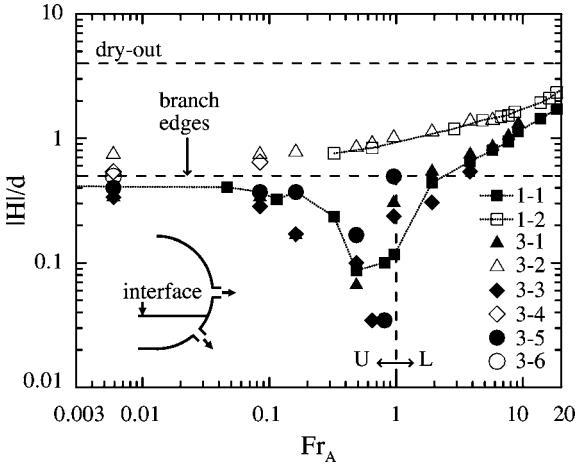

Fig. 7 OLE in side Branch A and secondary Branch B. Comparison with single discharge cases demonstrating the effect of varying Fr_B.

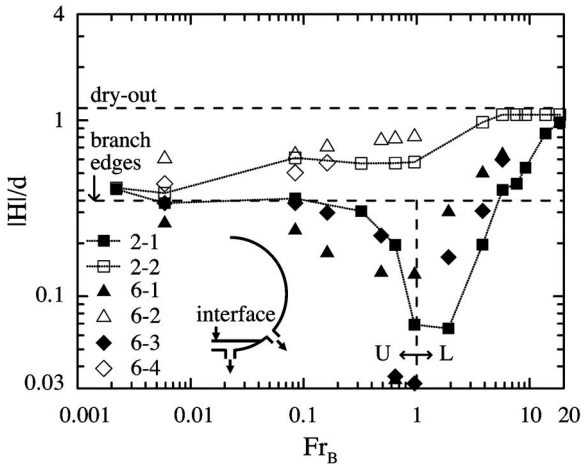

Fig. 8 OLE in a side Branch B with secondary Branch C. Comparison with single discharge cases demonstrating the effect of varying Fr_C.

4.1.2 Surface Wetness. The DLL method consistently demonstrated a higher critical height, at the same Froude number, than the ILL method. At higher Froude numbers, $Fr_1 > 10$, the difference between using the ILL and DLL methods was less significant. A difference between both methods was surface wetness prior to OLE. The surface between the interface and primary branch inlet was dry using the ILL method, but it was wet using the DLL method. Comparison of the critical height between ILL and DLL methods, therefore, yields the effect of surface wetness. In practical scenarios, a surface can have any degree of wetness, and the critical height can be expected to lie in between the ILL and DLL results. At low Froude numbers, $Fr_1 < 1$, the critical height recorded by both methods tended to converge on the branch edge line.

4.1.3 Surface Tension. A unique observation in this study was the tendency for the critical height to approach $|H|/d=0$, at $Fr_1 = 1$, using the ILL method. (Physically, $|H|/d=0$ implies that the level of the air-water interface coincides with the primary branch centerline.) This result is attributed, in part, to surface tension. With $Fr_1 \leqslant 1$, inertia no longer dominates over gravitational forces, and surface tension effects become more pronounced as Fr_1 is decreased (Froude number is a ratio of inertia to gravitational forces from the definition in Eq. (2)). Since surface tension forces remain relatively constant, hypothetically, a larger primary branch diameter would reduce the visibility of its effects on the critical height. With a sufficiently large primary branch diameter, the critical height would not tend toward the asymptote at $|H|/d = 0$ and $Fr_1 = 1$. Increasing the branch diameter, while maintaining Fr_1 constant and below 1, increases the relative distance between the branch centerline and interface, since the critical height remains constant. The resulting value of $|H|/d$ would therefore approach the branch lower edge line with increasing diameter, and consequently, the surface tension effects are less visible. The scale of the test section was therefore an important consideration, as might be expected, for surface tension effects to be observed.

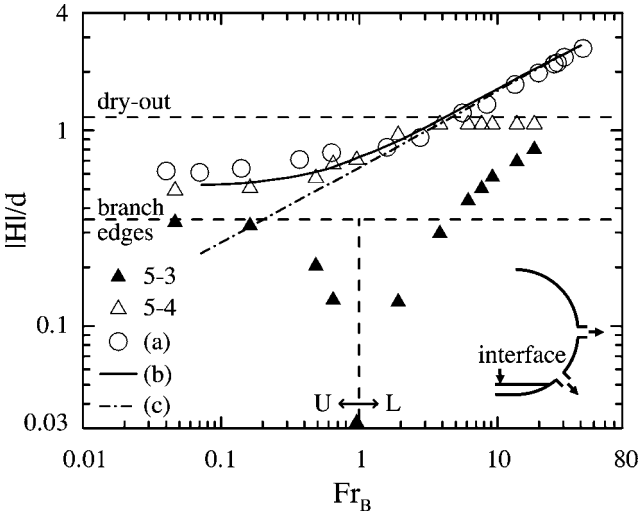

Fig. 10 Comparison between present results and Hassan et al. [10]; (*a*) experimental data for a flat vertical wall using DLL, (*b*) finite branch model, and (*c*) point-sink model by Armstrong et al. [6]

4.2 Single Discharge. The results for Case 1, OLE in side Branch A, are presented in Fig. 4 and compared with experimental results for a single discharging side branch on a flat vertical wall [5,9]. The present results agreed with Ref. [5] in that the ILL method yielded a lower value of $|H|/d$ than that of the DLL method. They had reported values of $Fr_1 > 10$; therefore, a significant difference between the methods could not be observed. The higher $|H|/d$ obtained in the present DLL results, as compared

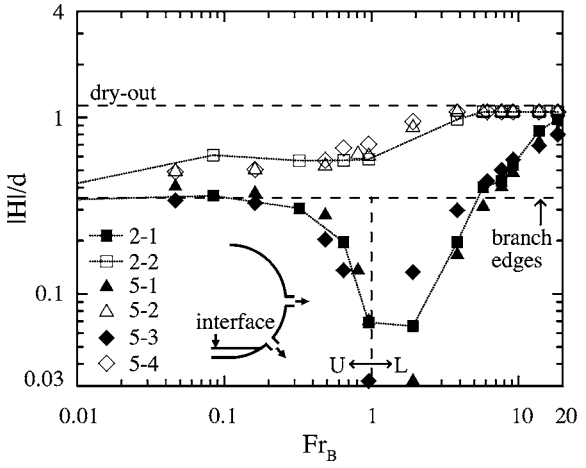

Fig. 9 OLE in a side Branch B with secondary Branch A. Comparison with single discharge cases demonstrating the effect of varying Fr_A.

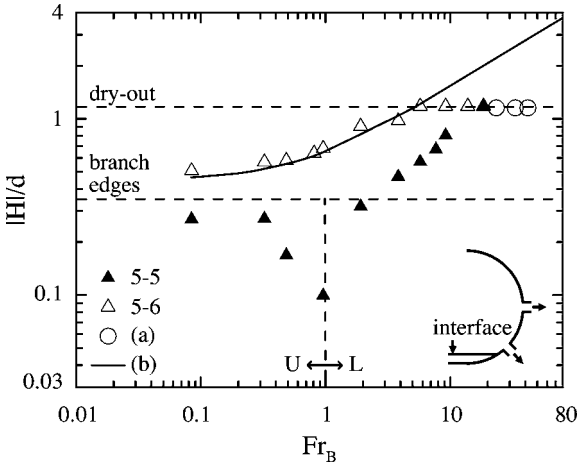

Fig. 11 Comparison between present results with (*a*) the experimental results (DLL) of Hassan et al. [12] and (*b*) finite branch model by Hassan et al. [10]

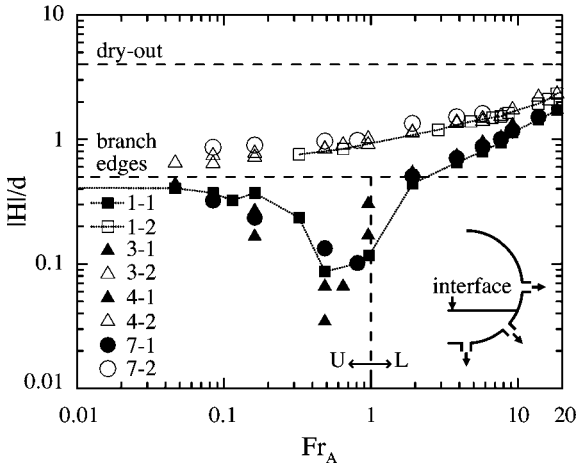

Fig. 12 OLE in side Branch A with secondary Branches B and C. Effect of l/d, Fr_B, and Fr_C on $|H|/d$ by comparison with single and dual discharge cases.

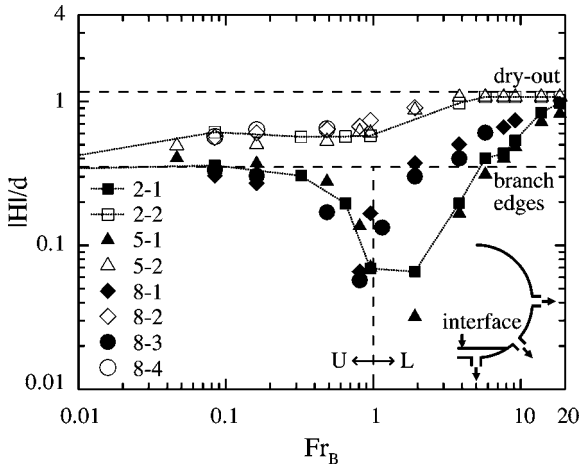

Fig. 14 OLE in Branch B with secondary Branches A and C. Effect of l/d and Fr_C by comparison with single discharge and dual discharge cases.

with the flat wall results, is likely the effect of wall curvature. Physically, the curvature assisted the flow of liquid into the branch, and postponed OLE. The curved wall provided a smooth transition for the liquid to flow from the horizontal to the vertical direction. The flat wall caused an abrupt directional transition, which resulted in a higher loss of liquid momentum and consequently a lower critical height. The present ILL results demonstrated a lower value of $|H|/d$ than the flat wall results. Since liquid did not flow into the branch until OLE, the difference was caused by an increase in flow resistance. The distance along the curved test section wall, between the interface and the primary branch inlet, was higher than the distance along the flat wall and caused the resistance increase.

The results for Case 1 were compared with analytical models for a single horizontal discharging branch on a flat vertical wall [3,6,11]. The present results were in good agreement with the previous models with $Fr_A > 10$. With $Fr_A < 10$, the DLL method demonstrated better agreement than the ILL method. Only Ref. [11] correctly predicted the lower branch edge physical limit. Their model, however, did not predict that the ILL results had the upper branch edge as the physical limit when $Fr_1 < 1$, since surface tension effects were not considered.

Results for Case 2 are presented in Fig. 5 for OLE in Branch B.

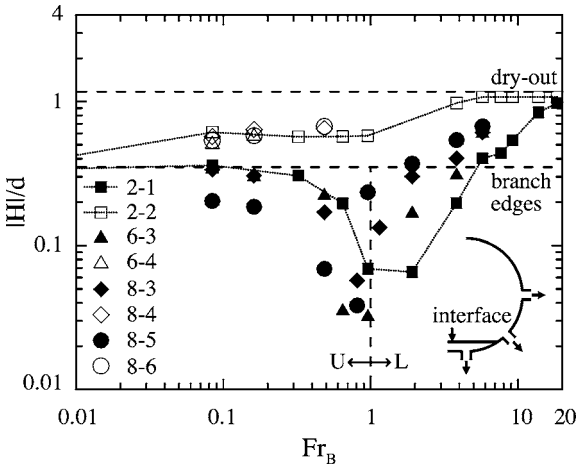

Fig. 13 OLE in Branch B with secondary Branches A and C. Effect of l/d and Fr_A by comparison with single discharge and dual discharge cases.

Experimental data for flat inclined walls were lacking in the literature; however, some limited experimental data were available from Ref. [12] for a curved wall with similar branch orientation. They reported the critical height for dry-out only, and it was found to be in agreement with the present results. An analytical model for a discharging branch whose axis is oriented at 45 deg from horizontal, and located on a flat inclined wall, was developed by Hassan et al. [10]. Their model was capable of predicting the DLL results with reasonable accuracy up to approximately $Fr_B = 10$. The critical height, using the ILL method, showed a large discrepancy in comparison with their model. This could be expected since the effects of surface tension and wall curvature were not considered in their model.

4.3 Dual Discharge. The dual discharge cases are presented in Figs. 6–11, and the values of l/d and discharge Froude numbers are listed in Table 1. The figures were designed to provide insight into the effects of a secondary discharge's location and Froude number (Fr_2). For Cases 3, 4, and 6, the secondary branch was below the air-water interface, whereas in Case 5, it was above. The single discharge cases are plotted with interconnecting dotted lines along with the dual discharge case for comparison purposes.

4.3.1 Secondary Discharge Below the Primary Discharge. The effects of the secondary branch, located below the gas-liquid interface, are presented in Figs. 6–8. These figures demonstrate the effects of varying the vertical separating distance between the two discharging branches, l/d, and discharge Froude number (Fr_1 and Fr_2) on the critical height. Gas entrainment occurred in the secondary branch at a critical value of $|H|/d$. At OGE in the secondary branch, no higher values of Fr_1 were recorded since reporting the two-phase mass flow rate, and quality, was beyond the scope of this study. In Cases 3, 4, and 6, the highest reported primary branch Froude number (Fr_1) represents the critical height when the OGE occurred in the secondary branch, causing simultaneous gas and liquid entrainments in the two discharging branches. In Fig. 6, the primary branch was A, and the secondary branch was C. In Fig. 7, the primary branch was A, and the secondary branch was B. In Fig. 8, the primary branch was B, and the secondary branch was C. Comparisons with the single discharge cases ($Fr_2 = 0$) showed that on average if $Fr_1 > 1$, increasing Fr_2 resulted in an increase in critical height. This is evident from Figs. 6 and 7. The ILL results presented in Fig. 8 demonstrated that the smallest interbranch spacing, l/d, had the most significant impact on critical height despite having the lowest recorded values of Fr_2.

The critical height was found to increase slightly with $Fr_1 > 1$ at low to moderate values of Fr_2; therefore, the secondary discharge

assisted OLE. When $Fr_1 < 1$, however, the critical height did not always increase with an increase in Fr_2. For example, in Figs. 6–8, the ILL results showed an average decrease in critical height, when compared to the single discharge cases, whereas the DLL results were found to increase.

4.3.2 Secondary Discharge Above the Primary Discharge. The case of a secondary branch located above the air-water interface, and also above the primary branch, is presented in Figs. 9–11. The primary branch was B and the secondary branch was A. Figure 9 demonstrates the effects of varying Fr_A on $|H|/d$. A comparison of the ILL and DLL results with the single discharge case showed that on average, the second discharge assisted the OLE, which was suggested by the increase in critical height.

In Figs. 10 and 11, comparisons with selected analytical models are presented. The models were established with two discharges on a flat wall. In Fig. 10, the present results are compared against analytical results for two discharges with $l/d=3$ and $Fr_2=5.5$ [6,10]. The slight differences in l/d and Fr_A between the current and the previous studies are considered negligible and did not have a significant impact on the critical height. The present DLL results showed a slightly lower value of $|H|/d$ when compared to experimental data for a discharge on flat vertical wall by Hassan et al. [10]. Their data were recorded using the DLL method, and the differences in $|H|/d$ are likely attributed to wall curvature. There was excellent agreement between the present DLL results and the finite branch model developed by Hassan et al. [10] up to dry-out. Good agreement with the point-sink model developed in Ref. [6], for $Fr_B > 1$, was also found. The critical height recorded with the ILL method, however, showed a large discrepancy from these two models. This disagreement is due to the effects of surface tension and wall curvature not being considered in their model. The agreement between the flat inclined wall model [10] and the current DLL results is further strengthened in Fig. 11. This figure shows a scenario where both primary and secondary branches had the same Froude number, $Fr_B = Fr_A$. Some experimental results for a curved geometry in Ref. [12] are also presented at dry-out with good agreement with the present results.

4.4 Triple Discharge

4.4.1 Two Secondary Discharges Below the Primary Discharge. In Fig. 12, the primary branch was A and the secondary branches were B and C. The figure demonstrates the effect of two secondary discharges located below the air-water interface. For comparison purposes, the single and dual discharge cases are presented to isolate the effects of each of the secondary branches. In comparison with the single discharge case, there is a decrease in $|H|/d$ using the DLL method, and an increase using the ILL method with $Fr_A > 1$. Comparing the triple with the dual discharge cases, an overall average increase in $|H|/d$ was found using either the ILL or DLL methods. The average increase in $|H|/d$ suggests that the two secondary discharges assisted the OLE. This result is somewhat surprising since the secondary discharges pull the liquid phase in a direction opposite to that of the primary branch, and a decrease in critical height might have been expected. The resulting increase in critical height suggests that possible interaction between the secondary discharges created a flow field that assisted liquid entrainment. Future flow field measurements are required to verify this observation.

The onset of two-phase flow, either gas or liquid entrainment, was found to occur simultaneously in two or three discharging branches. Images of the flow phenomena are shown in Figs. 15 and 16. Figure 15 shows simultaneous two-phase flow in both branches. Water was entraining into the primary Branch A while air was entraining into the secondary Branch C. Figure 16 shows the simultaneous two-phase flow in three discharging branches. Water was entraining into the upper primary Branch A while air was entraining into both lower secondary Branches B and C. Upon closer inspection, a stream of air was seen to travel between

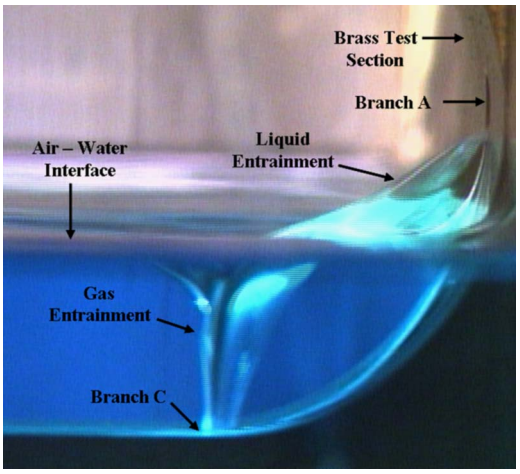

Fig. 15 Image of dual discharge with Branches A and C active, demonstrating simultaneous liquid and gas entrainment

the secondary Branches B and C. This gas stream emphasized that secondary discharges are not only interacting with the interface but also with each other.

4.4.2 Secondary Discharge Above and Below the Primary Discharge. Figures 13 and 14 demonstrate the triple discharge cases with a primary branch B and secondary Branches A and C. Results are compared with the single and dual discharge cases. The secondary branches are located above (Branch A) and below (Branch C) the primary branch. Figure 13 shows the effect of varying Fr_A, and Fig. 14 shows the effect of varying Fr_C. In Fig. 13, by comparing the triple and single discharge ILL results, an increase in $|H|/d$ was found when Fr_A was increased from 1.15 to 13.8 with $Fr_C=0.38$ and $Fr_B > 1$. An average increase in $|H|/d$, over either of the two dual discharge cases, was also observed. With $Fr_B < 1$, the results showed on average that $|H|/d$ is lower than the single discharge case. In Fig. 14, by comparing the triple and single discharge ILL results, an increase in $|H|/d$ was found when Fr_C was increased from 0.14 to 0.38 with $Fr_A=1.15$ and $Fr_B > 1$. Comparing the DLL results with the same secondary discharge values, an increase in $|H|/d$ was also found. The overall

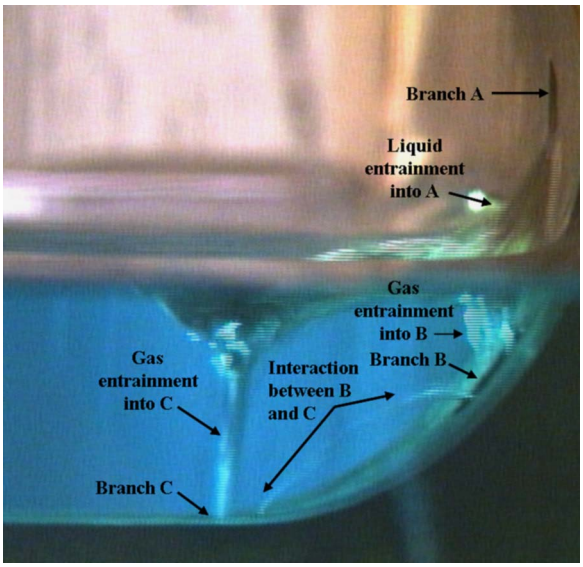

Fig. 16 Image captured of triple discharge with simultaneous gas entrainment in Branches B and C, and liquid entrainment in Branch A

increase in critical height above the single discharge case again suggests that the secondary branches assist the OLE. From these observations, it was concluded that for the investigated triple discharge cases, an increase in either of the secondary branch Froude numbers will, on average, result in an increase in the critical height.

5 Conclusions and Future Work

Single, dual, and triple discharge cases were presented, and OLE occurred in the branch above and closest to the air-water interface. The ILL and DLL methods, used to record OLE, presented unique results regarding the effects of surface wetness. These effects were demonstrated by comparing the critical height recorded from both methods. The ILL results showed important scaling considerations, which are attributed to the effects of surface tension. The effects of surface tension were seen to be significant with $Fr_1 < 1$, when inertia was no longer dominant. With a low to moderate secondary discharge Froude number, an average increase in the critical height was found. At higher secondary discharge Froude numbers, an average increase was not always found and the critical height did decrease in some cases. The most significant impact on the critical height, compared to single discharge cases, occurred with secondary discharges having the lowest value of l/d. Comparison with flat wall results showed that wall curvature caused the critical height to increase in the DLL results, and decrease in the ILL results. The finite branch models by Hassan et al. [10] and Maier et al. [9] were found to be representative of the dual and single discharge DLL results, respectively. Agreement was found even though they were developed with discharges on a flat rather than a curved wall. The point-sink models also showed reasonable agreement with the DLL results with $Fr_1 > 10$. The ILL results were not well predicted by any of the models tested.

The present experimental results can be enhanced by quantitative flow field measurements. These measurements could further explain the single, dual, and triple discharge flow fields, and would shed further insight into the effects of discharge strength and geometry. Presently, work is underway to gather these data using particle image velocimetry. In addition, work is being done to investigate the effects of cross-flow and stratified wavy flow on the two-phase flow field.

Acknowledgment

The financial support of the Natural Sciences and Engineering Research Council of Canada (NSERC) and the Canada Foundation for Innovation (CFI) is gratefully acknowledged.

Nomenclature

d = branch diameter (m)
Fr = Froude number, $\mathrm{Fr} = 4\dot{m}/\pi\sqrt{(gd^5\rho\Delta\rho)}$
H = critical height at OLE (m)
l = center-to-center distance between branches (m)
$\dot{m}$ = mass flow rate of single phase fluid entering branch (kg/s)
g = gravitational acceleration (m/s^2)
U = upper edge of the primary branch
L = lower edge of the primary branch

Greek

$\Delta\rho$ = difference between densities of heavier and lighter fluids (kg/m^3)
ρ = density of single phase fluid at the branch inlet (kg/m^3)

Subscripts

1 = primary branch where OLE occurs
2,3 = secondary branches for dual and triple discharges
A,B,C = branches located at 0 deg, 45 deg, 90 deg from horizontal axis
l,g = liquid and gas phases

Acronyms

CANDU = Canada deuterium and uranium
DLL = decreasing liquid level
ILL = increasing liquid level
LOCA = loss-of-coolant accident
OGE = onset of gas entrainment
OLE = onset of liquid entrainment

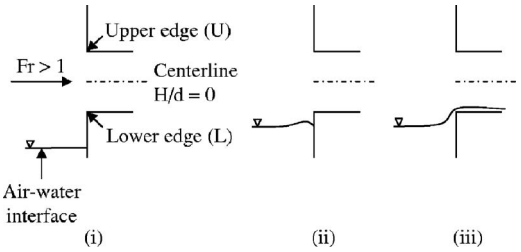

Fig. 17 Sketch of the ILL method when Fr>1

Appendix A: Sketches of Onset of Liquid Entrainment Using Increasing Liquid Level and Decreasing Liquid Level Methods

The following sketches are provided to enhance the interpretation of Figs. 4–14. In particular, they demonstrate the definitions of OLE for both methods of recording the critical height, DLL and ILL. Branch A is used for example purposes in all the sketches.

A high primary branch Froude number, $Fr > 1$, is presented in Fig. 17 using the ILL method to record the critical height. The interface is initially well below the branch inlet and the surface above the interface is dry, as in (i). The level of water is increased slowly until a deformation of the surface is observed, as in (ii). Finally, increasing the level of water further causes the interface to break, and a stream of water to be pulled up into the branch inlet, as in (iii).

For a low primary branch Froude number, $Fr < 1$, sketches are presented in Fig. 18 to demonstrate the ILL method. The air-water interface is initially well below the primary branch inlet, and the test section surface above the interface is dry, as in (i). At this point $H/d \gg 0.5$. The level of water is slowly increased, as in (ii), and the air-water interface now coincides with the lower edge of the branch inlet. At this level, $H/d = 0.5$. The level of water is increased further, as in (iii), OLE has not yet occurred, and the interface sticks to the branch lower edge. At this point, H/d is

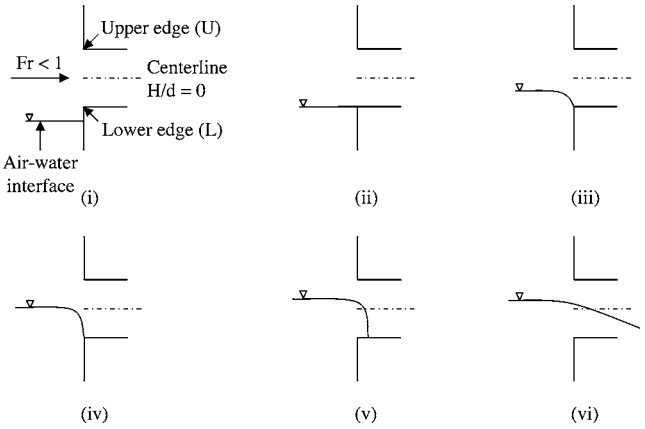

Fig. 18 Sketch of the ILL method when Fr<1

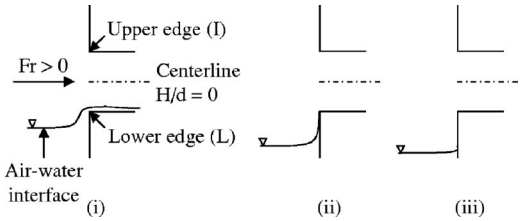

Fig. 19 Sketch of the DLL method when Fr>0

between 0 and 0.5. Increasing the level of water further, the interface and the branch centerline coincide, resulting in a value of $H/d=0$, as in (iv). By increasing the level of water further, the interface moves slightly into the branch inlet without OLE occurring, as in (v). The height at this point is above the branch centerline and the value of H/d is negative, between −0.5 and 0. A slight increase in the level of water and a sudden break in the interface will occur, resulting in water to flow into the branch, as in (vi). At this point, the OLE is defined, and the critical height H/d is recorded.

Sketches of the DLL method, for any primary branch Froude number, are presented in Fig. 19. Water is already being entrained into the primary branch, as in (i). By decreasing the level of water, as in (ii), the stream of water still flows into the branch inlet; however, it is much thinner. Decreasing water level further, the stream stops entraining into the branch, as in (iii). At this point, the OLE is defined and the critical height is recorded using the DLL method.

References

[1] Zuber, N., 1980, "Problems in Modeling of Small Break LOCA," Nuclear Regulatory Commission Report No. NUREG-0724.

[2] Smoglie, C., and Reimann, J., 1986, "Two-Phase Flow Through Small Branches in a Horizontal Pipe With Stratified Flow," Int. J. Multiphase Flow, **12**, pp. 609–625.

[3] Yonomoto, T., and Tasaka, K., 1988, "New Theoretical Model for Two-Phase Flow Discharged From Stratified Two-Phase Region Through Small Break," J. Nucl. Sci. Technol., **25**, pp. 441–455.

[4] Micaelli, J. C., and Memponteil, A., 1989, "Two-Phase Flow Behavior in a Tee-Junction: The CATHARE Model," in *Proceedings of the Fourth International Topical Meeting on Nuclear Reactor Thermal-Hydraulics*, Karlsruhe, Germany, Vol. 2, pp. 1024–1030.

[5] Hassan, I. G., Soliman, H. M., Sims, G. E., and Kowalski, J. E., 1998, "Two-Phase Flow From a Stratified Region Through a Small Side Branch," ASME J. Fluids Eng., **120**, pp. 605–612.

[6] Armstrong, K. F., Parrott, S. D., Sims, G. E., Soliman, H. M., and Krishnan, V. S., 1992, "Theoretical and Experimental Study of the Onset of Liquid Entrainment During Dual Discharge From Large Reservoirs," Int. J. Multiphase Flow, **18**, pp. 217–227.

[7] Hassan, I. G., Soliman, H. M., Sims, G. E., and Kowalski, J. E., 1996, "Experimental Investigation of the Two-Phase Discharge From a Stratified Region Through Two Side Branches Oriented Horizontally," Exp. Therm. Fluid Sci., **13**, pp. 117–128.

[8] Hassan, I. G., Soliman, H. M., Sims, G. E., and Kowalski, J. E., 1996, "Discharge From a Smooth Stratified Two-Phase Region Through Two Horizontal Side Branches Located in the Same Vertical Plane," Int. J. Multiphase Flow, **22**, pp. 1123—1142.

[9] Maier, M. R., Soliman, H. M., and Sims, G. E., 2001, "Onsets of Entrainment During Dual Discharge From a Stratified Two-Phase Region Through Horizontal Branches With Centerlines Falling in an Inclined Plane: Part 2—Experiments on Gas and Liquid Entrainment," Int. J. Multiphase Flow, **27**, pp. 1029–1049.

[10] Hassan, I. G., Soliman, H. M., Sims, G. E., Kowalski, and J. E., 1999, "The Onset of Liquid Entrainment During Discharge From Two Branches on an Inclined Wall," Can. J. Chem. Eng., **77**, pp. 433–438.

[11] Maier, M. R., Soliman, H. M., and Sims, G. E., 2001, "Onsets of Entrainment During Dual Discharge From a Stratified Two-Phase Region Through Horizontal Branches With Centerlines Falling in an Inclined Plane: Part 1—Analysis of Liquid Entrainment," Int. J. Multiphase Flow, **27**, pp. 1011–1028.

[12] Hassan, I. G., Soliman, H. M., Sims, G. E., and Kowalski, J. E., 1997, "Single and Multiple Discharge From a Stratified Two-Phase Region Through Small Branches," Nucl. Eng. Des., **176**, pp. 233–245.

[13] Ahmad, T., and Hassan, I., 2006, "Experimental Investigation on the Onset of Gas Entrainment From a Stratified Two-Phase Region Through Multiple Branches Mounted on a Curved Surface," ASME J. Fluids Eng., **128**, pp. 726–733.

Numerical Simulation of Cavitation Around a Hydrofoil and Evaluation of a RNG κ-ε Model

Lingjiu Zhou
College of Water Conservancy and Civil Engineering,
China Agricultural University,
Beijing, China 100083
e-mail: zlj09@263.net

Zhengwei Wang
Department of Thermal Engineering,
Tsinghua University,
Beijing, China 100084
e-mail: wzw@mail.tsinghua.edu.cn

Cavitating flow around a hydrofoil was simulated using a transport equation-based model with consideration of the influence of noncondensable gases. The cavity length and the pressure distributions on the suction side can be well predicted for stable cavities using the standard renormalization-group (RNG) κ-ε turbulence model with proper noncondensable gas mass fraction. The unstable cavity shedding at lower cavitation numbers was not well predicted by the standard RNG κ-ε turbulence model. A modified RNG κ-ε turbulence model was evaluated by comparing the calculated spatial-temporal pressure distributions on the suction wall with experimental data. The results showed that the predicted cavity growth and shedding cycle and its frequency agree well with the experimental data. However, the pressure increase caused by interaction of the reentrant flow and the cavity interface is overestimated, which caused the time-averaged pressure on the front part of the hydrofoil to be overestimated. The time-averaged pressure on the rear of the hydrofoil was low because the small cavity shedding on the rear part of the cavity was not predicted. [DOI: 10.1115/1.2816009]

Introduction

Cavitation occurs in a wide variety of fluid engineering systems including pumps, water turbines, propellers, and pipes. In most cases, cavitation is an undesirable phenomenon, causing significant degradation in performance and damage as well as vibration and noises. Noticeable efforts have been made in numerical simulations of cavitating flows in recent years. Most cavitation models are based on the pseudohomogeneous flow theory proposed by Kubota et al. [1], which modeled the two phase fluid as a mixture of liquid and its vapor sharing the same velocity and pressure. Reynolds-averaged Navier-Stokes (RANS) equations were solved for the mixture to obtain the velocity, pressure, and turbulence quantities. Additional equations were deduced to solve for the vapor and the liquid volume fractions.

One of the methods used to model cavitation and condensation was to use a proper state law for the mixture. Delannoy and Kueny [2] proposed a barotropic state law that strongly links the mixture density to the static pressure, which describes the mixture density in the incompressible parts, in the pure vapor parts, and in the transition zone of the flow field. This model together with modifications of the turbulence viscosity was successfully adopted to simulate cloud cavity shedding in a Venturi-type duct [3,4]. Iga et al. [5,6] used a state law similar to the barotropic state law concept, which described the mixture density as function of pressure and vapor mass fraction. Their results also agreed with the experimental data.

Another approach is the transport equation-based model (TEM), which solves an additional transport equation for either the mass or volume fraction. A source term is used to model the mass transfer caused by evaporation and condensation. Several models have been proposed for the source term. Senocak and Shyy [7,8] compared three models to develop an interfacial dynamics-based-cavitation model and pointed out that although pressure distributions predicted by different models agreed well with each other, the predicted density distributions differed. This implies that the compressibility characteristics embodied in each cavitation model differ.

In practical cavitating flows, in most engineering equipment, the operating liquid contains a finite amount of noncondensable gases dissolved in the liquid due to leakage or aeration. Noncondensable gases not only change the initial critical cavitation pressure but also affect the flow field through volume expansion and condensation. Different methods have been used to treat the noncondensable gases. Most methods have been based on a transport equation. Some methods have assumed that the densities of the liquid, vapor, and noncondensable gas are all constant. Kunz et al. [9] used an additional transport equation for the noncondensable gas. Unlike other pressure-correction-based methods, they used a dual-time, preconditioned, implicit artificial compressibility algorithm. Yuan and Schnenn [10] used the same concept but solved the transport equations using a pressure-correction method. Singhal et al. [11] also included the effect of noncondensable gases in their "full cavitation model." They considered the noncondensable gas to have a constant mass fraction and with an ideal gas density. This assumption seemed to be more reasonable since the effect of volume change of noncondensable gas was included. The model of Singhal et al. was validated by many cases related to fixed cavities and was adopted by the commercial software FLUENT for cavitating flows.

However, the noncondensable gas mass fraction was then found to excessively affect cavity behavior in practical calculations. In addition, the standard turbulence models failed to predict the instabilities for low cavitation numbers, as was also pointed out by Delgosha et al. [3,4], who then modified the turbulent viscosity (a modified renormalization-group (RNG) κ-ε model) to simulate cloud cavity shedding in a Venturi-type duct. The barotropic state law concept was adopted in their calculations to deal with the cavitation precession. Inspired by their work, the present work combines the modified turbulent viscosity with the full cavitation model. Calculations were performed for various cavitation numbers with emphasis on the influence of noncondensable gas mass fraction and the turbulence model in the simulations. The unsteady behavior of cloud cavity shedding is analyzed and the turbulence model is evaluated based on experimental data.

Contributed by the Fluids Engineering Division of ASME for publication in the JOURNAL OF FLUIDS ENGINEERING. Manuscript received January 17, 2007; final manuscript received June 30, 2007; published online December 19, 2007. Review conducted by Steven Ceccio.

Governing Equations and Cavitation Model

The fluid was assumed to be a mixture of liquid, vapor, and noncondensable gases. The flow was assumed to be pseudohomogeneous so the multiphase fluid components were assumed to share the same velocity and pressure distributions. Therefore, only one set of Favre-averaged Navier–Stokes equations was used to describe the flow. The continuity and the momentum equations for the mixture are

$$\frac{\partial \rho}{\partial t} + \nabla \cdot (\rho \mathbf{V}) = 0 \tag{1}$$

$$\frac{\partial (\rho \mathbf{V})}{\partial t} + \nabla \cdot (\rho \mathbf{V}\mathbf{V}) = -\nabla P + \nabla \cdot \left\{ (\mu + \mu_t) \left[(\nabla \mathbf{V} + \nabla \mathbf{V}^T) - \frac{2}{3} \nabla \cdot \mathbf{V} I \right] \right\} \tag{2}$$

where P is the mixture pressure, ρ is the mixture density, and $\mathbf{V}$ is the mixture velocity vector. The laminar viscosity μ is defined as a density-weighted average of the three components. μ_t is the turbulent viscosity closed by the RNG κ-ε model [12]. The mixture density ρ is defined by

$$\frac{1}{\rho} = \frac{f_v}{\rho_v} + \frac{f_{\text{ncg}}}{\rho_{\text{ncg}}} + \frac{1 - f_v - f_{\text{ncg}}}{\rho_l} \tag{3}$$

with

$$f_v = \frac{a_v \rho_v}{\rho} \quad f_{\text{ncg}} = \frac{a_{\text{ncg}} \rho_{\text{ncg}}}{\rho} \quad f_l = \frac{a_l \rho_l}{\rho} = 1 - f_v - f_{\text{ncg}} \tag{4}$$

where f_v, f_{ncg}, f_l are the component mass fractions, ρ_v, ρ_{ncg}, ρ_l are the component densities, and a_v, a_{ncg}, a_l are the component volume fractions of the vapor, gas, and liquid components. During calculation, f_{ncg} was assumed to be a very small constant. The cavitation model used to simulate vapor generation and condensation rates is

$$\frac{\partial (a_v \rho_v)}{\partial t} + \nabla \cdot (a_v \rho_v \mathbf{V}) = \frac{\partial (\rho f_v)}{\partial t} + \nabla \cdot (\rho f_v \mathbf{V}) = -C_c \frac{\sqrt{k}}{\lambda} \rho_l \rho_l \sqrt{\frac{2 \max(p - p_v, 0)}{3 \rho_l}} f_v + C_e \frac{\sqrt{k}}{\lambda} \rho_l \rho_v \sqrt{\frac{2 \max(p_v - p, 0)}{3 \rho_l}} \times (1 - f_v - f_{\text{ncg}}) \tag{5}$$

The noncondensable gases' density was calculated using the ideal gas law:

$$\rho_{\text{ncg}} = \frac{WP}{RT} \tag{6}$$

The combined vapor and gas volume fraction $a_v + a_{\text{ncg}}$ is the final void fraction.

The model uses the recommended empirical factors $c_e = 0.02$, $c_c = 0.01$ and the surface tension coefficient $\lambda = 0.0717$ N/m.

Hydrofoil Geometry and Discretization

The effect of the noncondensable gas mass fraction and the turbulence model were assessed by modeling cavitating flow around a hydrofoil, which was experimentally studied by Leroux et al. [13]. The hydrofoil used for the simulation was a two-dimensional cambered NACA66(mod) foil with the coordinates given by Leroux et al. [13]. The relative maximum thickness was 12% at 45% from the leading edge and the relative maximum camber was 2% at 50% from the leading edge. The chord length was $C = 0.150$ m. The foil was fixed within a 1 m long and 0.192 m wide square cross test section. The angle of attack was

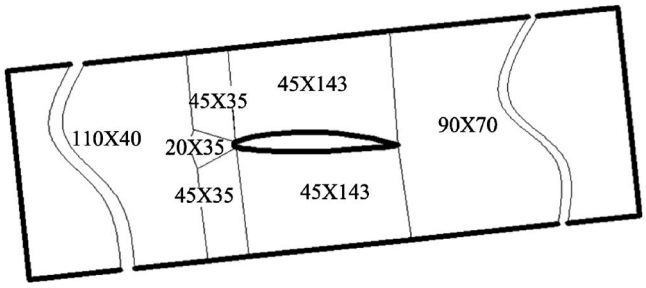

Fig. 1 Calculation domain and seven block structured grid with 27,961 nodes

6 deg. The freestream velocity was 5.33 m/s. Several pressures were monitored during calculations to study the pressure oscillations caused by the cavitation. On suction side, these points were named P0, P05, P1–P9 with P0 located at $x = 0$, P05 at $x = 0.05C$, P1 at $x = 0.1C$, P2 at $x = 0.2C$, etc.

The geometry was simplified to a 2D problem. The mesh was generated with seven block structured grid, as shown in Fig. 1. The mesh size was carefully selected to ensure the nondimensional normal distance from the wall (y^*) located in the log-law region since the standard wall function was adopted for near wall treatment. For a grid with 27,961 nodes, the distributions of y^* of the wall-adjacent cell's centroid were within 30–300 (see Fig. 2), so this grid was used for the following calculations.

The time-dependent equations were discretized using the control-volume technique with the SIMPLEC scheme. The second-order upwind scheme was used for the convection terms with the central difference scheme used for the diffusion terms in the momentum equations and the transport equations for κ and ε. The pressure staggering option (PRESTO) was used for the pressure interpolation. The QUICK scheme was used for the vapor mass fraction transport equation. For above grid, several time steps, 0.001 s, 0.0005 s, and 0.0001 s, were tested with $\Delta t = 0.0005$ s, found to give reasonable results with relatively short calculational times so it was used in the calculations.

Calculated Results

Simulations were performed for noncavitating flows to verify the angle of attack. The pressure distribution at an attack angle of 6 deg is plotted in Fig. 3, which shows that the calculated results agree well with the experimental data (all the experimental data in this paper are from Leroux et al. [13]).

Influence of f_{ncg} on the Simulation of Cavitating Flows With Stable Cavities. The standard RNG κ-ε turbulence model was used in calculations for cavitation numbers varying from 1.25 to 1.67 with mass fraction f_{ncg} from 1×10^{-8} to 1×10^{-6}. The influ-

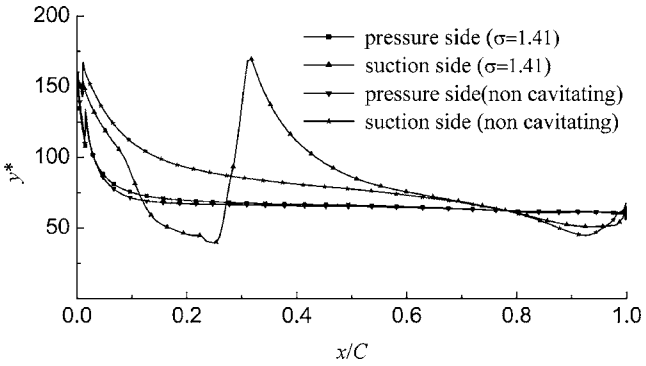

Fig. 2 Distributions of y^* of the wall-adjacent cell's centroid for noncavitating and cavitating flow

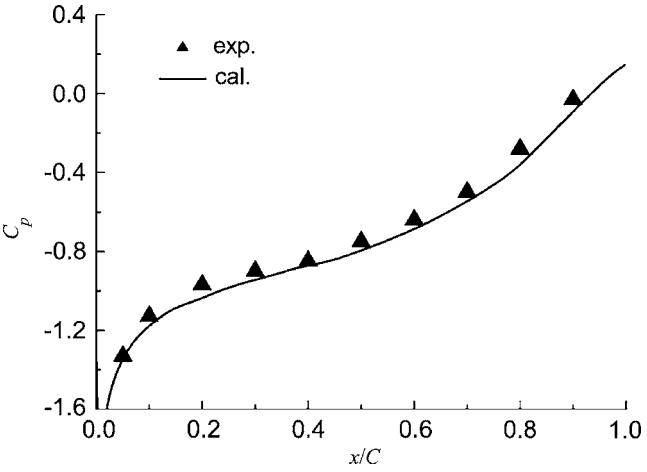

Fig. 3 Comparison of calculated result and experimental data for a noncavitating flow

ence of the mass fraction, f_{ncg}, was investigated with the results shown in Fig. 4. For a constant cavitation number, the cavity length and thickness increased with increasing noncondensable gas mass fraction up to f_{ncg} of about 1×10^{-7}. The cavity length then increased more slowly with increasing noncondensable gas mass fraction from 1×10^{-7} to 1×10^{-6} (see Fig. 4); however, the cavity thickness increased faster. Higher noncondensable gas mass fractions (1×10^{-5}) gave odd cavity shapes with the interface even reaching the upper wall of the test section, which were obviously wrong thus not presented.

The noncondensable gas mass fraction is expected to greatly influence the calculated cavity length of the pressure distribution. In the model of Singhal et al. the combined vapor and gas volume fraction a_v+a_g was used as the final void fraction. Using a_g calculated using Eqs. (4) and (6):

$$a_{\text{ncg}} = \frac{\rho f_{\text{ncg}}}{\rho_{\text{ncg}}} = \rho f_{\text{ncg}} \frac{RT}{WP} \tag{7}$$

Therefore, in this model, the noncondensable gases not only affect the mass transfer rate between the liquid and vapor (in Eq. (5), the vapor generation term) but also strongly affect the flow field as its volume increases with decreasing pressure (Eq. (7)). The calculated results show that in most of the cavity, noncondensable gas volume fraction is quite high. This also explains the fact that Eq. (5) has much lower empirical factors, c_e and c_c, than other models [7,8] that do not include noncondensable gas effects.

Figure 5 compares pressure distributions on the suction side of the profile, which shows that the cavity length and pressure distribution on the wall can be reasonably predicted if the noncondensable gas mass fraction is properly selected. For the case in Fig. 5, $f_{\text{ncg}}=6\times10^{-8}-8\times10^{-8}$ give the best results with higher noncondensable gas for lower cavitation numbers. Lower f_{ncg} (less than 6×10^{-8}) experienced some convergence difficulties.

The experimental data had more gradual pressure increases near the downstream end of the cavity than that shown in calculated results. Figure 5 shows that the calculated pressure gradient was quite steep in the closure region of the cavity with a very stable cavity. These imply that the closure region is not well predicted. Katz and Gopalan [14] observed that for sheet cavities, the cavity shapes in the closure region are highly irregular and unsteady. They indicated that cavity collapse in the closure region involves substantial increases in turbulence and momentum and displacement thickness in the boundary layer. However, the present model did not consider the interaction between the turbulence and the vapor collapse in the closure region, which might explain the lack of accuracy in the closure region.

When the predicted cavity length exceeded half the chord, the cavity became unstable, as was also observed in the experiments. The results with $f_{\text{ncg}}=8\times10^{-8}$ for $\sigma=1.25$ show that the standard RNG κ-ε model predicted an unstable cavity expanding and shrinking within $0.35C-0.6C$ with a frequency of 4.5 Hz. The typical vapor contours and velocity vectors are shown in Fig. 6. The pressure at P4 is shown in Fig. 7. There was no cavity shedding in the calculated results but the experiments revealed cloud shedding for this condition with the main frequency of the pressure oscillations of 3.625 Hz. Therefore, although the calculations predicted cavity instabilities for $\sigma=1.25$, the unsteady behavior was not correctly simulated by the standard RNG κ-ε model.

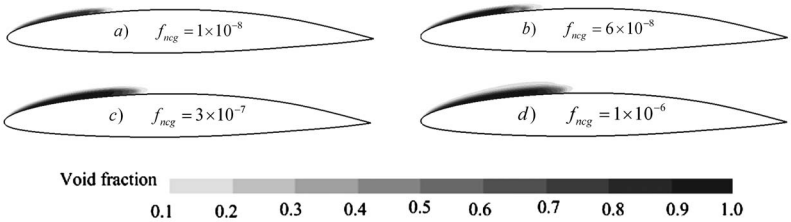

Fig. 4 Calculated cavity shape for $\sigma=1.41$ using various f_{ncg} with the standard RNG κ-ε model

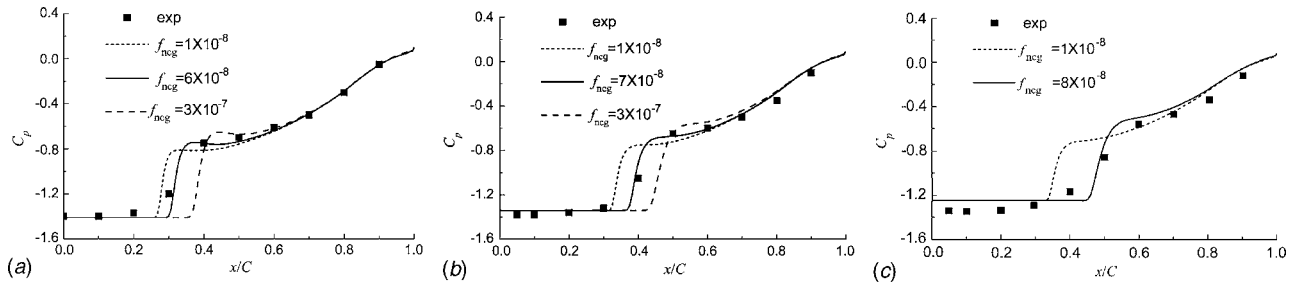

Fig. 5 Predicted pressure distribution on the suction side for various noncondensable gas mass fractions

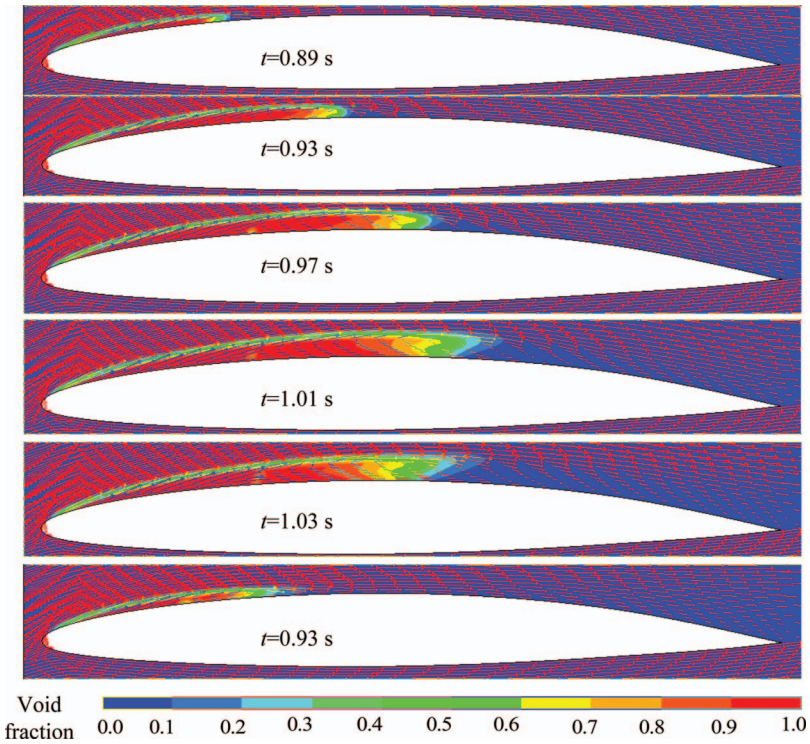

Fig. 6 Calculated void fraction contours and velocity vectors for $\sigma=1.25$ using the standard RNG κ-ε model, $f_{ncg}=8\times10^{-8}$ (to get a clear view, every four vector is displayed)

Simulations With a Modified Renormalization-Group κ-ε Model. Delgosha et al. [4] suggested a modification to the standard RNG κ-ε model, which simply reduced the mixture turbulent viscosity. In the standard RNG κ-ε model, the turbulent viscosity is defined as

$$\mu_t = \rho c_\mu \frac{k^2}{\varepsilon} \tag{8}$$

where $c_\mu=0.085$.

The modified turbulent viscosity is defined as

$$\mu_t = f(\rho) c_\mu \frac{k^2}{\varepsilon} \tag{9}$$

where

$$f(\rho) = \rho_v + (a_l)^n(\rho_l - \rho_v) \tag{10}$$

This modification was found to significantly improved simulations of the cloud shedding.

Various values of n were used in the modified RNG κ-ε model. The results showed that with $f_{ncg}=8\times10^{-8}$, $n=3-10$ gave similar results. The predicted shedding frequency was about 3.57 Hz using $n=3$ and 3.75 Hz using $n=10$, which are both close to the experimental frequency. The behavior and the development of the cavity cycle were also inspected in detail. The wall pressure fluctuations at the various points are shown in Fig. 8 for $n=3$. Only part of numerical results is shown in order to compare with the experimental results. The time axis for numerical results was panned in such a way to align the beginning of a new cycle of numerical results at 0.17 s, the initial point for the experimental cycle. Generally, the calculated pressure distributions agreed reasonably well with the experimental data and the cavity growth is predicted reasonably well. A detailed discussion is as follows.

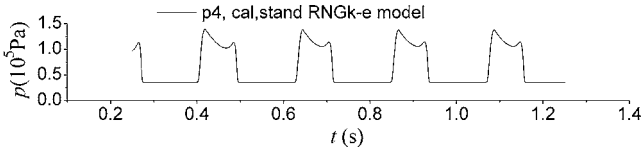

Fig. 7 Calculated pressure variations at P4 for $\sigma=1.25$ using the standard RNG κ-ε model, $f_{ncg}=8\times10^{-8}$

Discussion. The calculated cavity growth can be divided into three stages. Period A is the growth of the sheet cavity, which lasts for about 0.13 s (from 0.17 s to 0.30 s). Comparison of the spatial-temporal pressure distributions on the suction wall with experimental data shows that the sheet cavity growth period is well predicted in Period A. The sheet cavity before destabilization was about $0.7C$ long in agreement with the experimental data. Initially, the cavity has a smooth interface. Then, the reentrant flow develops at the rear of the cavity (at about $t=0.215$ s). As the cavity length exceeds 1/3 of the chord, the interface becomes wavy and the reentrant flow pushes further toward the front (see Fig. 8, $t=0.255$ s), which makes the cavity interface move upward and the cavity grow thicker. The main flow above the interface accelerates and the pressure near the rear of the cavity decreases, which causes the cavity to grow further until the cavity length reaches about $0.7C$. The pressure at points $P1-P7$ decreases to the vaporization pressure in an orderly succession.

However, some differences were noticeable. The calculated results failed to predict the small shedding on the rear part of the sheet cavity (labels a and b in Fig. 8) observed in the experiments due to the fact that the interaction between the turbulence and the vapor collapse in the closure region was not included in the model, as mentioned earlier for the stable cavity results. For the same reason, the average pressure on the rear part was estimated to be lower, as shown in Fig. 10.

Both the calculated results and the experimental data showed the pressure perturbations, which cut the cavity into two parts (see Fig. 8). Period B (from $t=0.30$ s to 0.41 s) in Fig. 9 shows that

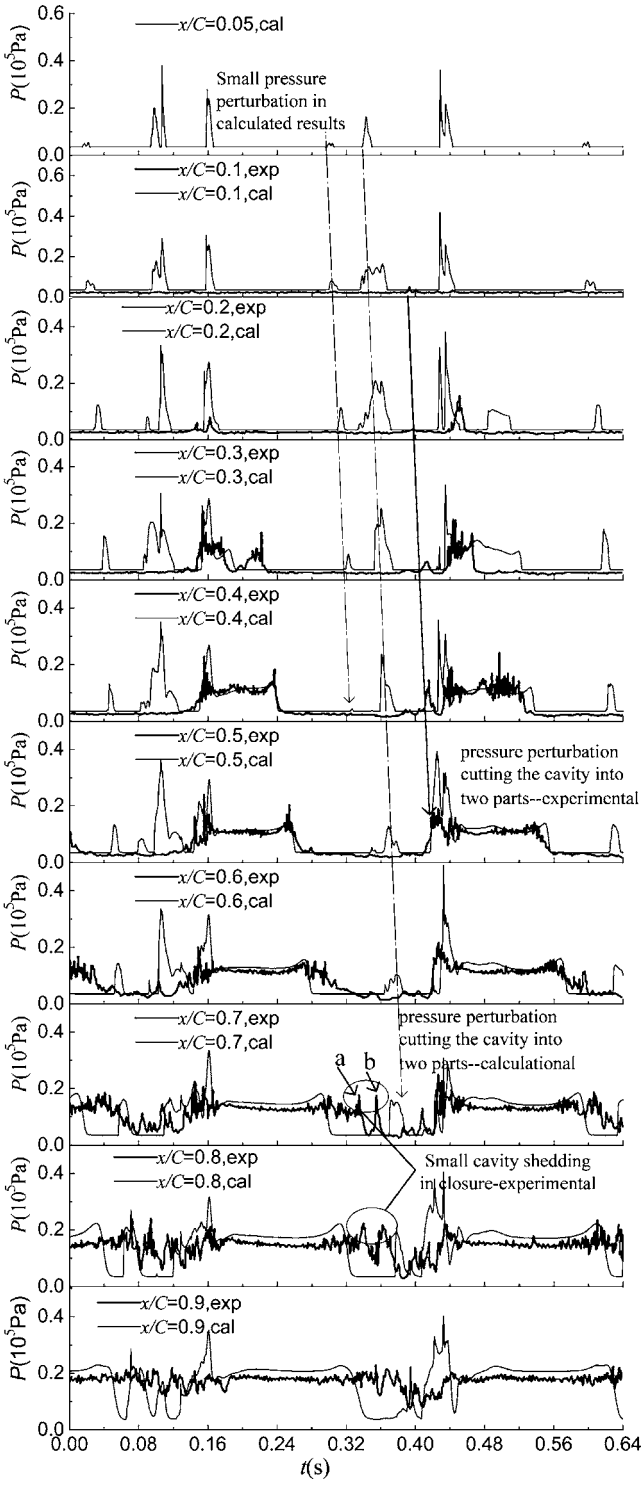

Fig. 8 Predicted pressure fluctuations during cavity growth and destabilization for $\sigma=1.25$ using the modified RNG κ-ε model, $f_{ncg}=8\times10^{-8}$

this is related to the interaction between the reversed flow and the cavity interface, which was confirmed by other researchers [15,16]. The standard RNG κ-ε model failed to predict the unstable cavity cycle, which was more accurately predicted by the modified RNG κ-ε model since the modified RNG κ-ε model reduced the turbulence viscosity within the high void fraction region. Figures 6 and 9 show that both the standard RNG κ-ε model and the modified RNG κ-ε model predicted the reversed flow in the bottom of the sheet cavity; however, the standard RNG κ-ε model did not predict that the reverse flow would reach the front of the hydrofoil. With the modified RNG κ-ε model, the reversed flow developed toward the front with negative velocities on most of the suction surface. This is consistent with the experimental results of George et al. [17] that longer partial cavities at larger attack angles showed consistently negative gas-phase velocities near the hydrofoil midchord. The reversed flow perturbed the cavity interface near the front of the hydrofoil and caused rolling up of the cavity, with this process being closely related to the vortex movement, as shown in Fig. 9. These results suggest that the interaction between the reversed flow and the cavity interface is closely related to the reduction of the turbulent viscosity. Although Delgosha et al. [4] stated that the modified model included the compressibility effect, they also noticed that the final effect of the modification was to reduce the turbulent viscosity in the vapor/liquid mixture zone. As was pointed out by Ceccio and Iyer [18] in their experiments on developed cavitation in a shear layer, the cavitation within the cores of streamwise vortices decoupled the stretching and rotation rate of these flow structures and reduced the Reynolds stresses and cross-stream velocity fluctuations. Therefore, the presence of cavitation within the shear layer may change the effective rheology of the flow. This effect may also exist in the present case with an obvious shear layer (Fig. 9). Equation (10) includes this effect in a simple way; thus, the results are improved regardless of which barotropic state law is used (the calculations of Delgosha et al. [4]) or if the full cavitation model (the present calculations) is used.

However, the modified RNG κ-ε model tends to overestimate the pressure increase caused by the interaction between the reentrant jet and the cavity interface. Figure 8 shows that the calculated pressure perturbations were much more violent on the front part of the surface and occurred a little earlier than in the experimental data. There is a small disturbance which lasts for about 0.02 s (from 0.30 s to 0.32 s) with small irregular pressure fluctuations from $0.1C$ to $0.4C$ (see Fig. 8). Then, major pressure perturbations occur caused by the shedding of the rear part of the cavity. This is initiated near the head (at $0.05C$) with a distinct pressure increase. However, in the experimental data, the major pressure perturbation was observed at approximately the middle of the cavity (at $0.4C$). In addition, the pressure perturbations lasted much longer in the calculated results than in the experimental data.

Both experimental and calculation results show that after the cavity is cut into two parts, the cavity near the head continues to grow and forms a sheet cavity while the rear part cavity moves downstream. Figure 9 shows that the moving of the rear part of the cavity is related to the rolling up of the vortex, which readjusts the velocity and pressure in the middle part of the chord. So, Fig. 8 shows a small pressure increase at each point in order, which corresponds to the growth of the front part of the cavity and the shedding of the rear part of the cavity.

The rear part of the cavity disappears in Period C. The overall pressure increase and cavity destabilization during the shedding of the rear part of cavity in Period C were predicted by the calculations. When the rear part of the cavity totally disappears into wake behind the hydrofoil, the pressure over the whole suction surface suddenly increases, which collapses sheet cavity on the front part. For some time, the whole surface is free of cavities. This period lasts for about 0.05 s (from $t=0.41$ s to 0.445 s) with another cycle then begins as the sheet cavity starts to grow again on the front part.

A shock wave is believed to occur when the rear part of the cavity collapses in the high pressure region downstream [13]. Since the present calculation assumed that the liquid phase was incompressible, the shock wave propagation could not be predicted. Figure 8 shows that the pressure increased suddenly at almost the same time (at $t=0.42$ s) at all points. The velocity vectors in Fig. 9 indicate that the shedding of the rear part of the

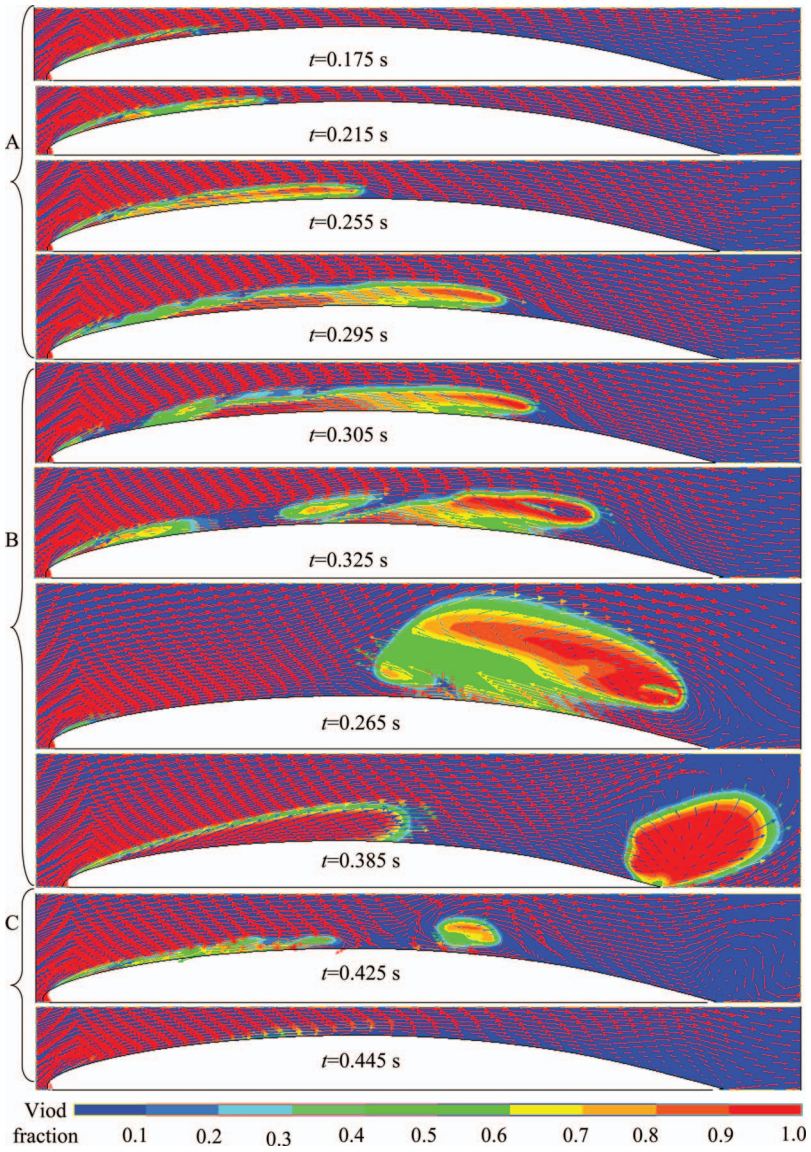

Fig. 9 Calculated void fraction contours and velocity vectors for $\sigma=1.25$ using the modified RNG κ-ε model, $f_{ncg}=8\times10^{-8}$ (to get a clear view, every four vector is displayed)

cavity is closely related to the vortex shedding. The vanishing of the cavity and the vortex reduced the blockage effects and caused the pressure increase, which quickly collapsed the remaining sheet cavity on the front part. The hydrofoil was then free of a cavitation region for a short period. The collapse of the main cavity near the back was the main reason for the pressure peak in this period. However, the predicted pressure peak was a little higher, which may due to the reason that the compressibility and bubble cloud effects were not included in the calculation: The experiments showed that the rear part cavity is bubble cloud, which can influence the fluid compressibility and wave speed and affect the collapsing behavior, while Fig. 9 shows that the calculated rear part cavity is bumpy.

Therefore, the pressure was overestimated on the front part of the hydrofoil, as shown in Fig. 10 because the pressure increase caused by interaction between the reentrant jet and the cavity interface was overestimated in Period B. The predicted pressure peak caused by the collapse of the main cavity near the back was also a little higher in Period C. The simplification from 3D problem to a 2D model can also lead to the differences of amplitude between the numerical and experimental pressure fluctuations. Therefore, much more research work is needed in the future.

Influence of *n*. The calculated results show that the index n had little influence on the frequency of the unstable cavity as long as n

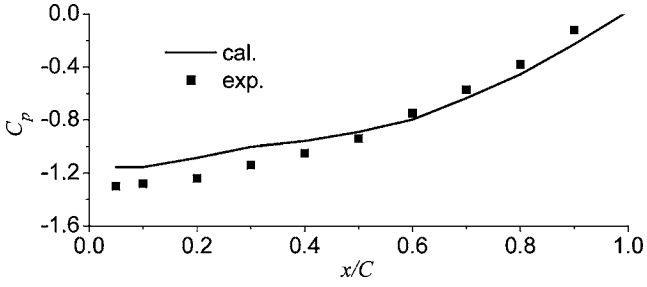

Fig. 10 Comparison of the pressure distribution on the suction surface for $\sigma=1.25$. The calculated data were obtained using the modified RNG κ-ε model, $f_{ncg}=8\times10^{-8}$.

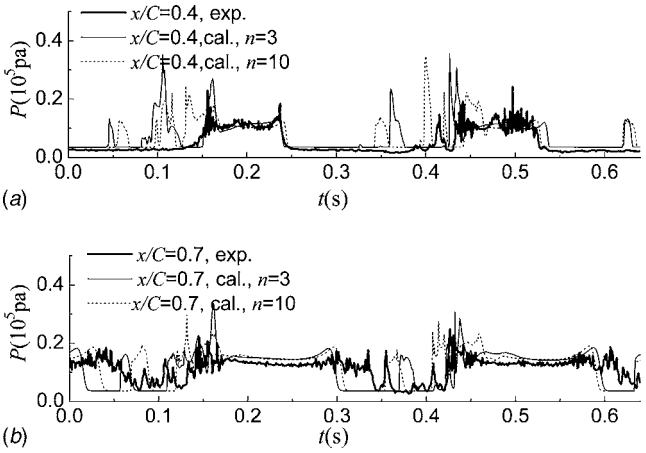

Fig. 11 Influence of parameter *n* on the predicted pressures at P4 and P7. $f_{ncg}=8\times10^{-8}$ was used for both $n=3$ and $n=10$.

was larger than 3. The cavity growth cycle for $n=10$ was also composed of three stages, the sheet cavity growth period, the pressure disturbance period with the cavity being cut into two parts, and the high pressure period after the shedding of the rear part of the cavity. The differences between the predictions for $n=10$ and $n=3$ in Fig. 11 are insignificant since the variations are similar to the variations in the experimentally measured cavity growth cycles, which were similar but not identical.

Conclusion

Cavitating flow around a hydrofoil was simulated using a TEM including noncondensable gas effects. The cavity length and the pressure distributions on the suction side were well predicted for stable cavities using the standard RNG κ-ε turbulence model with proper noncondensable gas mass fraction. However, the interaction between turbulence and the vapor collapse in the closure region was not included in the model, so the results were less accurate there.

The results showed that for lower cavitation numbers, the cavity was unstable when its length exceeded half the chord. The unstable cavity shedding at lower cavitation numbers was not well predicted by the standard RNG κ-ε turbulence model. A modified RNG κ-ε turbulence model was found to more accurately predict the shedding frequency by reducing the turbulent viscosity in the mixture region. The modified RNG κ-ε turbulence model was evaluated based on a detailed comparison of the calculated spatial-temporal pressure distributions on the suction wall with experimental data. The results showed that the cavity growth/shedding cycle characteristics and frequency agreed well with experimental data. The sheet cavity length before the rear cavity shedding was reasonably predicted. The calculated results also describe the interaction behavior between the reentrant flow and the cavity interface, which is one reason for the cavity destabilization. The sudden pressure increase along the whole wall caused by the collapse of the main cavity in the rear, which is another reason for the cavity destabilization, was also seen in the results. However, the time-averaged pressure on the front part of the hydrofoil was overestimated because the pressure increase caused by interaction between the reentrant flow and the cavity interface was overestimated. The time-averaged pressure on the rear of the hydrofoil was low because the small cavity shedding on the rear part of the cavity was not predicted.

Nomenclature

a_v, a_{ncg}, a_l = vapor, gas, and liquid volume fractions
C = hydrofoil chord (m)
C_p = pressure coefficient defined by $C_p=(p-p_r)/(0.5\rho u^2)$
f_v, f_{ncg}, f_l = vapor, gas, and liquid mass fractions
P = pressure (Pa)
P_r = pressure at reference point (Pa)
P_v = vaporization pressure (Pa), set as 3540 Pa in the present study
t = time (s)
u = freestream velocity (m/s)
$\mathbf{V}$ = velocity vector (m/s)
y^* = the nondimensional normal distance from the wall defined by $y^*=(\rho c_\mu^{1/4}k^{1/2}/\mu)y_d$, with y_d the distance to the wall
ρ = mixture density (kg/m^3)
μ = laminar viscosity ($N\,s/m^2$)
μ_t = turbulent viscosity ($N\,s/m^2$)
$\rho_v, \rho_{ncg}, \rho_l$ = vapor, gas, and liquid densities (kg/m^3)
σ = cavitation number defined by $\sigma=(p_r-p_v)/(0.5\rho u^2)$

Acknowledgment

The authors gratefully acknowledge the support from Key Technologies R&D Program for China's 11th Five-Year Plan (2006BAJ04B03).

References

[1] Kubota, A., Kato, H., and Yamaguti, H., 1992, "A New Modeling of Cavitating Flows: A Numerical Study of Unsteady Cavitation on a Hydrofoil Section," J. Fluid Mech., **240**, pp. 59–96.
[2] Delannoy, Y., and Kueny, J. L., 1990, "Two Phase Flow Approach in Unsteady Cavitation Modeling," *Cavitation and Multiphase Flow Forum*, Vol. 98, pp. 153–158.
[3] Delgosha, C. O., Reboud, J. L., and Delannoy, Y., 2003, "Numerical Simulation of the Unsteady Behaviour of Cavitating Flows," Int. J. Numer. Methods Fluids, **42**, pp. 527–548.
[4] Delgosha, C. O., Patella, F. R., and Reboud, J. L., 2003, "Evaluation of the Turbulence Model Influence on the Numerical Simulations of Unsteady Cavitation," ASME J. Fluids Eng., **125**, pp. 38–45.
[5] Iga, Y., Nohml, M., Goto, A., and Ikohagi, T., 2004, "Numerical Analysis of Cavitation Instabilities Arising in the Three-Blade Cascade," ASME J. Fluids Eng., **126**, pp. 419–429.
[6] Iga, Y., Nohml, M., Goto, A., Shin, B. R., and Ikohagi, T., 2003, "Numerical Study of Sheet Cavitation Breakoff Phenomenon on a Cascade Hydrofoil," ASME J. Fluids Eng., **125**, pp. 643–651.
[7] Senocak, I., and Shyy, W., 2004, "Interfacial Dynamics-Based Modelling of Turbulent Cavitating Flows, Part I: Model Development and Steady-State Computations," Int. J. Numer. Methods Fluids, **44**, pp. 975–995.
[8] Senocak, I., and Shyy, W., 2004, "Interfacial Dynamics-Based Modelling of Turbulent Cavitating Flows, Part II: Time-Dependent Computations," Int. J. Numer. Methods Fluids, **44**, pp. 997–1016.
[9] Kunz, R. F., Boger, D. A., Stinebring, D. R., Chyczewski, T. S., Lindau, J. W., Gibeling, H. J., Venkateswaran, S., and Govindan, T. R., 2000, "A Preconditioned Navier-Stokes Method for Two-Phase Flows With Application to Cavitation Prediction," Comput. Fluids, **29**, pp. 849–875.
[10] Yuan, W., and Schnerr, G. H., 2003, "Numerical Simulation of Two-Phase Flow in Injection Nozzles: Interaction of Cavitation and External Jet Formation," ASME J. Fluids Eng., **125**, pp. 964–969.
[11] Singhal, A. K., Athavale, M. M., Li, H. Y., and Jiang, Y., 2002, "Mathematical Basis and Validation of the Full Cavitation Model," ASME J. Fluids Eng., **124**, pp. 617–624.
[12] Yakhot, V., Orszag, S. A., Thangham, S., Gatski, T. B., and Speziale, C. G., 1992, "Development of Turbulence Models for Shear Flows by a Double Expansion Technique," Phys. Fluids A, **4**(7), pp. 1510–1520.
[13] Leroux, J. B., Astolfi, J. A., and Billard, J. Y., 2004, "An Experimental Study of Unsteady Partial Cavitation," ASME J. Fluids Eng., **126**, pp. 94–101.
[14] Katz, J., and Gopalan, S., 2000, "Flow Structure and Modeling Issues in the Closure Region of Attached Cavitation," Phys. Fluids, **12**(4), pp. 895–911.
[15] Pham, T. M., Larrarte, F., and Fruman, D. H., 1999, "Investigation of Unsteady Sheet Cavitation and Cloud Cavitation Mechanisms," ASME J. Fluids Eng., **121**, pp. 289–296.
[16] Kubota, S., Kato, H., Yamaguchi, H., and Meada, M., 1987, "Unsteady Structure Measurement of Cloud Cavitation on a Foil Section Using Conditional Sampling Technique," *International Symposium on Cavitation Research Facilities and Techniques*, Boston, pp. 161–168.
[17] George, D. L., Iyer, C. O., and Ceccio, S. L., 2000, "Measurement of the Bubbly Flow Beneath Partial Attached Cavities Using Electrical Impedance Probes," ASME J. Fluids Eng., **122**, pp. 151–155.
[18] Ceccio, S. L., and Iyer, C. O., 2002, "The Influence of Developed Cavitation on the Flow of a Turbulent Shear Layer," Phys. Fluids, **14**(10), pp. 3414–3431.

A Grid-Free Lagrangian Approach of Vortex Method and Particle Trajectory Tracking Method Applied to Internal Fluid-Solid Two-Phase Flows

Yoshiyuki Iso
Heat and Fluid Dynamics Department,
Research Laboratory,
IHI Corporation,
1 Shin-Nakahara,
Isogo, Yokohama,
Kanagawa 235-8501, Japan
e-mail: yoshiyuki_iso@ihi.co.jp

Kyoji Kamemoto
Graduate School of Engineering,
Yokohama National University,
79-5 Tokiwadai,
Hodogaya, Yokohama,
Kanagawa 240-8501, Japan
e-mail: kamemoto@ynu.ac.jp

We have developed a numerical simulation scheme combining a vortex method and a particle trajectory tracking method, which is applicable to internal unsteady two-phase flows. It is a completely grid-free Lagrangian–Lagrangian simulation, which is able to simulate the primary effect of vortical flow on the unsteady particle motion and dispersion. It can handle unsteady high Reynolds number flows. So far, no one has applied this kind of method internal multiphase flows, though many industrial multiphase flows are internal. In this study, internal liquid-solid two-phase flows in a vertical channel and a mixing tee have been calculated by the new method, in which use of the vortex introduction model enables the simulation of the dynamic behavior of separation or reattachment. In the mixing tee, solid particle phenomena such as depositions or particle-wall collisions have been simulated and measured. Numerical results based on simple two-dimensional flow and one-way model show good agreement with the experimental data. The results show that turbulent vortices dominate particle motion. It has been shown that the present method can be useful in the design of industrial multiphase flows with particle mixing, dispersion, deposition, and particle-wall collision because it is possible to simulate the effect of turbulent vortices on the particle motion. [DOI: 10.1115/1.2813139]

Keywords: vortex method, particle trajectory tracking method, fluid-solid two-phase flow, internal unsteady flow, grid-free simulation, lagrangian-lagrangian simulation,

1 Introduction

Two-phase flows, liquid-solid or gas-solid, are observed in many industrial processes such as transport, mixing, separation, chemical reaction, combustion, etc. Therefore, one of the most interesting and important problems is the prediction of two-phase flows. In these kinds of systems, some troubles and performance deficiencies such as erosion, deposition, and nonuniformity of solid particle distributions often occur. Consequently, for designing the devices including solid particle flows, it is necessary to predict not only fluid flow characteristics but also the particle distributions and the interaction of particles and walls. To design these devices with high efficiency and low cost, it is required that the numerical simulation can be applied to fluid-particle two-phase flow.

Generally, many fluid-particle flows in industrial processes can be characterized as with high Reynolds number, turbulent, unsteady, and vortical. In such flows, the turbulent vortices with several scales dominate unsteady solid particle motions. Therefore, it is important to simulate the primary effect of turbulent vortices on the unsteady particle motion and dispersion in these flows, for example, shear layers, jets, and mixing flows. For details, refer to Crowe et al. [1–3], Hishida et al. [4], and Ishima et al. [5].

In this study, we have made an attempt to apply a numerical simulation scheme combining a vortex method and a particle trajectory tracking method into internal unsteady two-phase flows. It is a Lagrangian–Lagrangian simulation. The unsteady vortex motions of fluid are tracked using a vortex method, and the unsteady solid particle motions, which are dominated by the vortex-induced fluid dynamical force, are tracked using a particle trajectory tracking method. The method has some special advantages. First, it can simulate unsteady, high Reynolds number, and vortical flows without using any conventional time-averaged turbulence model [6–8]. Second, it can track the process of development and dissipation of turbulent vortices and simulate the effect of several scale vortices on the unsteady particle motion [3]. Third, it is completely grid-free.

Due to such advantages, this method had been extended to simulations of multiphase flows in various external flows such as shear layers and jets. For details, refer to Chein and Chung [9], Wen et al. [10], Perkins and Joia [11], and Wang et al. [12], etc. Recently, a two-way model between both fluid and particle phases was suggested by Joia et al. [13], Uchiyama et al. [14,15], and Walther and Koumoutsakos [16]. However, there are few applications of them to internal multiphase flows, even internal single-phase flows, though many industrial flows are internal, which involve several problems such as erosion and deposition of solid particles.

The primary purpose of the present study is to clarify the applicability of the Lagrangian–Lagrangian method, which is simplified as a two-dimensional flow and one-way model, into internal unsteady liquid-solid two-phase flows of high Reynolds number and vortical flows.

2 Numerical Method

The present numerical method is schematically shown in Fig. 1. The fluid flow is calculated by a vortex method and the solid

Contributed by the Fluids Engineering Division of ASME for publication in the JOURNAL OF FLUIDS ENGINEERING. Manuscript received September 23, 2006; final manuscript received August 18, 2007; published online December 19, 2007. Review conducted by Joseph Katz.

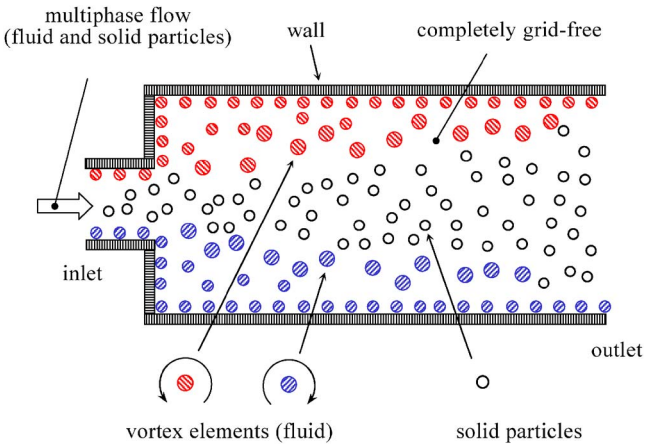

Fig. 1 Outline of present Lagrangian–Lagrangian simulation scheme applied to internal multiphase flows

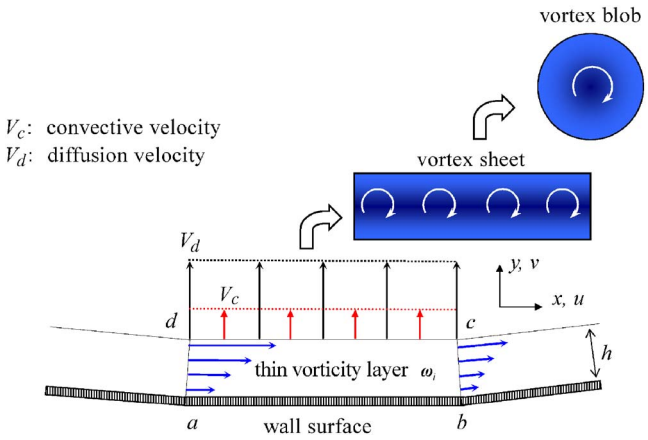

Fig. 2 Introduction of nascent vortex elements from the wall

particle flow by a particle trajectory tracking method. Both phases are treated by a completely grid-free Lagrangian–Lagrangian simulation without the generally used Eulerian grids. This makes it is possible to simulate solid particle motion directly, which are dominated by the vortex-induced fluid dynamical force. Additionally, since there is no grid, no requirements regarding the grid are to be satisfied, the proposed method is well posed to the solution of multiphase flow problems by trial and error or case studies. Details of the method and example applications into internal multiphase flows are described by the authors elsewhere [17,18].

2.1 Vortex Method. In the vortex method, the continuous vorticity field is discretized into a finite number of discrete vortex elements. It simulates the unsteady vortical flow by tracking the vortices, the strength and location of which change by convection and diffusion. For details, refer to Nakanishi and Kamemoto [19], Kamemoto [6], and Ojima and Kamemoto [7].

Governing equations of the method are based on the Navier–Stokes equations. Taking the rotation and divergence of these equations for viscous and incompressible flow gives the vorticity transport equation and the pressure Poisson equation,

$$\frac{\partial \boldsymbol{\omega}}{\partial t} + (\boldsymbol{u} \cdot \text{grad})\boldsymbol{\omega} = (\boldsymbol{\omega} \cdot \text{grad})\boldsymbol{u} + \nu \nabla^2 \boldsymbol{\omega} \tag{1}$$

$$\nabla^2 p = -\rho_f \, \text{div}(\boldsymbol{u} \cdot \text{grad}\, \boldsymbol{u}) \tag{2}$$

where $\boldsymbol{u}$ is the velocity vector, $\boldsymbol{\omega}$ is the vorticity vector defined as

$$\boldsymbol{\omega} = \text{rot}\, \boldsymbol{u} \tag{3}$$

ν is the kinematic viscosity, ρ_f is the density of fluid, p is the pressure, and ∇^2 is the Laplacian operator.

The velocity at an arbitrary location $\boldsymbol{r}$ in the fluid is obtained by applying the Biot–Savart law, as explained by Wu and Thompson [20],

$$\boldsymbol{u} = \int_V \boldsymbol{\omega}_i \times \nabla_i G dv + \int_S [(\boldsymbol{n}_j \cdot \boldsymbol{u}_j) \cdot \nabla_j G - (\boldsymbol{n}_j \times \boldsymbol{u}_j) \times \nabla_j G] ds \tag{4}$$

Here, the subscript i indicates variable or differentiation at a location $\boldsymbol{r}_i$ in the flow field, and the subscript j that on a boundary surface S. $\boldsymbol{n}$ is the normal unit vector at a point on a boundary surface. ∇ denotes the gradient operator. G is the fundamental solution of the scalar Laplace equation, which is written for two-dimensional flows as

$$G = \frac{1}{2\pi} \log\left(\frac{1}{|\boldsymbol{r} - \boldsymbol{r}_{i \text{ or } j}|}\right) \tag{5}$$

In the present method, the vorticity transport equation, Eq. (1), is numerically solved by the time-splitting scheme. If the vorticity of a discrete fluid element i at time t is written as $\boldsymbol{\omega}_i(t)$, an approximate Lagrangian expression for the change of vorticity can be obtained through convection and diffusion during a small time interval dt. In Eq. (1), the first term on the right-hand side arises from the three-dimensional stretching of vorticity, which always becomes zero for two-dimensional flows. The second term is the rate of viscous diffusion of vorticity. It is treated using the core spreading method proposed by Nakanishi and Kamemoto [19].

In this study, to discretize the vorticity, the computational domain is divided into two regions, namely, the boundary region and the interior region. In the thin boundary region, the vorticity is discretized using rectangular vortex sheets with constant vorticity distributions, while the vorticity is discretized using vortex blobs in the interior region.

The vortex blob possesses its own smoothed vorticity distribution and spherical core radius. As explained by Leonard [21], vorticity around the vortex blob i with core radius ε_i and total circulation Γ_i is described by a Gaussian distributed function. For two-dimensional flows, the vorticity distribution $\omega(\boldsymbol{r})$ due to the discrete vortex blobs is expressed as

$$\omega(\boldsymbol{r}) = \sum_{i=1}^{N} \frac{\Gamma_i}{\pi \varepsilon_i^2} \exp\left[-\left(\frac{|\boldsymbol{r} - \boldsymbol{r}_i|}{\varepsilon_i}\right)^2\right] \tag{6}$$

where N is the total number of vortex blobs.

Following Nakanishi and Kamemoto [19], the spreading of the core radius caused by the viscous diffusion, which is expressed by the second term on the right-hand side of Eq. (1), is represented as

$$\frac{d\varepsilon_i}{dt} = \frac{C^2 \nu}{2\varepsilon_i} \quad (C = 2.242) \tag{7}$$

In this study, we try to apply this grid-free simulation scheme into internal flows by using the following models. The boundary surfaces of the inlets, outlets, and walls surrounding the flow field are expressed by linear vortex panels. We decide on the strength of the vortex panels by using the boundary element method. The inlet boundary condition is imposed by an inlet velocity profile. The outlet boundary condition is imposed by the free outflow (zero gradients) and the mass conservation in the velocity field. The outlet condition is applied far enough downstream so that its application does not influence the flow field in the vicinity of points of interest. The wall boundary condition is the flow parallel to the wall (normal velocities are zero, $\boldsymbol{u} \cdot \boldsymbol{n}|_{\text{wall surface}} = 0$).

The mechanism of vortex element introduction on the wall is shown in Fig. 2. In internal unsteady flows, the vorticity field near the walls can be represented by proper distributions of vorticity layers and vortex elements on the walls so as to satisfy the nonslip

boundary condition. In the advanced method developed by Kamemoto [6], a thin vorticity layer with thickness h is assumed along the wall surface, and the surface of the outer boundary of the thin vorticity layer is discretized by a number of vortex sheet elements, as shown in Fig. 2. The nascent vortex elements are introduced from the thin vorticity layer into the flow field considering their convective and diffusion velocities. The vorticity ω_{iz} originally involved is given so as to satisfy the nonslip boundary condition,

$$\omega_{iz} = \frac{\partial v}{\partial x} - \frac{\partial u}{\partial y} \approx -\frac{\partial u}{\partial y} = \frac{(1/2)(\boldsymbol{n} \times \boldsymbol{u}_1 + \boldsymbol{n} \times \boldsymbol{u}_2)_z}{h} \tag{8}$$

Here, $\boldsymbol{u}_1$ and $\boldsymbol{u}_2$ are the velocity vectors at the panel edges. x and y correspond to parallel and normal directions at wall boundaries in Fig. 2, respectively.

The normal convective velocity V_c is calculated using the relation of continuity of the flow and the nonslip condition on the wall surface in the discrete element of the thin vorticity layer (a-b-c-d),

$$V_c = \frac{1}{\Delta S}\left[h\left(\frac{1}{2}\boldsymbol{u}_1 \cdot \boldsymbol{n}_{f1} + \frac{1}{2}\boldsymbol{u}_2 \cdot \boldsymbol{n}_{f2} \right) \right] \tag{9}$$

where ΔS is the panel area, and $\boldsymbol{n}_{f1}$ and $\boldsymbol{n}_{f2}$ are the normal unit vectors on side sections of the layer. These vectors are directed from the side sections of the layer to the center.

The diffusion velocity V_d is employed in the same manner as the vorticity layer spreading method proposed by Kamemoto [6],

$$V_d = \frac{C_2^2 \nu}{2h} \quad (C_2 = 1.136) \tag{10}$$

If the value of $V_c + V_d$ becomes positive, a nascent vortex element is introduced into the flow field. As above, the present introduction model of vortex elements enables the simulation of dynamic behaviors such as separation or reattachment of vortices without assuming the locations of separation.

2.2 Particle Trajectory Tracking Method. Solid particles were treated by the particle trajectory tracking method as a Lagrangian calculation. Particle-particle and particle-wall collisions are calculated by a deterministic method. In this paper, dilute liquid-solid two-phase flows are assumed. To simplify the problem, we assumed that the effect of solid particles on the liquid flow can be neglected (one-way model), and that all solid particles are rigid spheres; distributions of particle diameters, however, can be considered.

Based on the above assumptions, it is generally accepted that dominant forces on each solid particle are steady-state drag force, Magnus lift force, Saffman lift force, one of the unsteady drag forces called the virtual added mass force, and gravitational force. The force on the solid particles due to pressure gradient and one of the unsteady drag forces called the Basset force are neglected in this study. The equation of translational motion for a solid particle is

$$\frac{d\boldsymbol{u}_p}{dt} = \frac{1}{M_p}(\boldsymbol{F}_D + \boldsymbol{F}_{LM} + \boldsymbol{F}_{LS} + \boldsymbol{F}_{VM} + \boldsymbol{F}_G) \tag{11}$$

where $\boldsymbol{u}_p$ is the particle velocity vector, M_p the particle mass, and $\boldsymbol{F}$ the force vector on the particle; $\boldsymbol{F}_D$ is the steady-state drag force due to the relative velocity of the particle to the fluid, $\boldsymbol{F}_{LM}$ the Magnus lift force due to the rotational motion of the particle, $\boldsymbol{F}_{LS}$ the Saffman lift force due to the velocity gradient of the fluid, $\boldsymbol{F}_{VM}$ the unsteady drag forces of the virtual added mass force and the force due to the fluid acceleration around the particle, and $\boldsymbol{F}_G$ the gravitational force.

The steady-state drag force $\boldsymbol{F}_D$ is calculated as follows:

$$\boldsymbol{F}_D = \tfrac{1}{2} C_D A \rho_f |\boldsymbol{u}_r| \boldsymbol{u}_r \tag{12}$$

where A is the projected area of the particle normal to the flow, ρ_f the density of the fluid phase, and $\boldsymbol{u}_r$ the relative velocity given by $\boldsymbol{u}_r = \boldsymbol{u}_f - \boldsymbol{u}_p$ with $\boldsymbol{u}_f$ as the fluid velocity vector at the location of the particle center and $\boldsymbol{u}_p$ the particle velocity vector. C_D is the nondimensional drag coefficient, which changes with the particle Reynolds number $\mathrm{Re}_p = (|\boldsymbol{u}_r| d_p)/\nu$, where d_p is the particle diameter and ν is the kinematic viscosity of the fluid. We have used the empirical relation of Morsi and Alexander [22], namely,

Table 1 Empirical relation for steady-state drag coefficient C_D

Re_p	C_1	C_2	C_3
$\mathrm{Re}_p \leq 0.1$	0.0	24.0	0.0
$0.1 < \mathrm{Re}_p \leq 1$	3.69	22.73	0.0903
$1 < \mathrm{Re}_p \leq 10$	1.222	29.1667	−3.8889
$10 < \mathrm{Re}_p \leq 10^2$	0.6167	46.5	−116.67
$10^2 < \mathrm{Re}_p \leq 10^3$	0.3644	98.33	−2,778.0
$10^3 < \mathrm{Re}_p \leq 5 \times 10^3$	0.357	148.62	−47,500.0
$5 \times 10^3 < \mathrm{Re}_p \leq 10^4$	0.46	−490.546	578,700.0
$10^4 < \mathrm{Re}_p \leq 5 \times 10^4$	0.5191	−1662.5	5,416,700.0

$$C_D = C_1 + \frac{C_2}{\mathrm{Re}_p} + \frac{C_3}{\mathrm{Re}_p^2} \tag{13}$$

where the coefficients C_1, C_2, and C_3 are presented in Table 1.

The Magnus lift force $\boldsymbol{F}_{LM}$ follows

$$\boldsymbol{F}_{LM} = \frac{1}{2} C_{LM} A \rho_f |\boldsymbol{u}_r| \frac{\boldsymbol{u}_r \times \boldsymbol{\omega}_r}{|\boldsymbol{\omega}_r|} \tag{14}$$

where $\boldsymbol{\omega}_r$ is the rotational relative velocity vector of the particle, which is given by $\boldsymbol{\omega}_r = \boldsymbol{\omega}_p - (1/2)\cdot(\nabla \times \boldsymbol{u}_f)$ with $\boldsymbol{\omega}_p$ the rotational velocity vector of the particle. C_{LM} is the nondimensional lift coefficient, which changes with the peripheral velocity ratio $\Gamma_p = (d_p|\boldsymbol{\omega}_r|)/(2|\boldsymbol{u}_r|)$. We have used the empirical and theoretical relations of Maccoll [23], Davies [24], Rubinow and Keller [25] and Oesterle and Dinh [26],

$$C_{LM} = 2\Gamma_p \quad \text{for } \mathrm{Re}_p \leq 1 \tag{15}$$

$$C_{LM} = 0.45 + (2\Gamma_p - 0.45)\exp(-1.075\Gamma_p^{0.4}\mathrm{Re}_p^{0.7}) \quad \text{for } 10 \leq \mathrm{Re}_p \leq 140 \quad \text{and } 1 \leq \Gamma_p \leq 6 \tag{16}$$

$$C_{LM} = \min[0.5, 0.5\Gamma_p] \quad \text{otherwise} \tag{17}$$

The Saffman lift force $\boldsymbol{F}_{LS}$ for spherical particles in simple uniform shear flow is calculated by Saffman's expression (Saffman [27]), namely,

$$\boldsymbol{F}_{LS} = C_{\mathrm{Mei}} \frac{1.615 d_p^2 \mu}{\sqrt{\nu |\nabla \times \boldsymbol{u}_r|}} \cdot \boldsymbol{u}_r \times (\nabla \times \boldsymbol{u}_r) \tag{18}$$

where μ is the fluid viscosity. C_{Mei} is the modification factor in the case that the particle Reynolds number is high, as explained by Mei [28],

$$C_{\mathrm{Mei}} = (1 - 0.3314\beta^{1/2})\exp\left(-\frac{\mathrm{Re}_p}{10}\right) + 0.3314\beta^{1/2} \quad \text{for } \mathrm{Re}_p \leq 40 \tag{19}$$

$$C_{\mathrm{Mei}} = 0.0524\sqrt{\beta \mathrm{Re}_p} \quad \text{for } \mathrm{Re}_p > 40 \tag{20}$$

$$\beta = \frac{|\nabla \times \boldsymbol{u}_r| \cdot d_p}{2|\boldsymbol{u}_r|} \tag{21}$$

The unsteady drag force $\boldsymbol{F}_{VM}$ is calculated by the following:

$$\boldsymbol{F}_{VM} = \frac{1}{2}\rho_f \left(\frac{\pi}{6} d_p^3\right)\left(\frac{d\boldsymbol{u}_r}{dt}\right) \tag{22}$$

It arises when the particles are accelerated through the surround-

Table 2 Torque coefficients of equation of rotational motion for the range of rotational Reynolds number

Re_r	C_1	C_2	C_3
$\mathrm{Re}_r \leq 1$	0.0	16π	0.0
$1 < \mathrm{Re}_r \leq 10$	0.0	16π	0.0418
$10 < \mathrm{Re}_r \leq 20$	5.32	37.2	0.0
$20 < \mathrm{Re}_r \leq 50$	6.44	32.2	0.0
$50 < \mathrm{Re}_r \leq 100$	6.45	32.1	0.0

ing fluid.

The gravitational force $\boldsymbol{F}_G$ is calculated by

$$\boldsymbol{F}_G = \left(1 - \frac{\rho_f}{\rho_p}\right)\boldsymbol{M}_p \boldsymbol{g} \tag{23}$$

where ρ_p is the particles' density and $\boldsymbol{g}$ the gravitational acceleration.

The equation of rotational motion for a particle due to the fluid viscosity is expressed as

$$I_p \frac{d\boldsymbol{\omega}_p}{dt} = -\frac{1}{2} C_T \rho_f \left(\frac{d_p}{2}\right)^5 |\boldsymbol{\omega}_r| \boldsymbol{\omega}_r \tag{24}$$

Here, I_p is the moment of inertia of the spherical particle, namely,

$$I_p = \frac{8}{15}\pi \rho_p \left(\frac{d_p}{2}\right)^5 \tag{25}$$

The right-hand side of Eq. (24) is the viscous torque against particle rotation, which is theoretically obtained by Dennis et al. [29] and Takagi [30]. C_T is the nondimensional rotational torque coefficient, which is a function of the Reynolds number for rotational motion based on the relative angular velocity as $\mathrm{Re}_r = |\boldsymbol{\omega}_r| d_p^2/(4\nu)$, given by

$$C_T = \frac{C_1}{\sqrt{\mathrm{Re}_r}} + \frac{C_2}{\mathrm{Re}_r} + C_3 \mathrm{Re}_r \tag{26}$$

where the coefficients C_1, C_2, and C_3 are presented in Table 2.

Particle-particle and particle-wall collisions were calculated by a deterministic method (Tanaka and Tsuji [31] and Yamamoto et al. [32]). Translational velocities $\boldsymbol{u}_p^*$ and rotational velocities $\boldsymbol{\omega}_p^*$ of particles i and j after the collision are calculated by the equations of impulsive motion as

$$\boldsymbol{u}_{pi}^* = \boldsymbol{u}_{pi} + \frac{\boldsymbol{J}_{ij}}{\boldsymbol{M}_{pi}} \quad \boldsymbol{\omega}_{pi}^* = \boldsymbol{\omega}_{pi} + \frac{d_{pi}}{2I_{pi}} \boldsymbol{n}_{ij} \times \boldsymbol{J}_{ij} \tag{27}$$

$$\boldsymbol{u}_{pj}^* = \boldsymbol{u}_{pj} - \frac{\boldsymbol{J}_{ij}}{\boldsymbol{M}_{pj}} \quad \boldsymbol{\omega}_{pj}^* = \boldsymbol{\omega}_{pj} + \frac{d_{pj}}{2I_{pj}} \boldsymbol{n}_{ij} \times \boldsymbol{J}_{ij} \tag{28}$$

Here, $\boldsymbol{J}_{ij}$ is the impulsive force exerted on particle i, and $\boldsymbol{n}_{ij}$ is the normal unit vector directed from the center of particle i to the contact point. For the calculation of particle-wall collisions, the particle j is treated as the wall. We assumed that particle deformation is negligible, the coefficients of restitution and friction for all collisions are constant, the tangential impulsive force during the slip motion is given by Coulomb's friction law, and the slip between particles does not occur again after the initial slip dies out. According to these assumptions, $\boldsymbol{J}_{ij}$ can be calculated as follows:

$$\boldsymbol{J}_{ij} = -J_n \boldsymbol{n}_{ij} - J_t \boldsymbol{t}_{ij} \tag{29}$$

$$J_n = (1+e) M_{ij} \boldsymbol{n}_{ij} \cdot \boldsymbol{V}_{ij} \tag{30}$$

$$J_t = \min\left[\mu_f (1+e) M_{ij} \boldsymbol{n}_{ij} \cdot \boldsymbol{V}_{ij} \ \tfrac{2}{7} M_{ij} |\boldsymbol{V}_{f_{ij}}|\right] \tag{31}$$

In the above equations, $\boldsymbol{t}_{ij}$ is the tangential unit vector in the direction of the slip velocity of particle i to j, e is the coefficient of restitution, and μ_f is the coefficient of friction. M_{ij} is the reduced mass expressed as

$$M_{ij} = \frac{M_{pi} M_{pj}}{M_{pi} + M_{pj}} \quad \text{for particle-particle collision} \tag{32}$$

$$M_{ij} = M_{pi} \quad \text{for particle-wall collision} \tag{33}$$

$\boldsymbol{V}_{ij}$ is the relative velocity between the centers of mass,

$$\boldsymbol{V}_{ij} = \boldsymbol{u}_{pi} - \boldsymbol{u}_{pj} \tag{34}$$

$\boldsymbol{V}_{f_{ij}}$ is the slip velocity between particle surfaces,

$$\boldsymbol{V}_{f_{ij}} = \boldsymbol{V}_{ij} - (\boldsymbol{V}_{ij} \cdot \boldsymbol{n}_{ij}) \boldsymbol{n}_{ij} + \left(\tfrac{1}{2} d_{pi} \boldsymbol{\omega}_{pi} + \tfrac{1}{2} d_{pj} \boldsymbol{\omega}_{pj}\right) \times \boldsymbol{n}_{ij} \tag{35}$$

In the present study, particle-wall collisions are modeled employing irregular bouncing of particles off the wall by using the virtual wall model proposed by Tsuji et al. [33,34], in which the wall is replaced with a virtual wall having an angle relative to the real wall.

Physical motion of the particles is split up into two stages in order to reduce the computational load. In the first stage, all particles are moved based on the equation of motion without collisions. In the second stage, the particles colliding with neighboring particles or walls are searched by a deterministic method, and then the equations of impulsive motion for colliding particles are calculated by the method mentioned above. Here, for particle-particle collision, the velocities and rotational velocities of the collision pair are replaced by postcollision ones without changing the position. For particle-wall collision, the time interval Δt is subdivided into Δt_w and $\Delta t - \Delta t_w$, where Δt_w is the time before the collision. Each particle is moved in the first interval Δt_w using the precollision quantities and moved in $\Delta t - \Delta t_w$ according to the postcollision values.

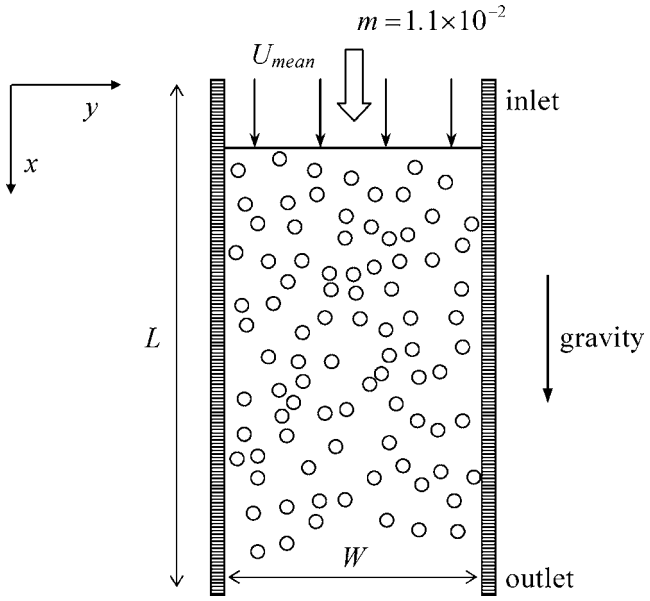

Fig. 3 Outline of the vertical channel flow problem

3 Liquid-Solid Two-Phase Flow in a Vertical Channel

3.1 Flow Configuration and Conditions. In the beginning, we calculated the two-dimensional liquid-solid two-phase flow in a vertical channel as a basic internal two-phase flow to validate the present method. The flow field is shown schematically in Fig. 3. Flow direction of both phases is downward. The Reynolds number is $\mathrm{Re} = U_c W/\nu = 5000$, based on the mean velocity on the centerline $U_c = 0.17$ m/s and the channel width $W = 0.03$ m. Here,

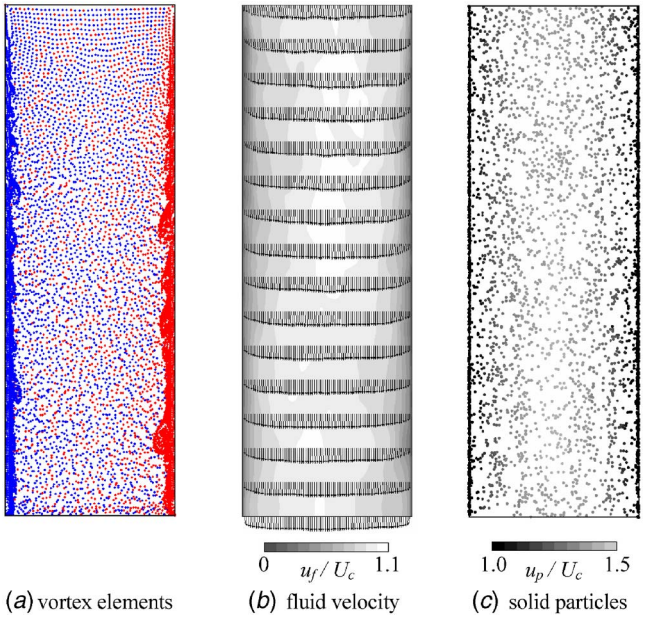

Fig. 4 Instantaneous distributions of vortex elements, fluid velocity, and solid particle

ν is the kinematic viscosity of water.

Periodic boundary conditions for both phases were applied in the streamwise direction due to restrictions on computational power. The length L of the computational region in the streamwise direction is $3W$.

Solid particles are introduced into the channel using random numbers, so as to satisfy a uniform distribution at the loading mass ratio, which is $m=1.1\times10^{-2}$. The density and diameter of the solid particles are $\rho_p=2590\ \mathrm{kg/m^3}$ (relative density: $\rho_p/\rho_f=2.59$) and $d_p=500\ \mu\mathrm{m}$, respectively.

The computational parameters are set as follows: The boundary panel size of the inlet, outlet, and wall is $\Delta l_{\mathrm{bp}}/W=0.025-0.1$, total number of boundary panel $N_{\mathrm{bp}}=200$, and the vorticity layer thickness on the wall boundary $h/W=0.00254$. The time step sizes of the fluid and solid particles are $\Delta t_f U_c/W=0.025$ and $\Delta t_p U_c/W=0.0025$, respectively.

The numerical simulation has been performed for the same conditions as those in the two-phase experiments of Hishida et al. [35].

3.2 Results. The numerical results of instantaneous distributions of vortex elements, fluid velocity, and solid particles are shown in Fig. 4. Also, the numerical results of the time-averaged streamwise velocities and the streamwise turbulence intensities of the fluid and solid particles are shown in Figs. 5 and 6. For the liquid flow aspect, the present numerical simulation by using a one-way model should be compared with the single-phase flow of the experimental data.

In this downward flow, the solid particle velocity is faster than that of the liquid because the density of solid particles is higher. The numerical results show good agreement with the experimental data of Hishida et al. [35]. The numerical result of the streamwise turbulence intensity of solid particles, however, is smaller than the experimental data. It is considered that this difference is affected by the assumption of the uniform solid particle size in this calculation, though actual solid particles (glass beads are used in the experiment) have the distribution of the particle diameter. As the conclusion, these validations clarified the applicability and the quantitative accuracy of the present numerical simulation scheme to a basic internal turbulent two-phase flow. However, under this condition of the mass loading of solid particles $m=1.1\times10^{-2}$ and the particle-fluid relative density $\rho_p/\rho_f=2.59$, the averaged volume concentration of particles is $C_V=4.25\times10^{-3}$, which previous studies [35] have shown to be enough to warrant inclusion of two-way coupling effects. Since the present numerical simulation is simplified as the one-way coupling, it cannot simulate that the liquid time-mean velocity and turbulence intensities are changed by the influence of solid particles such as the experimental data [35]. Therefore, we have a plan to extend the method to two-way coupling model in the future.

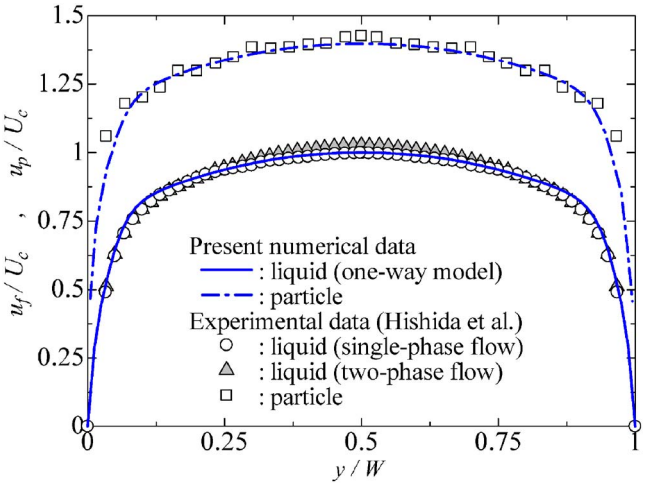

Fig. 5 Time-averaged streamwise velocities of liquid and solid particles

4 Liquid-Solid Two-Phase Flow in a Mixing Tee

4.1 Flow Configuration. We have applied our method to the two-dimensional liquid-solid two-phase flow in a mixing tee as a typical problem of mixing between liquid and solid particles in ducts. The flow field is shown in Fig. 7 schematically. The mixing tee not only is the basic component in industrial pipelines but is also used as a simple mixing device for multiphase flow. It is generally known that separation, recirculation, and adverse pressure distributions arise unsteadily after two flows are mixed perpendicularly, despite the simple configuration. For details, refer to Kawashima et al. [36,37], Blancard and Brunet [38], Khan et al. [39], Takahashi and Shiina [40], and Eroglu and Breidenthal [41].

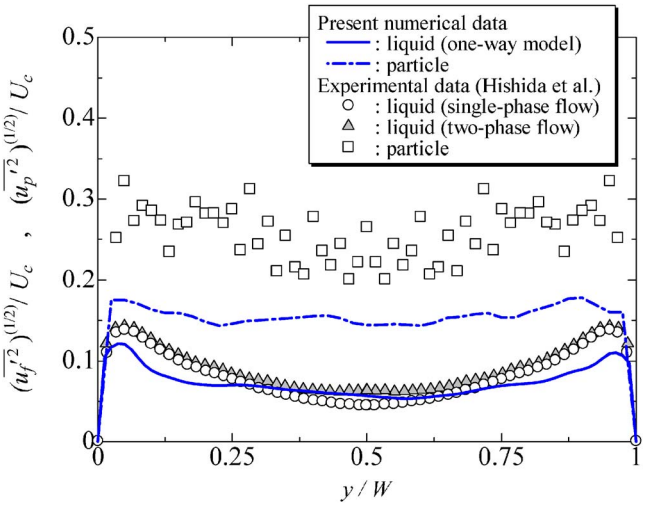

Fig. 6 Streamwise turbulence intensities of liquid and solid particles

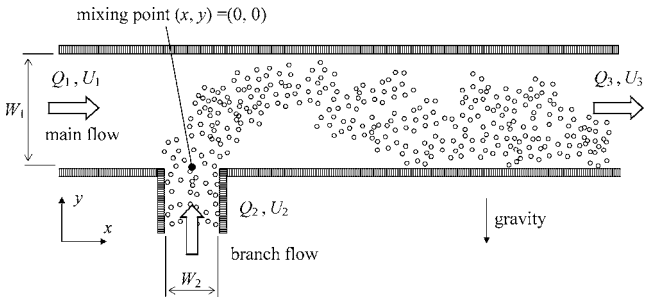

Fig. 7 Outline of the mixing tee problem

The solid particle flow pattern changes depending on the confluent flow rate ratio, and particle-wall collisions and particle depositions occur in some cases.

4.2 Conditions. In Fig. 7, the branch flow merges into the main flow at a right angle. The confluent corners have perpendicular edges. The Main and branch channel widths are W_1 and W_2, respectively, and the width ratio is $W_2/W_1=0.5$ ($W_1=20$ mm, $W_2=10$ mm). The two volumetric flow rates in the main and branch channels before confluence are Q_1 and Q_2, respectively; the confluent flow rate ratio Q_2/Q_1 is changed as $Q_2/Q_1=1,2,3$. The fluid momentum ratios M_2/M_1 are 2, 8, and 18. Q_2/Q_1 is controlled by changing only the volumetric flow rate of the branch channel. The velocity in the main channel is $U_1=0.25$ m/s, and the velocities in the branch channel are $U_2=0.5$ m/s, 1.0 m/s, 1.5 m/s. Reynolds numbers are $\mathrm{Re}=(U_3W_1)/\nu=10{,}000, 15{,}000, 20{,}000$, based on the average velocity U_3 and the width W_1 downstream of the confluent point. Here, ν is the kinematic viscosity of water.

Solid particles are introduced into the branch channel only using random numbers for initial locations, so as to satisfy uniform distribution at the volume concentration $C_V=0.01$. The density and averaged diameter of solid particles are $\rho_p=2590$ kg/m^3 (relative density: $\rho_p/\rho_f=2.59$) and $d_p=425$ μm, respectively. Uniform distribution of solid particle diameters is considered; the minimum and maximum diameters are $d_p=350$ μm and $d_p=500$ μm, respectively. The direction of gravity is downward in Fig. 7.

The computational parameters are set as follows: the boundary panel size of inlet, outlet, and wall is $\Delta l_{\mathrm{bp}}/W_1=0.05$, total number of boundary panel $N_{\mathrm{bp}}=470$, and the vorticity layer thickness on the wall boundary $h/W_1=0.00147$. The time step sizes of the fluid and solid particles are $\Delta t_f U_3/W_1=0.05$ and $\Delta t_p U_3/W_1=0.0025$, respectively.

4.3 Experimental Apparatus and Techniques. The confluent flow and solid particle motion have been investigated by measuring the flow patterns and the velocities of both phases in the mixing tee. The experimental apparatus is shown in Fig. 8. The liquid is water, and the solid particles are glass beads. The flows of the main and branch are circulated as closed loop by two pumps. The mixing tee is made of acrylic material. The runway intervals before confluence are 20 times the channel widths of the main and branch channels, respectively. The channel length after confluence is 50 times the main channel width. The channel depth is 15 times the main channel width. The solid particles are separated into the tank after confluence and conveyed into the branch channel only.

The schematic of the test section and measuring techniques are shown in Fig. 9. The solid particle motion was visualized by a sheet lamp. The velocities of both phases were measured using a laser Doppler velocimetry system (LDV) made by TSI Inc. The LDV probe can be moved in the streamwise and vertical directions by a traverse unit. The velocities were measured in the central section of the channel depth. The tracers of LDV were nylon particles of 4 μm diameter for the liquid and were the glass beads themselves for the solid particles.

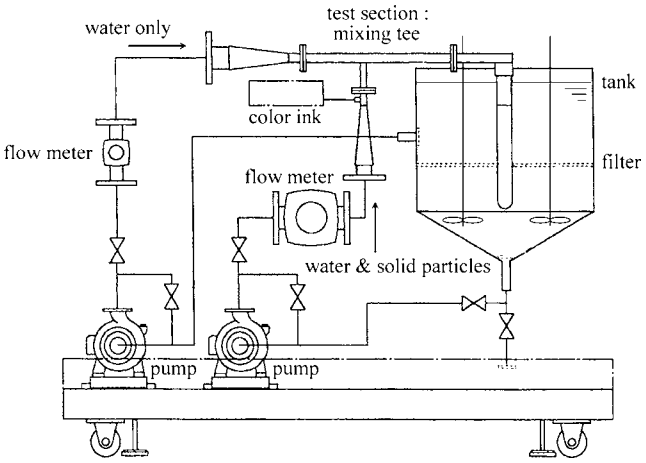

Fig. 8 Experimental apparatus of the liquid-solid two-phase flow in the mixing tee

The expanded uncertainty of measurement is estimated considering the flow regulation, traverse of the LDV probe, statistical work and calibration of LDV system, etc., to be about 8.9%. This expanded uncertainty is based on the converge factor ($k=2$), in which the confidence level is 95%.

4.4 Liquid Flow Aspects. Figure 10 shows snapshots of instantaneous distributions of vortex elements and fluid velocity obtained by the numerical simulation based on the one-way model. The condition of the confluent flow rate ratio is $Q_2/Q_1=2$, and the instantaneous nondimensional times are $tU_3/W_1=85.0$, 87.5, 90.0, and 92.5. The contour of velocity expresses the streamwise fluid velocity.

After two perpendicular flows merge in the mixing tee, the confluent flow deflects, and unsteady separations occur at the downward corner of the junction. First, the confluent flow is accelerated in the contraction region of the mixing point. Then, the flow is decelerated to the streamwise direction in the expansion. Consequently, unsteady flow separations are created and grow up from the bottom wall of the main channel because the adverse pressure gradients are strong in the flow direction. Such phenomena are also observed by ink trace visualization.

Under this condition, Reynolds number is $\mathrm{Re}=(U_3W_1)/\nu=15{,}000$. The Kolmogorov microscale η can be estimated by the ratio between the Kolmogorov microscale and the largest length scale $W_1=20$ mm such as $\eta/W_1\approx\mathrm{Re}_m^{-3/4}$, where Re_m is the Reynolds number based on the turbulence intensity I and the largest length scale. The averaged turbulence intensity is estimated as $I\approx 0.16\times\mathrm{Re}^{-1/8}=0.048$ of the outlet velocity in the main duct of $U_3=0.75$ m/s; therefore, $\mathrm{Re}_m=(U_3IW_1)/\nu=721$. Substituting Re_m into $\eta/W_1\approx\mathrm{Re}_m^{-3/4}$ gives the Kolmogorov microscale as about

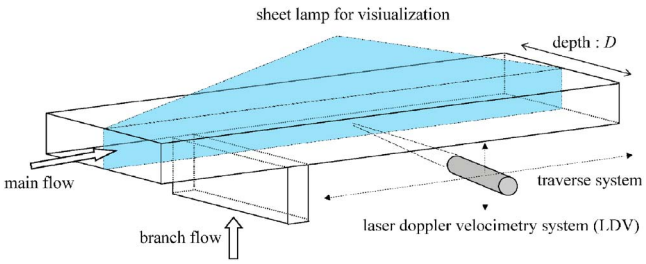

Fig. 9 Schematic of the measurement in mixing tee problem

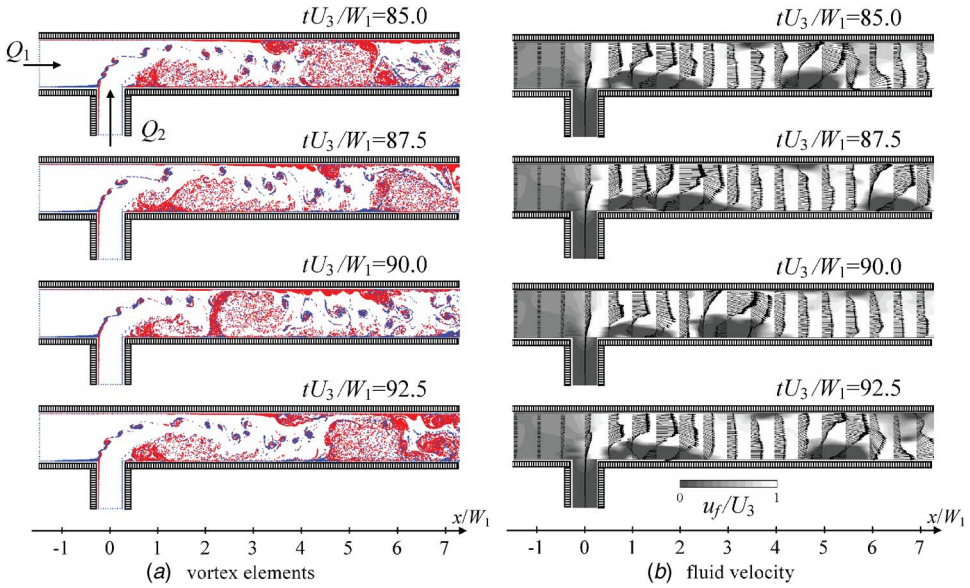

Fig. 10 Instantaneous distributions of vortex elements and fluid velocity (confluent flow rate ratio: $Q_2/Q_1=2$)

$\eta/W_1=0.0072$. Comparing between the minimum vortex element size obtained by numerical results and the Kolmogorov microscale estimated as above, the minimum vortex sheet size is $l_{vs}/\eta \approx 7$ and the minimum vortex blob size is $l_{vb}/\eta \approx 1.6$. Therefore, the minimum vortex element size treated in this numerical simulation is of the same order as the Kolmogorov microscale of the fluid flow. On the other hand, Fig. 10(*a*) shows that the broad scale vortices, especially the separation vortices generated from near the tee junction, are composed of the clusters of aggregated vortex elements, which develop approximately the largest length scale of the duct width. These vortex clusters interact with other neighboring clusters, and therefore aggregate, break up, and diffuse downward unsteadily. Also, the time-dependent liquid velocity at $x/W_1=3.5$ and $y/W_1=0.5$ is shown in Fig. 11. Because the broad scale vortices pass through the main duct after two perpendicular flows merge, numerical results show that the liquid velocity at a fixed point fluctuates unsteadily and randomly. As mentioned above, the present method can track the process of development and dissipation of broad scale turbulent vortices.

4.5 Solid Particle Flow Aspects. For the conditions $Q_2/Q_1=1,2,3$, we supposed that particle-wall collisions and particle depositions were changed by the confluent flow rate ratio and sought suitable conditions for the particle mixing.

Firstly, the forces on the solid particle are quantified under the condition of $Q_2/Q_1=2$. The comparison of the forces obtained by numerical results is shown in Fig. 12. Each force is averaged for all particles in the calculation region per a time step and normalized by the time-mean force of the steady-state drag force $\boldsymbol{F}_D$. The most dominant force is the steady-state drag force. The ratio of each force to the steady-state drag force is calculated as follows: The total lift force of Magnus and Saffman is $|\boldsymbol{F}_L|/|\boldsymbol{F}_D|=0.04$, the unsteady drag force (virtual added mass force) $|\boldsymbol{F}_{VM}|/|\boldsymbol{F}_D|=0.17$, and the gravitational force $|\boldsymbol{F}_G|/|\boldsymbol{F}_D|=0.3$. These numerical results denote that the total lift force of Magnus and Saffman is approximately a double-digit smaller than the steady-state drag force and

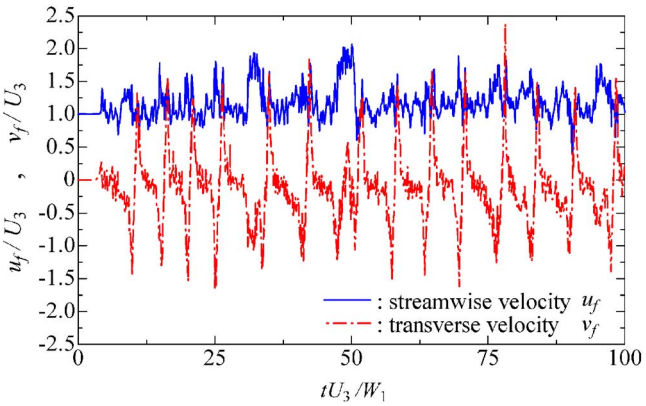

Fig. 11 Time-dependent liquid velocity at $x/W_1=3.5$ and $y/W_1=0.5$ (confluent flow rate ratio: $Q_2/Q_1=2$)

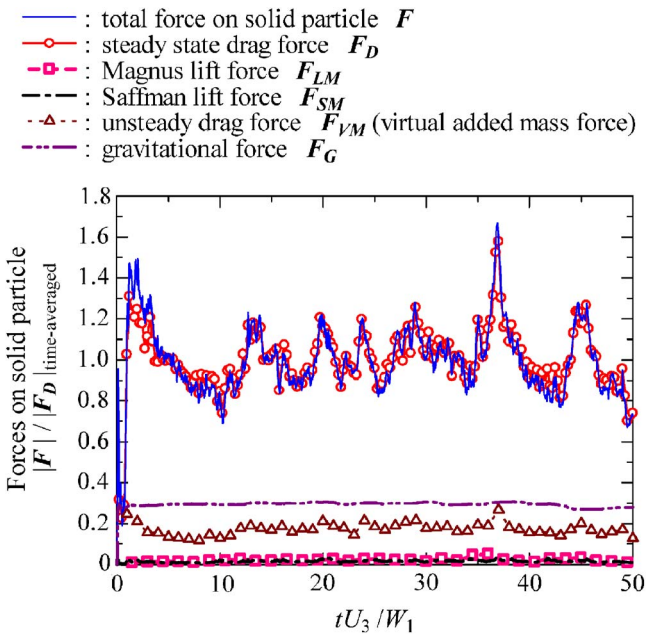

Fig. 12 Numerical results of the forces on solid particle (confluent flow rate ratio: $Q_2/Q_1=2$)

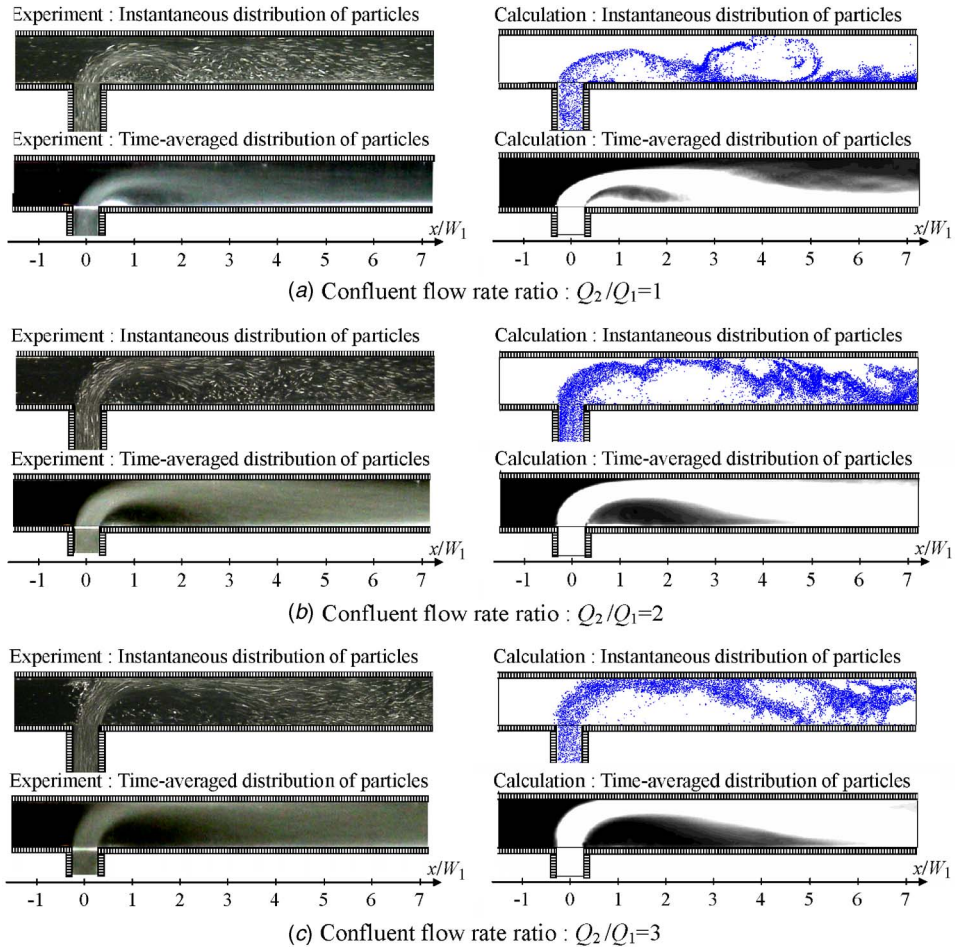

Fig. 13 Comparison between experiment and calculation for distribution of solid particles

can be negligible.

Secondly, the instantaneous and time-averaged distributions of solid particles are shown in Fig. 13, and numerical results are compared with experimental observations. Time-averaged experimental photographs were taken with long exposure. Additionally, Fig. 14 shows numerical results of time-averaged volume concentration of solid particles at $x/W_1=1$, 2, 3, and 4. Since the present numerical simulation assumes that the effect of solid particles on the fluid flow can be neglected (one-way model), it is considered that the accuracy of this calculation declines in the region of large local concentrations of solid particles, especially in the particle deposition region shown in Figs. 13 and 14. Therefore, the dynamic change of the solid particle flow pattern due to the three conditions of the confluent flow rate ratio is compared between the calculation and the experiment.

Under Condition (a) of $Q_2/Q_1=1$, particles move as a saltation flow on the bottom wall of the main channel, which is seen in both experiment and calculation. Particles are forced into the direction of gravity because the particles are heavier than liquid. Therefore, many particles settle down on the bottom wall at $x/W_1=2$. Almost settled particles do not lift because the turbulent flow of the mixing is small for $Q_2/Q_1=1$, and so particles move as a saltation flow. Besides, in the recirculation zone behind the downward corner of the junction, both experiment and calculation show that some particles are trapped and deposited. Thus, for $Q_2/Q_1=1$, the particle mixing in the confluent channel is not good.

Under Condition (b) of $Q_2/Q_1=2$, the turbulent flow acting on the mixing motion grows strongly. Experimental and numerical results show that particles mix nearly uniformly at $x/W_1=4$. As mentioned before, it is seen that the confluent flow deflects and unsteady separations occur at the downward corner of the junction. The confluent flow becomes unsteady and complex by the unsteady separation, which makes the particles mix throughout the confluent main channel. Thus, for $Q_2/Q_1=2$, the particle mixing is good.

Under Condition (c) of $Q_2/Q_1=3$, experimental and numerical results show that particles collide strongly on the upper wall just after the two perpendicular flows meet. Especially, hard particle-wall collisions occur at $x/W_1=0.5-1$. At this condition, the released particles from the branch channel have large inertia force in the upper direction. Accordingly, the particles collide with the upper wall because the particles cannot move along the suddenly curved liquid flow at the mixing tee. Thus, for $Q_2/Q_1=3$, the particle mixing is not good, since erosions or damage of the wall may arise due to heavy particle-wall collisions.

As a conclusion, it is considered that the confluent flow rate ratio $Q_2/Q_1=2$ is better suited for the particle mixing in the present configurations and the limited examined conditions of the Reynolds number of the fluid flow, the solid particle size, the particle-fluid density ratio, and others.

In this paper, we have examined the unsteady solid particle motion both numerically and experimentally and compared them. We found that the numerical results of solid particle motion are qualitatively in good agreement with the experimental observations, concerning solid particle flow patterns, particle-wall collisions, and depositions. Thus, for designing the devices including solid particle flows, numerical simulation will be a useful design tool to understand the solid particle motion in an effort to accomplish high efficiency and low cost.

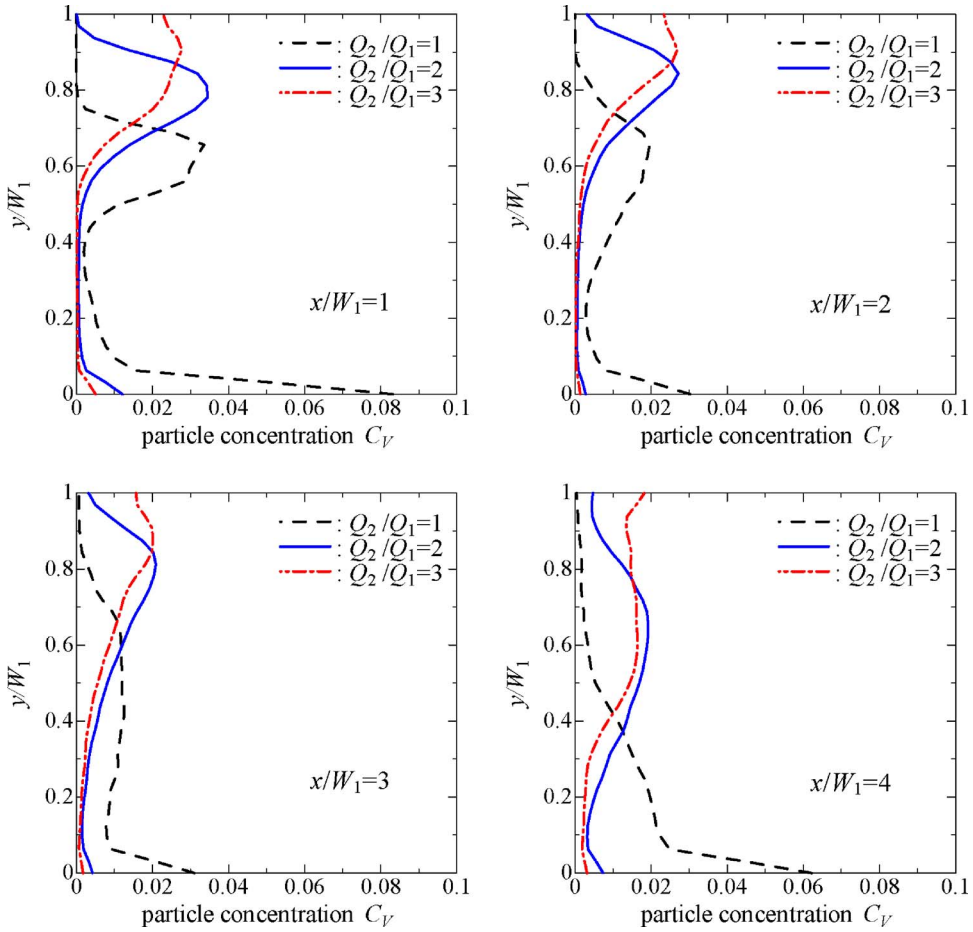

Fig. 14 Numerical results of time-averaged volume concentration of particles at x/W_1=1, 2, 3, and 4

4.6 Velocity Profiles of Liquid and Solid Particles. Figure 15 shows the time-averaged streamwise velocity profiles of liquid and solid particles, and compares numerical data with experimental data. The experimental data are measured by using LDV. The condition of the confluent flow rate ratio is Q_2/Q_1=2, and the locations are x/W_1=0 and 1.

At x/W_1=0, the branch flow is suddenly curved due to confluence. The released solid particles from the branch channel have inertia force in the upper direction, and so, the solid particle motion in the direction of liquid flow is delayed. Accordingly, the results showed that the solid particle streamwise velocity is smaller than that of the liquid.

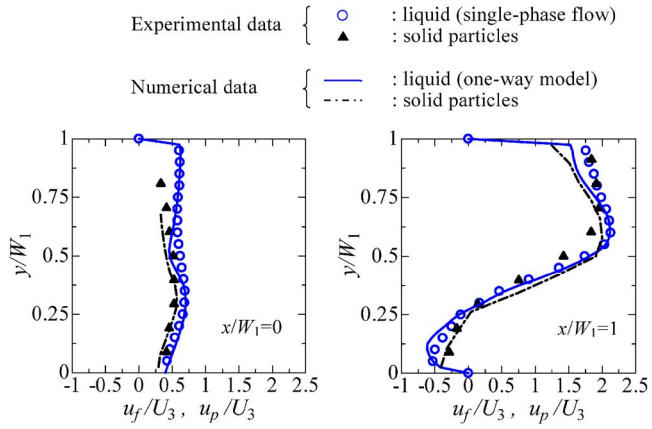

Fig. 15 Time-averaged streamwise velocity profiles of liquid and solid particles at x/W_1=0 and 1 (confluent flow rate ratio: Q_2/Q_1=2)

At x/W_1=1, solid particle velocity profile is approximately the same as that of liquid. The velocity profiles of both phases show a reverse flow region near the bottom wall and a contracting region in the upper zone because separation and recirculation arise from the downward corner of the junction.

Comparison with experimental data reveals that the numerical results show reasonably good agreement. As the conclusion, this study validates the application of our numerical method not only to external flows but also to internal unsteady two-phase flows, in which separation and recirculation occur due to flow mixing and adverse pressure gradients.

5 Conclusion

In this study, internal liquid-solid two-phase flows have been analyzed by the grid-free Lagrangian–Lagrangian simulation scheme using the vortex method and the particle trajectory tracking method, simplified as a two-dimensional flow and one-way model.

(1) For a vertical channel as a basic internal two-phase flow problem, numerical results of liquid flow and solid particles show good agreement with the experimental data. These validations prove the applicability and the quantitative accuracy of the present method into internal turbulent two-phase flow.
(2) For a mixing tee as a typical flow problem concerning mix-

ing of liquid and solid particles in ducts, numerical results of solid particle motions and velocity profiles agree reasonably well with the experimental data, with regard to solid particle flow patterns, particle-wall collisions, and depositions. Using our method to simulate the primary effect of turbulent vortices on the unsteady particle motion changed by volumetric flow rate ratio or geometry, we can obtain very useful information that is difficult to obtain by measurements for basic as well as actual devices.

In the latest research findings, we have extended the present method to more complex configurations, three-dimensional internal flows, and to consider a two-way coupling model [42,43]. In the future, we will go forward in evaluating this method for fluctuation characteristics of the three-dimensional turbulent fluid-solid two-phase flows.

References

[1] Crowe, C. T., 1982, "Review—Numerical Models for Dilute Gas-Particle Flows," ASME Trans. J. Fluids Eng., **104**(3), pp. 297–303.

[2] Crowe, C. T., Gore, R. A., and Troutt, T. R., 1985, "Particle Dispersion by Coherent Structures in Free Shear Flows," Part. Sci. Technol., **3**, pp. 149–158.

[3] Crowe, C. T., Chung, J. N., and Troutt, T. R., 1988, "Particle Mixing in Free Shear Flows," Prog. Energy Combust. Sci., **14**, pp. 171–194.

[4] Hishida, K., Ando, A., and Maeda, M., 1992, "Experiments on Particle Dispersion in a Turbulent Mixing Layer," Int. J. Multiphase Flow, **18**(2), pp. 181–194.

[5] Ishima, T., Hishida, K., and Maeda, M., 1993, "Effect of Particle Residence Time on Particle Dispersion in a Plane Mixing Layer," ASME J. Fluids Eng., **115**, pp. 751–759.

[6] Kamemoto, K., 2001, "Engineering Application of the Vortex Methods Developed in Yokohama National University (YNU)," *Proceedings of the Second International Conference on Vortex Methods*, Istanbul, Turkey, Sept. 26–28, pp. 197–209.

[7] Ojima, A., and Kamemoto, K., 2000, "Numerical Simulation of Unsteady Flow Around Three Dimensional Bluff Bodies by an Advanced Vortex Method," JSME Int. J., Ser. B, **43**(2), pp. 127–135.

[8] Kamemoto, K., and Ojima, A., 2000, "Applicability of the Vortex Methods for Aerodynamics of Heavy Vehicles," *The United Engineering Foundation Conference on the Aerodynamics of Heavy Vehicles: Trucks, Buses and Trains*, pp. 503–514.

[9] Chein, R., and Chung, J. N., 1987, "Effects of Vortex Pairing on Particle Dispersion in Turbulent Shear Flows," Int. J. Multiphase Flow, **13**(6), pp. 785–802.

[10] Wen, F., Kamalu, N., Chung, J. N., Crowe, C. T., and Troutt, T. R., 1992, "Particle Dispersion by Vortex Structures in Plane Mixing Layers," ASME J. Fluids Eng., **114**, pp. 657–666.

[11] Perkins, R. J., and Joia, I. A., 1995, "A Discrete Vortex Model for the Dispersion of Bubbles and Particles in a Plane Jet," *Proceedings of the Second International Conference on Multiphase Flow*, Kyoto, Japan, April 3–7, Paper No. PT-3, pp. 17–24.

[12] Wang, X. L., Chan, H. Y., Wang, H. Y., and Zhang, H. Q., 2001, "Quantitative Simulation of Gas-Particle Two Phase Plane Mixing Layer Using Discrete Vortex Method," Comput. Mech., **27**, pp. 418–425.

[13] Joia, I. A., Ory, E., and Perkins, R. J., 1998, "A Discrete Vortex Model of Particle Laden Jets," *Third International Conference on Multiphase Flow, ICMF'98*, Lyon, France, June 8–12.

[14] Uchiyama, T., and Naruse, M., 2002, "Numerical Simulation of Gas-Particle Two-Phase Mixing Layer by Vortex Method," Powder Technol., **125**, pp. 111–121.

[15] Uchiyama, T., and Fukase, A., 2005, "Three-Dimensional Vortex Method for Gas-particle Two-Phase Compound Round Jet," ASME J. Fluids Eng., **127**, pp. 32–40.

[16] Walther, J. H., and Koumoutsakos, P., 2001, "Three-Dimensional Vortex Methods for Particle-Laden Flows With Two-Way Coupling," J. Comput. Phys., **167**, pp. 39–71.

[17] Iso, Y., and Kamemoto, K., 2003, "Vortex Method for Lagrangian-Lagrangian Simulation Applied to Internal Liquid-Solid Two-Phase Flow," *Proceedings of the Second International Conference on Computational Methods in Multiphase Flow*, Santa Fe, NM, Nov. 3–5, pp. 159–168.

[18] Iso, Y., and Kamemoto, K., 2005, "Vortex Method and Particle Trajectory Tracking Method for Lagrangian-Lagrangian Simulation Applied to Internal Liquid-Solid Two-Phase Flows," *Proceedings of the Third International Conference on Vortex Flows and Vortex Models*, Yokohama, Japan, Nov. 21–23, pp. 287–292.

[19] Nakanishi, Y., and Kamemoto, K., 1993, "Numerical Simulation of Flow Around a Sphere With Vortex Blobs," J. Wind. Eng. Ind. Aerodyn. **46–47**, pp. 363–369.

[20] Wu, J. C., and Thompson, J. F., 1973, "Numerical Solutions of Time-Dependent Incompressible Navier-Stokes Equations Using an Integro-Differential Formulation," Comput. Fluids, **1**, pp. 197–215.

[21] Leonard, A., 1980, "Review—Vortex Methods for Flow Simulation," J. Comput. Phys., **37**, pp. 289–335.

[22] Morsi, S. A., and Alexander, A. J., 1972, "An Investigation of Particle Trajectories in Two-Phase Flow Systems," J. Fluid Mech., **55**(2), pp. 193–208.

[23] Maccoll, J. H., 1928, "Aerodynamics of a Spinning Sphere," J. R. Aeronaut. Soc., **32**, pp. 777–798.

[24] Davies, J. W., 1970, "The Aerodynamics of Golf Balls," J. Appl. Phys., **20**, pp. 821–828.

[25] Rubinow, S. I., and Keller, J. B., 1961, "The Transverse Force on Spinning Sphere Moving in a Viscous Fluid," J. Fluid Mech., **11**, pp. 447–459.

[26] Oesterle, B., and Dinh, T. B., 1998, "Experiments on the lift of a Spinning Sphere in a Range of Intermediate Reynolds Numbers," Exp. Fluids, **25**, pp. 16–22.

[27] Saffman, P. G., 1965, "The Lift on a Small Sphere in a Slow Shear Flow," J. Fluid Mech., **22**, pp. 385–400; 1968, "The Lift on a Small Sphere in a Slow Shear Flow," J. Fluid Mech., **31**, p. 624.

[28] Mei, R., 1992, "An Approximate Expression for the Shear Lift Force on a Spherical Particle at Finite Reynolds Numer," Int. J. Multiphase Flow, **18**(1), pp. 145–147.

[29] Dennis, S. C. R., Singh, S. N., and Inghan, D. B., 1980, "The Steady Flow Due to a Rotating Sphere at Low and Moderate Reynolds Numbers," J. Fluid Mech., **101**(2), pp. 257–279.

[30] Takagi, H., 1977, "Viscous Flow Induced by Slow Rotation of a Sphere," J. Phys. Soc. Jpn., **42**, pp. 319–325.

[31] Tanaka, T., and Tsuji, Y., 1991, "Numerical Simulation of Gas-Solid Two-Phase Flow in a Vertical Pipe: On the Effect of Inter-Particle Collision," *Gas-Solid Flows ASME/FED-121*, pp. 123–128.

[32] Yamamoto, Y., Potthoff, M., Tanaka, T., Kajishima, T., and Tsuji, Y., 2001, "Large-Eddy Simulation of Turbulent Gas-Particle Flow in a Vertical Channel: Effect of Considering Inter-Particle Collisions," J. Fluid Mech., **442**, pp. 303–334.

[33] Tsuji, Y., Morikawa, Y., Tanaka, T., Nakatsukasa, N., and Nakatani, M., 1987, "Numerical Simulation of Gas-Solid Two-Phase Flow in a Two-Dimensional Horizontal Channel," Int. J. Multiphase Flow, **13**(5), pp. 671–684.

[34] Tsuji, Y., Oshima, T., and Morikawa, Y., 1985, "Numerical Simulation of Pneumatic Conveying in a Horizontal Pipe," Kona, **3**, pp. 38–51.

[35] Hishida, K., Hanzawa, A., Sakakibara, J., Sato, Y., and Maeda, M., 1996, "Turbulent Structure of Liquid-Solid Two-Phase Channel Flow (I)," JSME, **62**(593) pp. 18–25; "Turbulent Structure of Liquid-Solid Two-Phase Channel Flow (II)," JSME, **62**(593) pp. 26–33.

[36] Kawashima, Y., Nakagawa, M., and Iuchi, S., 1982, "Characteristics of Mixing Due to Confluent Flow in a Two-Dimensional Right-Angled T-Shaped Flow Section," The Society of Chemical Engineers Japan, **8**(2), pp. 109–114.

[37] Kawashima, Y., Nakagawa, M., and Iuchi, S., 1982, "Flow Pattern at a Two-Dimensional, Right-Angled, T-Shaped Confluence," The Society of Chemical Engineers Japan, **8**(6), pp. 664–670.

[38] Blancard, J. N., and Brunet, Y., 1996, "Interaction Between a Jet Getting Out of a Thin Slit and Emerging Into a Cross Flow," ASME Fluids Eng. Div. Conf., **4**, pp. 39–46.

[39] Khan, A. A., Cadavid, R., and Wang, S. S.-Y., 2000, "Simulation of Channel Confluence and Bifurcation Using the CCHE2D Model," Proc. Inst. Civ. Eng., Waters. Maritime Energ., **142**, pp. 97–102.

[40] Takahashi, S., and Shiina, K., 2000, "Characteristics of Fluid Temperature Fluctuation in a Mixing Tee Pipe With Hot and Cold Water Flows," JSME, **66**(651), pp. 2905–2911.

[41] Eroglu, A., and Breidenthal, R. E., 2001, "Structure, Penetration, and Mixing of Pulsed Jets in Crossflow," AIAA J., **39**(3), pp. 417–423.

[42] Iso, Y., and Kamemoto, K., 2006, "Vortex Method and Particle Trajectory Tracking Method for Liquid-Solid Two-Phase Simulation Extended to Three-Dimensional Internal Flows," *The Japanese Society for Multiphase Flow Annual Meeting 2006*, Kanazawa, Japan, Aug. 4–6, pp. 326–327.

[43] Iso, Y., 2007, "Application of Vortex Method and Particle Trajectory Tracking Method into Numerical Simulation of Internal Multiphase Flows," Ph.D. thesis, Graduate School of Engineering, Yokohama National University, Japan.